สำนักหอสมุดกลาง พระจอมเกล้าลาดกระบัง

MICROWAVE PLASMA ENHANCED CHEMICAL VAPOR DEPOSITION SYNTHESIS AND CHARACTERIZATIONS OF NANOCRYSTALLINE DIAMOND FILMS

S.TIPAWAN KHLAYBOONME

เลขหมู่ 76495
เลขทะเบียน
วัน,เดือน,ปี 25 ส.ค. 2557

.b
.i

A THESIS SUBMITTED IN FULFILLMENT

OF THE REQUIREMENT FOR THE DEGREE OF

DOCTOR OF PHILOSOPHY IN APPLIED PHYSICS

FACULTY OF SCIENCE

KING MONGKUT'S INSTITUTE OF TECHNOLOGY LADKRABANG

2013

KMITL-2013-SC-D-030-018

This material is reserved for educational use only, not allowed for commercial use.

Forbidden to modify the content, and cite the document when use.

COPYRIGHT 2013

FACULTY OF SCIENCE

KING MONGKUT'S INSTITUTE OF TECHNOLOGY LADKRABANG

This material is reserved for educational use only, not allowed for commercial use.

Forbidden to modify the content, and cite the document when use.

หัวข้อวิทยานิพนธ์	การสังเคราะห์และตรวจวัดสมบัติผลึกระดับนาโนของฟิล์มเพชร โดยการตกสะสมไอเชิงเคมีเสริมด้วยพลาสมาที่กำเนิดด้วยคลื่นไมโครเวฟ
นักศึกษา	นางสาว ศ.ทิพวรรณ คล้ายบุญมี
รหัสประจำตัว	50067001
ปริญญา	ปรัชญาดุษฎีบัณฑิต
สาขาวิชา	ฟิสิกส์ประยุกต์
พ.ศ.	2556
อาจารย์ผู้ควบคุมวิทยานิพนธ์	รศ.ดร.วราวุฒิ เถาลัดดา

บทคัดย่อ

วิทยานิพนธ์เป็นการสร้างและออกแบบระบบการสังเคราะห์ฟิล์มบางเพชรที่มีขนาดผลึกระดับนาโนโดยการตกสะสมไอเชิงเคมีเสริมด้วยพลาสมาที่กำเนิดด้วยคลื่นไมโครเวฟ โดยระบบดังกล่าวได้ทำการสร้างขึ้นไว้ที่ห้องปฏิบัติการวิจัยฟิสิกส์พื้นผิวและเลเซอร์ สาขาวิชาฟิสิกส์ คณะวิทยาศาสตร์ สจล. การสังเคราะห์ฟิล์มบางเพชรจากระบบที่ได้ทำการสร้างและพัฒนาจึงเป็นเป้าหมายหลักของงานวิจัยนี้ โดยได้แบ่งจุดประสงค์ของวิทยานิพนธ์นี้ได้ออกเป็น 2 ข้อที่สำคัญด้วยกันคือ การออกแบบและสร้างรวมทั้งการพัฒนาระบบการปลูกฟิล์มเพื่อให้สามารถสังเคราะห์ฟิล์มบางเพชรที่มีผลึกระดับนาโนได้ และ เพื่อทำการศึกษากระบวนในการเกิดฟิล์มเพื่อเป็นพื้นฐานในการควบคุมกระบวนการของการเกิดฟิล์มซึ่งจะทำให้สามารถกำหนดและควบคุมสมบัติของฟิล์มบางได้ โดยระบบการปลูกฟิล์มบางเพชรนั้น ประกอบด้วย 3 ส่วนหลัก ๆ คือ รีแอกเตอร์สำหรับกำเนิดพลาสมา, ระบบสำหรับการกำเนิดและนำพาคลื่นไมโครเวฟเข้าสู่รีแอกเตอร์ และส่วนควบคุมอัตราการไหลของแก๊สและความดันภายในรีแอกเตอร์ สำหรับฟิล์มที่ทำการสังเคราะห์ขึ้นแล้วนั้น จะถูกนำไปตรวจวัดสมบัติของผลึกระดับนาโนทางด้านพื้นผิวและโครงสร้างระดับเคมีด้วยกล้องส่องกราดอิเล็กตรอนความละเอียดสูง, สเปกโทรสโกปีของรามาน, และ รีเฟกโตมิเตอร์ ในส่วนขององค์ประกอบของชนิดแก๊สที่มีอยู่ภายในพลาสมาจะถูกตรวจวัดด้วยสเปกโทรมิเตอร์เชิงแสงและชุดตรวจวัดอิมพีแดนซ์ของพลาสมา โดยความสัมพันธ์ของพื้นผิวและองค์ประกอบของผลึกฟิล์มบางเพชร กับ องค์ประกอบของแก๊สภายในพลาสมาจะเป็นตัวบ่งบอกกระบวนการในการเกิดเป็นฟิล์มบางเพชรได้

ในการใช้งานระบบการปลูกฟิล์มบางเพชรที่ได้ทำการสร้างและพัฒนาขึ้นมานั้น พบว่าสามารถปลูกฟิล์มบางเพชรที่มีขนาดผลึกระดับนาโนได้ โดยฟิล์มบางจะถูกสังเคราะห์ขึ้นจากแก๊สผสมระหว่าง แก๊สมีเทน กับ แก๊สไฮโดรเจน ปัจจัยของระบบที่มีความสำคัญต่อสมบัติของฟิล์ม

This material is reserved for educational use only, not allowed for commercial use.
Forbidden to modify the content, and cite the document when use.

ดังกล่าว ได้แก่ สภาพพื้นผิวของฐานรองรับ, ขั้นตอนในการสังเคราะห์ฟิล์มด้วยวิธีแบบ 2 ขั้นตอน, อิมพีแดนซ์ของพลาสมามา, ความดันภายในรีแอกเตอร์ และ ความเข้มข้นของแก๊สมีเทน จากการทดลองพบว่า ฟิล์มที่สังเคราะห์ลงบนพื้นผิวที่ได้รับการเตรียมพื้นผิวด้วยวิธีการขัดด้วยผงเพชรโดยใช้มือนั้น พบว่า ฟิล์มสามารถยึดติดลงบนฐานรองรับได้ดี และ ถ้าใช้ขั้นตอนการสังเคราะห์ฟิล์มแบบ 2 ขั้นตอนเข้าร่วมด้วย จะได้ฟิล์มที่มีความสม่ำเสมอและความเรียบบนผิวหน้าของฟิล์มมากขึ้น นอกจากนี้การใช้ขั้นตอนการสังเคราะห์ฟิล์มแบบ 2 ขั้นตอน ยังส่งผลให้อัตราการเกิดฟิล์มเพิ่มขึ้นจาก 430 นาโนเมตรต่อชั่วโมง เป็น 600 นาโนเมตรต่อชั่วโมง แต่จากการทดลองพบว่า อิมพีแดนซ์ของพลาสมาไม่มีผลต่ออัตราการเกิดฟิล์ม แต่กลับส่งผลต่อคุณภาพของฟิล์มบาง โดยพบว่า เมื่อทำการเปลี่ยนอิมพีแดนซ์ซึ่งเป็นผลให้ความหนาแน่นของอิเล็กตรอนภายในพลาสมามีค่ามากขึ้น จะได้ว่า สัดส่วนของคาร์บอน sp^3/sp^2 ในฟิล์มมีค่ามากขึ้น พีคที่แสดงตำแหน่งความเป็นเพชรเลื่อนจาก 1325 cm^{-1} ไปอยู่ที่ 1328.5 cm^{-1} และ ดัชนีหักเหเชิงแสงมีค่าเพิ่มขึ้นจาก 1.84 เป็น 2.16

สำหรับความดันภายในรีแอกเตอร์ พบว่า เมื่อความดันสูงขึ้นจาก 2 กิโลปาสกาล เป็น 25 กิโลปาสกาล ส่งผลให้อัตราการเกิดฟิล์มสูงขึ้นจาก 320 นาโนเมตรต่อชั่วโมง เป็น 450 นาโนเมตรต่อชั่วโมง ฟิล์มที่สังเคราะห์ขึ้นที่ความดัน 1 และ 2 กิโลปาสกาล พบว่าเป็นฟิล์มที่มีอัตราการดูดกลืนแสงสูงมาก ในขณะที่ฟิล์มที่สังเคราะห์ขึ้นที่ความดัน 5, 9 และ 25 กิโลปาสกาล มีค่าดัชนีหักเหเชิงเป็น 2.15, 2.21 และ 2.38 ตามลำดับ อย่างไรก็ตาม จากการผลการวัดด้วยสเปกโทรสโทรปีของรามานพบว่าขนาดผลึกเพชรมีขนาดใหญ่ขึ้นตามความดัน ซึ่งขนาดของผลึกเพชรดังกล่าวสามารถลดลงได้ด้วยการเพิ่มอัตราส่วนของแก๊สมีเทน โดยแก๊สมีเทนที่เพิ่มเข้าส่งผลทำให้ C_2 radical ภายในพลาสมามีค่าสูงขึ้น แต่กลับทำให้ CH radical มีค่าลดลง การเพิ่มขึ้นของ C_2 radical ส่งผลให้อัตราการเกิดผลึกเพชรที่มีขนาดเล็กมีอัตราสูงขึ้น ในขณะที่ CH radical ที่ลดลงนั้น ทำให้อัตราการเกิดฟิล์มนั้นช้าลง โดยจากการทดลอง พบว่า เมื่อความเข้มข้นของมีเทนเพิ่มจาก 1.5% เป็น 4.0% สเปกโทรสโกปีของรามานที่ตำแหน่งพีค 1140 cm^{-1} มีความเข้มลดลง ซึ่งแสดงให้เห็นว่าฟิล์มเพชรเกิดการเปลี่ยนขนาดผลึกของเพชรจากระดับนาโน เป็น ระดับอัลตรานาโน

คำสำคัญ : ผลึกเพชรระดับนาโน, พลาสมาไมโครเวฟ, การวัดอิมพีแดนซ์ของพลาสมา, สเปกโทรสโกปีของรามาน, และ รีเฟกโตมิทรีของแสงขาว.

This material is reserved for educational use only, not allowed for commercial use.
Forbidden to modify the content, and cite the document when use.

Thesis Title	Microwave Plasma Enhanced Chemical Vapor Deposition Synthesis and Characterizations of Nanocrystalline Diamond Films
Student	Miss S.Tipawan Khlayboonme
Student ID	50067001
Degree	Doctor of Philosophy
Program	Applied Physics
Year	2013
Thesis Advisor	Assoc. Prof. Dr. Warawoot Thowladda

ABSTRACT

In this thesis, a microwave plasma-enhanced chemical vapor deposition (MPECVD) apparatus has been constructed at Surface Physics and Laser Laboratory, Department of Physics, King Mongkut's Institute of Technology Ladkrabang. The goal of this research is to prepare nanocrystalline diamond (NCD) films from the constructed apparatus. This research has two main objectives. The first one is to design, construct, and develop the MPECVD apparatus for depositing NCD films. The second one is to study and understand growth mechanisms of the NCD films. The purpose-designed and built MPECVD apparatus is composed of three parts: a plasma reactor for precursor-vapor production and deposition, a part for microwave power generation and transfer of the power to the reactor, and a gas injection with a pressure control system. The deposited films were structurally characterized by field emission scanning electron microscopy, Raman spectroscopy, and whiteปlight reflectometry. *In situ* gas-phase species, including electron density, present in the plasma environment were monitored and measured during the growth process by optical emission spectroscopy and plasma impedance measurements. Morphology and composition of the deposited films and the gas-phase species were correlated to specify the growth mechanisms.

The purpose-built MPECVD reactor is successfully used to grow NCD films. The NCD films were deposited using a CH_4/H_2 gas mixture. The factors influencing the morphology and atomic-bonding structure of the films were studied. These factors are surface pretreatment method, two-step approach deposition, value of plasma impedance, reactor pressure, and methane concentration. The substrate surface pretreated by manual polishing with diamond powder caused the more surface energy to increase, that resulted in bettering the film formation sticky. In

This material is reserved for educational use only, not allowed for commercial use.
Forbidden to modify the content, and cite the document when use.

addition to the surface pretreatment, the films were carried out under a two-step deposition process enhanced the film formation continuous and smooth. The two-step process also increased growth kinetics. The growth rate increased from 430 nm/h for a single-step process to 600 nm/h for a two-step process. Whereas plasma impedance did not affect the growth kinetics but it affected the quality of the films. The plasma impedance that resulted in electron density in the plasma increasing promoted more sp^3-bonded carbon content in the films. The promoted sp^3-bonded carbon content resulted in diamond peak shifting from 1325 to 1328.5 cm^{-1} and refractive index increasing from 1.84 to 2.16.

In addition, the increased reactor pressure enhanced the growth kinetics. The growth rate increased from 320 nm/h for 2 kPa to 450 nm/h for 25 kPa. The films grown at 1 and 2 kPa were highly light absorbing material but the films grown at 5, 9, and 25 kPa were not. The refractive indexes of the films were 2.15 for 5 kPa, 2.21 for 9 kPa, and 2.38 for 25 kPa. However, Raman spectra showed the grain size of the films increased with increasing reactor pressure. The crystallite size of the films can be reduced by increasing methane concentration. The increased methane concentration encouraged C_2 radicals but discouraged CH radicals in the plasma. C_2 radicals did not play a role in the growth kinetics but bettered a renucleation rate. Raman spectra with decreasing intensity of the 1140 cm^{-1} peak revealed that the increasing methane concentration from 1.5% to 4.0% caused the phase transition from nanocrystallize to ultra-nanocrystallize diamond.

Keywords: Nanocrystalline diamond, Microwave plasma, Plasma impedance measurements, Raman spectroscopy, and White-light reflectometry.

This material is reserved for educational use only, not allowed for commercial use.

Forbidden to modify the content, and cite the document when use.

ACKNOWLEDGEMENTS

Firstly and foremost, I would like to express my highest respect and appreciation to my advisor, Assoc. Prof. Dr. Warawoot Thowladda, for giving me an opportunity to pursue my doctoral studies in his laboratory. I appreciate his effort, patient guidance, enthusiastic advice, assistance, and encouragement directed me during the completion of my thesis. I also appreciate his time devoted to giving advice and discussion throughout my thesis. I am highly grateful to be one of his students.

I would particularly like to give special thanks to Dr. Wirojana Tantraporn for providing funding and lying on a fascinating research to my laboratory.

I would like to give special thanks to Mr. Amorn Thedsakhulwong and Mr. Sompop Saejia for providing willing help and good friends of me.

I would like to acknowledge Department of Physics, KMITL, for allowing me to study for Doctoral degree.

Finally, I would like to express my thanks to my parent, my sister, and my brother for making my life meaningful and their willing help.

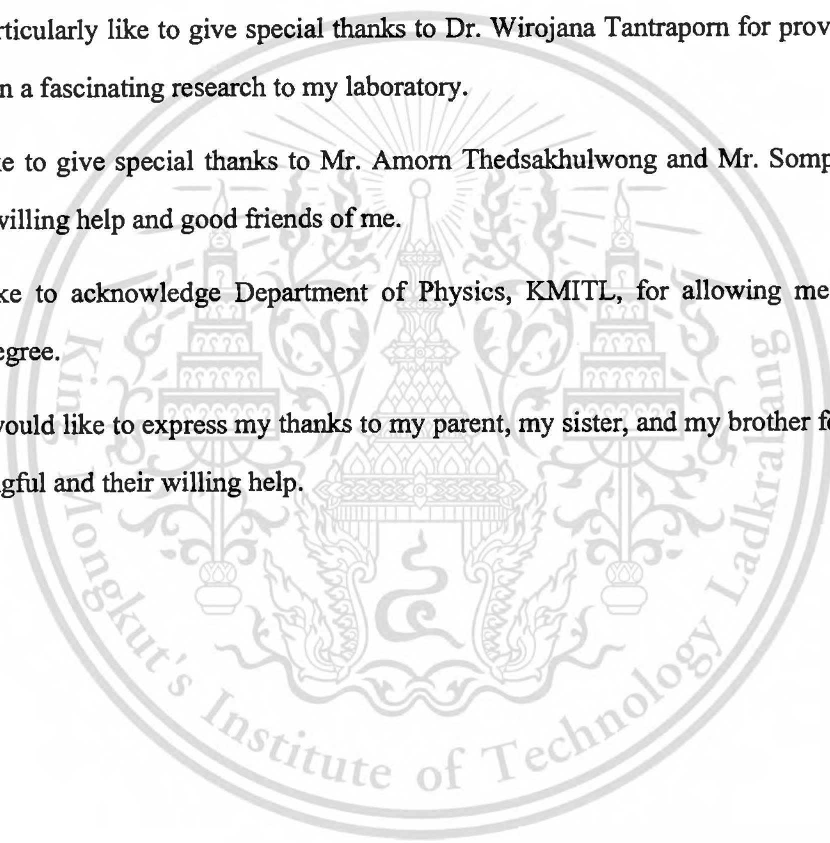

S.Tipawan Khlayboonme

This material is reserved for educational use only, not allowed for commercial use.
Forbidden to modify the content, and cite the document when use.

TABLE OF CONTENTS

PAGE

ABSTRACT (THAI)..I

ABSTRACT (ENGLISH)..III

ACKNOWLEDGEMENTS..V

TABLE OF CONTENTS..VI

LIST OF TABLES..XII

LIST OF FIGURES..XIII

CHAPTER 1 INTRODUCTION..1

1.1. Motivation..1

1.2. Objectives of Thesis..1

1.3. Research Background..2

1.4. Problem Statement..3

1.5. Thesis Scope..3

1.6. Thesis Outline..3

References..4

CHAPTER 2 THEORETICAL BACKGROUND..6

2.1 Literature Reviews of CVD Diamond..6

2.2 Phase Diagram of Carbon-based Materials..7

2.3 Crystal Structure and Properties of Diamond..8

2.4 Nanocrystalline Diamond..10

2.5 Chemical Vapor Deposition..12

2.5.1 Kinetics of CVD..13

This material is reserved for educational use only, not allowed for commercial use.
Forbidden to modify the content, and cite the document when use.

TABLE OF CONTENTS (cont.)

PAGE

2.5.2 Rate Limiting Steps 14

2.5.3 CVD Techniques 16

2.6 Microwave Plasma-enhanced CVD Technique for Diamond Growth 16

2.6.1 Microwave Plasma Source 17

2.6.2 Plasma-enhanced CVD of Diamond Growth 20

2.6.3 Gas-phase Chemistry and Gas-surface Reactions 21

2.6.4 Growth Model of Diamond Films 24

2.7 Nucleation Stage of Diamond Growth 28

2.8 Plasma Diagnosis Techniques 28

2.8.1 Measurements of Plasma Impedance 29

2.8.2 Plasma Diagnostics by OES 32

2.9 Characterization Techniques 36

2.9.1 Filed Emission Scanning Electron Microscopy (FE-SEM) with Energy Dispersive X-ray Spectroscopy (EDS) 36

2.9.2 Auger Electron Spectroscopy (AES) 37

2.9.3 Raman Spectroscopy 37

2.9.4 White Light Spectroscopic Reflectometry 41

References 44

CHAPTER 3 EXPERIMENTAL SETUP 56

3.1 The Microwave Plasma-enhanced Chemical Vapor Deposition System 56

3.1.1 Purpose-designed and built MPECVD systems 58

3.1.2 Plasma Reactor and Substrate Holder 64

3.1.3 Baseplate Design 65

This material is reserved for educational use only, not allowed for commercial use.
Forbidden to modify the content, and cite the document when use.

TABLE OF CONTENTS (cont.)

PAGE

3.1.4 Gas Flow Rate Control and Pressure Control Subsystem 67

3.1.5 Microwave Power Supply 68

3.1.6 *In situ* Plasma Diagnoses 70

3.2 Steps of Diamond Film Growth 72

3.2.1 Substrate Pretreatment Method 72

3.2.2 Diamond Deposition 73

3.3 Film Characterizations 74

3.3.1 Field Emission Scanning Electron Microscopy with Energy Dispersive X-ray Spectroscopy 74

3.3.2 Auger Electron Spectroscopy 75

3.3.3 Raman Spectroscopy 76

3.3.4 Micro White-light Reflectometry 78

3.4 Substrate Surface Characterizations 78

3.4.1 An Optical Microscope 78

3.4.2 Contact Angle Measuring Instrument 79

CHAPTER 4 CHARACTERIZATIONS OF MPECVD REACTOR **80**

4.1 Microwave Source Design 80

4.2 Operational Testing of the Purpose-built MPECVD Reactor 82

4.2.1 Testing of Vacuum and Gas-Flow Systems 82

4.2.2 Reactor-system Features 82

4.2.3 Microwave-power Supply Characteristics 83

4.2.4 Substrate Temperature 85

4.2.5 Effect of Shape of Gas Inlet Tube 86

This material is reserved for educational use only, not allowed for commercial use.
Forbidden to modify the content, and cite the document when use.

TABLE OF CONTENTS (cont.)

PAGE

4.3 Characterization of MPECVD Apparatus 89

4.3.1 Microwave Power-dependent MPECVD Apparatus 89

4.3.2 Reactor Pressure-dependent MPECVD apparatus 95

4.3.3 Effect of Methane Concentration 99

References 106

CHAPTER 5 SYNTHESIS AND CHARACTERIZATION OF NANOCRYSTALLINE DIAMOND FILMS 109

5.1 Nucleation and Growth Dynamics of Diamond Films 109

5.1.1 Design of Experiment 110

5.1.2 Effect of Surface Pretreatment Methods on Surface Morphology 111

5.1.3 Time-dependent Nuclei Density of Diamond 111

5.1.4 Surface Energy of Substrate 116

5.1.5 Summary 116

5.2 Trace Composition of Diamond films 117

5.2.1 Trace Element Composition of the Films by EDS Analysis 117

5.2.2 Trace Element Analysis of Diamond Films by AES Technique 119

5.2.3 Trace Oxygen Element in the Deposited Films 120

5.2.4 Summary 122

5.3 Two-step Approach Deposition Process 122

5.3.1 Design of Experiment 123

5.3.2 Diamond Film Morphologies 124

This material is reserved for educational use only, not allowed for commercial use.
Forbidden to modify the content, and cite the document when use.

TABLE OF CONTENTS (cont.)

PAGE

5.3.3 Non-diamond Carbon Content by Raman Spectroscopy 125

5.3.4 Optical Properties via White-light Reflectometer 127

5.3.5 Plasma Impedance and Plasma Species 128

5.3.6 Summary 131

5.4 Surface Pretreatment on the Film Formation with Two-step Approach 131

5.4.1 Design of Experiment 131

5.4.2 Diamond Films Formation at 5 kPa: FE-SEM and Raman Studies 132

5.4.3 Diamond Film Formation at 2 kPa: FE-SEM and Raman Studies 135

5.4.4 Summary 137

5.5 Pressure-dependent Nanocrystalline Diamond Films 138

5.5.1 Design of Experiment 138

5.5.2 FE-SEM Analysis 139

5.5.3 Raman Spectroscopy 141

5.5.4 Optical Properties via Reflectometry 142

5.5.5 Measurements of Plasma Impedance 143

5.5.6 NCD Films and Gas-phase Species 144

5.5.7 Summary 145

5.6 Plasma Impedance Tuning Effect on Nanostructured Diamond Films 146

5.6.1 Design of Experiment 147

5.6.2 Plasma Chemistry 148

5.6.3 Morphology and Structure of the Films 151

5.6.4 Summary 156

5.7 Methane concentration on Phase Transformation of NCD Films 156

This material is reserved for educational use only, not allowed for commercial use.

Forbidden to modify the content, and cite the document when use.

TABLE OF CONTENTS (cont.)

PAGE

5.7.1 Design of Experiment 157

5.7.2 Surface Morphology and Structure of the Films 158

5.7.3 Plasma Impedance and Plasma Species 162

5.7.4 Summary 166

References 167

CHAPTER 6 CONCLUSION 173

6.1 Nucleation and Growth Dynamics of Diamond Films 173

6.2 Two-step Approach Deposition Process 173

6.3 Reactor Pressure on NCD Films 174

6.4 Plasma Impedance Tuning Effect on Nanostructured Diamond Films 175

6.5 Methane Concentration on Phase Transformation of NCD Films 175

APPENDIX A PAPER I 177

APPENDIX B PAPER II 194

APPENDIX C ABOUT AUTHOR 203

This material is reserved for educational use only, not allowed for commercial use.

Forbidden to modify the content, and cite the document when use.

LIST OF TABLES

PAGE

Table 2.1 Some of outstanding properties of diamond and possible application for synthetic diamond films……………..……..………………………………9

Table 2.2 The optical emission line observed in this thesis for a mixture of CH_4/H_2 ……...35

This material is reserved for educational use only, not allowed for commercial use.
Forbidden to modify the content, and cite the document when use.

LIST OF FIGURES

PAGE

Figure 2.1 The phase diagram for diamond and graphite. 8

Figure 2.2 Structure of diamond crystal........ 9

Figure 2.3 Structure of some representative carbon allotropes........ 11

Figure 2.4 Schematic of NCD morphology (a) and UNCD morphology (b) 12

Figure 2.5 Basic steps in the CVD process........ 13

Figure 2.6 Sequence of events during CVD: (a) diffusion of reactants through boundary layer, (b) adsorption of reactants on substrate, (c) chemical reaction takes place, (d) desorption of adsorbed species, and (e) diffusion out of by-products through boundary layer. 14

Figure 2.7 Surface reaction limited growth in CVD........ 15

Figure 2.8 Mass transport limited growth in CVD. 15

Figure 2.9 Typical microwave power supply and simplified graph of power flow in a microwave plasma source........ 17

Figure 2.10 Reaction sequence in PECVD. 21

Figure 2.11 Three main processes occurring to the input gases during CVD diamond growth: activation, species transport, and surface chemistry........ 22

Figure 2.12 Schematic presentation of the surface processes during diamond growth: (a) hydrogen stabilized diamond surface, and (b) creation of a surface-radical site by hydrogen abstraction........ 24

Figure 2.13 A schematic diagram of a simplified version of the standard growth model for CVD diamond growth mechanism and, in red line, the new bonds formed........ 25

Figure 2.14 Schematic diagram of the various (100)-(2x1) reconstructed surface and bridge sites important for diamond growth and renucleation: (a) A hydrogen terminated diamond surface, (b) A surface radical site C_d^* , (c) A surface biradical site C_d^* . (d) A different type of surface biradical site, $C_d^* - C_d^*$, followed by its reaction with methyl to give a CH_2 surface group, and (e) The radical site also reacts with a C atom (or CH radical, not shown) to give a reactive-surface adduct, C_d^{**} 26

This material is reserved for educational use only, not allowed for commercial use.

Forbidden to modify the content, and cite the document when use.

LIST OF FIGURES (cont.)

PAGE

Figure 2.15 Schematic installation of the *STHT* 2.45 GHz AIAMS. 30

Figure 2.16 The different possibilities of visual light scattering: Rayleigh scattering, Stokes scattering, and anti-Stokes scattering. 38

Figure 2.17 Schematic of a micro-Raman spectrometer. 38

Figure 2.18 Raman spectra of carbon-based materials. 40

Figure 2.19 Schematic of laboratory setup for measurements of spectral reflectance. 42

Figure 2.20 Spectrum of the reflected light signal along with the wavelength shows the intensity changed at each wavelength. 42

Figure 3.1 Schematic of a purpose-designed and built MPECVD apparatus. 57

Figure 3.2 Cross-section geometry of the MPECVD apparatus. 58

Figure 3.3 An early purpose-built MPECVD apparatus (2007) which was equipped needle valves to control the volumetric gas-flow rates. 59

Figure 3.4 The later version of the MPECVD apparatus and baseplate. 60

Figure 3.5 Gas manifold: the MFC, supply line and shut-off valves. 61

Figure 3.6 Design of the MPECVD apparatus and rack. 62

Figure 3.7 Photograph of the last version of the MPECVD apparatus developed at Surface Physics and Laser Research Laboratory. 63

Figure 3.8 Photograph of the last version of the MPECVD apparatus (a) and the baseplate fixed to a liner ball bearing and shaft (b). 64

Figure 3.9 The reactor chamber with a baseplate was fixed to the linear ball bearing and shafts (a) and the reactor chamber attached to the cylindrical waveguide during plasma ignition (b). 64

Figure 3.10 Pyrex® bell jar after using as the plasma chamber for 30 min. 65

Figure 3.11 Bottom side of the baseplate 66

Figure 3.12 Top of the baseplate 66

Figure 3.13 Baseplate design water-cooling jacket of the baseplate. 66

Figure 3.14 Schematic representation of the gas supply system 67

This material is reserved for educational use only, not allowed for commercial use.

Forbidden to modify the content, and cite the document when use.

LIST OF FIGURES (cont.)

PAGE

Figure 3.15 The circuit of the microwave power supply. 68

Figure 3.16 A purpose-built microwave-power supply for a MPECVD reactor. 69

Figure 3.17 OceanOptics HR4000 spectrometer. 70

Figure 3.18 OceanOptics' SpectraSuite software interface. 71

Figure 3.19 Air-cooled HOMER-Series *STHT* V 1.5. 71

Figure 3.20 Example of *HomSoft* graphical user interface. 72

Figure 3.21 Hitachi S-4700 FE-SEM operated by TMEC. 74

Figure 3.22 BDL600 Back-Display LEED-AUGER spectrometer with a laboratory setup. 75

Figure 3.23 NT-MDT INTEGRA spectra. 76

Figure 3.24 Reinshaw inVia micro-Raman microscope. 76

Figure 3.25 The 514.5 Raman spectra from a Reinshaw inVia Raman microscope of a diamond single crystal (a) and highly orientated pyrolitic graphite (b). 77

Figure 3.26 Micro-optical reflectometer with a laboratory setup. 78

Figure 3.27 Optical microscope setup. 79

Figure 3.28 Contact angle measuring instrument with a laboratory setup. 79

Figure 4.1 Microwave setup used for growth of diamond films. 81

Figure 4.2 Color photographs of the plasma at two absorbed microwave-power: (a) 500 W and (b) 750 W. 83

Figure 4.3 The microwave power incident at the plasma chamber is as a function of AC voltage input of high-voltage transformer under a total mass flow rate of 200 sccm, reactor pressure 20 kPa, and 1%CH_4 in H_2 gas. 84

Figure 4.4 Substrate temperature versus absorbed microwave power into the plasma reactor under different pressures of the H_2 gas and mass flow rates of 200 sccm and 150 sccm. 85

This material is reserved for educational use only, not allowed for commercial use.

Forbidden to modify the content, and cite the document when use.

PAGE

Figure 4.5 (a) An U-shaped gas inlet, (b) SEM image showing the effect of configuration of gas inlet on the microstructure development of diamond films, and (c) isolated diamond particles of the ball-like-shaped clusters. 87

Figure 4.6 (a) A L-shaped gas-inlet tube and (b) FE-SEM image shows the effect of configuration of gas inlet on the microstructure development of diamond films and an inset cross-section image. 88

Figure 4.7 (a) A straight gas-inlet tube with 15 mm high from the substrate surface, (b) SEM image showing the effect of configuration of gas inlet on the microstructure development of diamond films, and (c) isolated diamond particles of the ball-like-shaped clusters. 88

Figure 4.8 Normalized plasma impedance of H_2 and 0.9%CH_4 in H_2 plasmas is as a function of absorbed microwave power under a reactor pressure of 5 kPa and an inset magnified Smith chart. 90

Figure 4.9 Normalized electron density as a function of absorbed microwave power under a reactor pressure of 5 kPa. 91

Figure 4.10 Normalized electron temperature as a function of absorbed microwave power at a reactor pressure of 5 kPa. 91

Figure 4.11 The optical emission intensity of H_β and intensity ratio of H_δ to H_β is as a function of absorbed microwave power at a pressure of 5 kPa in H_2 plasma and 0.9% CH_4 in H_2 plasma. 92

Figure 4.12 The normalized electron density versus the optical emission intensity of H_β. 93

Figure 4.13 The *in situ* optical emission spectra from CH_4-H_2 mixed gas under various absorbed microwave power. 94

Figure 4.14 Emission intensities of CH(B), CH(A), C_2(d-a), CH^+, and H_β as a function of absorbed microwave power. 95

This material is reserved for educational use only, not allowed for commercial use.
Forbidden to modify the content, and cite the document when use.

LIST OF FIGURES (cont.)

PAGE

Figure 4.15 Normalized plasma impedance of H_2 and 0.9%CH_4- H_2 plasmas as a function of reactor pressure ranging from 2 to 30 kPa at a fixed applied microwave power and an inset magnified Smith chart. 96

Figure 4.16 The normalized electron density and temperature as a function of reactor pressure. All electron densities are normalized to a measured value of H_2 plasma operated at a pressure of 5 kPa and absorbed microwave power of 702 W. 96

Figure 4.17 OES peak intensities from the H_2 plasma as a function of reactor pressure for H_β, H_γ, H_δ and $I(H_\delta)/I(H_\beta)$ ratio acting as electron temperature T_e 97

Figure 4.18 The *in situ* optical emission spectra from CH_4-H_2 mixed gas under various reactor pressures. 98

Figure 4.19 Emission intensities from CH(B), CH(A), C_2(d-a), CH^+, and H_β are plotted as a function of the reactor pressure. 99

Figure 4.20 Emission intensity ratio of CH(B), CH(A), C_2(d-a), and CH^+ to H_β as a function of the reactor pressure. 99

Figure 4.21 Plasma impedance under various methane concentrations. 100

Figure 4. 22 The normalized electron density and temperature of CH_4-H_2 plasma at a reactor pressure of 5 kPa and under various CH_4 flow rates. 101

Figure 4.23 The relative changes of electron temperature determined by two methods: plasma impedance measurements (PIM) and optical emission spectroscopy (OES). 102

Figure 4.24 Optical emission spectra of the H_2-CH_4 plasma under various methane concentrations: Waterfall graph (a) and Stack lines graph (b). 103

Figure 4.25 Optical emission lines of CH(B) CH(A), CH^+, C_2(d-a), and H_β species as a function of CH_4 flow rate at the reactor pressure of 5 kPa 104

Figure 4.26 Emission intensities of CH(B), CH(A), C_2(d-a), and CH^+ to H_β as a function of the methane concentrations. 105

This material is reserved for educational use only, not allowed for commercial use.

Forbidden to modify the content, and cite the document when use.

PAGE

Figure 5.1 Optical microscope images of Si wafer surfaces at different polishing methods: (a) untreated mirror-polished, (b) ultrasonic-polished, and (c) manual-polished Si substrates. 111

Figure 5.2 FE-SEM images of diamond nucleation on Si substrate surface polished by mechanically hand with 0-1/2 micro-size diamond powder for 30 min at different deposition times: (a) 15 min, (b) 30 min, (c) 45 min, (d) 60 min, (e) 120 min, and (f) 360 min. 112

Figure 5.3 FE-SEM images of diamond nucleation on Si substrate surface polished by ultrasonically vibrating with 0-3 micro-size diamond powder for 90 min at different deposition times: (a) 15 min, (b) 30 min, (c) 45 min, (d) 60 min, (e) 120 min, and (f) 6 h. 113

Figure 5.4 FE-SEM images of development of diamond growth on mirror-polished Si substrate-surface under deposition time of 6 h. 114

Figure 5.5 Kinetics of the nucleation density on Si substrate surfaces pretreated by two methods: manual and ultrasonic polishing. 115

Figure 5.6 Kinetics of the mean size of the diamond nuclei on Si substrate surfaces pretreated by two methods: manual and ultrasonic polishing. 115

Figure 5.7 Images of deionized water contact angle on Si substrate surfaces under various pretreatment methods: (a) mirror polishing, (b) ultrasonic polishing for 90 min, and (c) manual polishing for 30 min. 116

Figure 5.8 Diamond-film compositions measured by EDS analysis. The ratio of O to C was around 16 : 100. 117

Figure 5.9 (a) A cross-section image of the film measured composition of the interlayer near substrate and (b) the cross-section image showing positions on the interlayer measured by EDS. 118

Figure 5.10 EDS analysis mapping images of the diamond film at two interlayer positions near substrate shown in **Figure 5.9**(b): (a) Position 1, and (b) Position 2. The ratio of O to C was around 15 : 1. 118

This material is reserved for educational use only, not allowed for commercial use.

Forbidden to modify the content, and cite the document when use.

LIST OF FIGURES (cont.)

PAGE

Figure 5.11 AES spectra of the deposited films. 119

Figure 5.12 Auger spectra of (a) a deposited film and (b) graphite. The values of D width are given in the figure. 120

Figure 5.13 Auger spectra of the silicon surfaces (a) as-cleaned, (b) after a piranha process, (c) after (b) and then dipping in diluted HF solution, and (d) after (c) and then *in situ* cleaning in H_2 plasma. 121

Figure 5.14 FE-SEM images and inset cross-section images of the films deposited by (a) single-step process with 0.9%CH_4, (b) single-step process with 2.0%CH_4, and (c) two-step process. 124

Figure 5.15 Raman spectra with raw data and various fit components of the deposited films after subtraction of the photoluminescence background: (a) single-step process with 0.9%CH_4, (b) single-step process with 2.0%CH_4, and (c) two-step process. 126

Figure 5.16 The reflectance spectra of the films deposited by (a) single step with 0.9% CH_4, (b) single step with 2.0% CH_4, and (c) two-step process with changing CH_4 concentration. 128

Figure 5.17 Normalized electron densities and electron temperatures versus process time for 2.0%CH_4 single-step, 0.9%CH_4 single-step and two-step deposition processes. 129

Figure 5.18 Emission intensities of C_2(d-a) to H_β versus process time for single-step and two-step approach deposition processes. 129

Figure 5.19 Emission intensities of CH(A) to H_β versus process time for single-step and two-step approach deposition processes. 130

This material is reserved for educational use only, not allowed for commercial use.
Forbidden to modify the content, and cite the document when use.

LIST OF FIGURES (cont.)

PAGE

Figure 5.20 FE-SEM top-view and cross-section images of microstructure of the films deposited under a reactor pressure of 5 kPa and on the substrate surface pretreated by three polishing methods: (a) no pretreatement (mirror), (b) ultrasonic polishing, and (c) manual polishing. 133

Figure 5.21 Raman spectra of NCD films deposited on surfaces pretreated with different pretreatment methods and under a reactor pressure of 5 kPa. The large feature around 900-1000 cm^{-1} is the second order from Si substrate. 134

Figure 5.22 FE-SEM top-view and cross-section images of microstructure of the films deposited under a reactor pressure of 2 kPa and on the substrate surface pretreated with three polishing methods: (a) no pretreatement (mirror), (b) ultrasonic polishing, and (c) manual polishing. 136

Figure 5.23 Raman spectra of NCD films deposited on surfaces pretreated with different pretreatment methods and under a reactor pressure of 2 kPa. 137

Figure 5.24 FE-SEM images of NCD films grown on Si substrates under various pressures: (a) 25 kPa, (b) 9 kPa, (c) 5 kPa, (d) 2 kPa, and (e) 1 kPa and cross-section images. 140

Figure 5.25 Growth rate of NCD films as a function of the reactor pressure. 140

Figure 5.26 Raman spectra with the photoluminescence background of NCD films under various pressures: 1, 2, 5, 9, and 25 kPa 141

Figure 5.27 Reflectance spectra of the NCD films grown under various reactor pressures: (a) 25 kPa, (b) 9 kPa, and (c) 5 kPa. 142

Figure 5.28 Relative change of n_e and ratios of optical emission intensity of CH(A-X) to H_β, I(CH)/I(H_β), as a function of the reactor pressure. 143

This material is reserved for educational use only, not allowed for commercial use.

Forbidden to modify the content, and cite the document when use.

LIST OF FIGURES (cont.)

PAGE

Figure 5.29 Normalized plasma impedance of H_2 and CH_4-H_2 plasma under different plasma impedances: (solid oval line) impedance inducing a high n_e, and (dashed oval line) impedance inducing a low n_e. 149

Figure 5.30 Electron density versus process time under different impedances of the plasma. 149

Figure 5.31 The square of ratios of CH(B), CH(A), and H_2 to $H\beta$ versus process time under two plasma modes: low and high electron density plasmas. 150

Figure 5.32 Surface morphologies of nanodiamond films under two electron-density plasmas: (a) low electron density and (b) high electron density. 151

Figure 5.33 FE-SEM cross-section images of nanodiamond films under two electron-density plasmas: (a) low electron density and (b) high electron density. 152

Figure 5.34 Raman spectra of both films after subtraction of the photoluminescence background (top) low and (bottom) high electron density in plasma. 152

Figure 5.35 The reflectance spectra of films grown under two plasma modes: low and high electron densities. 154

Figure 5.36 FE-SEM images of diamond films grown on Si substrates under various CH_4 concentrations: (a) 1.5%, (b) 3.0%, (c) 3.5%, and (d) 4.0%. Film changes from NCD to UNCD phase. 159

Figure 5.37 Magnified and inset cross-section images of the films synthesized at two CH_4 concentrations: (a) 1.5%, (b) and (c) 4.0%. 160

Figure 5.38 Raman spectra of the films grown at different CH_4 concentrations: 1.5%, 3.0%, 3.5%, and 4.0%. 161

Figure 5.39 Normalized impedance of CH_4/H_2 plasma under various CH_4 concentrations: 0%, 0.75%, 1.5%, 3.0%, 3.5% and 4.0%, and an inset magnified Smith chart. 162

This material is reserved for educational use only, not allowed for commercial use.
Forbidden to modify the content, and cite the document when use.

LIST OF FIGURES (cont.)

PAGE

Figure 5.40 Emission spectra of CH_4-H_2 plasma under various methane concentrations. 163

Figure 5.41 The relative changes of electron density and emission intensity of H_β as a function of CH_4/H_2 concentration. 163

Figure 5.42 The emission intensity ratios of CH, CH^+, and H_β to C_2 as a function of CH_4 concentration. 164

This material is reserved for educational use only, not allowed for commercial use.
Forbidden to modify the content, and cite the document when use.

CHAPTER 1

INTRODUCTION

1.1. Motivation

In recent years, diamond films have become an increasing attention material because of their extreme and in many case superlative properties [1]. The particular nanocrystalline diamond (NCD) films have been identified as a potentially useful material more than microcrystalline diamond (MCD) films in such fields of science and technology as micro- and nano-electromechanical devices [2, 3], field emission device applications [4] as well as optical and biomedical applications [5, 6].

In addition to the remarkable properties of the NCD films, the motivation of this research has also come from a requirement of my laboratory (Surface Physics and Laser Research Laboratory, Department of Physics, Faculty of Science, King Mongkut's Institute of Technology Ladkrabang) to increase potential in experience for thin film deposition. Chemical vapor deposition (CVD) has been widely used for material-processing technology and depositing a very wide range of materials [7]. Concurrent with my laboratory interests in the plasma application and has experienced for several years in construction of the microwave-induced plasma source. Therefore, the synthesis of NCD films by microwave plasma-enhanced chemical vapor deposition (MPECVD) technique has been selected for this research. The MPECVD reactor will be constructed for preparing the NCD films at Surface Physics and Laser Research Laboratory.

1.2. Objectives of Thesis

Specific objectives for this thesis are as follows:

1) To design and construct a MPECVD reactor for preparation of diamond and NCD films.

2) To develop the constructed MPECVD reactor to provide desired properties of the films.

3) To synthesis diamond and NCD films by the purpose-built MPECVD reactor and then characterize them.

4) To study and understand the growth mechanisms of the films.

This material is reserved for educational use only, not allowed for commercial use.
Forbidden to modify the content, and cite the document when use.

5) To apply the spectral line ratio method for resolved measurements of relative values of electron temperature.

6) To apply the values of plasma impedance for resolved measurements of relative value of electron density and temperature.

7) To investigate the optical emission intensities of gas-phase species and plasma impedance affecting on the film properties.

8) To correlate gas-phase species present in the plasma with the resulting characterization of the NCD films grown.

1.3. Research Background

Diamond possesses many technically useful properties: excellent thermal conductivity, high dielectric strength, optical transparency down to the deep UV part of the spectrum, and chemical inertness. For over three decades, research was primarily focused on MCD films [8]. The MCD films consist of large grain (5-10 μm) and rough surfaces thereby limit its applications. The limited applications of MCD films have been surpassed by synthesizing a new class of material known as nanocrystalline diamond (NCD) films. The NCD films have recently attracted considerable interest as they overcome [9]. One of the great problems of MCD films is the great surface roughness [10, 11]. The NCD films have certain properties distinct from MCD films such as smaller grain size, higher grain boundary density, higher degree of sp^2 carbon content, smoother surface morphology, and modifiable surface structures. These properties have resulted in significant improvements in important properties for specific applications such as tribology, optics, and biomedicine. The properties of NCD film strongly depend on each deposition technique as well as operating conditions for the growth.

Nanocrystalline diamond films can be synthesized by a variety of CVD techniques using carbon containing precursor gas mixture [12, 13]. Among them, the microwave plasma-enhanced chemical vapor deposition (MPECVD) technique has proved to be convenient strategy for the coating of various substrates and an efficient over other techniques [14-16]. The NCD films consist of diamond crystals surrounded by few atomic layers of non-diamond carbon compounds as amorphous carbon, *trans*-poly acetylene, and graphite [17]. The diamond crystal morphology as well as the non-diamond matrix is defined by the growth conditions as seeding density, gas

This material is reserved for educational use only, not allowed for commercial use.
Forbidden to modify the content, and cite the document when use.

mixture, pressure, temperature, and energy of particles. In addition, for MPECVD technique, an impedance tuning is also one of the important process parameters leading to encounter a problem of accurate control of the plasma process.

1.4. Problem Statement

The challenge for the thesis requires a start-to-finish effort, from the design, construction, and developments of the deposition system that can deposit desired and uniform NCD films to characterize the films and diagnose the plasma finally. The plasma diagnoses, including measurements of plasma impedance, contribute to control plasma chemistry affecting the film properties. Correlation between material grown and gas-phase species present in the plasma is an important step in understanding and specifying the growth mechanism of the films. Although there have many reports on the growth mechanism of NCD film, the growth mechanism is still controversial. Indeed, it is difficult to define even particular forms of the NCD films due to the variation between laboratories and even reactor designs.

1.5. Thesis Scope

This thesis focuses attention on the design and development of a configuration of a MPECVD reactor to provide good efficiency of power transfer from a microwave generator to plasma reactor and to control uniformity of the film deposition. It also focuses on various aspects of nucleation, growth, and characterizations of the NCD films. The *in situ* gas-phase species are monitored by an optical emission spectrometer and an impedance analyzer. The effect of plasma impedance associated with electron density in the plasma on the plasma chemistry as well as film properties is also examined. The synthesized films are mainly characterized by field emission scanning electron microscopy, Raman spectroscopy, and white light reflectometry. In order to fully exploit NCD, a greater understanding and identifying of the CVD growth process is essential to produce a material suitable for specific applications.

1.6. Thesis Outline

Not including this introductory chapter, the thesis has five chapters. Chapter 2 contains literature review and reviews the description of CVD reactors, mechanism growth of diamond films, plasma diagnostic techniques and film characterization techniques. Chapter 3 covers the technical details of the experimental setup. In chapter 4, the characteristics of the purpose-

This material is reserved for educational use only, not allowed for commercial use.
Forbidden to modify the content, and cite the document when use.

designed and built MPECVD apparatus and the influence of the operating condition on the plasma properties will be characterized and examined. Chapter 5 presents the NCD film characterizations. Finally, the conclusion is described in the sixth chapter.

References

[1] Williams O.A. "Nanocrystalline Diamond" **Diamond Relat. Mater.,** vol. 20, 2011. Pp. 621-640.

[2] Williams O.A., Nesladek M., Daenen M., Michaelson S., Hoffman A., Osawa E., Haenen K. and Jackman R.B. "Growth, Electronic Properties and Applications of Nanodiamond" **Diamond Relat. Mater.,** vol. 17, 2008. Pp. 1080-1088.

[3] Zou Y.S., Yang Y., Chong Y.M., Ye Q., He B., Yao Z.Q., Zhang W. J., Lee S.T., Cai Y. and Chu H.S. "Chemical Vapor Deposition of Diamond Films on Patterned GaN Substrates via a Thin Silicon Nitride Protective Layer" **Cryst. Growth Des.,** vol. 8, 2008. Pp. 1770–1773.

[4] Jou S., Huang B.R., Wu M.C. "Nanocrystalline Diamond Film as Cathode for Gas Discharge Sensors" **Thin Solid Films,** vol. 518, 2010. Pp.4458-4461.

[5] Mochalin V.N., Shenderova O., Ho D. and Gogotsi Y., The Properties and Applications of Nanodiamonds" **Nature Nanotechnology,** vol. 7, 2012. Pp.11-23.

[6] Nebel C.E., Rezek B., Shin D., Uetsuka H. and Yang N. "Diamond for Bio-sensor Applications" **J. Phys. D: Appl. Phys.** vol. 40, 2007. Pp. 6443-6466.

[7] Sivaram S. **Chemical vapor deposition: Thermal and Plasma Deposition of Electronic Materials**. New York: International Thomson Publishing, Inc. 1995.

[8] Ramesham R. "Fabrication of Diamond Microstructures for Microelectromechanical Systems (MEMS) by a Surface Micromachining Process" **Thin Solid Films,** vol. 340, 1999. Pp.1-6.

[9] Kulisch W. and Popov C. On the Growth Mechanisms of Nanocrystalline Diamond Films. **Phys. Stat. Sol. (a),** vol. 203, 2006. Pp. 203-219.

This material is reserved for educational use only, not allowed for commercial use.
Forbidden to modify the content, and cite the document when use.

[10] Koidl P. and Klages C.P. "Optical Applications of Polycrystalline Diamond" **Diamond Relat. Mater.,** Vol. 1, 1992. Pp. 1065-1074.

[11] Hong S.P., Yoshikawa H., Wazumi K. and Koga Y. "Synthesis and Tribological Characteristics of Nanocrystalline Diamond Film using CH_4/H_2 Microwave Plasmas" **Diamond Relat. Mater.**, vol. 11, 2002. Pp. 877-881.

[12] Lifshitz Y., Lee C.H., Wu Y., Zhang W.J., Bello I. and Lee S. T. "Role of Nucleation in Nanodiamond Film Growth" **Appl. Phys. Lett.** Vol. 88, 2006. Pp. 243114.

[13] Wang C.S., Chen H.C., Cheng H.F. and Li I.N. Synthesis of Diamond using Ultra-nanocrystalline Diamonds as Seeding Layer and Their Electron Field Emission Properties, **Diamond Relat. Mater.** Vol. 18, 2009. Pp.136-140.

[14] Xiao X., Birrell J., Gerbi J. E., Auciello O. and Carlisle J.A. "Low Temperature Growth of Ultrananocrystalline Diamond" **J. Appl. Phys.,** vol. 96, 2004. Pp. 2232-2239.

[15] Marinlovic S.N. "Diamond Synthesized at Low Pressure" **Chemistry and Physics of Carbon,** vol. 29, 2004. Pp.71-207.

[16] Cicala G., Monéger D., Cornacchia D., Pesce P., Magaletti V., Perna G. and Capozzi V. Tamborra M., Toward Smooth MWPECVD Diamond Films: Exploring the Limits of the Hydrogen Percentage in $Ar/H_2/CH_4$ Gas Mixture, **Surf. Coat. Technol.,** vol. 21, 2012. Pp.152-157.

[17] Kriele A., Williams O.A., Wolfer M., Hees J.J., Smirnov W. and Nebel C.E. "Formation of Nano-pores in Nano-crystalline Diamond Films" **Chem. Phys. Lett.,** vol.507, 2011. Pp. 253-259.

This material is reserved for educational use only, not allowed for commercial use.
Forbidden to modify the content, and cite the document when use.

CHAPTER 2

THEORETICAL BACKGROUND

The major objective of this thesis is to design and build a MPECVD reactor for deposition of NCD films. The other objective is also to understand the mechanisms of chemical processes that are crucial to be key parameters for the growth. The correlation between films grown and gas-phase chemistry present in the plasma is more important to specify which mechanisms determine diamond formation. In this chapter, the important theories will be presented and discussed.

2.1 Literature Reviews of CVD Diamond

Diamond has been prized for centuries as a gemstone of exceptional brilliance and luster. But to a scientist diamond is a semiconductor and interesting for its range of exceptional and extreme properties [1], such as high breakdown field, high saturation velocity, high carrier mobility, and the highest thermal conductivity of all materials. This makes diamond extreme in the group of wide-bandgap semiconductors, which includes e.g., silicon carbide (SiC) and gallium nitride (GaN). Diamond electronic devices, such as power diodes and high-frequency field effect transistors, could in principle deliver outstanding performance due to diamond's excellent intrinsic properties. Other applications where diamond is expected to excel include radiation detectors, neutron detectors, X-ray optics, biological applications, IR sensors etc. [2-4]. It is considered to be the material for future power electronic devices and for extreme conditions.

In fact, bulk diamond cannot be effectively engineered into the many physical configurations required to exploit all desired combinations of its properties. Hence, several researchers have investigated suitable alternative methods to produce synthetic diamond. The development in the synthesis of diamond leads to the ability to grow diamond in the form of thin films or coating on a variety of shapes with controlled grain size and enables the exploitation of more combinations of the extreme properties of diamond for the specific applications.

Diamond synthesis can be achieved through several techniques. The two main techniques are high-pressure high-temperature synthesis (HPHT) and chemical vapor deposition (CVD). The first public announcement of successful diamond synthesis was made by the General Electric Corporation in 1955. The diamond was synthesized by HPHT technique [5] in which diamond was synthesized from metal solvated carbon at pressures of ~55,000 atmospheres and

This material is reserved for educational use only, not allowed for commercial use.
Forbidden to modify the content, and cite the document when use.

temperatures of ~ 1800 °C. However, HPHT diamond invariably contains many crystal defects and impurities. CVD diamond, on the other hand, can be grown under conditions of high purity resulting in fewer impurities. The first attempt at creating diamond using this process was reported by Eversole in 1949 [6]. In 1952, William G. Eversole [7] of the Union Carbide Corporation reported the first successful growth of diamond using a low-pressure CVD technique in which pressures of less than an atmosphere and temperatures of around 800-1000 °C [8]. Eversole had actually succeeded in late 1952, even before results of the HPHT technique were published.

The last two decades have witnessed an increasing interest in CVD diamond film growth. This is essentially due to two reasons: the unique physical properties of diamond and the spectacular technical advancement achieved by CVD techniques [9]. The CVD technique involves a gas-phase chemical reaction occurring above a solid surface causing deposition onto the surface. Although early reports about the successful CVD of diamond films under low pressure and moderately elevated temperatures in the region of thermodynamic instability were skeptically taken by some scientists. This technique was not also very effective since large amounts of graphite were co-deposited with diamond and growth rates were extremely low. However, Eversole's work was followed up by Angus and co-workers who provided evidence of the use of atomic H (atomic hydrogen) as an etchant for graphite [10]. In addition, in 1982, Matsumoto *et al.* [11, 12] made a breakthrough in CVD diamond technology. They used hot filament (~ 2000°C) to directly activate hydrogen and hydrocarbon which were passed through a hot-filament technique. The adding atomic-H to the CVD process stabilizes the thermodynamically metastable diamond surfaces and promotes diamond growth, preferentially etching non-diamond carbon deposits and bettering growth rates of one $\mu m.h^{-1}$ [13]. Since then, various activating methods for diamond CVD such as DC-plasma, RF-plasma, microwave plasma, electron cyclotron resonance-microwave enhanced plasma CVD (ECR-MPECVD), and their modifications have been established.

2.2 Phase Diagram of Carbon-based Materials

CVD has been widely accepted as an ideal deposition technique to grow diamond films; however, the CVD diamond growth is difficult due to its metastable nature (i.e., kinetically stable but not thermodynamically stable). The deposition conditions favor nucleation of both diamond and graphite crystals. Phase diagram of carbon-based materials is shown in **Figure 2.1** [14].

This material is reserved for educational use only, not allowed for commercial use.
Forbidden to modify the content, and cite the document when use.

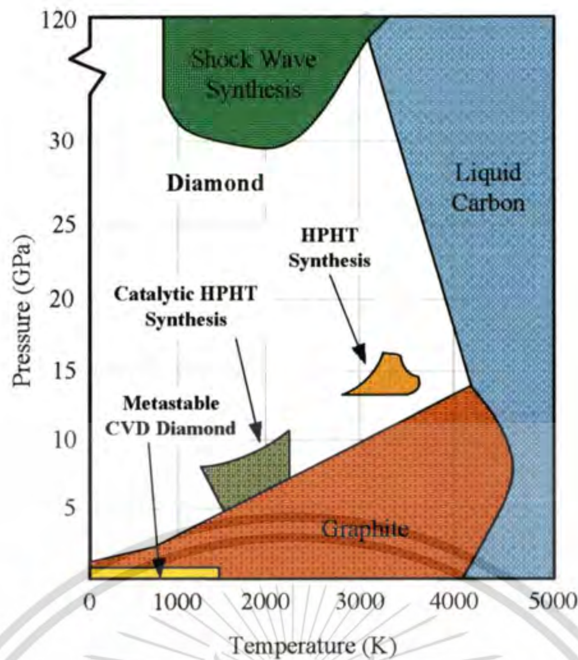

Figure 2.1 The phase diagram for diamond and graphite [14].

It can be found that the growth regime of CVD diamond is surrounded by the growth of graphitic carbon. The relationship between diamond and graphite is a thermodynamic and kinetic one. At normal temperatures and pressures, graphite is only a few eV more stable than diamond, and the fact that diamond exists at all is due to the very large activation barrier for conversion between the two. There is no easy mechanism for this conversion and so transforming diamond into graphite, or vice versa, requires almost as much energy as destroying the entire lattice and rebuilding it. Once diamond is formed, therefore, it cannot reconvert back to graphite because the barrier is too high. Therefore, diamond is said to be metastable, since it is kinetically stable, not thermodynamically stable. Diamond is created deep underground under conditions of extreme pressure and temperature. Under these conditions diamond is actually the more stable of the two forms of carbon, and so over a period of millions of years carbonaceous deposits slowly crystallize into single crystal diamond gemstones.

2.3 Crystal Structure and Properties of Diamond

The two most important forms of carbon are graphite and diamond. In the former, which is the more stable allotrope, carbon atoms are arranged in a hexagonal lattice. Diamond becomes the more stable allotropic configuration of carbon at high temperature and high pressure. It has a modified centered cubic (FCC) structure with two atoms per primitive unit cell as shown in **Figure 2.2.**

This material is reserved for educational use only, not allowed for commercial use.
Forbidden to modify the content, and cite the document when use.

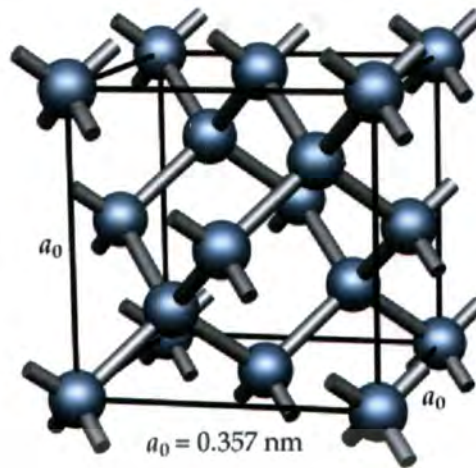

Figure 2.2 Structure of diamond crystal [15].

The (111) planes of the diamond are along the bond direction with a lattice constant (a_0) of 3.567 Å and a bond length of 1.54 Å [15]. Due to this unique chemical bonding and atomic density of 1.76×10^{23} cm^{-3}, diamonds have several extraordinary material properties [5, 16], which make it promise to be the material for a large range of applications. A selection of these is given in **Table 2.1** that lists some of the remarkable properties of diamond.

Table 2.1 Some of outstanding properties of diamond and possible applications for synthetic diamond films [17-19].

Physical Property	Possible application
Hardest known material: 9×10^{9} kg m^{-2}	Cutting tools
Highest thermal conductivity at 300 K: 2000 $Wm^{-1}K^{-1}$	Heat spreaders
High resistivity (insulator): Breakdown Voltage 10^{7} Vm^{-1}	Electrical insulation layer for microcircuitry
Semiconducting when suitable doped	Electronic devices and sensors
Negative electron affinity (NEA)	Cold cathode electron sources
Chemical inertness	Electrochemical sensors
Biological inertness	In vitro applications (coatings/sensors)

This material is reserved for educational use only, not allowed for commercial use.
Forbidden to modify the content, and cite the document when use.

When compared to almost any other materials, diamond almost always comes out on top. As well as being the hardest known material, it is also the least compressible, and the stiffest material, the best thermal conductor with an extremely low thermal expansion, chemically inert to most acids and alkalis, transparent from the deep UV through the visible to the far infrared. It is also one of the few materials known with a negative electron affinity (or work function).

Diamond has some of the extraordinary material properties required not only for cutting tools and abrasive coatings but also for microelectronics and microelectromechnical systems (MEMS) and applications. However, bulk diamond cannot be effectively engineered into the many physical configurations required to exploit all desired combinations of its properties. The developing in the synthesis of diamond by the CVD technique provides the ability to deposit diamond in the form of thin films with controlling the size of diamond crystallites. This makes diamond exploit in more combination enabled their exploitation of more combinations of the extreme properties for specific applications.

Diamond films with crystallite size in nanometer have drawn newly remarkable attention because they have a low coefficient of friction and low electron emission threshold voltage [20]. The small grain size (approximately 5–100 nm) gives films valuable tribology and field emission properties, compared with those of conventional microcrystalline diamond films. Therefore, these films have been proposed that applications for MEMS devices, metal-semiconductor field effect transistors MESFETs, electrochemical electrodes, and biochemical devices can be created by taking advantage of these excellent properties [17, 21].

2.4 Nanocrystalline Diamond

There are wide varieties of different carbon nanostructures; however, they have a few basic things in common. First, all of these materials are predominantly made up of pure carbon, and as such can be called carbon allotropes. The range of these materials starts with the well-known allotropes of diamond and graphite, and continues onto encompass fullerenes, graphene, and more complex structure such as carbon nanotubes. The structures of some representative carbon allotropes are shown in **Figure 2.3**.

This material is reserved for educational use only, not allowed for commercial use.
Forbidden to modify the content, and cite the document when use.

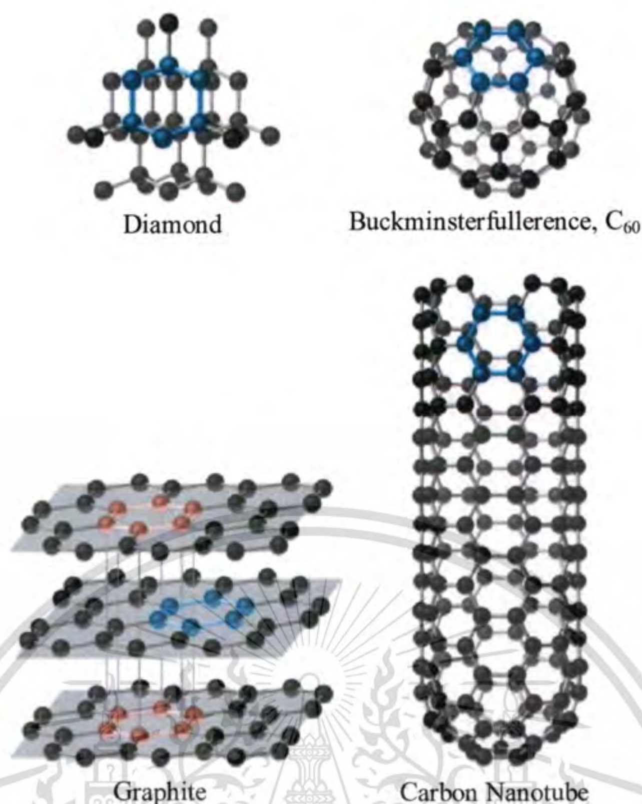

Figure 2.3 Structure of some representative carbon allotropes [22, 23].

Diamond consists of a rigid three-dimensional array of carbon atoms, making it one of the hardest substances known. In contrast, graphite forms from extended planes of covalently bonded hexagonal rings of carbon atoms that can slide across one another easily. Fullerenes are spherical or ellipsoidal molecules with six- and five-membered rings of carbon atoms, and nanotubes are sheets of graphite rolled up into a cylinder. On the one hand, NCD formed of diamond crystals surrounded by few atomic layers of non-diamond carbon compounds as amorphous carbon, *trans*-polyacetylene (t-PA) and graphite [24].

The NCD films are synthetic poly or single crystalline thin film diamonds whose size ranged from a few hundreds of nanometers to a few nanometers. It is the crystal size that is used to classify these materials into four categories namely ultra-nanocrytsatalline diamond (UNCD), nano-crystalline diamond (NCD), micro-crystalline diamond (MCD) films and single crystalline diamond. The schematic picture shown in **Figure 2.4** depicts significant difference in NCD and UNCD morphologies.

This material is reserved for educational use only, not allowed for commercial use.
Forbidden to modify the content, and cite the document when use.

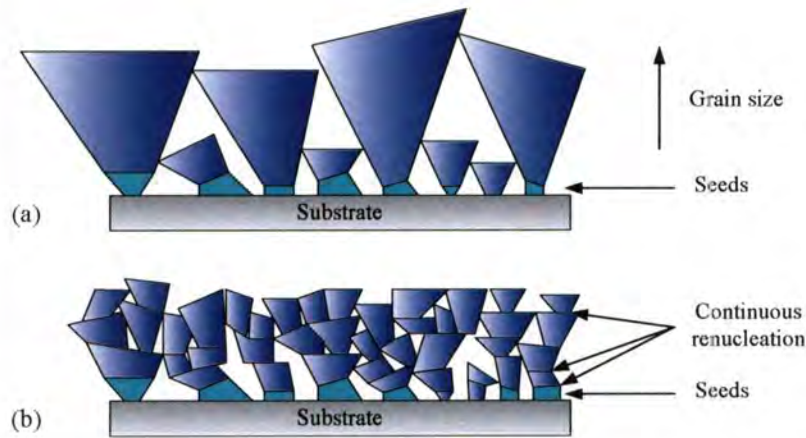

Figure 2.4 Schematic of NCD morphology (a) and UNCD morphology (b) [25].

Unlike natural diamond which is produced through geological processes, NCD films are very small and this makes them relatively easy to manipulate their properties because of the large surface area and reproducible synthesis. One further interesting thing about these particles is that their mechanical properties are comparable to natural diamond and these can be exploited at nano-scale, to make miniaturized devices that can withstand harsh environments. In addition, MCD films consist of large columnar grains that are highly faceted and rough, making them necessary to polish the surface of MCD films in order to improve their friction and wear characteristics [26]. The NCD films, which have smooth surface, low friction coefficient, feasibility of being etched with dry process, high sp^3 content, and also low electron emission threshold voltage, have therefore been recognized as a promising candidate for various applications like abrasion resistant material, electrochemical systems, etc. [27, 28]. Thus, the synthesis of smooth and thick NCD films is of great technological interest due to its above-mentioned applications.

2.5 Chemical Vapor Deposition

Chemical vapor deposition (CVD) [29-31] is a deposition process in which chemical precursors are transported in the vapor phase to decompose on a heated substrate to form a film. The films may be epitaxial, polycrystalline, or amorphous depending on the materials and operating conditions of a reactor. Those precursors can either react with other reaction gases or decompose while they are the gas phase (homogeneous reaction), or they can be adsorbed on the substrate surface and react with reaction gases or decompose (heterogeneous reaction). The result of both types of the reaction is the formation of gaseous by-products and a solid thin film on the substrate. The basic steps in the CVD process are shown in **Figure 2.5**.

...d for commercial use.
Forbidden to modify the content, and cite the document when use.

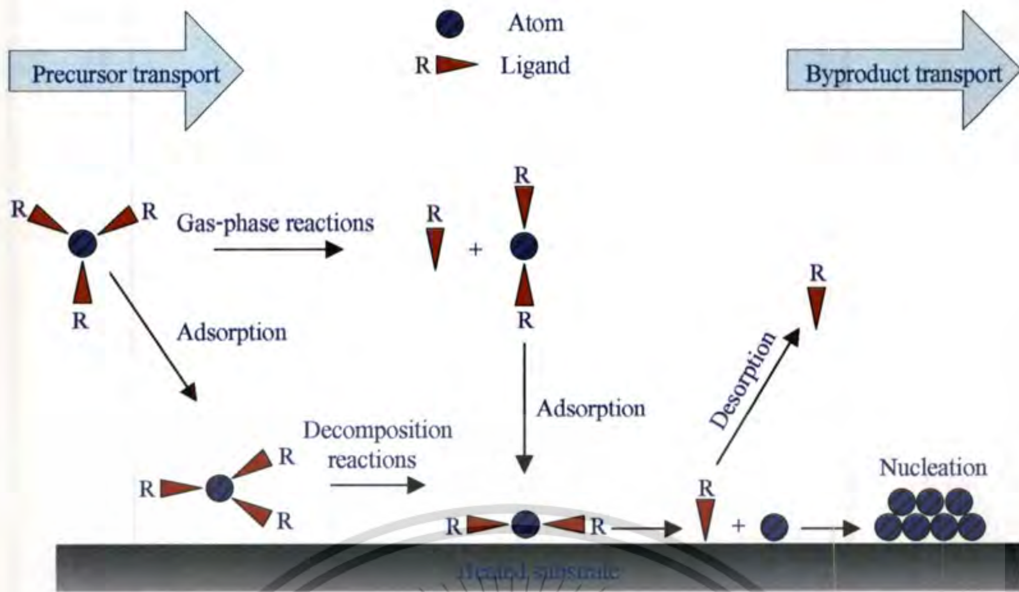

Figure 2.5 Basic steps in the CVD process [29].

The CVD process can be thought of as the result of two processes. The first one involves reactions in a gas phase environment to produce the precursor of diamond growth (dissociation). The second one is the process of adding material to the growing solid by the reactions between the precursor and growth surface, and the relaxation of this material to a lower free energy configuration or accommodation to the underlying lattice structure (deposition). On the growth surface, adsorption, diffusion, reaction, and desorption of various species continue leading to the nucleation of the grown particles. It is this chemical process, which distinguishes CVD from physical deposition processes such as evaporation, sputtering, and molecular beam epitaxy. The exact arrangement of CVD apparatus can vary widely depending on the particular application

2.5.1 Kinetics of CVD

Studies on the kinetics and mechanisms of CVD reactions provide useful information such as activation energy and limiting steps of deposition reactions which are important for the understanding of deposition processes. The main problem in the CVD kinetics studies is the complexity of the deposition process. Exact kinetic analysis is therefore usually not possible as the kinetic data is dependent on reactor designs. These are several possible rate-limiting factors but mass transport and surface kinetics control are the most predominant [31]. Mass transport control exists if the transport of the reactant/reaction products across the boundary layer determines the deposition rate. If the mass transport though the boundary layer is sufficiently large, the system is controlled by surface kinetic reactions.

This material is reserved for educational use only, not allowed for commercial use.
Forbidden to modify the content, and cite the document when use.

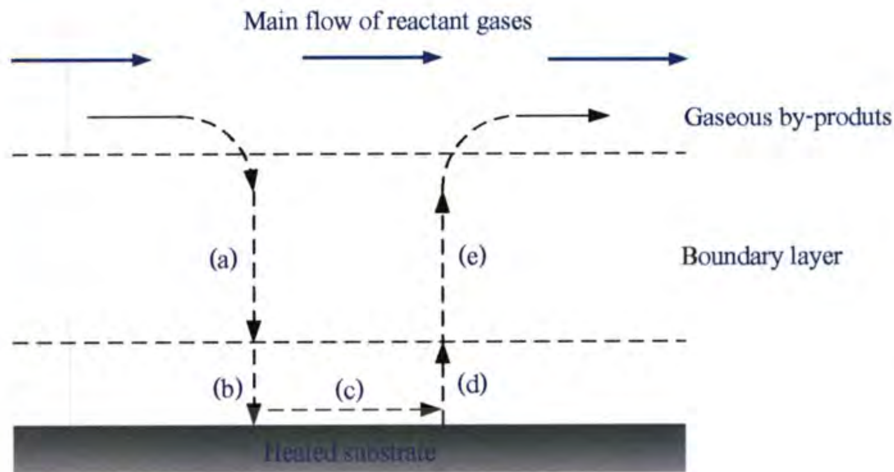

Figure 2.6 Sequence of events during CVD: (a) diffusion of reactants through boundary layer, (b) adsorption of reactants on substrate, (c) chemical reaction takes place, (d) desorption of adsorbed species, and (e) diffusion out of by-products through boundary layer. [29]

A normal CVD process involves complex flow dynamics since gases are flowing into the reactor, reacting, and then by-products are exhausted out of the reactor. The sequence of events during a CVD reaction is show in **Figure 2.6** and as follows:

1) Precursor gases input into the chamber by pressurized gas lines and mass transport of precursors from the main flow region to the substrate through the boundary layer (a).
2) Adsorption of precursors on the substrate (normally heated) (**Figure 2.6** b))
3) Chemical reaction on the surface (**Figure 2.6** c))
4) Atoms diffuse on the surface to growth sites.
6) Desorption of by-products of the reactions (**Figure 2.6**d)).
7) Mass transport of by-products to the main flow region (**Figure 2.6** e)).

2.5.2 Rate Limiting Steps

During CVD the growth rate of the film is limited by either surface reaction kinetics, mass transport (diffusion) of precursors to the substrate, or the feed rate of the precursors. Surface reaction controls the rate when growth occurs at low temperatures (where the reaction occurs slowly) and dominates at low pressures (the boundary layer is thin and reactants easily diffuse to the surface), see **Figure 2.7**. Since reactants easily diffuse through the boundary layer, the amount of reactant at the surface is independent on reactor pressure. Therefore, it is the reactions and motions of the precursors adsorbed on the surface, which will determine the overall growth rate of

Forbidden to modify the content, and cite the document when use.

the film. A sign of surface reaction limited growth would be dependence of the growth rate on substrate orientation, since the orientation would certainly not affect the thermodynamics or mass transport of the system.

A deposition limited by mass transport is controlled by the diffusion of reactants through the boundary layer and diffusion of by-products out of the boundary layer. Mass transport limits reactions when the temperature and pressure are high. These conditions increase the thickness of the boundary layer and make it harder for gases to diffuse through (**Figure 2.8**). In addition, decomposition of the reactants is typically quicker since the substrate is at a higher temperature. When mass transport limits the growth, either increasing the gas velocity or rotating the substrate during growth will decrease the boundary layer and increase the growth rate.

Feed rate limits the deposition when nearly all the reactant is consumed in the chamber. The feed rate is more important for a hot wall reactor since the heated walls will decompose a large amount of the precursor. Cold wall reactors tend to have higher deposition rates since the reactants are not depleted by the walls.

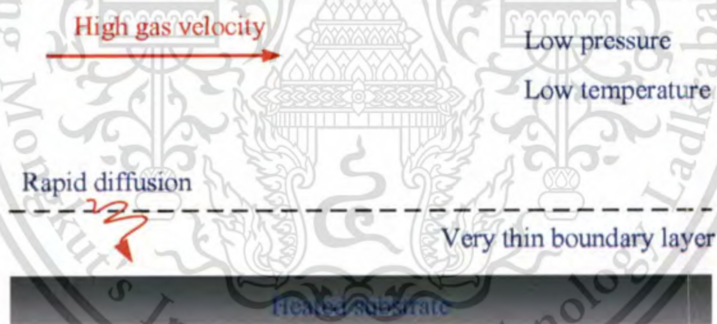

Figure 2.7 Surface reaction limited growth in CVD [29].

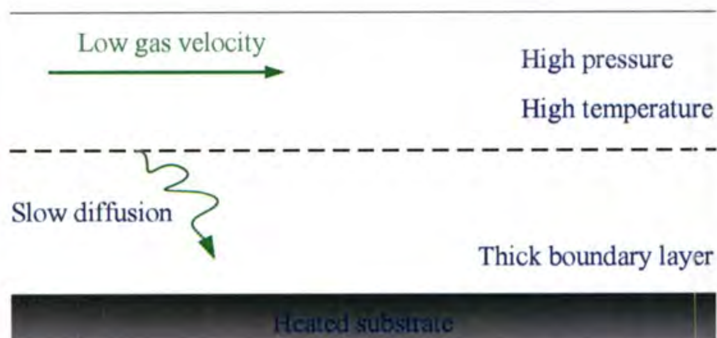

Figure 2.8 Mass transport limited growth in CVD [29].

This material is reserved for educational use only, not allowed for commercial use.
Forbidden to modify the content, and cite the document when use.

2.5.3 CVD Techniques

Chemical vapor deposition involves the dissociation and/or chemical reactions of the gas precursors in an active environment of heat, light, or plasma. These activations result that the growth of diamond films from vapor phase on non-diamond substrates at practical rates was accomplished with the development of plasma- and thermal- enhanced CVD methods, in which a hydrocarbon gas (usually methane) mixed in low concentrations with hydrogen is energized thermally or in plasma, prior to contact with a heated substrate. These include the development of filament-assisted thermal CVD [11, 12], laser-assisted thermal CVD [32], RF-plasma CVD [33], microwave plasma-enhanced CVD [34], direct-current arc plasma jet CVD [35], etc. Although there are a lot of ways to activate the gases, the role of the different species will be the same. Among the CVD methods for diamond growth, hot filament and microwave-plasma CVD are most widely used techniques for growing diamond films. Due to the temperature upper limit of the filament material, hot-filament processes operate at significantly lower gas temperatures than plasma processes, and consequently produce less atomic hydrogen. The low gas phase concentrations give relatively lower growth rates than the plasma methods.

Microwave plasma-enhanced CVD (MPECVD) is one of the most widely used techniques in synthesis of CVD diamond due to its distinct advantages over other methods [36]. Microwave deposition, being an electrodeless process, avoids contamination of the films due to electrode erosion. Furthermore, the microwave discharge at 2.45 GHz, being a higher frequency process than the RF discharges at 13.5 MHz, produces the higher plasma density with higher energy electrons. This should result in higher concentrations of H atoms and hydrocarbon radicals. In addition, the microwave can excite and ionize more gas molecules [37], and microwave discharge has been demonstrated the stability in operation over a wide pressure regime from a few mTorr to 1 atmosphere [16, 38, 39]. In the following section, we introduce the MPECVD technique which is the technique used in this thesis for deposition of NCD films.

2.6 Microwave Plasma-enhanced CVD Technique for Diamond Growth

Microwave plasma CVD has become dominant in both industrial and research facilities worldwide [6, 40]. Microwaves dissociate the molecules in the gas to generate plasma containing carbon atoms for depositing onto the substrate surface. The substrate is heated by the absorption of microwaves, the bombardment by energetic plasma species, and exothermic recombination of radicals such as atomic hydrogen on the diamond-growing surface.

This material is provided for educational purposes only. Not allowed for commercial use.
Forbidden to modify the content, and cite the document when use.

สำนักหอสมุดกลาง พระจอมเกล้าลาดกระบัง

2.6.1 Microwave Plasma Source

Microwave plasma is a type of plasma that is sustained by power supplies operating at frequencies of 2.45 GHz. A schematic diagram of a typical plasma source showing all the parts essential to perform the specified tasks is shown in **Figure 2.9**. In microwave plasma or microwave discharge, the electric field oscillates with the frequency of the power supply and a breakdown electric field value for the working gas must be reached in order to form and self-sustain the plasma [41].

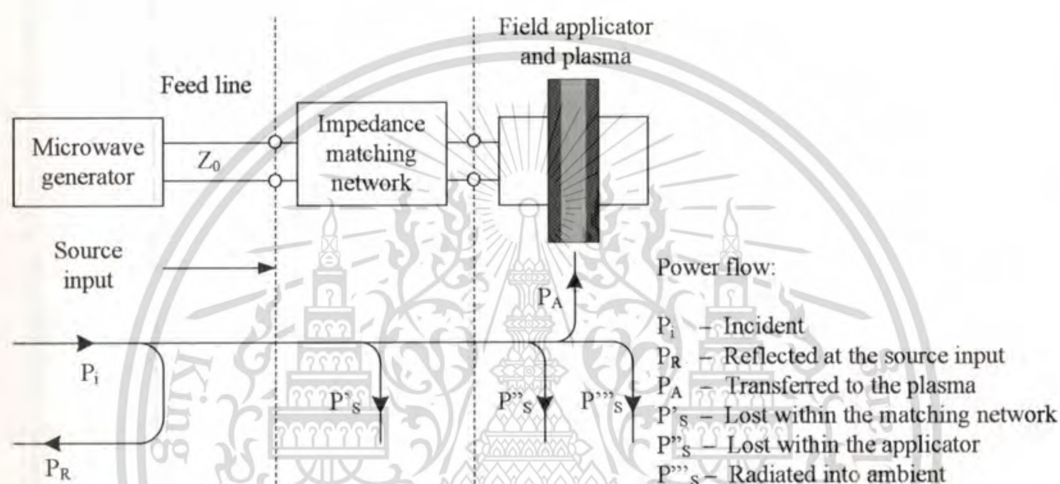

Figure 2.9 Typical microwave power supply and simplified graph of power flow in a microwave plasma source [16, 41].

Efficiency of power transfer from a microwave frequency generator to the plasma source is defined as the fraction of power delivered by the generator at the source input that is absorbed by the plasma. Optimum power transfer requires that the reflected power is to be minimal. The average microwave power entering the applicator enclosing the plasma can be derived from the conventional formalism of the microwave circuit theory. To simplify this problem, the cumulative power loss, including loss within the matching network together with the applicator and due to radiation into ambient, has been assumed to be negligible. The voltage and current of amplitudes, U and I, respectively, at the input of the field applicator can be defined so that their product gives the power entering the applicator. Therefore, the average power flowing inward across A and that dissipated and stored within the enclosed volume V:

This material is reserved for educational use only, not allowed for commercial use.
76495
Forbidden to modify the content, and cite the document when use.

$$\frac{1}{2}UI^* = -\frac{1}{2}\int_A \left(\mathrm{E} \times \mathrm{H}^*\right) \cdot dA$$
$$= -\omega \int_V \varepsilon_p'' \varepsilon_0 \mathrm{E}_{rms}^2 dV + i\omega \left(\int_V \mu_0 \mathrm{H}_{rms}^2 dV - \int_V \varepsilon_p' \varepsilon_0 E_{rms}^2 dV \right) \quad (2.1),$$
$$\equiv P_A + i2\omega\left(W_M - W_P\right)$$

where A denotes integration over the input closed surface area and $\varepsilon_p = \varepsilon_p' + i\varepsilon_p''$ denotes the relative plasma permittivity. The resistive part P_A of the power flux is a Joule-like loss term, and it denotes the power deposited in the plasma that is the total power absorbed by electrons in the plasma. The reactive part, $2\omega\left(W_M - W_P\right)$, relates to energy storage processes within the active zone. W_M and W_P denote the average energy stored in the magnetic field and in the electric field in a plasma medium with permittivity of $\varepsilon_p'\varepsilon_0$, respectively.

Considering uniform plasma in the presence of a background gas that is driven by a small amplitude time-varying electric field, we can introduce plasma conductivity with

$$\sigma = \sigma_p' + j\sigma_p'' = \frac{n_e e^2}{m_e} \frac{1}{\nu_m + \omega j} \quad (2.2).$$

Here, n_e is electron density, e is the electron charge, m_e is the electron mass, ω is the driving frequency, and υ_m is the average elastic collision frequency of an electron with the atoms or molecules of the gas. σ_p' and σ_p'' are real and imaginary parts of normalized plasma conductivity. Note that, to analyze the conductivity of materials exposed to alternating electric fields, it is necessary to treat conductivity as a complex number called admittivity. In the absence of collisions (i.e. $\upsilon_m = 0$), $\sigma = j\sigma_p''$ is an imaginary number. This expresses that the plasma behaves like a lossless medium, the only motion being the ordered oscillations of the electrons, induced by the field. There is no energy transfer from the electromagnetic field to the electrons and from the latter to the background gas: in this case, the plasma medium is entirely passive. Collisions introduce disorder into this motion and constitute the mechanism by which power can flow from the electromagnetic field to the electron fluid and from the latter to the gas background.

From the definition of P_A in Equations (2.1) and (2.2) together with a correlation between plasma conductivity and plasma permittivity, $\left(\sigma_p = \sigma_p' + j\sigma_p'' = \left[-\varepsilon_p'' + j\left(\varepsilon_p' - 1\right)\right]\omega\varepsilon_0\right)$, the rate of gain of energy of electrons from the electric field or the power P_A absorbed by electrons in the plasma is given by:

This material is reserved for educational use only, not allowed for commercial use.
Forbidden to modify the content, and cite the document when use.

$$P_A \equiv \int_V \sigma'_p E_{rms}^2 dV = \frac{e^2}{m_e \upsilon_m} E_e^2 \int_V n_e dV \quad (2.3),$$

where E_e is the effective electric field strength which is related to the actual electric field E_{rms}, given by

$$E_e^2 = \frac{\upsilon_m^2}{\omega^2 + \upsilon_m^2} E_{rms}^2 \quad (2.4).$$

Therefore, absorbed microwave power from Equation (2.3) can be used to obtain an estimate of the electron density assuming the total power absorbed is consumed into ionization

$$\int_V n_e dV = P_A \frac{m_e v_m}{e^2 E_e^2} \quad (2.5).$$

When most of the input power goes to ionization, the input power P is related to the ionization frequency v_i and ionization energy ε_{iz}, as $P_A = v_i e \varepsilon_{iz}$ [42, 43]. A substitution for the ionization frequency utilizing Equation (2.3) gives

$$v_i = \frac{P_A}{e\varepsilon_{iz}} = \frac{eE_e^2}{m_e v_m \varepsilon_{iz}} \int_V n_e dV \quad (2.6).$$

Using the ionization frequency form the kinetic theory with the electron velocity taken as the thermal velocity over a Maxwellian distribution, then [42, 43]:

$$v_i = \frac{8eT_e}{3\pi v_m m_e \Lambda^2} \quad (2.7),$$

where T_e is the average electron temperature (eV) and Λ is the characteristic diffusion length. For example, the diffusion length for cylindrical plasma is given by

$$\Lambda = \left(\frac{1}{\left(\frac{\pi}{\ell}\right)^2 + \left(\frac{2.405}{a}\right)^2} \right)^{1/2} \quad (2.8).$$

Here, ℓ is the length of the discharge, a is the radius of the plasma, and the 2.405 is root of the zero order Bessel function for the solution of diffusion equation in cylindrical geometry.

This material is reserved for educational use only, not allowed for commercial use.
Forbidden to modify the content, and cite the document when use.

Substituting for v_i from Equation (2.6) into Equation (2.7) one can obtain an expression for the average electron temperature:

$$T_e = \frac{3\pi}{8} \frac{E_e^2}{\varepsilon_{iz}} \Lambda^2 \qquad (2.9).$$

A solution for the electron plasma temperature is an important parameter in determining the nature of the plasma. It affects the various reaction rate coefficients for electron impact on heavy species. It is evident that one can obtain a measure of the electron plasma temperature based on the assumption that all microwave power is absorbed in the plasma and consumed into ionization. Both Equations (2.5) and (2.9) are useful in determining plasma parameters in a microwave discharge, however, the temperature and density are an average value over the entire discharge.

2.6.2 Plasma-enhanced CVD of Diamond Growth

Plasma is generated for a variety of thin film processes including sputtering, etching, ashing, and plasma-enhanced CVD (PECVD). The PECVD, sometimes called plasma-assisted CVD (PACVD), has the advantage that plasma activated reactions occurs at much lower temperatures compared to those in thermal CVD. For example, the thermal CVD of silicon nitride occurs between 700 °C and 900 °C, the equivalent PECVD process is achieved between 250 °C and 350 °C.

Plasma is a partially ionized gas consisting of electrons and ions. It is electrically conductive with the primary charge carriers being the electrons. The light mass of the electron allows it to respond much more quickly to change in the field than the heavier ions. In the high frequency electric field, the light electrons are quickly accelerated by the field but do not increase the temperature of the plasma because of their low mass. The heavy ions cannot respond to the quick changes in direction and therefore their temperature stays low. Electron energies in the plasma have a Maxwellian distribution in the 0.1 – 20 eV range. These energies are sufficiently high to excite molecules or break chemical bonds in collisions between electrons and gas molecules. The high-energy electrons inelastically collide with gas molecules resulting in excitation or ionization. The reactive species generated by the collisions do not have the energy barriers to reactions that the parent precursors do. Therefore, the reactive ions are able to form films at temperatures much lower than those required for the thermal CVD. The general reaction sequence for PECVD is shown in **Figure 2.10**.

This material is reserved for educational use only, not allowed for commercial use.
Forbidden to modify the content, and cite the document when use.

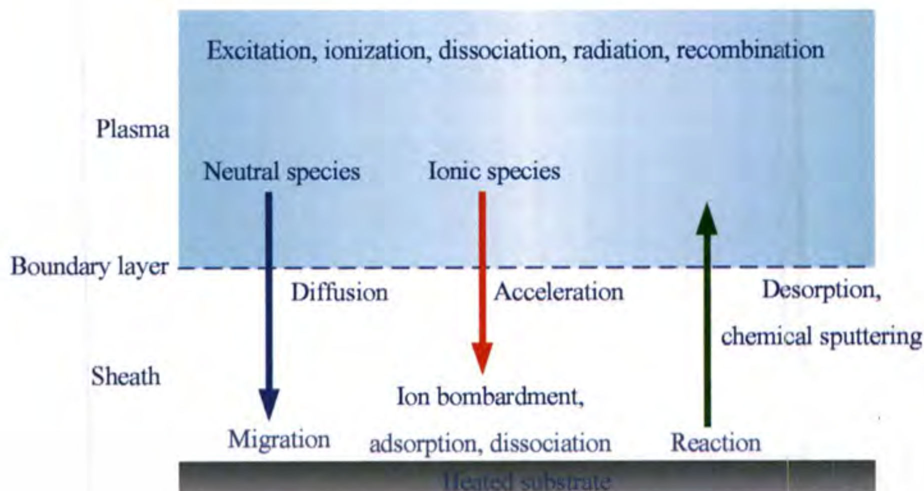

Figure 2.10 Reaction sequence in PECVD [44].

Reactant gases flowing in the bulk must diffuse through the boundary layer to reach the substrate surface. The boundary layer thickness increases with lowering in gas velocity. In addition to the processes that occur in thermal CVD, reactive species resulting from electron dissociation of parent molecules also diffuse to the surface. The reactive species have lower activation energies for chemical reactions and usually have higher sticking coefficients to the substrate. Therefore, the PECVD reaction is dominated by the reactive species on the surface and not any of the parent precursor molecules that also diffuse to the surface.

2.6.3 Gas-phase Chemistry and Gas-surface Reactions

CVD process for diamond growth [45-47] involves the gas phase decomposition of gaseous reactant, a dilute hydrocarbon-hydrogen gas mixture, as well as gas-surface reactions. The gas-phase chemistry and reactions on the growth surface are schematically summarized in **Figure 2.11**. There are three main processes involved in CVD diamond growth. Initially reactant gases, including methane and hydrogen gases, are activated and gas phase chemistry and physics play roles in forming reactive species. Secondly, species that pass through the activation zone are transported to the substrate. Mass transport in gas goals is to deliver gas uniformly to substrate (uniform film). The nature of the transport process depends on the gas pressure, flow rate, gas velocity, reactor geometry, and gas properties employed. The transport processes are quite different among the reactor types. The microwave plasma reactor is diffusion dominated.

This material is reserved for educational use only, not allowed for commercial use.
Forbidden to modify the content, and cite the document when use.

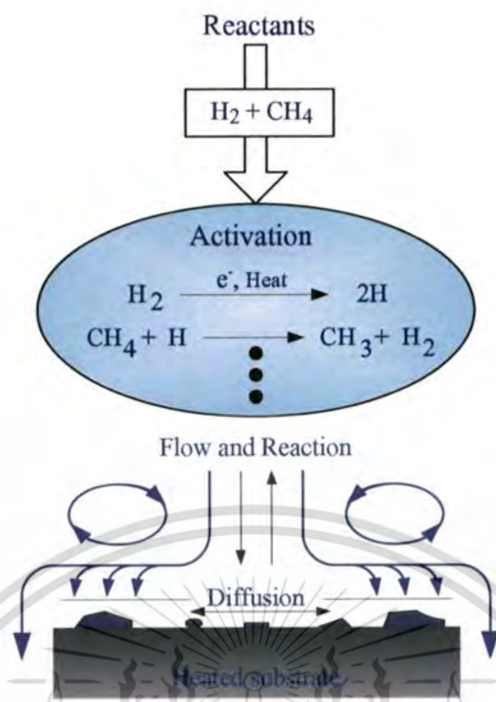

Figure 2.11 Three main processes occurring to the input gases during CVD diamond growth: activation, species transport, and surface chemistry [45]

A high concentration of hydrogen atoms close to the substrate surface is crucial in the deposition process, since H atoms perform a number of important functions. First, H atoms can etch surface graphitic (sp^2) carbon many times faster than diamondlike (sp^3-bonded) carbon. Second, the H atoms help to terminate the "dangling bonds" on the diamond surface, thus stabilizing the surface, while the growth is taking place. In addition, the H atoms react with large gas phase hydrocarbon fragments, splitting them into small pieces, thus preventing polymer build up. Finally, atomic H creates radical sites on the surface by undergoing H-abstraction reactions, removing some of the terminal hydrogen. It is generally believed [47] that the main growth species in the standard CVD diamond growth is the CH_3 radical, which adds to the diamond surface stepwise following successive hydrogen abstraction by H atoms. Thus, a high concentration of atomic H at the surface is a prerequisite for MCD deposition.

Alternative methods of diamond growth involve various forms of plasma-assisted CVD using carbon-containing species mixed in low concentration with hydrogen. Plasma is generated either by various forms of electrical discharges or by induction heating. The role of the plasma is to generate hydrogen atoms and to produce proper carbon precursors for the growth of diamond. Atomic hydrogen is produced by electron impact dissociation of molecular hydrogen:

This material is reserved for educational use only, not allowed for commercial use.
Forbidden to modify the content, and cite the document when use.

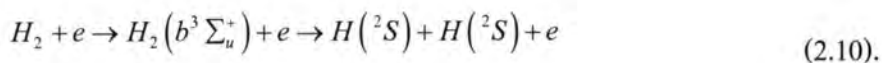

$$H_2 + e \rightarrow H_2\left(b^3 \Sigma_u^+\right) + e \rightarrow H\left(^2S\right) + H\left(^2S\right) + e \qquad (2.10).$$

The net production of H atoms (H radicals) stems from dissociation of hydrogen molecules appearing to go through the repulsive $b^3 \Sigma_u^+$ state [48]. The initiation of the gaseous chemistry is dominated by dissociation of molecular hydrogen into atomic H.

The subsequent gaseous chemistry is driven by reactions of atomic H with hydrocarbon species and a series of complex reactions among the hydrocarbon species. Considering the case of CH_4, the most commonly used hydrocarbon source gas; H atoms drive the series of H-shifting reactions involving abstractions:

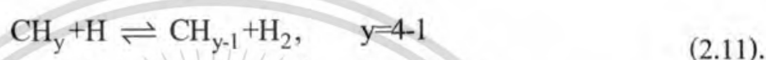

$$CH_y + H \rightleftharpoons CH_{y-1} + H_2, \qquad y=4\text{-}1 \qquad (2.11).$$

These reactions lead to the presence of much more hydrocarbon species, particularly CH_3 radical, which plays an important role in growth of diamond films. In addition, C_2H_x species can be formed by CH_x radical recombination (dimerization reactions):

$$CH_x + CH_y \rightleftharpoons C_2H_{x+y-1} + H \qquad (2.12)$$

and

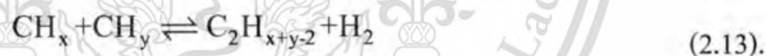

$$CH_x + CH_y \rightleftharpoons C_2H_{x+y-2} + H_2 \qquad (2.13).$$

The total gas-phase number densities, the H-atom densities, the various CH_y and C_2H_x species densities, and thus the reaction rates of inter-conversion between these species, are all sensitive functions of location within the reactor. This complexity is further compounded by gas-surface reactions and gas transport that, in MPECVD reactors, is largely diffusive, and thus is dependent on mass and species.

Finally, on the surface, adsorption, diffusion, reaction, and desorption of various species occur leading to the nucleation of diamond particles, suppression of graphitic (or sp^2) carbon, and ultimately the growth of a continuous diamond film. These are complex processes, which depend on the type of substrate, its temperature, and the flux of species incident at the surface; and they determine the morphology and quality of the diamond film.

This material is reserved for educational use only, not allowed for commercial use.
Forbidden to modify the content, and cite the document when use.

2.6.4 Growth Model of Diamond Films

To obtain a diamond film with the desired morphology combined with controlled electronic and mechanical properties requires detailed understanding of the many parameters affecting the growth. The difficulty with this is that the exact details of the growth mechanism remain controversial. The so-called "standard growth mechanism" [40, 49] is a reasonably robust description of the general CVD diamond process. Although a detailed chemical mechanism of diamond growth would be complex, involving perhaps hundreds of reactions, the essence of diamond growth chemistry can be reduced to a few generic steps (essentially surface activation, adsorption on open sites, desorption, and incorporation into the lattice).

The standard model of diamond CVD has the following key elements. Firstly, the diamond lattice is stabilized and prevented from a rearrangement to graphitic carbon by termination with H atoms, as shown in **Figure 2.12**(a). Secondly, the H atoms created by the gaseous activation process abstract hydrogen from the diamond growth surface, thereby creating surface radical sites, C_d^*, shown in **Figure 2.12**(b). The formation rate of these surface radical sites (dangling bonds) is determined by the rate of H abstraction. The most likely fate for this surface radical site – given the high concentration of H atoms nearby – is that an H simply attaches to it, stabilising the surface, and the excess bond energy is dissipated into the surface as heat. It turns out that the formation of the surface radical sties is almost exactly a function of the equilibrium between H abstraction and H addition reactions, which are both sensitive functions of the substrate temperature as much as of the gas temperature.

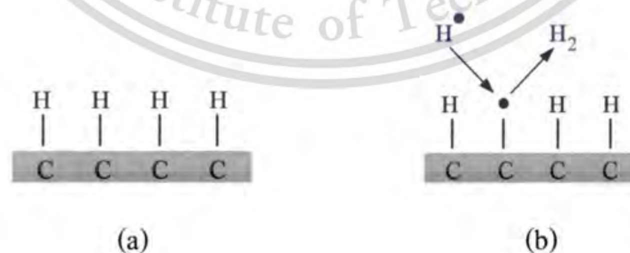

Figure 2.12 Schematic presentation of the surface processes during diamond growth: (a) hydrogen stabilized diamond surface and (b) creation of a surface-radical site by hydrogen abstraction [50].

This material is reserved for educational use only, not allowed for commercial use.
Forbidden to modify the content, and cite the document when use.

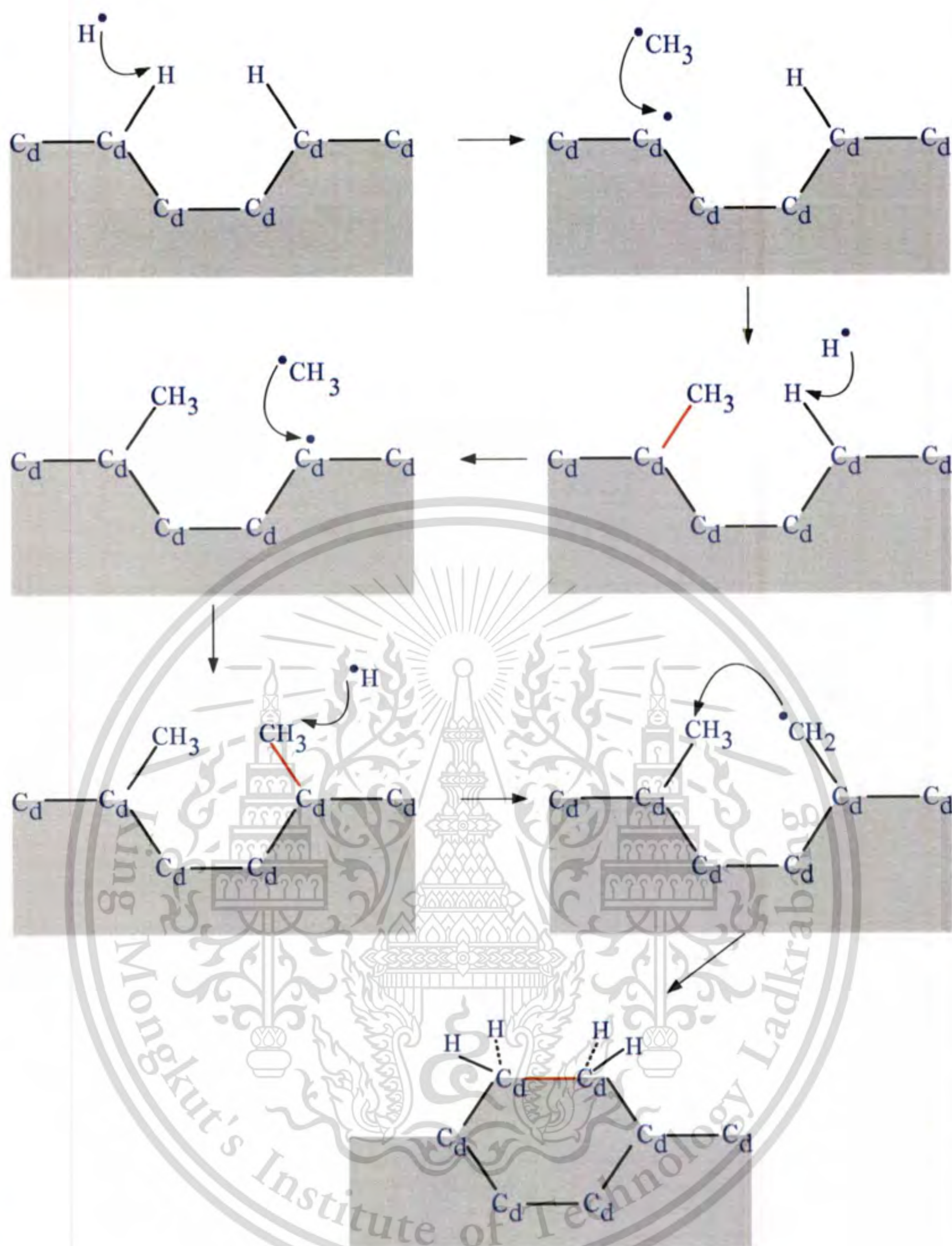

Figure 2.13 A schematic diagram of a simplified version of the standard growth model for CVD diamond growth mechanism and, in red line, the new bonds formed [51].

However, occasionally, instead of an H atom, a CH_3 radical (created in the plasma by reactions between CH_4 and H atoms) can add to a surface radical site, so adding one carbon to the lattice, as seen in **Figure 2.13**. This 'pendant' (dangling) CH_3 group, however, is quite vulnerable, and can easily be etched or desorb back into the gas phase, in which case we are back to square one. But if the process of H abstraction, dangling bond creation, and CH_3 addition, were to occur again, on a site adjacent to the pendant CH_3, then there is the possibility that the new carbons can link up and finally be locked into the lattice. This can propagate the diamond lattice. The

Forbidden to modify the content, and cite the document when use.

schematic of the reaction process occurring at the diamond surface leading to stepwise addition of CH_3 species and diamond growth is shown in **Figure 2.13**.

According to D.G. Goodwin [52], the diamond growth rate G and the relative defect density rate of defect X_{def} determining film quality estimated from the standard growth model can be estimated by the following formulae:

$$G \propto \frac{[CH_3][H]}{5\times10^{-9}+[H]} \quad (2.14),$$

and

$$X_{def} \propto \frac{G}{[H]^2} \quad (2.15).$$

Here, [H] is the atomic-H concentration and $[CH_3]$ is the methyl concentration on the surface. Goodwin proposed CH_3 as the species reacting in his model and arrived to a defect fraction proportional to $G/[H]^2$.

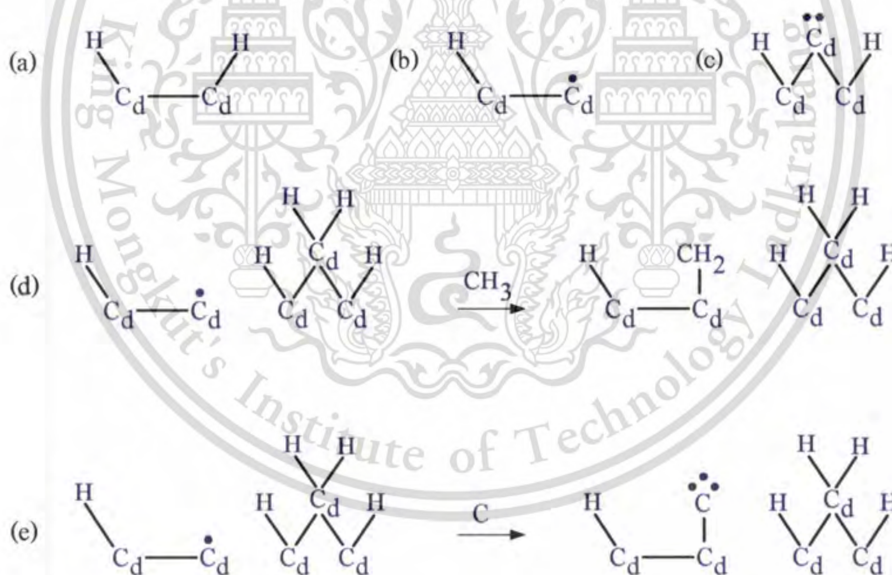

Figure 2.14. Schematic diagram of the various (100)-(2x1) reconstructed surface and bridge sites important for diamond growth and renucleation: (a) A hydrogen terminated diamond surface, (b) A surface radical site C_d^*, (c) A surface biradical site C_d^*. (d) A different type of surface biradical site, $C_d^* - C_d^*$, followed by its reaction with methyl to give a CH_2 surface group, and (e) The radical site also reacts with a C atom (or CH radical, not shown) to give a reactive-surface adduct, C_d^{**} [53].

This material is reserved for educational use only, not allowed for commercial use.
Forbidden to modify the content, and cite the document when use.

As stated by P.W. May *et al.* [53, 54], the modified version of the standard growth model seen in **Figure 2.14** is based on the consideration for the effect of all the C_1 hydrocarbon radicals (CH_3, CH_2, CH and C atoms) on both monoradical and biracial sites on a (100) diamond surface. Monoradial sites have a single dangling bond, and biracial sites have two dangling bonds on adjacent carbons. In this model, abstraction of surface H atoms by gas phase atomic H are the reactions which drive the chemistry of growth. The various types of the surface radical that result from abstraction are shown in **Figure 2.14**.

For typical diamond CVD conditions, the fraction of available biradical sites is 10 times lower than that of monoradical sites, but CH_3 have more steric hindrance. Thus, the prerequisites for MCD film formation are high H concentration (to generate sufficient surface biradical sites), high CH_3 concentration, and the rapid migration across the surface of CH_2 groups (catalysed by H atom abstractions). As well as CH_3, addition of the other less abundant but highly reactive C1 species, particular atomic C, to either type of radical site at high H atom concentration, can also be a route to growth. Due to their smaller size, atomic C and CH have less steric hindrance and can add to both surface biradical sites and radical sites (see **Figure 2.14**). Thus, even for low C atom concentrations [C] / [CH_3] ~0.1, their contribution to the growth rate can become important since they can add to the more abundant radical sites. In addition, the resulting adduct structure C_d^{**} (see **Figure 2.14**(e)) would remain reactive since it would still contain dangling bonds, making this a very high energy site. Therefore, the total growth rate will be obtained by the sum of all C_1 hydrocarbon radicals adding to both radical sites:

$$G_{total}=G_{CH_3}+G_{CH_{x,x=0,1,2}} \quad (2.16).$$

However, the increased relative contribution of the biradical mechanism enhances the probability that other reactive hydrocarbon species (C_2, C_2H, etc.) from the gas can add to these biradical sites. Such reactive species then have the opportunity to cross-link on the surface, creating a strongly bonded defect (maybe even non-etchable). This surface defect could either act as a renucleation point for a new epitaxial layer, or, if it is misaligned with the existing lattice, a new crystallite growing in a different direction to that of the main bulk. This last possibility is often termed 'renucleation', and leads to a decrease in the average crystal size [53]. If renucleation occurs frequently, the crystallite size can drop from mm to μm, and eventually to nm, and the films are termed SCD, MCD and UNCD, accordingly.

This material is reserved for educational use only, not allowed for commercial use.
Forbidden to modify the content, and cite the document when use.

2.7 Nucleation Stage of Diamond Growth

The primary challenge of CVD diamond growth is to enable the deposition on substrates, such as silicon, on which diamond does not naturally nucleate. A key issue in diamond CVD on nondiamond substrates has been the control and optimization of diamond nucleation during the early stages of the deposition process. In a recent study, the nucleation density is shown to play a crucial role in improving the mechanical properties as well as the thermal diffusivity in ultra-thin NCD films [55]. Smoothness and compositional uniformity also significantly increase strength and resistance to fracture in the NCD films [56, 57]. Controlling on the initial nucleation density via surface pretreatments is the key to obtain ultra-thin, continuous, and highly sp^3-bonded diamond films on any substrate, including Si wafers. It is common practice to pretreat the substrate surface prior to the diamond film deposition, using mechanical polishing with micropowder or nanopowder diamond or ultrasonic bath with a diamond power suspension, to induce the initial diamond nucleation and growth as well as to increase the diamond nucleation density [58]. Mechanical pretreatment of the substrate, which results in surface roughening on a microscopic scale, is routinely applied to achieve a nucleation density high enough to yield closed films.

2.8 Plasma Diagnosis Techniques

In microwave plasma system, energy from the microwave electric filed ionizes the gas, which is primary H_2 with small amounts of hydrocarbon. Electrons in the microwave plasma are the main factor responsible for transferring energy from the external field to the discharge gas. Hence, detailed information that concerns electron number density and electron temperature is frequently used as the starting point for understanding associated with plasma phenomena including particle collision processes, gas-phase reactions, and surface-gas interactions [59]. Accurate and reliable information concerning plasma parameters, electron density, electron temperature, and concentration of gas-phase species, is an important first step in many different kinds of plasma-related researches. Furthermore, in the case of diamond films grown by plasma-enhanced CVD, the mechanisms of chemical processes in the plasma is also crucial for optimizing the whole process and appears to be key parameters for the growth. They depend on concentration of gas-phase species and their attendant energy. At the most basic level, knowledge of these parameters not only is critical to the understanding of complex plasma behavior but also

This material is reserved for educational use only, not allowed for commercial use.
Forbidden to modify the content, and cite the document when use.

provides a basis for optimizing the growth conditions to control the film properties and reach the maximum growth rate. Consequently, the diagnostic technique necessitates the extraction of the parameters of plasma.

Many diagnostic techniques [60-62] such as Langmuir probe, optical emission spectroscopy (OES), and microwave diagnostics have been used for diagnosis of gas-phase species, including electron, in the plasma. The most common technique is Langmuir probe measurements [63-66]. Although providing important information on the plasma, Langmuir probe technique is an invasive method resulting in plasma distortion and this technique is only suitable for measuring parameters of cold plasmas. On the other hand, this technique is inappropriate for plasma with high gas temperature on account of heating and erosion the probe during inserting it into the plasma.

In this thesis, an optical spectrometer and an impedance analyzer were used for *in situ* and real-time measurements of plasma parameters. The optical spectrometer used for measuring optical emission intensity of gas-phase species. The 2.45-GHz automatic impedance analyzer with a matching system, which measures plasma impedance, was applied to characterize CVD-plasma parameters particularly the trends of electron density and electron temperature. Both OES and measurements of plasma impedance have a main advantage over a Langmuir probe because they can monitor throughout the process without perturbing the plasma during the deposition process and alternating the exciting electromagnetic fields. Moreover, *in situ* measurements by the two methods are possible simultaneously without having an effect on each other.

2.8.1 Measurements of Plasma Impedance

The plasma acts as an electrical load of the microwave circuit of the MPECVD apparatus. The changing of its physical and chemical properties becomes appearing as those of plasma impedance. The plasma impedance has influenced chemical-process mechanisms occurring in the gas-phase environment to produce precursors for the film growth. Therefore, the monitor and manipulation of the plasma impedance can give an insight in further understanding and controlling of the growth process. As reported by Muller *et al.* [67], plasma-working conditions influence plasma impedance associating with electron density in the plasma. In addition, Hosomi *et al.* [68, 69] reported the effect of the xenon gas addition into plasma on plasma impedance and diamond film growth. They suggested the addition of xenon and argon gases increases electron density promoting H and other radicals in the gas phase.

This material is reserved for educational use only, not allowed for commercial use.
Forbidden to modify the content, and cite the document when use.

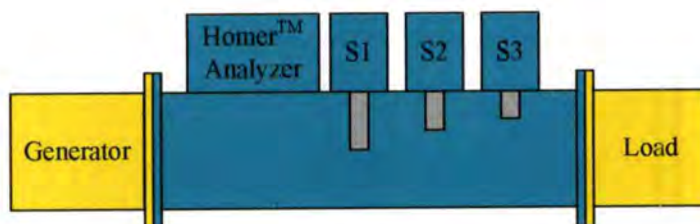

Figure 2.15 Schematic installation of the *STHT* 2.45 GHz AIAMS [68].

For this thesis, the method of plasma impedance measurement employed the *STHT* 2.45-GHz Automatic Impedance Analyzer and Matching System (*STHT* 2.45 GHz AIAMS). The *STHT* 2.45 GHz AIAMS integrates HOMER™ impedance analyzer and a three-stub tuner in one compact unit; it works under the fullpower operating conditions of magnetron-based microwave generators. Its schematic installation is shown in **Figure 2.15**.

The HOMER™ part measures both magnitude and phase of reflection coefficient as well as incident, reflected, and absorbed power, and frequency. The stub tuner part consists of three stepping-motor-driven capacitive stubs spaced in mutual distances of nominally one quarter of guide wavelength. The HOMER™ part is based on the six-port reflectometer (SPR) principle [70, 71]. SPR is capable of measuring complex reflection coefficient of a load as well as the incident, reflected and absorbed powers. The conceptual simplicity of SPR facilitates its stable and temperature-independent operation of over long periods. Reflectometers of this type are especially suitable for industrial applications where on-line monitoring and controlling under full working power is required.

The impedance of microwave-induced plasma has been affected by electron density and temperature in the plasma [40, 41, 62, 67, 72-74]. To extract electron density from measurements of plasma impedance and simplify this problem, we assumed that the power loss is negligible. The electron density and temperature can be examined from the correlation between reflection coefficient Γ_L and plasma impedance Z_p normalized by a waveguide-impedance. By measuring the complex reflection coefficient of plasma by the *STHT* 2.45 GHz AIAMS, electron density can be calculated using the following expressions:

$$\Gamma_L = \frac{Z_p - 1}{Z_p + 1} \qquad (2.17),$$

To analyze the conductivity of materials exposed to alternating electric fields, it is necessary to treat conductivity as a complex number called the admittivity. Therefore,

This material is reserved for educational use only, not allowed for commercial use.
Forbidden to modify the content, and cite the document when use.

$$\frac{1}{Z_p} = \sigma_p = \sigma'_p + j\sigma''_p = \frac{n_e e^2}{m_e} \frac{1}{\upsilon_m + j\omega} \tag{2.18}$$

Here, the plasma conductivity that is in inverse relation to the plasma impedance is a complex number whose real and imaginary parts describe the resistive (energy dissipation) and reactive (energy storage) properties of the plasma, respectively. The electron density besides real and imaginary parts of the plasma conductivity σ_p is also related as

$$n_e = \frac{m_e}{e^2} \frac{\left(\upsilon_m^2 + \omega^2\right)}{\upsilon_m} \sigma'_p \tag{2.19}$$

and

$$n_e = \frac{m_e}{e^2} \frac{\left(\upsilon_m^2 + \omega^2\right)}{\omega} \sigma''_p \tag{2.20}$$

To apply Equations (18–20) in determination of electron density requires the measurement of the complex plasma impedance and the measurement or estimate of the elastic collision frequency. The collision frequency is also a function of electron energy distribution function (EEDF), gas temperature, reactor pressure and type of working gas [67, 74, 75]. Since the complex plasma impedance for a given working gas mainly depends on EEDF, electron density, and pressure. Changing these parameters causes to a change in the plasma impedance. Consequently, the plasma impedance reflects not only electron density but also electron temperature in the plasma.

From the definition of admittance σ ($I = \sigma U$; thus, $I^* = \sigma^* U^*$), substituting $I^* = \sigma^* U^*$ into Equation (2.1) gives

$$\frac{1}{2}\sigma^* U U^* = P_A + j2\omega\left(W_M - W_P\right) \tag{2.21}$$

In this equation, the input admittance represents admittance of the field applicator loaded with the plasma, so

This material is reserved for educational use only, not allowed for commercial use.
Forbidden to modify the content, and cite the document when use.

$$\sigma \equiv \sigma'_p + j\sigma''_p + j\sigma''_0 = \frac{2P_A - j4\omega\left[W_M - \left(W_E - W_K\right)\right]}{UU^*} \quad (2.22),$$

where $$j\sigma''_0 = j\frac{4\omega\left(W_E - W_M\right)}{UU^*} \quad (2.23).$$

Here, W_E is the average energy stored in the electric field in a free space and $j\sigma''_0$ is the input admittance of the same network in the absence of the plasma discharge. Such case implies the total average kinetic energy related to the ordered motion of electrons under the influence of the high-frequency field$\left(W_K\right)$is zero. If $W_M = W_E$, while the discharge is presenting, corresponding to a condition of the maximum power transfer, then $\sigma = \sigma_p$ so

$$\sigma = \sigma'_p + j\sigma''_p = \frac{2P_A + j4\omega W_K}{UU^*} \quad (2.24).$$

That accounts for the presence of the plasma discharge in the applicator.

Considering Equation (2.24), σ'_p and σ''_p are connected with the energy absorbed from electromagnetic field by the electrons and then either spent in collisions with heavy particles or stored as kinetic energy. In other word, it shows that σ'_p related to the loss term is proportional to P_A as well as n_e; and it shows that σ''_p related to reactive energy stored in the plasma is proportional to W_K. The relation between W_K related to energy stored in the electrons and σ''_p being the imaginary part of the complex plasma conductivity are also related by

$$W_K = kT_e = \frac{UU^*}{4\omega}\sigma''_p = \frac{P_A}{2\omega}\frac{\sigma''_p}{\sigma'_p} \quad (2.25).$$

Since electron temperature in the plasma is given by the energy that is reserved after it makes inelastic collisions with the background of heavy particles [41, 64], this elucidates obviously that W_K is proportional to electron temperature. Therefore, the measurements of the complex plasma impedance, including absorbed microwave power, are capable of determining the trend of electron density and electron temperature in the plasma.

2.8.2 Plasma Diagnostics by OES

There have been several attempts to diagnose chemical species in the plasma by OES in the diamond deposition process [9, 76-78]. OES has long been recognized as a valuable technique for monitoring and optimizing plasma process because of its high sensitivity and flexibility in operation [79-81]. OES is a nonperturbative technique used to measure the emission from excited

This material is reserved for educational use only, not allowed for commercial use.
Forbidden to modify the content, and cite the document when use.

states of species, which are normally formed by electron impact excitation of the corresponding ground state species. Complemented by other techniques like mass spectroscopy [82], OES may lead to an understanding of the relationship between the plasma chemistry, the microstructural, and properties of the films. Although the emission spectroscopy does not provide directly the information about the species that are being absorbed on the substrate during the film growth; however, the presence and relative concentration of different species in the plasma and the microstructure of the films are strongly correlated.

The emission intensity from the discharge for the transition $(i \rightarrow j)$ of the species x is given by the following expression [83, 84]:

$$I_x(i \rightarrow j) = c_x k_{x,i} n_e N_x g(\lambda) \tag{2.26}.$$

Here, C_x is a constant independent of discharge conditions, $k_{x,i}$ is the rate constant for excitation of the species x to the excited state i by electron collisions, n_e is the electron concentration, N_x is the concentration of the species x, and g(λ) is the probability that the photon of that wavelength will be collected and counted by the detector. The electron concentration n_e and the electron energy distribution, which determines $k_{x,i}$, are functions of discharge conditions such as power, pressure, electric field, gas composition, and electrode geometry in a very complicated way, which cannot be calculated in general. The concentration of species x can vary with discharge parameters if x is produced or consumed by chemical reaction in the discharge. The radiative and nonradiative transition rates can be affected by collisions of the atom or molecule with other atoms or molecules or by the electric field produced by electron in the discharge.

OES based on the determination of a relative intensity of two spectral lines is the one of an attractive and reliable nondisturbing means to measure plasma parameters [84-86]. Disregarding the difficulties in calculating the absolute detector sensitivity, the measurements of single discharge intensity cannot uniquely determine the electron temperature since the photon flux depends on both the electron concentration and electron temperature. To overcome these difficulties, it is common to measure the line ratio of two-emission line. From Equation (2.26), the emission intensity ratio of the two lines is given by

This material is reserved for educational use only, not allowed for commercial use.
Forbidden to modify the content, and cite the document when use.

$$\frac{I_1}{I_2} \sim \left(\frac{k_1}{k_2}\right)\left(\frac{N_1}{N_2}\right) \tag{2.27}$$

For the same species, the intensity ratio of two lines, e.g. $\frac{I_{H\beta}}{I_{H\alpha}}$ or $\frac{I_{H\gamma}}{I_{H\beta}}$, is proportional to the rate constant of excitation of the species, which reflects an electron mean energy in the discharge, i.e., the electron temperature. On the one hand, for the Boltzmann population distribution [62, 83, 87-91], the relative intensity between two spectral lines of the same species corresponding to transition j and k can be expressed as

$$\frac{I_{ji}}{I_{ki}} = \left(\frac{A_{ji} g_i \lambda_{ki}}{A_{ki} g_k \lambda_{ij}}\right) \exp\left(-\frac{E_j - E_k}{k_B T_{exc}}\right) \tag{2.28}$$

Here, λ is wavelength, g_j and g_k are the degeneracy of the state j and k, A_{ji} and A_{ki} are atomic transition probability for spontaneous emission, E_j and E_k are the energy thresholds of the state j and k, T_{exc} is the excitation temperature, and k_B is the Boltzmann constant. The use of OES only provides the excitation temperature and not electron temperature [83, 92]. According to our experimental operating conditions with the reactor pressure ranging from 20 mbar to 300 mbar [62], we assume that the plasma is in a local thermal equilibrium (LTE) in which the excitation temperature values close to the electron temperature ones. Furthermore, we have also assumed that the secondary reactions of the plasma are small enough to neglect the number of the secondary radicals. Consequently, variation trend of the intensity ratio can be interpreted as variation trend of the electron temperature [93].

For different species, the intensity ratio is correlated with their rate constants of excitation and their concentrations. When they exist in an excited environment and have two emission lines of close energy, the intensity ratio reflects their relative concentrations. The relative intensities of the species in the emission spectra also suggest the dominant chemical constituents present in the gas chemistry.

The chemistry in most diamond CVD is dominated by charge neutral reactions of ground state radicals and atoms formed in the discharge, and there are models predicting C atoms and CH_3 radicals [94, 95] as well as C_2 and C_2H_2 [96, 97] as the dominate precursors to diamond growth. In order to characterize the reactive environment for diamond CVD, experiments to determine the ground state concentration of H, C, C_2, CH, CH_3, and C_2H_2 have been undertaken

This material is reserved for educational use only, not allowed for commercial use.
Forbidden to modify the content, and cite the document when use.

using an nonintrusive optical diagnostic technique in a wide variety of diamond producing reactors. OES, as this technique is known, has been used to show the existence of H, C_2 and CH species in CH_4/H_2 plasma [98]. For this thesis, the optical emission lines, therefore, which have been chosen and observed for the mixture of CH_4 /H_2 plasma, are shown in **Table 2.2.**

The diamond film quality varies dramatically with the deposition method and conditions, and a large body of research has been undertaken to develop a simple relationship between OES from species, the ground concentration of that species, and the quality of deposited diamond film. Klein–Douwel *et al.* [99] found a correlation between C_2 emission and the diamond film quality for material grown in a oxyacetylene flame. In a microwave plasma reactor, Lang *et al.* [100] found the diamond film quality to correspond to H atom actinometry measurements [101]. Gruen *et al.* [102] found that OES signals from C_2 emission in microwave plasma relate to the growth rate, but not the emission from either H or CH. In a hot filament reactor, Cui *et al.* [103] observed emission from H and CH_1 relates to high quality diamond, and CH emission to indicate the presence of amorphous carbon films.

Table 2.2: The optical-emission lines observed in this thesis for a mixture of CH_4/H_2 [104, 105].

Species	Transition	Peak Position (nm)
Hβ	n' = 4 ⟶ n = 2	486.1
Hγ	n' = 5⟶ n = 2	434.1
Hδ	n' = 6 ⟶n = 2	410.0
H_2	$G^1\Sigma_g^+ \rightarrow B^1\Sigma_u^+$	462.9
CH	$B^2\Delta \rightarrow X^2\Pi$ $A^2\Delta \rightarrow X^2\Pi$	387.0 431.5
CH^+	$A^1\Pi \rightarrow X^1\Sigma$	417.5
C_2	$d^3\Pi_g \rightarrow a^3\Pi_u$	516.5
CN	$B^2\Sigma \rightarrow X^2\Sigma$	388.3

This material is reserved for educational use only, not allowed for commercial use.

Forbidden to modify the content, and cite the document when use.

2.9 Characterization Techniques

In the advancement of science and technology the discovery of novel materials, those are having varied characteristics and applications have played an important role. Characterization is an important step in the development of exotic materials. The complete characterization of any material consists of phase analysis, compositional characterization, structural elucidation, and surface characterization, which have strong bearing on the properties of materials. This has led to the emergence of variety of advanced techniques in the field of materials science.

In this thesis, the structural properties of the films were studied by field emission scanning electron microscopy (FE-SEM). Chemical composition measurements were made by Raman spectroscopy and setup white-light reflectometry. In addition, the correlation between material grown and gas-phase species present in the plasma environment can identify the mechanism growth of the films.

2.9.1 Filed Emission Scanning Electron Microscopy (FE-SEM) with Energy Dispersive X-ray Spectroscopy (EDS)

A scanning electron microscope (SEM) is a type of electron microscope that images a sample by scanning it with a high-energy beam of electrons in a raster scan pattern. Electrons generated from an electron gun enter a surface of a sample and generate many low energy secondary electrons. The intensity of these secondary electrons is governed by the surface topography of the sample. An image of the sample surface is therefore constructed by measuring secondary electron intensity as a function of the position of the scanning primary electron beam [106, 107]. However, developers and researchers into novel materials for use in nanotechnology demand high resolution SEM. A field-emission cathode in the electron gun of a scanning electron microscope provides narrower probing beams at low as well as high electron energy, resulting in both improved spatial resolution and minimized sample charging and damage. With the help of the high spatial resolution in imaging of this instrument, we get an insight into the crystal structure of the films.

In addition to secondary electrons imaging, backscattered electrons imaging and EDS analysis are also useful tools widely used for chemical analysis. EDS used an analytical model depending on the X-ray excitation of samples for characterizing peaks of X-ray spectrum based on atomic structure [106, 107]. The intensity of backscattered electrons generated by electron bombardment can be correlated to the atomic number of the element within the sampling volume.

Forbidden to modify the content, and cite the document when use.

Hence, qualitative elemental information can be revealed. The characteristic X-rays emitted from the sample serve as fingerprints and give elemental information of the samples including semi-quantitative analysis, quantitative analysis, and defect compositional analysis.

2.9.2 Auger Electron Spectroscopy (AES)

AES provides information about the composition and chemical state of the outermost material comprising a solid surface or interface [106, 107]. Therefore, in AES, a primary electron beam is used as energy source to excite inner level electrons of an atom to escape from the atom. When this happens, the outer level electron will quickly move down to the electron hole in the inner layer and release energy; this energy will excite another outer level electron to escape the atom. The excited electron that escapes atomic bonding and leaves from the specimen surface is called an Auger electron. Analyzing the Auger electron, which possesses the same characteristics of the atom, gives us ingredient information of the material. In addition, the chemical structure of materials may result in (i) a shift in the energy of an Auger peak, (ii) a change in the shape of an Auger electron energy distribution often called the line shape, or (iii) a change in the Auger signal strengths of an Auger transition [108].

2.9.3 Raman Spectroscopy

Raman spectroscopy have been proven to be a valuable tool for the characterization of various carbon phases and is an established spectroscopic technique for measuring the chemical identity and structure of carbon-based materials by a simple non-destructive and non-contact method of measurements. It is most sensitive to highly symmetric covalent bonds with little and can distinguish between sp^2 and sp^3 carbon sites. It is capable of discerning even slight changes in structure, making it to be a very valuable tool on the characterization of carbon nanomaterials.

Raman spectroscopy relies on inelastic scattering, or Raman scattering, of monochromatic light, usually from high intensity laser radiation with wavelengths in the blue-green spectral region (488-514.5 nm). Raman scattering occurs when light impinges upon a molecule and interacts with the electron cloud and the bonds of that molecule. For the spontaneous Raman scattering, which is a form of light scattering, a photon excites the molecule from the ground state to the virtual energy state, shown in **Figure 2.16**.

This material is reserved for educational use only, not allowed for commercial use.
Forbidden to modify the content, and cite the document when use.

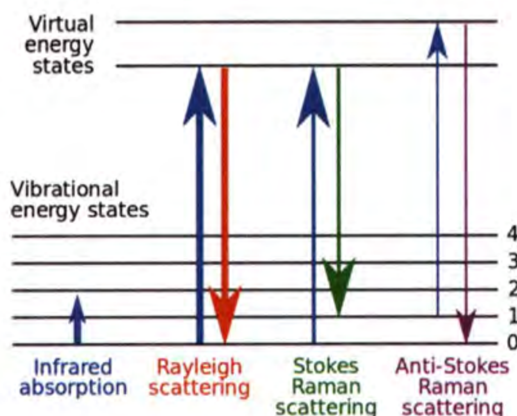

Figure 2.16 The different possibilities of visual light scattering: Rayleigh scattering, Stokes scattering, and anti-Stokes scattering [109].

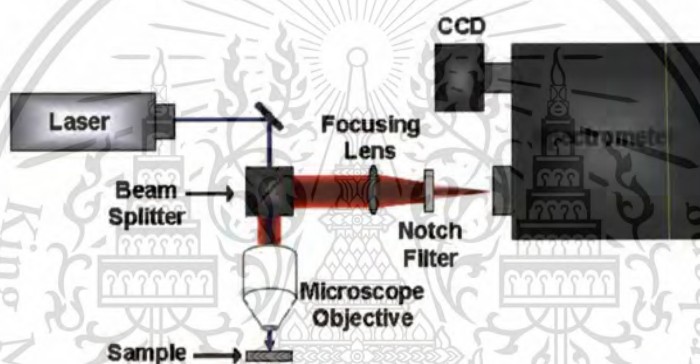

Figure 2.17 Schematic of a micro-Raman spectrometer [110].

The different possibilities of visual light scattering are as follows - Rayleigh scattering, Stokes scattering, and anti-Stokes scattering. Rayleigh scattering is no exchange of energy so the incident and emitted photons have the same energy. Stokes scattering is the atom or molecule absorbs energy and the emitted photon has less energy than the absorbed photon). Finally, anti-Stokes scattering is that the atom or molecule loses energy and the emitted photon has more energy than the absorbed photon [109]. The schematic of a micro-Raman spectroscopy, which uses a microscope to magnify its spatial resolution, is shown in **Figure 2.17**.

When the molecule relaxes, it emits a photon and it returns to a different rotational or vibrational state. The difference in energy between the original state and this new state leads to a shift in the emitted photon's frequency away from the excitation wavelength. Raman scattering, which is a light scattering phenomenon, should not be confused with absorption (as with fluorescence) where the molecule is excited to a discrete (not virtual) energy level. If the molecules relax and then back to the final vibrational state that they started in, the reemitted

Forbidden to modify the content, and cite the document when use.

photon has the same energy as the original photon. This type of scattering is known as Rayleigh scattering. However, it is possible for the molecules to relax back to the final vibrational state that is different in energy that they started in. If the final vibrational state of the molecule is more energetic than the initial state, then the emitted photon will be shifted to a lower frequency in order for the total energy of the system to remain balanced. This shift in frequency is designated as a Stokes shift. If the final vibrational state is less energetic than the initial state, then the emitted photon will be shifted to a higher frequency, and this is designated as an anti-Stokes shift.

In colloquial usage, Raman shifts are typically in wavenumbers, which have units of inverse length. In order to convert between spectral wavelength and wavenumbers of shift in the Raman spectrum, the following formula can be used:

$$\Delta\omega = \frac{1}{\lambda_0} - \frac{1}{\lambda_1} \qquad (2.29).$$

Here, $\Delta\omega$ is the Raman shift expressed in wavenumber, λ_0 is the excitation wavelength, and λ_1 is the Raman spectrum wavelength. Most commonly, the units chosen for expressing wavenumber in Raman spectra is inverse centimeters (cm^{-1}).

The typical Raman spectrum of a single crystal diamond, highly ordered pyrolytic graphite (HOPG), microcrystalline diamond, and nanocrystalline diamond are shown in **Figure 2.18** (a-d). It is well known that the Raman spectrum of a single crystal diamond is characterized with a sharp single band at 1332 cm^{-1} corresponding to the sp^3 hybridization of diamond. The Raman spectrum of graphite has two bands representing the dis-ordered carbon (D-band) at 1350 cm^{-1} and graphitic carbon (G-band) 1580 cm^{-1}. Both the bands are the signatures of sp^2-bonded carbon. A highly ordered pyrolytic graphite (HOPG) consists of hexagonal sp^2 network. The Raman signatures of a microcrystalline diamond has a sharp well distinct feature at 1332 cm^{-1} and a mild background at ~ 1480 – 1550 cm^{-1}, representing the sp^3 and sp^2 characteristics, respectively (**Figure 2.18** (c)). As MCD consists of large grains, the intensity of the peak at 1332 cm^{-1} is predominant. However, in NCD, as the grain size decreases, a completely different Raman characteristic is observed.

This material is reserved for educational use only, not allowed for commercial use.
Forbidden to modify the content, and cite the document when use.

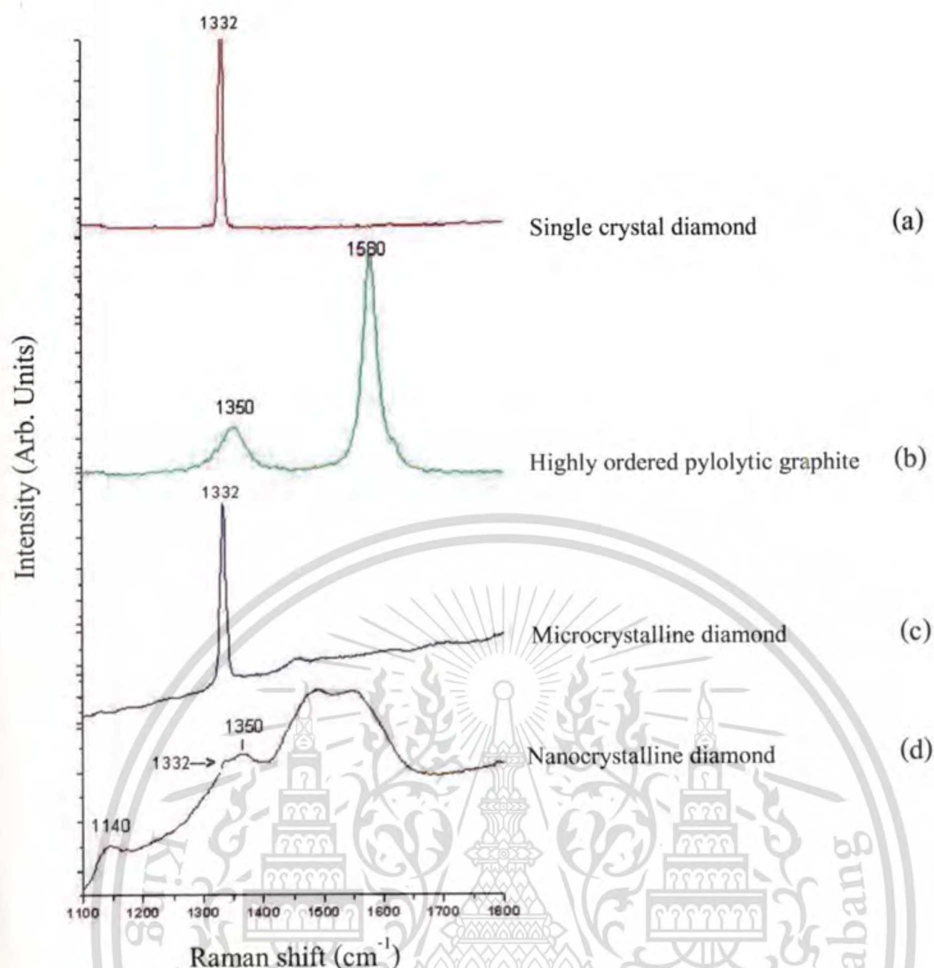

Figure 2.18 Raman spectra of carbon-based materials [111].

Visible Raman being more sensitive (~ order of 50 times) to the sp^2-bonded carbon than is for the sp^3, results in a broader Raman scattering for the former [112]. Hence, the spectra for the NCD films predominantly show the scattering due to sp^2-bonded carbon, even though the majority of the film is sp^3-bonded carbon. The Raman spectra of NCD films are composed of the typical features [113]: The diamond-related sharp line at 1332 cm^{-1} and the sp^2-related grain boundary contributions arising from either disordered amorphous carbon (D-band at ≈ 1350 cm^{-1} and G-band at ≈ 1600 cm^{-1}) or from *trans*-polyacetylene-like fragments (features at ≈1150 cm^{-1} and ≈1480 cm^{-1}). Some researchers however believe that the peaks at ≈ 1150 and ≈1480 cm^{-1} are due to confined phonon modes [114, 115]. In addition, a sixth broad component is found at around 1200-1250 cm^{-1}. This component does not show up as a distinct maximum, but becomes visible with a peak fitting procedure. This Raman intensity is interpreted as a broadened vibrational density of states (VDOS) of small diamond grains. As all these feature are broad and

This material is reserved for educational use only, not allowed for commercial use.
Forbidden to modify the content, and cite the document when use.

overlap considerably, a peak fitting routine is used to determine the spectral components, peak position, widths, and shapes.

Another important feature of Raman spectra of diamond films is the significant shift in the G peak. It is well established that the G peak present in the Raman spectra of sp^2 carbon materials shifts to higher value under applied stress (P) according to [116]

$$\Delta\left(\text{G-peak position}\right)=5\left[\text{cm}^{-1}/\text{GPa}\right]\times\text{P}\left[\text{GPa}\right] \quad (2.30).$$

The film-induced stress accumulating in the deposited films relaxes through several mechanisms; the significant one is the graphite-diamond phase transformation. Another one is drastic surface roughening that is observed to accompany the nano-diamond phase nucleation [117]. Therefore, the stress can be examined considering impurities, structural defects, and grain boundaries of the films. In addition, the stress may be examined considering the hydrogen adsorption and desorption process occurring on the surface during the film growth process.

2.9.4 White Light Spectroscopic Reflectometry

Optical techniques determine thin-film characteristics using measuring the interaction between the film and light. They can measure the thickness and optical constants of the film. Optical constants describe how light propagates through and reflects from a material. Optical techniques are usually the preferred method for measuring thin films because they are accurate, non-destructive, and require little or no sample preparation. The two most common optical measurement methods are spectral reflectance/transmittance and ellipsometry [118]. Spectral reflectance measures the amount of light reflected from a thin film over a range of wavelengths. It is much simple and less expensive than ellipsometry, but it is restricted to measure less complex structures. The amplitude and periodicity of the reflectance of thin films are determined by the films thickness, optical constants, and other properties such as interface roughness. The schematic setup of spectral reflectance measurement is shown in **Figure 2.19**. A thin film on a substrate can act as an etalon, creating an interference pattern superimposed on the surface reflectivity when viewed in reflection, as shown in **Figure 2.20**. The spacing of the sinusoidal peaks, when combined with the index of refraction of the material, can be used to calculate the thickness of the material.

This material is reserved for educational use only, not allowed for commercial use.
Forbidden to modify the content, and cite the document when use.

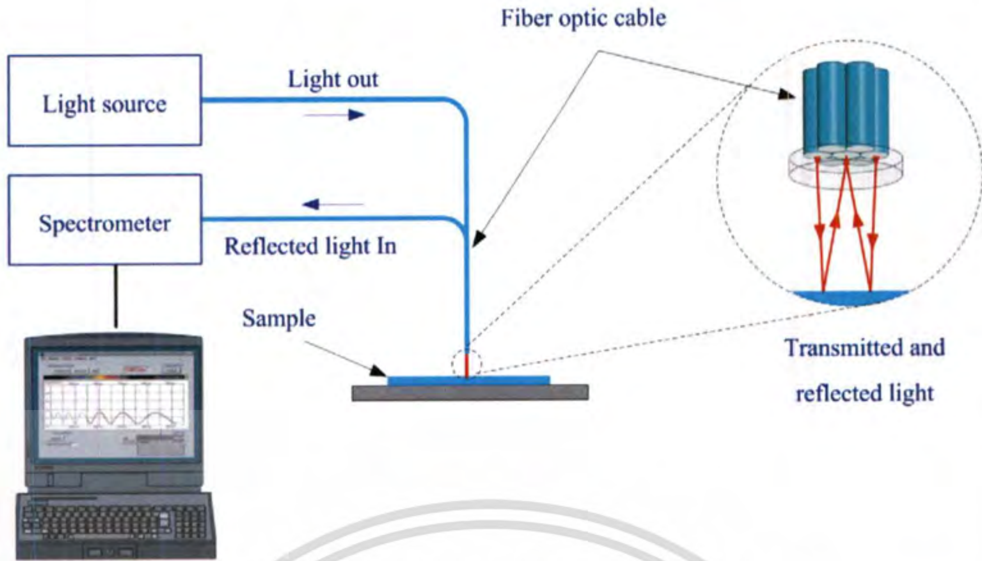

Figure 2.19 Schematic of laboratory setup for measurements of spectral reflectance.

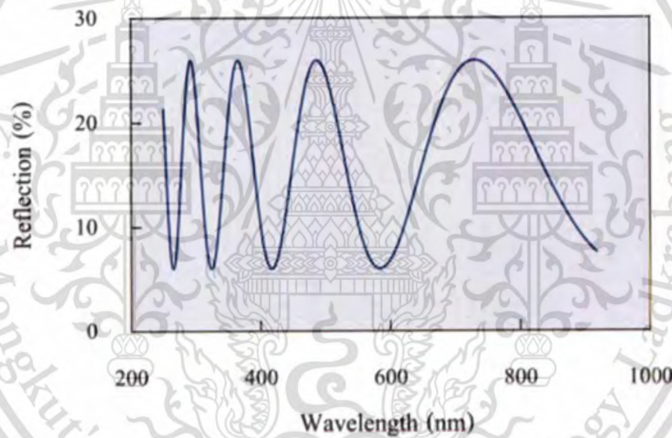

Figure 2.20 Spectrum of the reflected light signal along with the wavelength shows the intensity changed at each wavelength.

The absolute reflectance $R(\lambda)$ of the thin-film structure is given by [119, 120]

$$R(\lambda)=\frac{I_{mea}(\lambda)-I_{bkg}(\lambda)}{I_{ref}(\lambda)-I_{bkg}(\lambda)}R_{ref}(\lambda) \tag{2.31}$$

Here, $R_{ref}(\lambda)$ is the theoretical reflectance of the reference sample, $I_{mea}(\lambda)$ is the thin-film reflection spectrum, $I_{ref}(\lambda)$ is the reference spectrum, and $I_{bkg}(\lambda)$ is the background spectrum. Irradiance is proportional to the time average of the magnitude of the electric field

This material is reserved for educational use only, not allowed for commercial use.
Forbidden to modify the content, and cite the document when use.

intensity squared. The total irradiance at a given point in space that is due to the superposition of the electric field intensity from two sources emitting parallel waves of the same frequency is

$$I(\lambda)=I_1(\lambda)+I_2(\lambda)+2\sqrt{I_1(\lambda)I_2(\lambda)}\cos\Delta\phi(\lambda) \tag{2.32}$$,

where I_1 and I_2 are the irradiances of the two sources and $\Delta\phi$ is the phase difference resulting from the path difference between the sources. The waves completely overlap and then the irradiance is a maximum when the phase difference is

$$\Delta\phi(\lambda)=2M\pi, \quad M=0,1,2,... \tag{2.33}$$.

From the relation between phase difference and the optical path difference, ΔOPD , therefore, constructive interference (i.e., maxima) occurs when the following relation is satisfied:

$$2M\pi=\frac{2\pi}{\lambda}\Delta OPD(\lambda) \tag{2.34}$$.

M represents the maximum number. This calculation assumes that the index of refraction is independent of light wavelength. We can perform a number of mathematical steps to rearrange this in the form of a linear equation of the form y = mx + b.

$$\nu=\frac{c}{2nd}M \tag{2.35}$$.

Analysis of the wavelength position of the minima or maxima shown in **Figure 2.20** can determine either the thin film's thickness (with the known refractive index of the film) or its refractive index (with the known film thickness). The phase of white-light fringes is dependent on wave number in the same manner that the phase of monochromatic light fringes (produced with a He–Ne laser, for example) is dependent on path-length difference. In other words, the appearance of fringes at the output of the spectrograph occurs because the monochromatic components of the white light interfere with different phase with respect to each other.

For this thesis, the refractive index n of the diamond films are determined by reflectance spectra. The low value of n as compared with to bulk diamond but also to polycrystalline CVD diamond films (2.41) and the high absorption have been explained by the nanocomposite matrix of the films [121]. The presence of an amorphous carbon matrix lower the index and leads, as it contains also sp^2 carbon, to absorption.

This material is reserved for educational use only, not allowed for commercial use.
Forbidden to modify the content, and cite the document when use.

References

[1] Isberg J. "Diamond Electronic Devices." **AIP Conference Proceedings.** vol. 1292, 2010. Pp.123-128.

[2] Thumm M. "MPACVD-diamond Windows for High-power and Long-pulse Millimeter Wave Transmission." **Diamond Relat. Mater.** vol. 10, 2001. Pp.1692-1699.

[3] Iwakaji Y., Kanasugi M., Maida O. and Ito T. "Characterization of Diamond Ultraviolet Detectors Fabricated with High-quality Single-crystalline Chemical Vapor Deposition Films." **Appl. Phys. Lett.** vol.94, 2009. 223511.

[4] Tang K., Wang L. J., Huang J., Ma Y., Hu G., Zhu X. F. and Xia Y. B. "Diamond Film Ultraviolet Detectors with Different Diamond Grain Size." **Journal of Physics: Conference Series.** vol. 152, 2009. 012015.

[5] Robert F. Davis. **Diamond Films and Coatings.** New Jersey: Noyes Publication. 1993.

[6] Russell J. Hemley, Yu-Chun Chen, and Chih-Shiue Yan. "Growing Diamond Crystals by Chemical Vapor Deposition." **Elements.** Vol. 1, 2005. Pp.105-108.

[7] Eversole W.G. **"Synthesis of Diamond."** U.S. patent no. 3030188, April 1962.

[8] DeVries R.C. "Synthesis of Diamond under Metastable Conditions." **Anu. Rev. Mater. Sci.** vol.17, 1987. Pp. 161-187.

[9] Cicalaa G., Monégerb D., Cornacchiab D., Pesceb P., Magalettic V., Pernad G., Capozzid V. and Tamborrae M. "Toward Smooth MWPECVD Diamond Films: Exploring the Limits of the Hydrogen Percentage in $Ar/H_2/CH_4$ Gas Mixture" **Sur. Coat. Tech.** vol. 211, 2012. Pp. 152-157.

[10] Angus J.C., Will H.A. and Stanko W.S. "Growth of Diamond Seed Crystals by Vapor Deposition" **J. Appl. Phys.** vol.39, 1968. Pp. 2915-2923.

[11] Matsumoto S., Sato Y., Kamo M. and Setaka N. "Growth of Diamond Particles from Methane-Hydrogen Gas" **J. Mat. Sci.** vol.17, 1982. Pp. 3106-3112.

[12] Matsumoto S., Sato Y., Kamo M. and Setaka N. "Vapor Deposition of Diamond Particles from Methane" **Jpn. J. Appl. Phys.** vol.21, 1982. Pp. L183-L185.

This material is reserved for educational use only, not allowed for commercial use.

Forbidden to modify the content, and cite the document when use.

[13] Spitsyn B.V., Bouilov L. L., Derjaguin B. V. "Vapor Growth of Diamond on Diamond and Other Surfaces" **J. Crys. Growth.** vol.52, 1981. Pp. 219-226.

[14] Bundy F. P. "The P, T Phase and Reaction Diagram for Elemental Carbon" **J. Geophys. Res.** vol.85, no.B12, 1980. Pp.6930-6936.

[15] Lee S. T., Lin Z. and Jiang X. "CVD Diamond Films: Nucleation and Growth" **Mater. Sci. Eng.** vol. 25, 1999. Pp. 123-154.

[16] Jes Assmussen and D. K. Reinhard, Editors. **Diamond films Handbook.** New York : Marcel Dekker, Inc. 2002.

[17] Vadym N. Mochalin, Olga Shenderova, Dean Ho and Yury Gogotsi, "The Properties and Applications of Nanodiamonds" **Nature Nanotechnology.** vol. 7, 2012. Pp.11-23.

[18] Fabisiak K. and Staryga E. "CVD Diamond: From Growth to Application" **Journal of Achievements in Materials and Manufacturing Engineering.** vol.37, 2009. Pp.264-269.

[19] Varney M.W., Aslam D.M., Janoudi A., Chan H. Y. and Wang D. H. "Polycrystalline-Diamond MEMS Biosensors Including Neural Microelectrode-Arrays" **Biosensors.** vol.1, 2011. Pp. 118-133.

[20] Gruen D. M. "Nanocrystalline Diamond Films" **Annu. Rev. Mater. Sci.** vol.29, 1999. Pp.211-259.

[21] Mitura S., Mitura K., Niedzielski P., Louda P. and Danilenko V. "Nanocrystalline Diamond, Its Synthesis, Properties and Applications" **Journal of Achievements in Materials and Manufacturing Engineering.** vol.16, 2006. Pp. 9-16.

[22] Neto Castro A. H., Guinea F. and Peres N. M. R. "Drawing Conclusions from Graphene", **Physics World.** vol.19, 2006. Pp. 33-37.

[23] Averill B. and Eldredge P. "**General Chemistry: Principles, Patterns, and Applications, v.1.0.**"[Online].Available: http://newsletter.flatworldknowledge.com/bookhub/reader/4309?e=averill_1.0-ch07_s04. 2013.

This material is reserved for educational use only, not allowed for commercial use.
Forbidden to modify the content, and cite the document when use.

[24] Kriele A., Williams O. A., Wolfer M., Hees J. J., Smirnov W. and Nebel C. E. "Formantion of Nano-pores in Nano-crystalline Diamond Films" **Chem. Phys. Lett.** vol.507, 2011. Pp. 253-259.

[25] Williams O.A., Nesladek M., Daenen M., Michaelson S., Hoffman A., Osawa E., Haenen K. and Jackman R.B. "Growth, Electronic Properties and Applications of Nanodiamond" **Diamond Relat. Mater.** vol.17, 2008. Pp. 1080-1088.

[26] Hong S. P., Yoshikawa H., Wazumi K. and Koga Y. "Synthesis and Tribological Characteristics of Nanocrystalline Diamond Film using CH_4/H_2 Microwave Plasmas" **Diamond Relat. Mater.** vol.11, 2002. Pp. 877-881.

[27] Davies A.R., JField.E., Takahashi K. and Hada K. "Tensile and fatigue strength of free-standing CVD diamond" **Diamond Relat. Mater.** vol.14, 2004. Pp. 6-10.

[28] Nebel C. E. **"Diamond Electronic Devices and its Future."** [Online]. Available : http://www.cs.waseda.ac.jp/gcoe/jpn/publication/symposium/img/080722C-Nebel.pdf. 2013.

[29] Masaryk University Information System. **"Chemical Vapor Deposition."** [Online]. Available: http://is.muni.cz/el/1431/podzim2007/C7780/um/L24_CVD.pdf. 2007.

[30] Pierson H. O. "Handbook of Chemical Vapor Deposition" Park Ridge: Noyes Publications, (1992).

[31] Jong-Hee Park, Editor. **Surface Engineering Series Volume 2 – Chemical Vapor Deposition.** Scarborough: ASM International®. 2001.

[32] Kitahama K., Hirata K., Nakamatsu H., Kawai S., Fujumori N., Imai T., Yoshino H. and Doi A. "Synthesis of Diamond by Laser-induced Chemical Vapor Deposition" **Appl. Phys. Lett.** vol. 49, 1986. Pp. 634-635.

[33] Matsumoto S. "Chemical Vapour Depostion of Diamond in RF Glow Discharge" **J. Mater. Sci. Lett.** vol. 4, 1985. Pp. 600-602.

[34] Kamo M., Sato Y., Matsumoto S. and Setaka N. "Diamond Synthesis from Gas Phase in Microwave Plasma" **J. Cryst. Growth.** vol. 62, 1983. Pp. 642-644.

This material is reserved for educational use only, not allowed for commercial use.
Forbidden to modify the content, and cite the document when use.

[35] Kurihara K., Dasaki K., Kawarada M. and Koshino N. "High rate synthesis of diamond by dc plasma jet chemical vapor deposition" **Appl. Phys. Lett.** vol. 52, 1988. Pp. 437-438.

[36] Gracio J. J., Fan Q. H. and Madaleno J. C. "Diamond Growth by Chemical Vapour Deposition" **J. Phys. D: Appl. Phys.** vol. 43, 2010. 374017.

[37] Zander A.T. and Hieftje G.M. "Microwave-supported Discharges" **Appl. Spectrosc.** vol. 35, 1981. Pp. 357-371.

[38] Computer Simulation Technology. **"Microwave Plasma Sources."** [Online]. Available: http://www.cst.com/Content/Applications/Article/Microwave+Plasma+Sources. 2013.

[39] Stephen M. Rossnagel, Jerome J. Cuomo and William D. Westwood, Editors. **Handbook of Plasma Processing Technology: Fundamentals, Etching, Deposition, and Surface Interactions.** New Jersey: Noyes Publication. 1990.

[40] Butler J. E., Mankelevich Y. A., Cheesman A., Ma J. and Ashfold M. N. R. "Understanding the Chemical Vapor Deposition of Diamond: Recent Progress" **J. Phys: Condens. Matter.** vol. 21, 2009. 364201.

[41] Michel Moisan and Jacques Pelletier, Editors. **Microwave Excited Plasmas.** Amsterdam: Elsevier Science B.V. 1999.

[42] Sanborn C. Brown. **Basic Data of Plasma Physics: The fundamental Data on Electrical Discharge in Gases.** New York: AIP Press. 1993.

[43] J Reece Roth. **Industrial Plasma Engineering Volume 1: Principles.** London: IOP Publishing, Inc. 2000.

[44] Mitsuharu Konuma. **Film Deposition by Plasma Techniques**. New York: Springer-Verlag. (1992).

[45] Butler J. E. and Woodin R. L. "The Film Diamond Growth Mechanisms [and Comment]" **Phil. Trans. R. Soc. Lond. A.** vol. 342, 1993. Pp. 209-224.

[46] May P. W., Harvey J. N., Smith J. A. and Mankelevich Yu. A. "Reevaluation of the Mechanism For Ultrananocrystalline Diamond Deposition from $Ar/CH_4/H_2$ Gas Mixtures" **J. Appl. Phys.** vol. 99, 2006. 104907.

This material is reserved for educational use only, not allowed for commercial use.

Forbidden to modify the content, and cite the document when use.

[47] Harris S. J. and Goodwin D. G. "Growth on the Reconstructed Diamond (100) Surface" J. **Phys. Chem.** vol.97, 1993. Pp. 23-28.

[48] Krogh O., Wicker T. and Chapman B. "Summary Abstract: Collisional Energy Transfer in Nobel Gas/Hydrogen Plasma" **J. Vac. Sci. Technol. A.** vol. 4, 1986. Pp. 1796-1797.

[49] Mark A. Prelas, Galina Popovici, Louis K. Bigelow, Editors. **Handbook of Industrial Diamonds and Diamond Films.** New York: Marcel Dekker, Inc. 1998.

[50] Kulisch W. and Popov C. "On the Growth Mechanisms of Nanocrystalline Diamond Films" **Phys. Stat. Sol. (a).** vol.203, 2006. Pp. 203-219.

[51] May P. W. "Diamond Thin Films: A 21st-century Material" **Phil. Trans. R. Soc. Land. A**. vol.358, 2000. Pp. 473-495.

[52] Goodwin D. G., "Scaling Laws for Diamond Chemical-vapor Deposition. I. Diamond Surface Chemistry" **J. Appl. Phys.** vol. 74, 1993. Pp. 6888-6894.

[53] May P.W., Ashfold M.N.R. and Mankelevich Y.A. "MCD, NCD & UNCD Chemical Vapour Deposition: Experimental and Modelling of the Factors that Affect the Growth Rate, Nucleation and Crystal Size" **J. Appl. Phys.** vol. 101, 2007. 053115.

[54] May P. W. and Mankelevich Y. A. "From Ultrananocrystalline Diamond to Single Crystal Diamond Growth in Hot Filament and Microwave Plasma-Enhanced CVD Reactors: a Unified Model for Growth Rates and Grain Sizes" **J. Phys. Chem. C.** vol. 112, 2008. Pp. 12432-12441.

[55] Xiao X., Birrell J., Gerbi J.E., Auciello O. and Carlisle J. A. "Low Temperature Growth of Ultrananocrystalline Diamond" **J. Appl. Phys.** vol. 96, 2004. Pp. 2232-2239.

[56] Espinosa H.D., Peng B., Prorok B.C., Moldovan N., Auciello O., Carlisle J.A., Gruen D.M. and Mancini D.C. "Fracture Strength of Ultrananocrystalline Diamond Thin Films—Identification of Weibull Parameters" **J. Appl. Phys.** vol. 94, 2003. Pp. 6076-6084.

[57] Lifshitz Y., Lee C. H., Wu Y., Zhang W. J., Bello I. and Lee S. T. "Role of Nucleation in Nanodiamond Film Growth" **Appl. Phys. Lett.** vol.88, 2006. 243114.

[58] Lee S. T., Lin Z. and Jiang X. "CVD Diamond Films: Nucleation and Growth" **Mater. Sci. Eng. R.** vol. 25, 1999. Pp. 123-157.

This material is reserved for educational use only, not allowed for commercial use.

Forbidden to modify the content, and cite the document when use.

[59] Bowden M. D., Kogano M., Suetome Y., Hori T., Uchino K. and Muraoka K., "Comparison of Electron Property Measurements in An Inductively Coupled Plasma Made by Langmuir Probea Laser Thomson Scattering Techniques" **J. Vac. Sci. Technol. A.** vol. 17, 1999. Pp. 493-499.

[60] A.A. Ovsyannikov and M.F. Zhukov, Editors. **Plasma Diagnostics.** Cambridge: Cambridge International Science Publishing, Inc. 2000.

[61] Donne'A.J.H. "Introduction to Plasma Diagnostics" **Trans. Fusion Sci. Technol.** vol.49, 2006. Pp. 349-356.

[62] Alfred Grill. **Cold Plasma in Materials Fabrication: From fundamentals to Applications.** New York: IEEE Press. 1994.

[63] Koirala S.P., Abu-safe H. H., Mensah S. L., Naseem H. A. and Gordon M. H. "Langmuir Probe and Optical Emission Studies in a Radio Frequency (rf) Magnetron Plasma used for the Deposition of Hydrogenated Amorphous Silicon" **Surf. Coat. Technol.** vol.203, 2008. Pp. 602-605.

[64] Yoon S.F., Tan K.H., Rusli, Ahn J. and Huang Q.F. "Effect of Microwave Power on Diamond-like Carbon Films Deposited using Electron Cyclotron Resonance Chemical Vapor Deposition" **Diamond Relat. Mater.** vol.9, 2000. Pp. 2024-2030.

[65] Teii K. "Diagnostics of the Diamond Depositing Inductively Coupled Plasma by Electrostatic Probes and Optical Emission Spectroscopy" **J. Vac. Sci. Technol. A.** vol.17, 1999. Pp. 138-143.

[66] Hoyong Park, S. J. You, and Wonho Choe, "Correlation between Excitation Temperature and Electron Temperature with Two Groups of Electron Energy Distributions" **Phys. Plasma.** vol.17, 2010. 103501.

[67] Müller A., Emme M., Korzec D. and Engemann J. "Direct Power Coupling into a Waveguide Cavity Plasma Source" **Surf. Coat. Technol.** vol.116-119, 1999. Pp. 674-678.

[68] Hosomi T., Maki T. and Kobayashi T. "Enhanced Diamond Film Growth by Xe-added Microwave Plasma CVD" **Thin Solid Films.** vol. 368, 2000. Pp. 269-274.

This material is reserved for educational use only, not allowed for commercial use.
Forbidden to modify the content, and cite the document when use.

[69] Hosomi T. Maki T., Kobayashi T., Yoshizako Y. and Taniguchi M. "Roleo Xenon Additive in Microwave Plasma-assisted (H_2+CH_4) Chemical Vapor Deposition of Diamond Thin Film" **J. Appl. Phys.** vol.84, 1998. Pp. 6059-6063.

[70] S-TEAM Lab. **"User's Handbook: Homer Hot Measurement and Tuning System."** [Online]. Available: http://www.s-team.sk/download/HomerHbook5001.pdf. 2013

[71] Vladimir Bilik. **"Six-Port Measurement Technique: Principles, Impact, Applications."** [Online]. Available: http://www.s-team.sk/download/SixPortTechnique.pdf. 2002.

[72] Mehrdad Mehdizadeh. **Microwave/RF Applications and Probes for material Heating, Sensing and Plasma Generation a Design Guide.** Sam Diego: Elsevier Inc. 2010.

[73] Michael A. Lieberman and Allan J. Lichtenberg. **Principles of Plasma Discharges and Materials Processing.** 2nd ED. New York: John Wiley& Sons, Inc. 1994.

[74] Koemtzopoulos R.C., Economou D. J. and Pollard R. "Hydrogen Dissociation in a Microwave Discharge for Diamond Deposition" **Diamond Relat. Mater.** vol. 2, 1993. Pp. 25-35.

[75] Yu. P. Raizer. **Gas Discharge Physics.** 2nd ED. Berlin: Springer. 1997.

[76] Liao W. H., Wei D. H. and Lin C. R. "Synthesis of Highly Transparent Ultrananocrystalline Diamond Films from a Low-Pressure, Low-Temperature Focused Microwave Plasma Jet" **Nanoscale Research Letters.** vol. 7:82, 2012.

[77] Zhu X. D., Hu M., Zhan R. J., Wen X. H. and Zhou H. Y. "Diagnostics of Plasma Emission Spectra during Electron Assisted Chemical Vapor Deposition of Diamond Films" **Phys. Plasma.** vol. 5, 1998. Pp.1541-1544.

[78] Liao Y., Li C. H., Ye Z. Y., Chang C., Wang G. Z. and Fang R. C. "Analysis of Optical Emission Spectroscopy in Diamond Chemical Vapor Deposition Diamond Related Materials" **Diamond Relat. Mater.** vol. 9, 2000. Pp. 1716-1721.

[79] Zhu W., Inspektor A., Badzian A. R., McKenna T. and Messier R. "Effect of Noble Gases on Diamond Deposition from Methane-hydrogen Microwave Plasmas" **J. Appl. Phys.** vol. 68, 1990. Pp. 1489-1496.

This material is reserved for educational use only, not allowed for commercial use.
Forbidden to modify the content, and cite the document when use.

[80] John P., Rabeaua J. R., Wilsonb J. I. B. "The Cavity Ring-Down Spectroscopy of C_2 in a Microwave Plasma" **Diamond Relat. Mater.** vol.11, 2002. Pp. 608-611.

[81] J.A. Smith, K.N. Rosser, H. Yagi, M.I. Wallace, P.W. May, M.N.R. Ashfold "Diamond deposition in a DC-arc Jet CVD system: investigations of the effects of nitrogen addition" **Diamond Relat. Mater.** vol. 10, 2001. Pp. 370-375.

[82] Zhou H., Watanabe J., Miyake M., Ogino A., Nagatsu M. and Zhan R. "Optical and Mass Spectroscopy Measurements of $Ar/CH_4/H_2$ Microwave Plasma for Nano-crystalline Diamond Film Deposition" **Diamond Relat. Mater.** vol. 16, 2007. Pp. 675-678.

[83] Massereau-Guilbaud V., Géraud-Grenier I. and Plain A. "Determination of the Electron Temperature by Optical Emission Spectroscopy in a 13.56 Mhz Dusty Methane Plasma: Influence of the Power" **J. appl. Phys.** vol. 106, 2009. 113305.

[84] Kampas F.J. "An Optical Emission Study of the Glow-Discharge Deposition of Hydrogenated Amorphous Silicon from Argon-silane Mixtures" **J. Appl. Phys.** vol. 54, 1983. Pp. 2276-2280.

[85] Boffard J. B., Lin C. C. and DeJoseph Jr C. A. "Application of Excitation Cross Sections to Optical Plasma Diagnostics" **J. Phys. D: Appl. Phys.** vol. 37, 2003. Pp. R143-R16.

[86] Moshkalyov S. A., Diniz J. A., Swart J. W., Tatsch P. J. and Machida M. "Deposition of Silicon Nitride by Low-pressure Electron Cyclotron Resonance Plasma Enhanced Chemical Vapor Deposition in $N_2/Ar/SiH_4$" **J. Vac. Sci. Technol. B.** vol. 15, 1997. Pp. 2682-2687.

[87] Larijani M. M., Normand F. L. and Crégut O., "An Optical Emission Spectroscopy Study of the Plasma Generated in the DC HF CVD Nucleation of Diamond" **Appl. Surf. Sci.** vol. 253, 2007. Pp. 4051-4059.

[88] Jośe A. C. Broekaert. **Analytical Atomic Spectrometry with Flames and Plasmas**. 2nd ED. Weinheim: Wiley-VCH Verlag GmbH&Co., KGaA. 2005.

[89] Wiese W.L. and Fuhr J.R. "Accurate Atomic Transition Probabilities for Hydrogen, Helium, and Lithium" **J. Phys. Chem. Ref. Data.** vol. 38, 2009. Pp. 565-719.

This material is reserved for educational use only, not allowed for commercial use.
Forbidden to modify the content, and cite the document when use.

[90] Barshilia H. C., Mehta B. R. and Vankar V. D. "Optical Emission Spectroscopy during the Bias-enhanced Nucleation of Diamond Microcrystals by Microwave Plasma Chemical Vapor Deposition Process" **J. Mater. Res.** vol. 11, 1996. Pp. 2852-2860.

[91] Shimozuma M., Tochitani G. and Tagashira H. "Optical Emission Diagnostics of H_2+CH_4 50-Hz–13.56-MHz Plasmas for Chemical Vapor Deposition" **J. Appl. Phys.** vol.70, 1991. Pp. 645-648.

[92] Gordillo-V′azquez F. J., Camero M. and G′omez-Aleixandre C., "Spectroscopic Measurement of the Electron Temperature in Low Pressure Radiofrequency $Ar/H_2/C_2H_2$ and $Ar/H_2/CH_4$ Plasmas Used for the Synthesis of Nanocarbon Structures" **Plasma Sources Sci. Technol**. vol.15, 2006. Pp. 42-51.

[93] Lee Y. S., In J. H., Ahn S. K. Seo S. H., Chang H. Y., You D. J., Ahn S. W. and Lee H. M., "The Trend of Electron Temperature and Electron Density in the Process of Microcrystalline Silicon Solar Cells" **Curr. Appl. Phys.** vol.10, 2010. Pp. S234 – S236.

[94] Goodwin D. G. "Simulations of High-rate Diamond Synthesis: Methyl as Growth Species" **Appl. Phys. Lett.** vol.59, 1991. Pp. 277-279.

[95] Coltrin M. E. and Dandy D. S. "Analysis of Diamond Growth in Subatmospheric dc Plasma-gun Reactors" **J. Appl. Phys.** vol. 74, 1993. Pp. 5803-5820.

[96] Redfern P. C., Horner D. A., Curtiss L. A. and Gruen D. M. "Theoretical Studies of Growth of Diamond (110) from Dicarbon" **J. Phys. Chem.** vol. 100, 1996. Pp. 11654-11663.

[97] Frencklach M. and Wang H. "Detailed Surface and Gas-Phase Chemical Kinetics of Diamond Deposition" **Phys. Rev. B.** vol. 43, 1991. Pp. 1520-1545.

[98] Inspektor A., Liou Y., McKenna T. and Messier R. "Plasma CVD Diamond Deposition in C-H-O Systems" **Surf. Coat. Technol.,** vol. 39-40, 1989. Pp. 211-221.

[99] Klein-Douwel R. J. H., Spaanjaars J. J. L. and Ter. Meulen J. J. "Two-dimensional Distributions of C_2, CH, and OH in a Diamond Depositing Oxyacetylene Flame Measured by Laser Induced Fluorescence" **J. Appl. Phys.** vol. 78, 1995. Pp. 2086-2096.

This material is reserved for educational use only, not allowed for commercial use.
Forbidden to modify the content, and cite the document when use.

[100] Lang, J. Stiegler, Y. v. Kaenel, and E. Blank, **Diamond Relat. Mater.** 5, 1171 (1996).

[101] Barshilla H. C. and Vankar V. D. "Concentration of Atomic Hydrogen in the Ground State in a CH_4-H_2 Microwave Plasma" **J. Appl. Phys.** vol. 80, 1996. Pp. 3694-3700.

[102] Gruen D. M., Zuiker C. D., Krauss A. R. and Pan X. "Carbon Dimer, C_2, as a Growth Species for Diamond Films from Methane/Hydrogen/Argon Microwave Plasmas" **J. Vac. Sci. Technol. A.** vol. 13, 1995. Pp. 1628-1632.

[103] Cui J. and Fang R "Characterization of the diamond growth process using optical emission spectroscopy" **J. Appl. Phys.** vol. 81, 1997. Pp. 2851-2857.

[104] Liang Q., Chin C. Y., Lai J., Yan C. S., Meng Y., Mao H. K. and Hemley R. "Enhanced Growth of High Quality Single Crystal Diamond by Microwave Plasma Assisted Chemical Vapor Deposition at High Gas Pressures" **Appl. Phys. Lett.** vol. 94, 2009. 024103.

[105] Liao Y., Li C.H., Ye Z.Y., Chang C., Wang G.Z. and Fang R.C. "Analysis of Optical Emission Spectroscopy in Diamond Chemical Vapor Deposition" **Diamond Relat. Mater.** vol. 9, 2000. Pp. 1716-1721.

[106] Leonard C. Feldman and James W. Mayer. **Fundamentals of Surface and Thin Film Analysis.** New York: Elsevier Science Publising Co., Inc. 1986.

[107] J. M. Walls. **Methods of Surface analysis.** New York: Cambridge University Press. 1989

[108] Ramaker D. E. "Chemical Effects in the Carbon KVV Auger Line Shapes" **J. Vac. Sci. Technol. A.** vol.7, 1989. Pp. 1614-1622.

[109] Ewen Smith and Geoffrey Dent. **Modern Raman Spectroscopy: A practical approach.** Chichester: John Wiley & Sons Ltd. 2005.

[110] Payne C. and Barron A. R. "**Surface-Enhanced Raman Spectroscopy for the Study of Surface Chemistry.**" [Online]. Available: http://cnx.org/content/m34522/latest/?collection=col10699/latest. 2010.

[111] Jeedigunta S. "**Growth and Characterization of Nanocrystalline Diamond Films for Microelectronics and Microelectromechanical Systems.**" Doctor of Philosophy of University of South Florida. 2008.

This material is reserved for educational use only, not allowed for commercial use.

Forbidden to modify the content, and cite the document when use.

[112] Klauser F., Steinmüller-Nethl D., Kaindl R., Bertel E. and Memmel N. "Raman Studies of Nano- and Ultra-nanocrystalline Diamond Films Grown by Hot-Filament CVD" **Chem. Vap. Deposition.** vol.16, 2010. Pp. 127–135.

[113] Ferrari A.C. and Robertson J., "Raman Spectroscopy of Amorphous Nanostructure Diamond Like Carbon and Nanodiamond" **Phil. Trans. R. Soc. Lond. A.** vol. 362, 2004. Pp. 2477-2512.

[114] Nemanich R.J., Glass J.T., Lucovsky G. and Schroder R.E. "Raman Scattering Characterization of Carbon Bonding in Diamond and Diamondlike Thin Films" **J. Vac. Sci. Technol. A.** vol. 6, 1988. Pp. 1783-1787.

[115] Sowers A.T., Ward B.L., English S. and Nemanic R.J. "Growth, Microstructure and Field-emission Properties of Nitrogen Doped Diamond Films", **J. Appl. Phys.** vol. 86, 1999. Pp. 3973-3982.

[116] Heiman A., Lakin E., Zolotoyabko E. and Hoffman A. "Microstructure and Stress in Nano-crystalline Diamond Films Deposited by DC Glow Discharge CVD" **Diamond Relat. Mater.** vol.11, 2002. Pp. 601-607.

[117] Heiman A., Gouzman I., Christiansen S. H., Strunk H. P., Comtet G., Hellner L., Dujardin G., Edrei R. and Hoffman A. "Evolution and Properties of Nanodiamond Films Deposited by Direct Current Glow Discharge" **J. Appl.Phys.** vol.89, 2001. Pp. 2622-2630.

[118] Mikropack **"Thin-Film-Metrology Spectroscopic Reflectometer."** [Online]. Available: http://www.mikropack.de/e/tfm/refle/index.html. 2013.

[119] Kim S. H., Lee S. H., Lim J. I. and Kim K. H. "Absolute Refractive Index Measurement Method over a Broad Wavelength Region Based on White-light Interferometry" **Appl. Optics.** vol.49, 2010. Pp. 910-914.

[120] Hlubina P., Ciprian D., Luňáček J. and Lesňák M. "Thickness of SiO2 Thin Film on Silicon Wafer Measured by Dispersive White-light Spectral Interferometry" **Appl. Phys. B.** vol.84, 2006. Pp. 511-516.

This material is reserved for educational use only, not allowed for commercial use.
Forbidden to modify the content, and cite the document when use.

[121] Kulisch W., Popov C., Sasaki T., Sirghi L., Rauscher H., Rossi F. and Reithmaier J. P. "On the Development of the Morphology of Ultrananocrystalline Diamond Films" **Phys. Status Solidi A.** vol.208. 2011. Pp. 70-80.

This material is reserved for educational use only, not allowed for commercial use.
Forbidden to modify the content, and cite the document when use.

CHAPTER 3

EXPERIMENTAL SETUP

In this chapter the design of a MPECVD reactor used for the deposition of diamond films will be described, including its gas supply system, microwave power supply, baseplate, etc. The present chapter will also look at the plasma diagnostic techniques, film characterizations including laboratory set-up for a visible light reflectometer and a contact angle measuring instrument. The *in-situ* optical emission spectroscopy and measurements of plasma impedance have been chosen to diagnosis the plasma. The morphology and lateral structure of the films were investigated by field emission-scanning electron microscopy (FE-SEM). The surface composition and structure of the diamond film were analyzed by Auger electron spectroscopy (AES), energy dispersive X-ray spectroscopy (EDS), Raman spectroscopy, and white light reflectometry.

3.1 The Microwave Plasma-enhanced Chemical Vapor Deposition System

A schematic diagram of a MPEVCD bell-jar reactor system designed and constructed at Surface Physics and Laser Research Laboratory is shown in **Figure 3.1** and a cross-section drawing of its section is shown in **Figure 3.2**. The MPECVD reactor system consists of several subsystems, including a microwave coupling subsystem. Microwave power with a frequency of 2.45 GHz was generated using a Sharp 2M167B-M10 900 W air-cooled magnetron powered by a laboratory-made microwave power supply. The magnetron was coupled to a standard WR340 rectangular waveguide at the one end and microwaves propagate in a fundamental mode of TE_{108}. A moveable short terminated at the other end adjusted the resonant cavity of the rectangular waveguide. A marker indicated a position of this moveable short.

This material is reserved for educational use only, not allowed for commercial use.
Forbidden to modify the content, and cite the document when use.

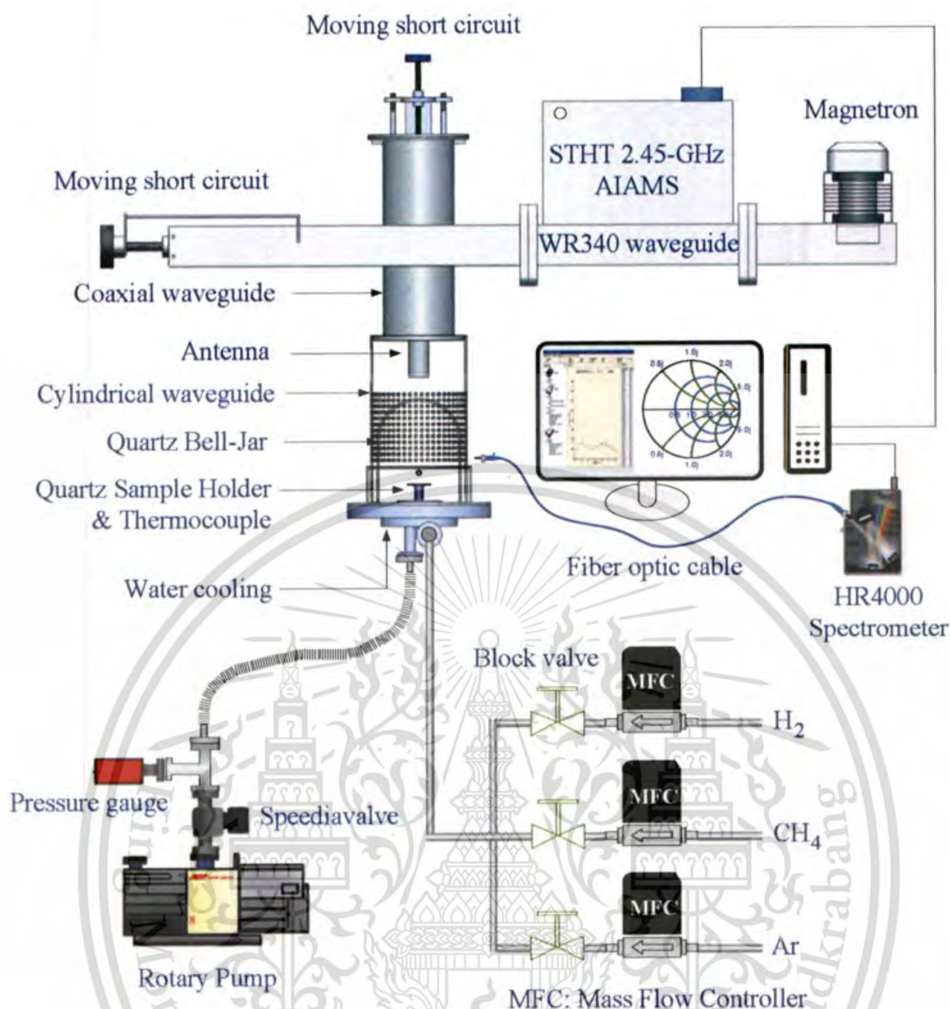

Figure 3.1 Schematic of a purpose-designed and built MPECVD apparatus.

A mode converter being a section of a cylindrical waveguide couples microwave energy from the rectangular waveguide into a reactor chamber by means of an antenna. The cavity height and diameter of the cylindrical waveguide produces a dominate microwave mode that is identified as the TE_{111} mode. A sliding short at the one end of the cylindrical waveguide produces standing wave pattern and maximizes energy coupling between the two waveguides. The other end of the cylindrical waveguide was terminated by a stainless steel baseplate. A quartz bell jar acting as a plasma reactor chamber was placed on the baseplate. A Si wafer used as a substrate is place on a quartz substrate holder. The substrate is floating electrically. A mechanical pump evacuated the reactor.

This material is reserved for educational use only, not allowed for commercial use.
Forbidden to modify the content, and cite the document when use.

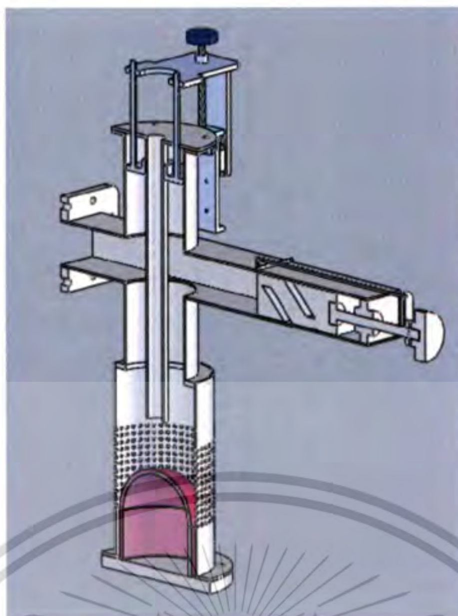

Figure 3.2 Cross-section geometry of the MPECVD apparatus.

The *STHT* 2.45 GHz AIAMS including a matching system is included in the section of the rectangular waveguide. In addition to plasma-impedance control, it also provides information on plasma impedance associated with electron temperature and density. Furthermore, measurements of plasma impedance and an optical spectrometer are also employed in the MPECVD system. It provides the intensities of the optical emission from the plasma. These intensities can be used to specify densities of the gas-phase species.

3.1.1 Purpose-designed and built MPECVD systems

There have been several design variations of the MPECVD system that have been developed at Surface Physics and Laser Research Laboratory, KMITL in 2007-2010. The requirement of the distinct improvement in the detailed design of each MPECVD subsystems is to optimize the operation for diamond growth. The major subsystem of the MPECVD reactor system is the microwave coupling subsystem, i.e., the external microwave circuit and applicator coupling subsystem. Components of this subsystem are a microwave generator, waveguides, an antenna, sliding shorts, and a STHT 2.45 GHz AIAMS with a three-stub tuner acting as the matching system. The tuning elements, which match the impedance of the microwave circuit to the reactor load, are also included in this subsystem. These tuning elements mean antenna adjustments, resonant cavity length adjustments, and substrate position adjustments further the three-stub tuner adjustments. These adjustments not only control the impedance matching, which determines the

This material is reserved for educational use only, not allowed for commercial use.
Forbidden to modify the content, and cite the document when use.

reflected power, but also influence the plasma-discharge uniformity, which has a direct impact on the uniformity of the diamond deposition on the substrate surface.

The purpose of an early designed and built version is shown in **Figure 3.3**. The purpose for design this system was to adjust elements of the microwave-coupling system to optimize the microwave energy transfer to create and maintain the plasma discharge uniformity. The other purpose is to optimize temperature of the electrically floating substrate. The substrate temperature is determined primarily by the input microwave power and the position of the substrate in the reactor chamber. However, when the MPECVD reactor was first designed and built at the beginning of this thesis, it was not designed to operate for long period of time. It cannot continue operating more than 1 h.

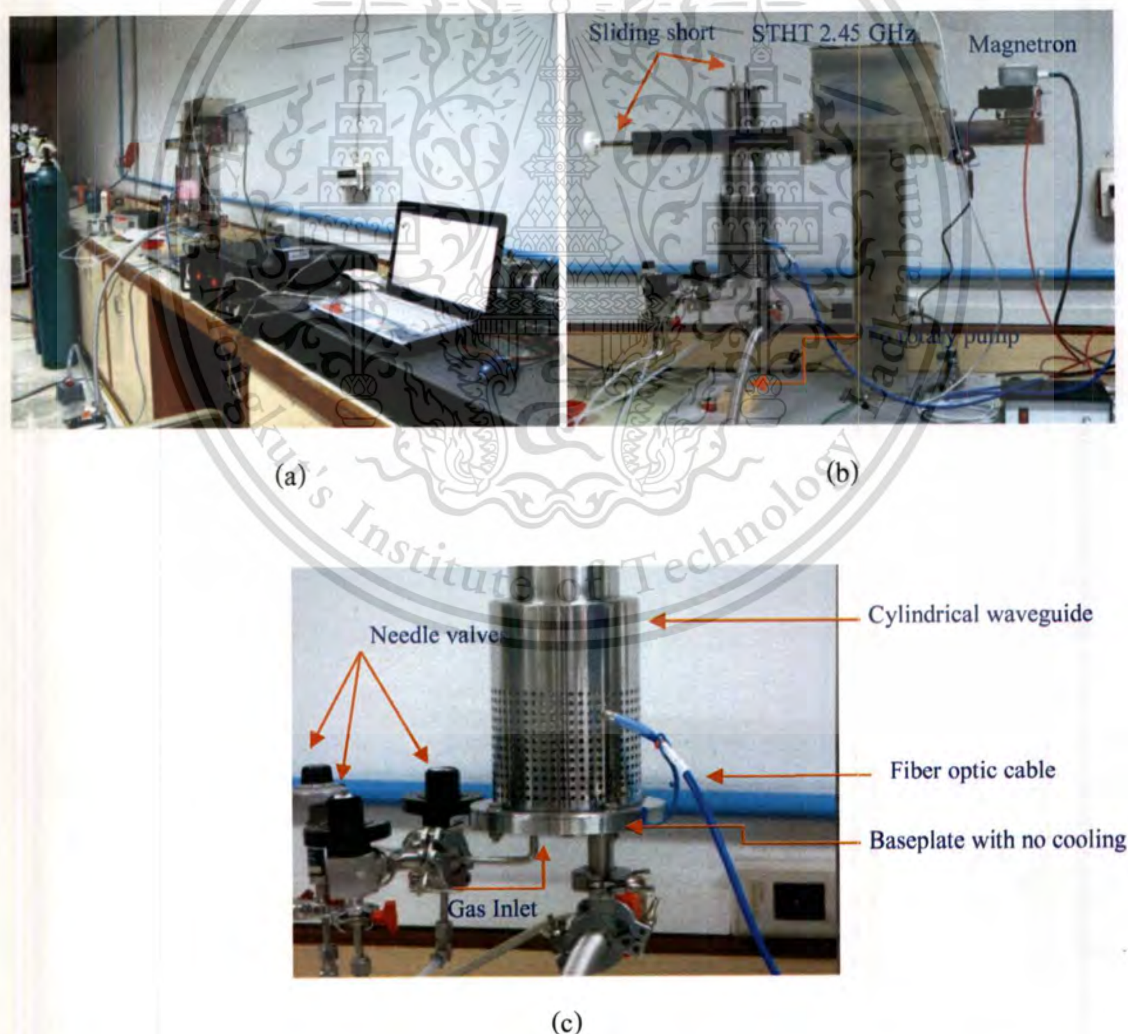

Figure 3.3 An early purpose-built MPECVD apparatus (2007) which was equipped needle valves to control the volumetric gas-flow rates.

This material is reserved for educational use only, not allowed for commercial use.
Forbidden to modify the content, and cite the document when use.

Although this MPECVD apparatus design proven successful in generating and sustaining microwave plasma, it was limited in functionality to sustained operation below operating time and power. Sustained operating with a longer time and the high power led to the failure of Viton® O-ring sealing vacuum integrity between the baseplate and the plasma reactor due to the effect of thermal runaway. This threshold can be increased time and power if the baseplate was forced-water cooled. As the baseplate heats due to contact with the high plasma density, which increases temperature of the Viton® O-ring even further.

The next system version is shown in **Figure 3.4**. Water cooling inlet/outlet shown in **Figure 3.4**(c) is used for heat removal from the baseplate. **Figure 3.4**(c) also shows a quartz substrate holder, which was newly designed and placed on the baseplate. A silicon wafer used as a substrate was placed on the quartz substrate holder.

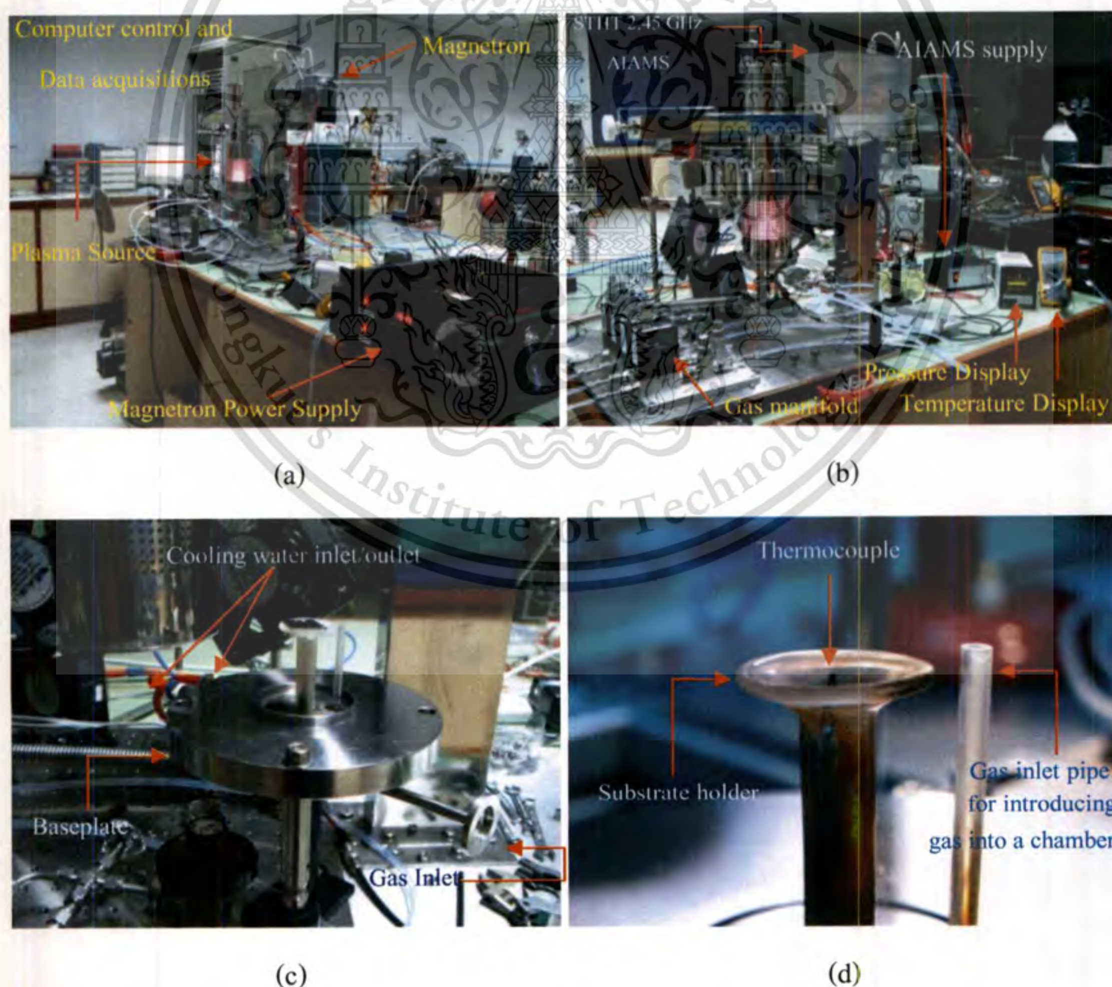

Figure 3.4 The later version of the MPECVD apparatus and baseplate.

This material is reserved for educational use only, not allowed for commercial use.
Forbidden to modify the content, and cite the document when use.

The both sliding shorts were newly designed to improve efficiency of the impedance tuning. The internal sliding short is contactless. These sliding shorts can be equipped with a fine - tuning and a locked system. The lowering of radiated into ambient and lost within microwave circuit indicated the microwave circuit was properly matched more than that of the first version.

In addition, a K type thermocouple was also attached at the bottom section of the baseplate. It measures substrate temperatures and contacts at the back of the substrate. Due to immersing in the plasma, the substrate was heated to the desired temperature by microwave-plasma induction, instead of auxiliary heating. A 1.5-mm inner diameter straight quartz tube acting as the gas inlet introduced the reaction gas mixture into the reactor chamber. It passed into the reactor chamber and was 46 mm high from the inner wall of the baseplate. The shape of this gas inlet has been experimentally chosen after optimization. It strongly influences the gas flow pattern in my CVD reactor.

The precursor gases controlled by a custom designed and fabricated aluminum manifold is shown in **Figure 3.5**. The manifold contains Aera® FC7700CD mass flow controllers (MFCs), Swagelok® SS-DLS4 ¼ in. diaphragm-sealed valves, Swaglok® tubing fitting and connectors, and Swaglok® PFA tubing. Unit instruments Aera® FC7700CD MFCs provide measurements of gas flow rates. When purchased, the MFCs were calibrated for a particular reference gas and have a maximum obtainable flow rate. An Advanced Energy® ROD-4A control unit that is for up to four MFCs powers the MFCs. This control unit displays and provides accurate digital control of the individual gas flow rate.

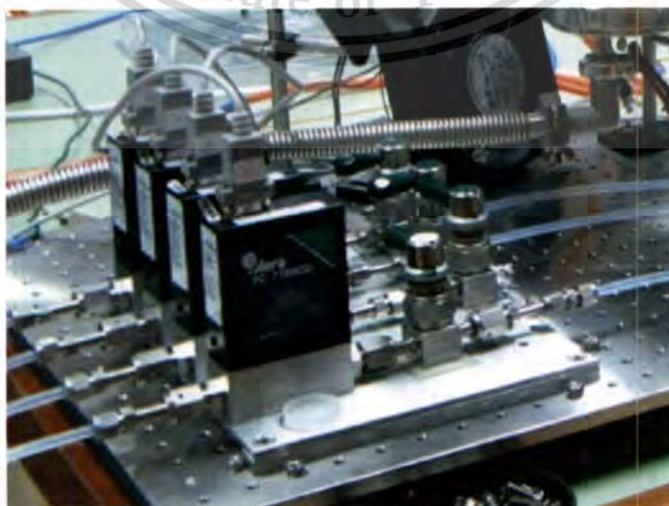

Figure 3.5 Gas manifold: the MFC, supply line and shut-off valves.

This material is reserved for educational use only, not allowed for commercial use.
Forbidden to modify the content, and cite the document when use.

The last version of the whole MPECVD reactor apparatus was mounted on a custom designed and fabricated extruded aluminum rack, as shown in **Figure 3.6** and as photography in **Figure 3.7**. The gas manifold, shown in **Figure 3.5**, was designed and modified to fit into the grooves of the aluminum stand. The power supplies and displays were mounted on aluminum shelves built into the stand as also in **Figure 3.7** and **Figure 3.8**. The substrate temperature was displayed via a FLUKE 80TK thermocouple module on a HP 34401A Multimeter display interfacing with a computer.

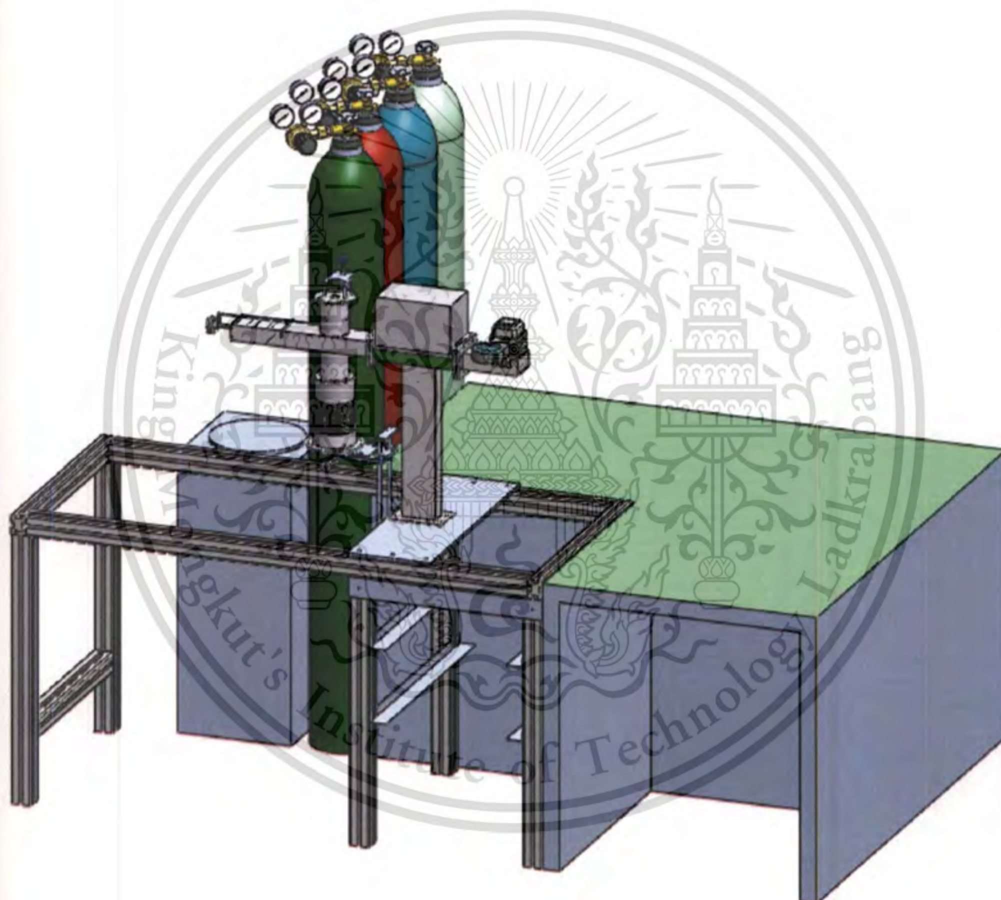

Figure 3.6 Design of the MPECVD apparatus and rack.

This material is reserved for educational use only, not allowed for commercial use.
Forbidden to modify the content, and cite the document when use.

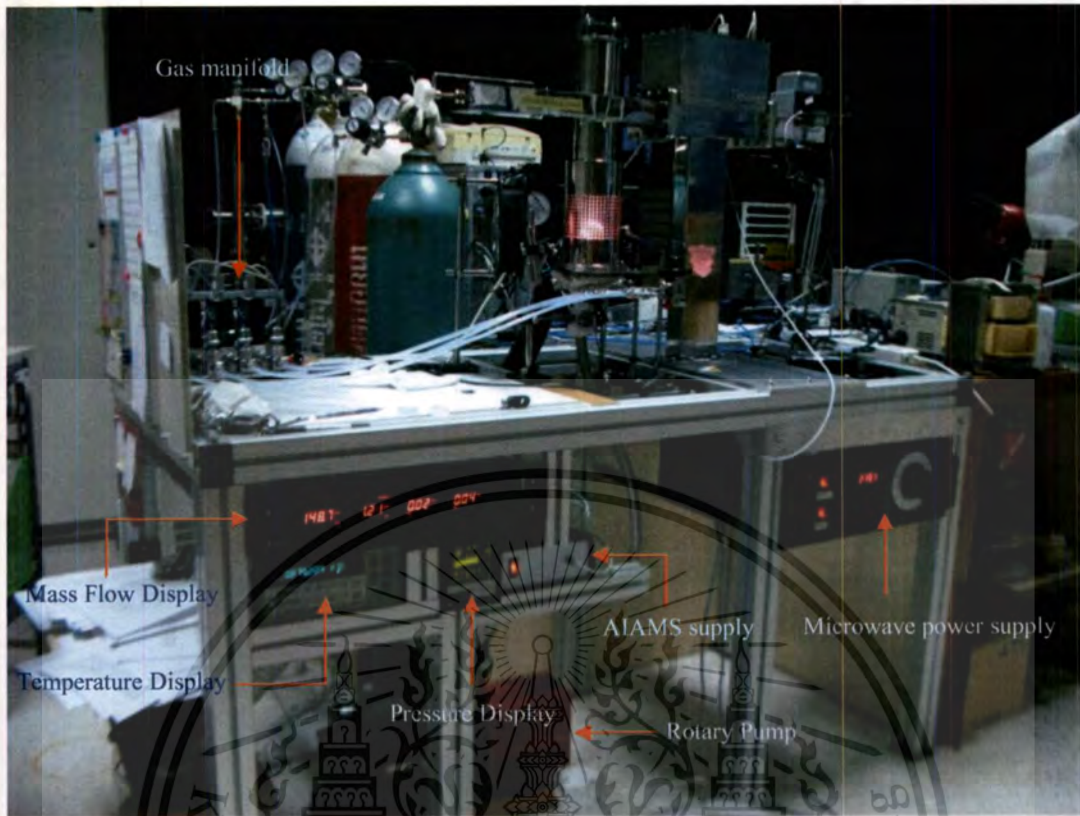

Figure 3.7 Photograph of the last version of the MPECVD apparatus developed at Surface Physics and Laser Research Laboratory.

In the initial design, the baseplate with a reactor chamber was attached to the cylindrical waveguide by removing manually. As compared to **Figure 3.4**(c), **Figure 3.8**(b) shows that a linear ball baring and shaft fits with the groove of the aluminum and attaches to the baseplate, making it smooth movement and simplifying it fixed to the cylindrical waveguide. **Figure 3.9** shows that the baseplate with the reactor chamber assembled in the linear ball baring and shaft and then attached to the cylindrical waveguide.

This material is reserved for educational use only, not allowed for commercial use.
Forbidden to modify the content, and cite the document when use.

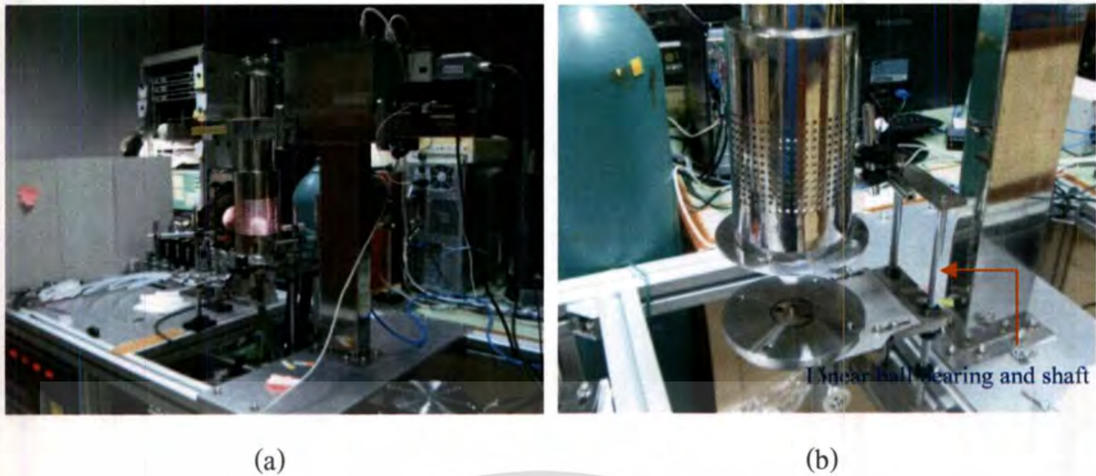

(a) (b)

Figure 3.8 Photograph of the last version of the MPECVD apparatus (a) and the baseplate fixed to a liner ball bearing and shaft (b).

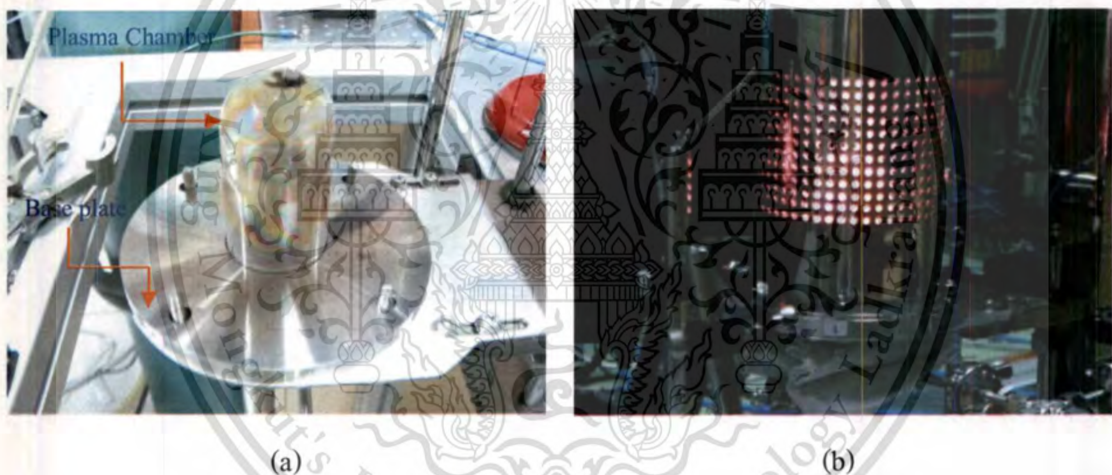

(a) (b)

Figure 3.9 The reactor chamber with a baseplate was fixed to the linear ball bearing and shafts (a) and the reactor chamber attached to the cylindrical waveguide during plasma ignition (b).

3.1.2 Plasma Reactor and Substrate Holder

The quartz bell jar of 45 mm diameter with a height of 90 mm was used as the plasma reactor chamber. The plasma reactor chamber is made of quartz because the microwaves travel through the quartz rather than bouncing off or heating it. A plasma reactor chamber made of Pyrex® was fabricated initially but this was found to be unsatisfactory in the plasma environment.

This material is reserved for educational use only, not allowed for commercial use.
Forbidden to modify the content, and cite the document when use.

(a) (b)

Figure 3.10 Pyrex® bell jar after using as the plasma chamber for 30 min.

Figure 3.10 shows that the Pyrex® bell jar got too hot and became melted after it was used as the plasma reactor chamber around only 30 min but the quartz bell jar did not. Pyrex® is not a microwave transparent material but quartz is. Therefore, a substrate holder is also made of quartz. The substrate placed on the holder is 43 mm high from the bottom of the baseplate, which is the position of antinode standing wave. This position was also experimentally obtained after optimization. The Si wafer substrate with the size of 20x30 mm^2 is placed on the substrate holder. The substrate is heated due to microwave induction with no additional active heating or cooling utilized.

3.1.3 Baseplate Design

The bottom section of the stainless steel baseplate consists of two ports, a vacuum feedthrough, shown in **Figure 3.11**. These two ports were connected to a mechanical vacuum pump and a gas supply system. The vacuum feedthrough allows a ceramic sheathed K type thermocouple to pass into the center of the reactor chamber. On the top of the baseplate shown in **Figure 3.12**, both the reactor chamber and the substrate holder were placed in the axiality of the cylindrical waveguide. A Viton® O-ring seal embedded in a shallow groove on the baseplate ensures vacuum integrity between the base plate and the reactor chamber. It also limits the maximum microwave power that can be used, as it is liable to burn if it becomes too hot. Therefore, water cooling is used for cooling the base plate. A design of the water jacket around the base plate is shown in **Figure 3.13**.

This material is reserved for educational use only, not allowed for commercial use.
Forbidden to modify the content, and cite the document when use.

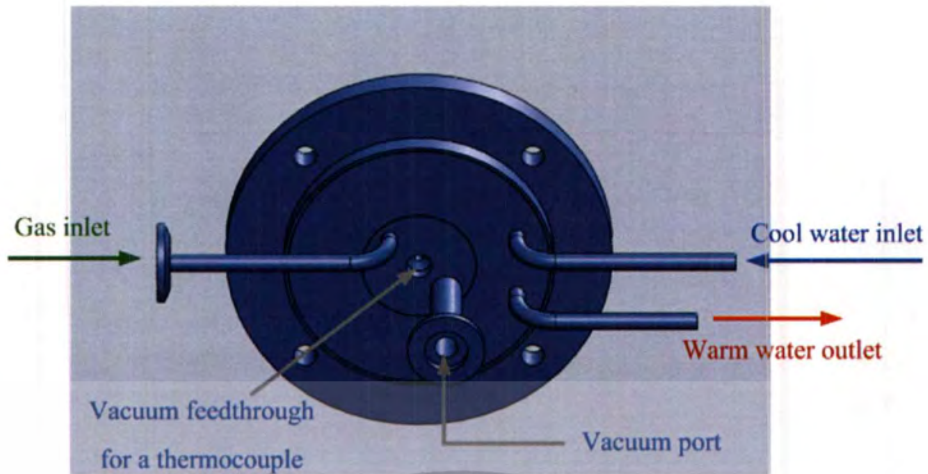

Figure 3.11 Bottom side of the baseplate

Figure 3.12 Top of the baseplate

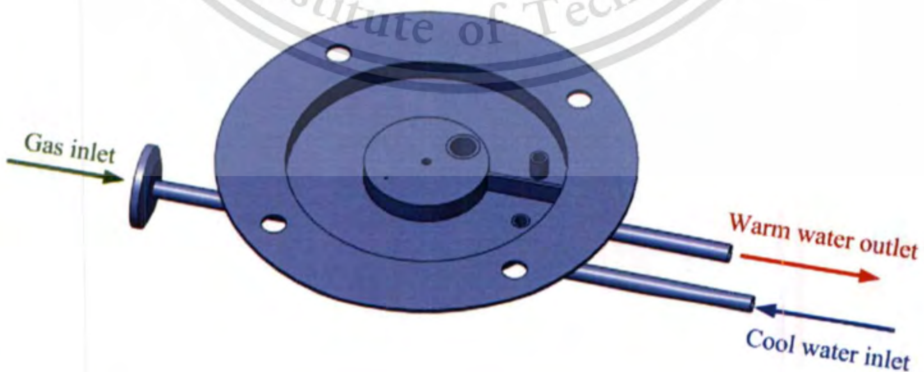

Figure 3.13 Baseplate design water-cooling jacket of the baseplate.

The water jacket is a metal sheath having intake and outlet vents to allow water to be pumped through the void. The length of the intake vent is shorter than that of the outlet vent.

This material is reserved for educational use only, not allowed for commercial use.
Forbidden to modify the content, and cite the document when use.

Therefore, the water can be pumped up to the top wall of the baseplate and then flows down to the tank. The flow of inlet water with a temperature of 10 °C to the cooling baseplate allows precise temperature control of the base plate.

3.1.4 Gas Flow Rate Control and Pressure Control Subsystem

An Acatel 2012 2012A dual stage rotary vane mechanical vacuum pump evacuated the reactor chamber via the one port at the bottom section of the baseplate as described above. A base pressure of the reactor is one Pa. A Leybold Vacuum THERMOVAC TR211gauge head was used to measure the base and deposition pressures. This gauge head is capable of measuring pressures between 10^{-2} and 10^{5} Pa and is a finely measured pressure gauge in pressure ranging from one to 50 kPa that used for the deposition of diamond films. The THERMOVAC TR211 gauge head was operated in connection with a Leybold Vacuum COMBIVAC CM31 instrument. The COMBIVAC CM31 powers the gauge head and digitally displays a measured pressure with respect to the selected measurement unit. In addition, a gas supply system consisting of gas lines, regulating valves, mass flow controllers and non-return valves supplied and monitored different gases into the reactor chamber. **Figure 3.14** shows the gas supply system.

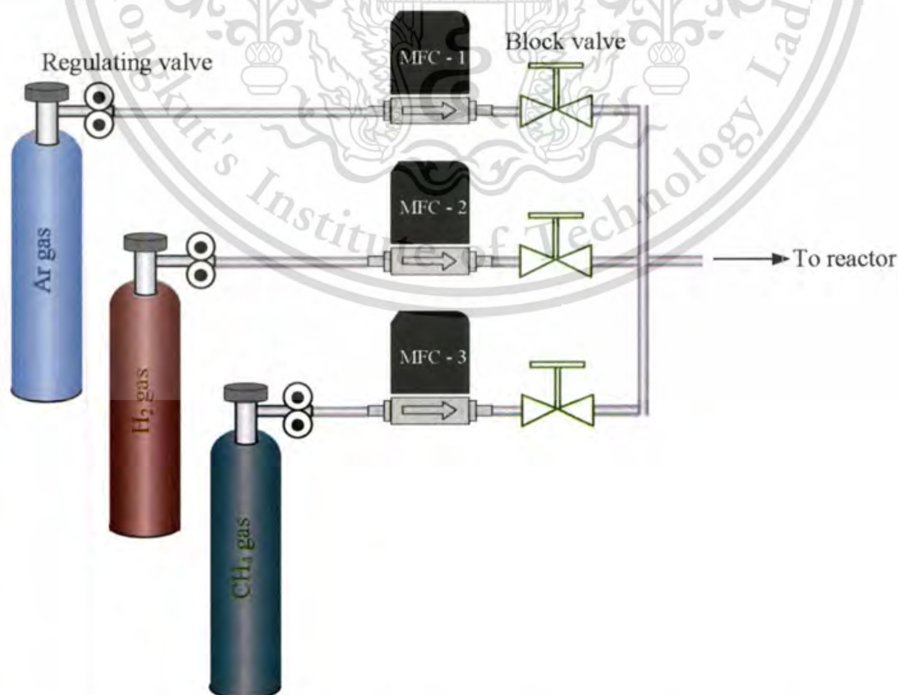

Figure 3.14 Schematic representation of the gas supply system.

This material is reserved for educational use only, not allowed for commercial use.
Forbidden to modify the content, and cite the document when use.

The CONCOA precision regulating valve connected to each gas cylindrical controls the pressure at which the gas exits the cylindrical into the gas line. The regulating valves are used to step down the output pressure of cylinders to 20 PSI. The purity of hydrogen and argon gas is ultrahigh purity grade 5.0 and that of methane gas is high purity grade 4.0. The gas flow rates inside the chamber are controlled by Aera® FC-7700CD MFCs. Two Swagelok® SS-DLS4 diaphragm valves open and close entry of the gas towards the reactor chamber. The mass flow rate of each gas is monitored by an Advanced Energy® ROD-4A MFC control unit and display. The gas leaving the MFCs is mixed before entering the gas inlet pipe leading to the reactor chamber. Before the beginning of the deposition process, the system is flushed with a constant flow rate of argon gas. The gas flow rate and pressure can be controlled independently. The desired pressure in the reactor chamber is maintained and controlled by a BOC Edwards® SP 16K speedialvalve with Nitrile diaphragm valve located between the pump and the reactor chamber. This speedialvalve acts as a throttle valve.

3.1.5 Microwave Power Supply

For this thesis, the microwave power supply has been built from accessories of a home-microwave oven to create the plasma in the vacuum-reactor chamber. The purpose of the microwave power supply is to provide the voltage and current needed to power a magnetron or a microwave generator to produce the required 2.45 GHz of microwave energy. A circuit of the microwave-power supply used for this thesis is shown in **Figure 3.15**.

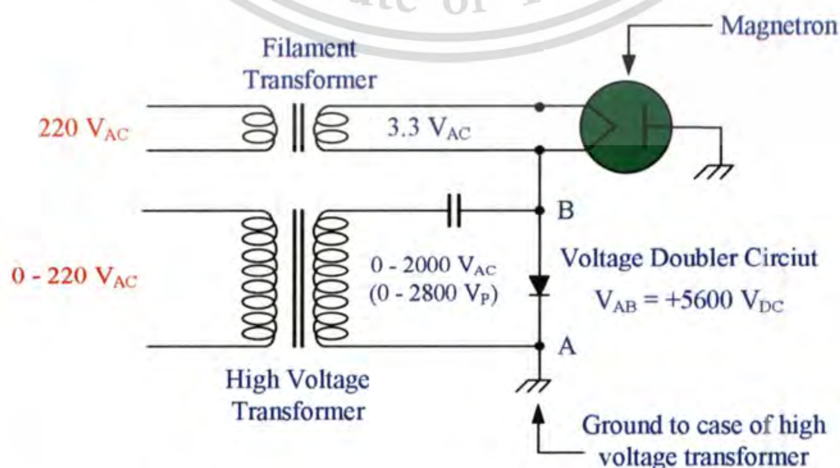

Figure 3.15 The circuit of the microwave power supply.

This material is reserved for educational use only, not allowed for commercial use.
Forbidden to modify the content, and cite the document when use.

The circuit consists of a magnetron, a high-voltage capacitor, a high-voltage diode and two transformers (a filament transformer and a high-voltage transformer). Microwave power supply's high voltage circuitry uses the transformer, diode, capacitor to effectively convert AC voltage to DC voltage flowing to the magnetron. On the other hand, the circuit consists of basically two sections; a low voltage section which actually controls the current of the magnetron filament and a high-voltage section which controls the voltage give magnetron to power up. The high-voltage section consists of a high-voltage transformer, a high-voltage capacitor, and a high-voltage diode. Both capacitor and diode function together to effectively the already-high voltage. This called a voltage-doubler circuit. This diode converts the voltage to DC and this capacitor discharges voltage of 2800 V and send it to the magnetron. This adds to the 2800 volts that comes direct from the high-voltage transformer and gives the magnetron the voltage of 5600 volts.

Based on the microwave circuit, microwave power can be controlled by adjusting either the low voltage applied to the filament or the high voltage accelerating electrons. The low voltage being applied to the filament is usually only 3 to 4 V_{AC}, depending on the magnetron model, while the high voltage on the cathode is a negative 5600 V_{DC}. Therefore, the adjustment of input voltages of the high-voltage transformer has provided a more accurate power than that of the other one. The relation between AC voltage applying to the high-voltage transformer and the microwave power will be discussed in the next chapter. Furthermore, capacitances of the high-voltage capacitor also influence to provide the voltage need to power the magnetron. This influencing was also reported. The purpose-built microwave-power supply for the magnetron is shown in **Figure 3.16**. A heat sink was also attached to the high-voltage transformer making it continued operating more than 10 h and no damaged due to becoming too hot.

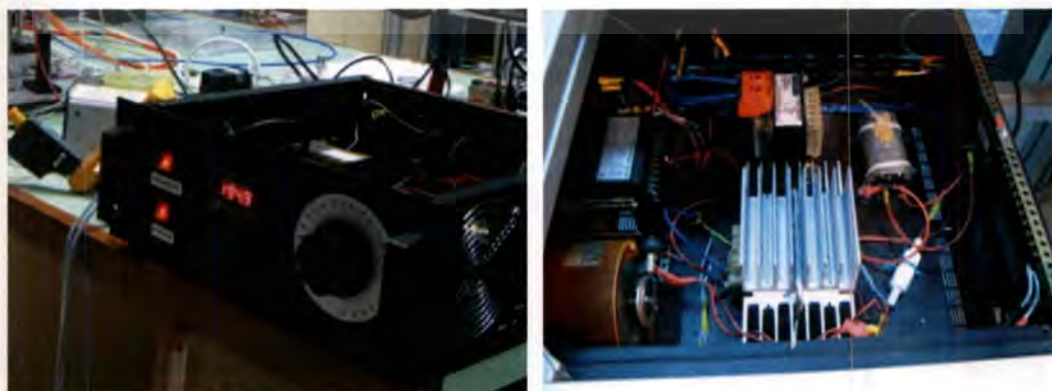

Figure 3.16 A purpose-built microwave-power supply for a MPECVD reactor.

This material is reserved for educational use only, not allowed for commercial use.
Forbidden to modify the content, and cite the document when use.

3.1.6 *In situ* Plasma Diagnoses

In this thesis, the plasma is *in situ* diagnosed by an optical spectrometer and an impedance analyzer. The gas-phase species, including electron density and temperature, are *in situ* monitored by an optical spectrometer and an impedance analyzer with a matching system. The spectrometer uses OES technique to monitor *in situ* the relative concentration of activated species in the plasma. **Figure 3.17** shows the spectrometer that is an OceanOptics HR4000 spectrometer with the wavelengths ranging from 200 to 1100 nm. For collecting the plasma emission, one end of an optical fiber was placed at the center of the reactor chamber and the other was connected to the spectrometer through a 25 μm entrance slit, and data were acquired with the OceanOptics' SpectraSuite software. Window of this software is shown in **Figure 3.18**.

Figure 3.17 OceanOptics HR4000 spectrometer.

This material is reserved for educational use only, not allowed for commercial use.
Forbidden to modify the content, and cite the document when use.

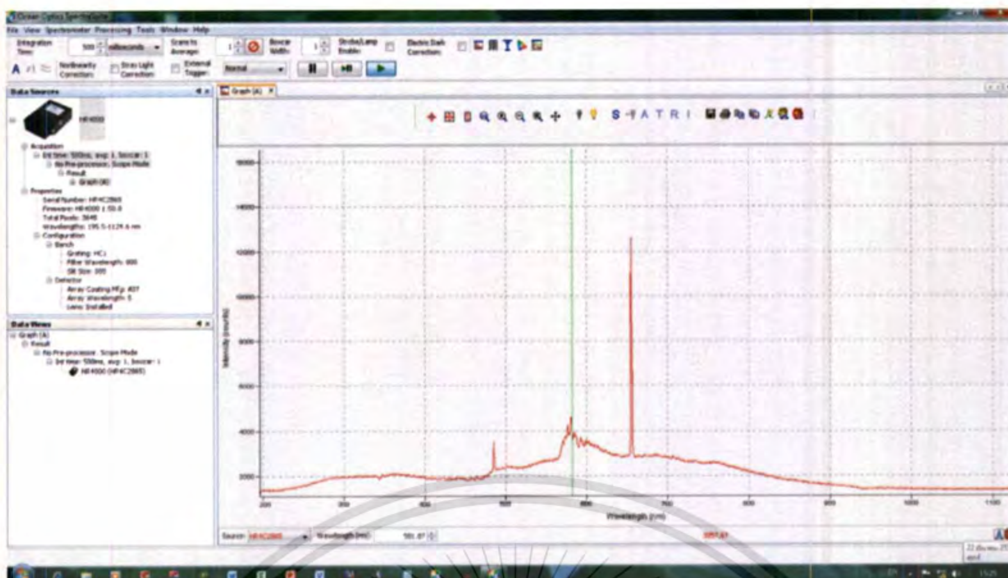

Figure 3.18 OceanOptics' SpectraSuite software interface.

The impedance analyzer with a matching system is an S-TEAM Lab HOMER-Series *STHT* V 1.5, as shown in **Figure 3.19** Air-cooled HOMER-Series *STHT* V 1.5.. It included in the section of the rectangular waveguide was employed to measure the plasma impedance in the plasma reactor. It based on electrical measurement is successfully used as an alternative to plasma diagnosis in real-time mode. The STHT 2.45 GHz AIAMS is controlled via S-TEAM Homer Windows Visualization and Control software, named *HomSoft*. Example of *HomSoft* graphical user interface window is shown in **Figure 3.20**.

Figure 3.19 Air-cooled HOMER-Series *STHT* V 1.5.

This material is reserved for educational use only, not allowed for commercial use.
Forbidden to modify the content, and cite the document when use.

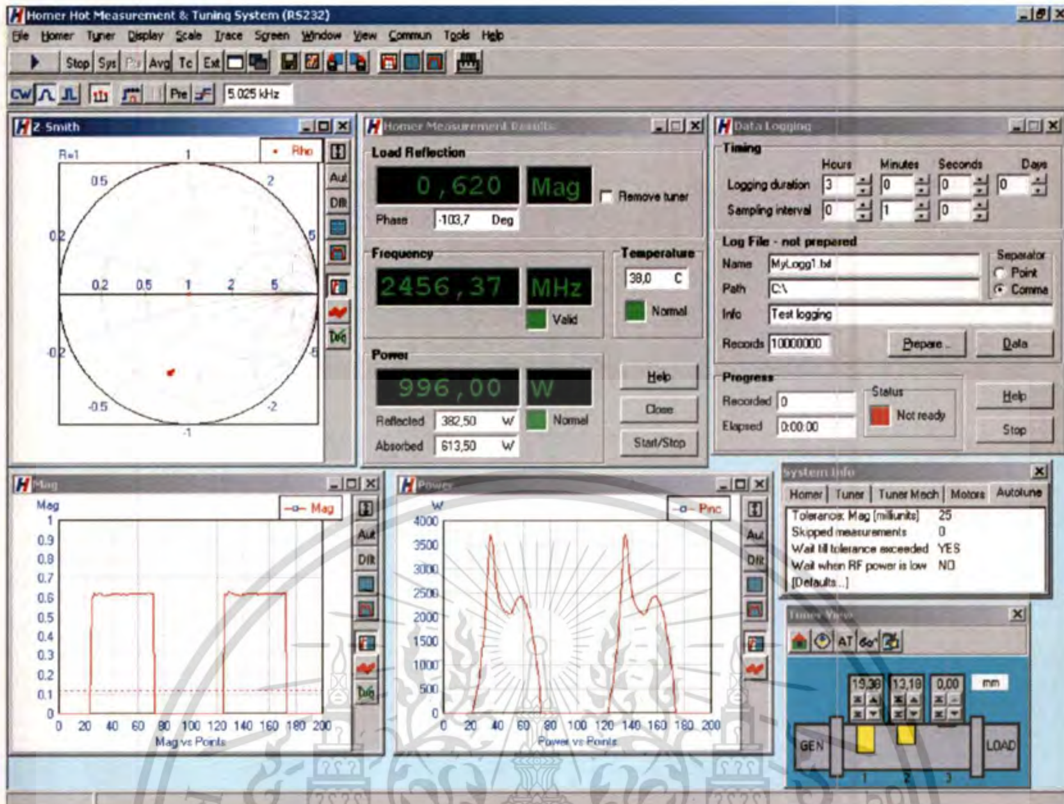

Figure 3.20 Example of *HomSoft* graphical user interface.

The HOMER^{TM} system cannot only monitor the plasma impedance but also can control the plasma impedance via three-stub tuner located in the system. Here plasma impedance was defined as load impedance seen from the HOMER^{TM} system and was normalized by the waveguide impedance. The HOMER^{TM} system remote sensed the impedance values and displayed as a Smith chart by a computer.

3.2 Steps of Diamond Film Growth

In all the experiments discussed in this dissertation, mirror-polished and B-doped Si(100) wafers with 500 μm in thickness were used as the substrate material. There are steps to prepare and grow diamond film on the substrate.

3.2.1 Substrate Pretreatment Method

Si wafer were cleaved into 20 x30 mm^2 sections to meet the dimension requirement for the substrate holder and deposition chamber. After all substrates were cleaved, they firstly were cleaned and pretreated the surface by the procedure outline below:

This material is reserved for educational use only, not allowed for commercial use.
Forbidden to modify the content, and cite the document when use.

1) Firstly, the substrate was degreased by an ultrasonic bath with acetone and methanol solutions, sequentially, for 20 minutes for each solution.
2) To promote the initial diamond nucleation on the mirror-polished Si wafer surface, the substrate surface was pretreated by either manual polishing with 0-1/2 μm diamond powder for 1 h or ultrasonicating with a 0-3 μm diamond powder suspension in isopropanol for 3 h. The diamond powder is Diamond TECH Quality® precision graded micron polishing powder.
3) Then, it is followed by an ultrasonic bath with acetone and methanol, sequentially, for 15 minutes for each solution again to remove residual diamond powder.
4) Then the substrate was rinsed in DI water.
5) After this the substrate was etched the native oxide layer by dipping into 1 part of HF and 25 parts DI water solution for 1 minute followed by rinsed with DI water for 30 seconds
6) Finally, the substrate was cleaned by an ultrasonic bath with acetone and methanol solutions, sequentially, for 10 minutes for each solution, and then dried by nitrogen gas with grade 5.0.

After the substrate was ex-situ pretreatmented and cleaned, it was conducted into the deposition chamber. In the chamber, the substrate surface was exposed to hydrogen plasma for 20 min to remove residual carbon. The operating conditions, including microwave power, a total gas flow rate, and a reactor pressure, for the H_2 plasma-cleaning step are all same as those for the diamond growth step.

3.2.2 Diamond Deposition

All depositions were carried out using CH_4/H_2 gas mixtures. The diamond deposition step was performed immediately following the H_2-plasma cleaning step. Methane gas was introduced into H_2 plasma to begin the deposition step. The deposition step was stopped by turning off the CH_4 source gas supply. The H_2 plasma was left on for a further 5 minutes while the CH_4 gas in the reactor were pumped away to leave a pure H_2 gas flow. Then, the supplied microwave-power was decreased gradually to avoid stress caused by different coefficients of thermal expansion between the substrate and the diamond film. After the microwave power was turned off and then the H_2

This material is reserved for educational use only, not allowed for commercial use.
Forbidden to modify the content, and cite the document when use.

gas supply was also turned off, the substrate temperature was reduced down to 80 °C. The reactor was evacuated at the base pressure until the substrate temperature was cooled down to a room temperature. It was then safe to remove the film from the reactor by isolating the pump and opening the vent valve.

3.3 Film Characterizations

The structural properties of NCD films were studies by analytical and metrology techniques including field emission scanning electron microscopy, Raman spectroscopy, and white-light interferometry. Their operating principles and physics have been covered in Chapter 2 for this dissertation.

3.3.1 Field Emission Scanning Electron Microscopy with Energy Dispersive X-ray Spectroscopy

Morphologies and the lateral structures of the films were investigated by Hitachi S-4700 FE-SEM, which is housed and operated by Thai Microelectronic Center (TMEC) Thailand. **Figure 3.21** shows the FE-SEM. The grain size was estimated by inspecting FE-SEM images. The lateral structure and thickness of the films were examined from cross-sectional FE-SEM images. The growth rates were calculated by the film thickness divided by the growth time. In addition, the elemental compositions of the films were analyzed by EDS analysis.

Figure 3.21 Hitachi S-4700 FE-SEM operated by TMEC.

This material is reserved for educational use only, not allowed for commercial use.
Forbidden to modify the content, and cite the document when use.

3.3.2 Auger Electron Spectroscopy

The elemental compositions on the surfaces of substrates after cleaning processes and of the films after deposition process were analyzed by OCI Vacuum Microengineering BDL600 Back-Display LEED-AUGER spectrometer. **Figure 3.22** shows the LEED-AUGER spectrometer, which has been set up and operated by Surface Physics and Laser Research Laboratory, KMITL. The base pressure for this setup is 1×10^{-8} Pa and remains around 1×10^{-6} Pa during operation. During AES analysis process, the corresponding surface is submitted to incident electrons and electrons emitting are collected and analyzed. Consequently, diamond film samples are subjected to sample-charging effects because of their insulating nature. Therefore, the analysis of thick diamond films by AES has proved difficult due to sample charging of insulting diamond films.

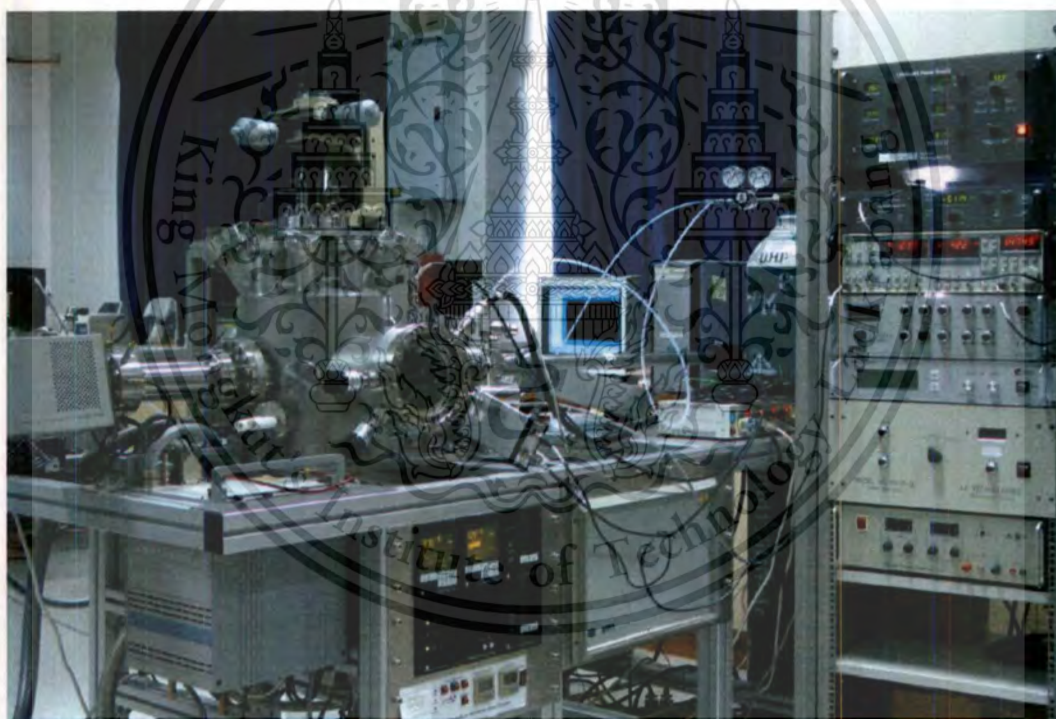

Figure 3.22 BDL600 Back-Display LEED-AUGER spectrometer with a laboratory setup.

This material is reserved for educational use only, not allowed for commercial use.
Forbidden to modify the content, and cite the document when use.

3.3.3 Raman Spectroscopy

The atomic bonding configurations of carbon bonding in the deposited films were explored by micro-Raman spectroscopy at room temperature. Micro-Raman measurements have been carried out in a Reinshaw inVia Raman microscope using argon-ion laser excitation wavelength of 514.5 nm and NT-MDT NTEGRA spectra using argon-ion laser excitation wavelength of 488 nm. They are housed and operated by respective the Gem and Jewelry Institute of Thailand (Public Organization) and National Nanotechnology Center (NANOTEC) Thailand. The both Raman measurements are shown in **Figure 3.23** and **Figure 3.24**.

Figure 3.23 NT-MDT INTEGRA spectra.

Figure 3.24 Reinshaw inVia micro-Raman microscope.

This material is reserved for educational use only, not allowed for commercial use.
Forbidden to modify the content, and cite the document when use.

Raman spectra from a Reinshaw inVia Raman microscope of a diamond single crystal and highly orientated pyrolitic graphite are shown in **Figure 3.25**. Unlike those of diamond single crystal and highly orientated pyrolitic graphite, Raman spectra of NCD films are composed of several features. Therefore, in this thesis, Raman spectra were deconvoluted after baseline subtraction into six broad peaks by three fitting functions, i.e. Gaussian for the peaks at ≈1140, ≈1250 and ≈1480 cm^{-1}, Lorentzian for the bands at 1332 and 1351 cm^{-1} and Breit-Wigner-Fano for the band at 1578 cm^{-1}.

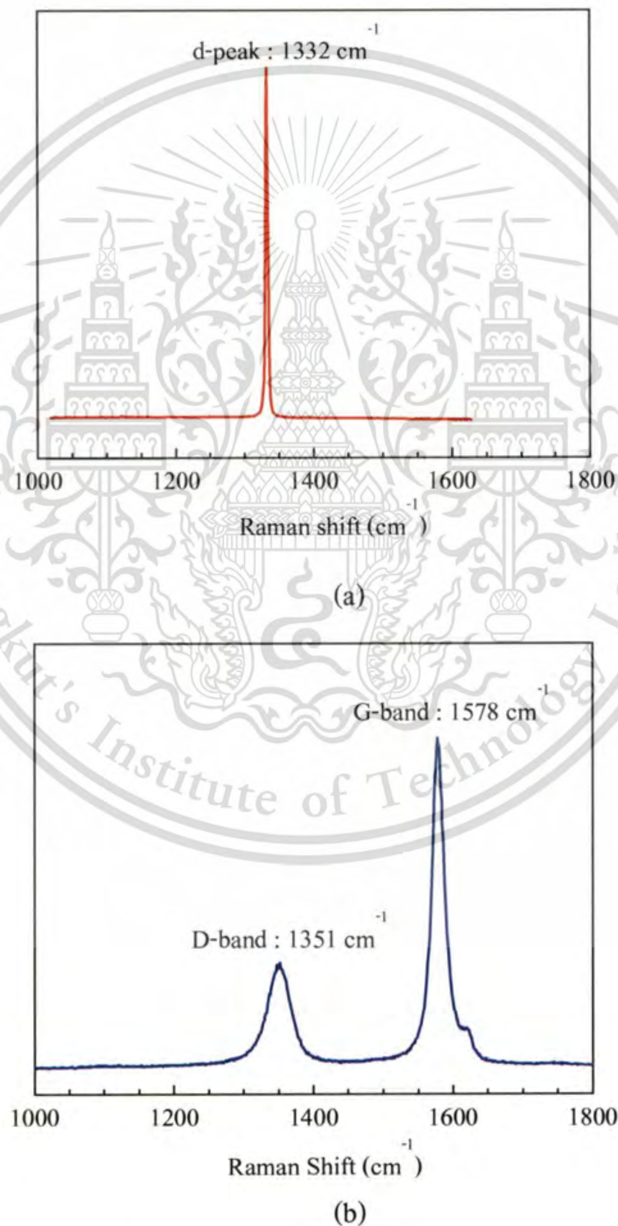

Figure 3.25 The 514.5 Raman spectra from a Reinshaw inVia Raman microscope of a diamond single crystal (a) and highly orientated pyrolitic graphite (b).

This material is reserved for educational use only, not allowed for commercial use.
Forbidden to modify the content, and cite the document when use.

3.3.4 Micro White-light Reflectometry

Optical properties were examined by reflectance measurements with a laboratory set-up for a visible light reflectometer as shown in **Figure 3.26**. The reflectometer measures the amount of light reflected from a thin film over a range of wavelengths, with the incident light normal to the sample surface. The reflectometry system consists of an OcenOptics DH2000-BAL deuteriom tungsten halogen light source, an OcenOptic HR4000 spectrometer, and an OcenOptic R200-7 reflection/backscattering probe. It also uses a microscope to magnify its spatial resolution. The entire system sets up in minutes and measurements can be made by anyone with basic computer skills. Reflectance spectra observed in operating software reveal oscillations caused by optical interference within the layers of the thin film substrate.

Figure 3.26 Micro-optical reflectometer with a laboratory setup.

3.4 Substrate Surface Characterizations

In addition to AES analysis, an optical microscope and measurements of their contact angles also examined surfaces of the substrates before these substrates were used for film deposition

3.4.1 An Optical Microscope

An Olympus SZ-11 Zoom Stereo optical microscope fitted with a Motic 350 digital camera was used to observe morphologies of the substrate surfaces after scratching methods. Flaws on the surfaces are different due to the scratching methods. The optical microscope set-up is shown in **Figure 3.27**.

This material is reserved for educational use only, not allowed for commercial use.
Forbidden to modify the content, and cite the document when use.

Figure 3.27 Optical microscope setup.

3.4.2 Contact Angle Measuring Instrument

In this thesis, drop shape analysis is a convenient way to measure contact angles, conventionally measured through deionized water. Thereby determine surface energy of the substrate before the substrate was used to deposit the films. The contact angle measuring instrument with a laboratory set-up is shown in **Figure 3.28**. This laboratory set-up is a manual instrument for contact angle measuring technique with a low investment barrier. It is equipped with a Cannon G8 digital camera used to capture the drop shape on the surface. The contact angles measuring instrument is used for determining the surface free energies, which have been influenced by the scratching. The correlation of contact angles with uniformity of the deposited films will be also discussed.

Figure 3.28 Contact angle measuring instrument with a laboratory setup.

This material is reserved for educational use only, not allowed for commercial use.
Forbidden to modify the content, and cite the document when use.

CHAPTER 4

CHARACTERIZATIONS OF MPECVD REACTOR

This chapter presents the detail in the design for subsystems of a microwave plasma-enhanced chemical vapor deposition (MPECVD) apparatus. It also presents characterizations of the efficiency of the purpose-designed and built MPECVD apparatus. At first stage, the reactor chamber and gas flow system will be tested for leaks, then, the conditions in which a stable microwave-discharge have been investigated. The temperature-dependent input microwave power of the substrate has been also investigated. Another important of a set of design variables to be considered is the gas-inlet tube configuration. The gas-inlet tube configuration influencing a controlled, uniform, and repeatable deposition of the films will be also discussed in this chapter.

4.1 Microwave Source Design

Microwave sources are used for a variety of applications in which it is necessary to energize a material, for this thesis in the formation of plasma for diamond-growth processing. The non-uniform fields produce equally non-uniform plasma, which causes variations in the plasma processing parameters. These variations can greatly affect the film quality. In this thesis, the microwave source was employed a fixed microwave field-generating probe in a cylindrical output waveguide and tuning for providing impedance matching to a wide range of a plasma load. Microwave set-up used for growth of diamond films is shown in **Figure 4.1**. Microwave power generated from a magnetron was delivered to the plasma reactor via a WR340 rectangular waveguide and then coupled to the plasma load, as previously described in Section 3.2 of Chapter 3.

The rectangular waveguide has internal dimensions of 43x86 mm and microwaves propagate in the fundamental of TE_{108} mode. The free space wavelength for the TE_{10} mode is 12.24 cm at 2.45 GHz with a guide wavelength of 17.28 cm. The *STHT* 2.45 GHz Auto Impedance Analyzer and Matching System (*STHT* 2.45 GHz AIAMS) is included in the section of this waveguide. It matches plasma load and source impedances with the use of a motorized three-stub tuner. It integrates a Homer^{TM} analyzer and a Homer^{TM} mototuner in one compact. The analyzer is a high-power impedance and power analyzer instrument and the mototuner is a motorized three-stub high-power impedance tuner. At the one end of the rectangular waveguide

This material is reserved for educational use only, not allowed for commercial use.
Forbidden to modify the content, and cite the document when use.

opposed to the magnetron was also attached a precision sliding short with a knob. This sliding short is the non-contacting sliding plunger design, which provides low friction surfaces for reduced wear. In addition, this sliding short is a choke-type plunger design shown in **Figure 4.1**. Reactive choke overcomes the severe disruption to H-filed boundary condition by the variation in wall contact while the short is moving [1] and, therefore, suppress power loss and arcing during high power operation. Furthermore, the section of the WR340 waveguide in which the electric field is a maximum was attached to a coaxial waveguide with an antenna, as shown in **Figure 4.1**. This antenna with a diameter of 25.4 mm located in the coaxial waveguide is made of hollow-cylindrical stainless steel and placed parallel to the electric field. It couples the microwave energy from the rectangular waveguide to the cylindrical waveguide. The one end of the coaxial waveguide was equipped with a simple non-contacting sliding short. Further tuning of the microwave circuit is possible by this sliding short-circuit.

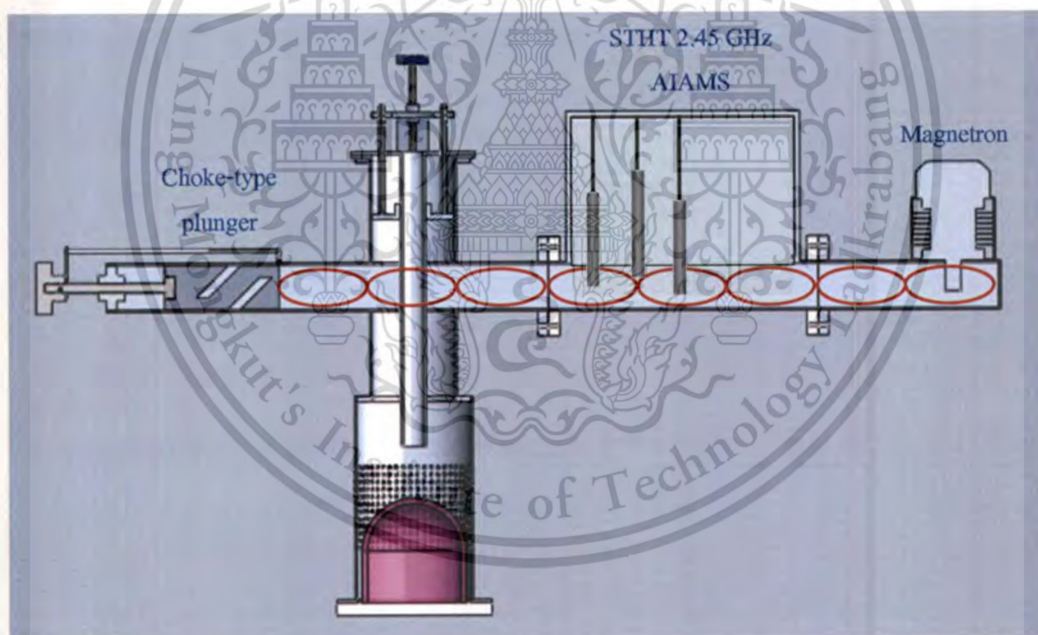

Figure 4.1 Microwave setup used for growth of diamond films.

The cylindrical waveguide has an inner diameter of 110 mm with a height of 142 mm and it is terminated by the stainless steel baseplate at the one end. As with the waveguide, electromagnetic field modes are supported in the cavity. The cavity height and diameter of this waveguide produces a dominate microwave mode that is identified as a TE_{111} mode. The cutoff frequency of the TE_{111} mode for this waveguide is 1.56 GHz and a guide wavelength is 16.30 cm at 2.45 GHz. However, in reality, the cylindrical waveguide are internally far more complex than

Forbidden to modify the content, and cite the document when use.

simple cylinders due to the presence of service ports, a thermocouple, a substrate holder with the substrate and a reactor chamber. In general it is only possible to predict the standing wave pattern within the entire MPECVD apparatus as shown in **Figure 4.1**.

As can be seen from the diagram, the plasma reactor is a section of the cylindrical waveguide. Microwaves enter the reactor and are reflected from the baseplate where boundary conditions require the electric field to be zero. The plasma is easiest to initiate when the superposition of forward traveling and reflected waves produce a standing wave pattern with a microwave circuit of the MPECVD apparatus. Once the plasma has been initiated, the plunger position is adjusted to give a minimum of reflected power. The adjustment means that the condition necessary for matching efficiently to, and maintaining, a plasma are different from those necessary to initiate one. This is consistent with theory since the resonant frequency of a cavity will change when any dielectric, such as plasma, is added [2, 3].

4.2 Operational Testing of the Purpose-built MPECVD Reactor

4.2.1 Testing of Vacuum and Gas-Flow Systems

The reactor chamber can be pumped down to 0.1 Pa, which is the ultimate pressure in the Acatel vacuum pump. The mass flow controllers were tested for flow rates at a constant supply pressure determined by the gas cylinder regulators. The zero and full flow rate of the mass flow controllers were also checked and found to match the calibrated specifications. The gas flow rate and pressure can be controlled independently by the speediavalve located between the vacuum pump and the plasma reactor. No leaks were detected from the manual shut-off valves and the connecting joints in the gas supply lines of the gas supply system. Furthermore, while plasma is operating at a maximum of power, the emission from CN at the center peak of 388.0 nm did not display. This peak indicates air leakage.

4.2.2 Reactor-system Features

The purpose-built MPECVD reactor system is operated at 2.45 GHz, 900 W with long-term operation possible and no plasma instabilities. It is capable of continuing operating with a long period of time more than 12 h at the maximum power. The reactor can be run under various conditions (pressure, power, gas types etc.) It is a versatile MPECVD reactor, which is a flexible

This material is reserved for educational use only, not allowed for commercial use.
Forbidden to modify the content, and cite the document when use.

reactor, and microwave coupling design allow microwave processing ranging from high pressure (> 30 kPa) to medium pressure (0.5 kPa).

Photographs of the CH_4-H_2 microwave-plasma discharge in the reactor chamber at the gas pressure of 5 kPa with different microwave powers are shown in **Figure 4.2**. Color photographs of each of the plasma can be seen differently. The microwave power determined the diffusion, collisional quenching and heating, and heat transfer within the discharge. Visually, these effects manifested themselves via differences in the color and brightness of the plasma.

(a) (b)

Figure 4.2 Color photographs of the plasma at two absorbed microwave-power: (a) 500 W and (b) 750 W.

4.2.3 Microwave-power Supply Characteristics

One of the major subsystems of the MPECVD reactor is that a microwave power supply, which gives the magnetron the voltage and current need to power. As described in chapter 3, this supply has basically 2 sections, the low voltage section which actually serves a low voltage to heat up the magnetron filament and the high voltage section which serves a high voltage to accelerate electrons emitting from the filament straight toward the positive anode of the magnetron. The high voltage section consists of the high voltage transformer and the doubling circuits including a high-voltage capacitor. Both AC voltages applied to the high-voltage transformer and capacitance of the high-voltage capacitor influence the magnetron to give power. The characteristic of the microwave power supply as a function of the AC voltages at different capacitance is shown in **Figure 4.3**. These capacitors have been used in a part of the circuit of a home-use microwave oven. Therefore, there are many sources to supply these capacitors. Their

This material is reserved for educational use only, not allowed for commercial use.
Forbidden to modify the content, and cite the document when use.

capacitances are 0.91 μF with a 2,350 VAC voltage rating, 1.02 μF with a 2,100 VAC, 1.03 μF with a 2,500 VAC, and 1.13 μF with a 2,100 VAC.

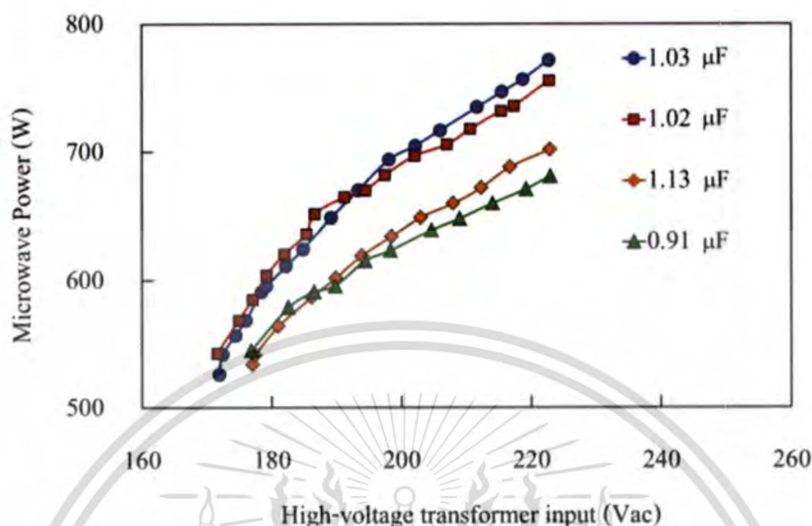

Figure 4.3 The microwave power incident at the plasma chamber is as a function of AC voltage input of high-voltage transformer under a total mass flow rate of 200 sccm, reactor pressure 20 kPa, and 1%CH_4 in H_2 gas.

The microwave power generated from the magnetron depended on not only AC voltages applied to the high-voltage transformer but also the capacitance of the high-voltage capacitor, as shown in **Figure 4.3**. The capacitance of 1.03 μF offered with 2,500 VAC voltage rating is the premier choice for performance in requirements of the Sharp 2M167B-M10 900 W magnetron. The diode and capacitor work together to convert the AC voltage to the DC voltage. The RC charge time of the circuit is limited by the value of the capacitor that it presents a relatively reactance and the value of the relatively resistance of the conducting diode; whereas the rate of discharge of the capacitor is determined by the value of capacitance and the value of the load resistance. The capacitor in microwave circuitry is similar to batteries because it is capable of charging with electrical energy and then discharge to keep current continually flowing to the magnetron. Therefore, the RC charge time has been selected to harmonize with the rate of discharge. This harmonization has improved the performance of the magnetron to provide the higher power. However, the efficiency of magnetrons from typical consumer microwave ovens does not reach 100%. The other are dissipated as heated, mostly in the magnetron tube.

This material is reserved for educational use only, not allowed for commercial use.
Forbidden to modify the content, and cite the document when use.

4.2.4 Substrate Temperature

The substrate temperature is one of the major parameters influencing the process of diamond film deposition. A dependence of the substrate temperature on the microwave power into the plasma reactor for H_2 plasma is shown in **Figure 4.4**. For all gas pressures, the substrate temperature increased with microwave power, as expected. An insignificant increase in the substrate temperature was observed with a decrease in the pressure of the reactor chamber. The substrate temperature is quite pressure-independent. However, the significant increase in the substrate temperature was observed with a decrease in the mass flow rate of gas.

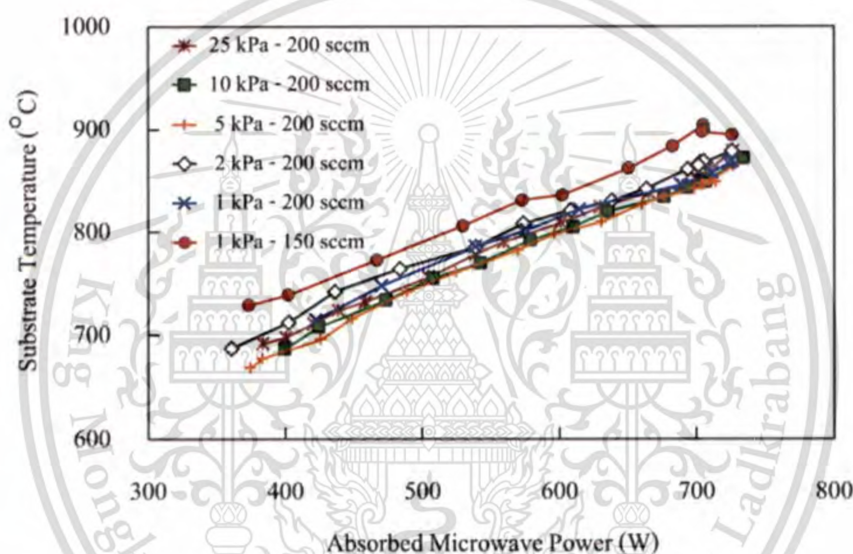

Figure 4.4 Substrate temperature versus absorbed microwave power into the plasma reactor under different pressures of the H_2 gas and mass flow rates of 200 sccm and 150 sccm.

Although the dominant thermal flux to heat up the substrate in the conventional microwave plasma is due to charged or neutral species with kinetic energy [4]. There are two factors that could be attributed the cause of the higher substrate temperature for the lowering of the gas flow rate. Firstly, the higher of substrate temperature is due to the lowering of the convective heat transfer. The heat transfer by convection is characteristic of vacuum in which gas molecules have assisted in cooling. On the one hand, while the reactor pressured was keeping constant at 1 kPa, the mass flow rate was decreased from 200 to 150 sccm. This makes the pumping speed decreased by 25% to keep the pressure constant; and then results in a decrease in the gas velocity. The decreased velocity of gas molecules causes Reynolds number of flow in the reactor chamber

This material is reserved for educational use only, not allowed for commercial use.
Forbidden to modify the content, and cite the document when use.

to drop. For the dropping in Reynolds number, the efficiency of the gas molecules-assisting cooling and the heat transfer coefficient are rather lower.

Secondly, the lowering of the mass flow rate also lowers the loss tangent of the plasma. The plasma properties rest on the complex relative permittivity, $\varepsilon_p = \varepsilon'_p - j\varepsilon''_p$, and the loss tangent, $\tan\delta = \varepsilon''/\varepsilon'$. It is thoroughly equivalent to use either the complex plasma conductivity σ_p or the complex relative permittivity ε_p, as these parameters are related by $\sigma_p \equiv \sigma'_p + j\sigma''_p = \left[-\varepsilon''_p + j\left(\varepsilon'_p - 1\right)\right]\omega\varepsilon_0$, as stated in Section 2.6.1 of CHAPTER 2. It was found by measuring plasma impedance that the loss tangent of plasma at 1 kPa with 150 sccm is higer than that of plasma at 1 kPa with 200 sccm. The loss tangent and dielectric loss predicts the ability of the material to convert the incoming energy into thermal energy and determine the effect of the electromagnetic field on the material [2].

4.2.5 Effect of Shape of Gas Inlet Tube

The main problem in the CVD kinetics studies is the complexity of the deposition process. The difficulty arises not only from the various steps of the CVD process, temperature, concentration gradient and geometric effects but also from gas flow patterns in the reactor chamber. Although the CVD system for diamond growth is generally composed of a gas deliver-system; there is MFCs for manipulating the gas flow rates during the CVD process. However, in addition to control of gas flow rate, the goal of the flow is to deliver the gas-flow pattern uniformly to the substrate. The gas-flow pattern determines gas residence time as well as heating and influences gas-surface reaction. Gas flow patterns are of greatest important for growth of films with uniform thickness and composition, particularly at high pressure and high flow rate in a reactor chamber that is too small [5]. The further increasing the operating pressure and flow rate promotes turbulent flows. It is commonly believed that turbulence should be avoided in the CVD process. The turbulent flows, however, are characterized by good mixing, in principle advantageous for both film growth and film uniformity. The flow pattern therefore needs to be optimized.

As stated in Section 3.2.1 of Chapter 3, the flow pattern in my CVD reactor is influenced by the shape of the gas-inlet pipe which injects gas into the chamber. The highly turbulent flow patterns cause varied deposition rate and uniformity of deposited films. It should be therefore at least minimized for satisfactory process control and reproducibility of the deposition. The complete problem of the gas flow through the system is too complex to be described and to be

The material is reserved for educational use only, not allowed for commercial use.
Forbidden to modify the content, and cite the document when use.

predicted by numerical simulations and observed by a flow visualization technique here. For this thesis, the shape of this gas inlet was chosen experimentally by optimization of the deposition rate, uniformity, and reproducibility of the deposited films. The gas inlet used for this thesis is a quartz tube with an outer diameter of 4 mm and an inner diameter 2.5 mm. It was found experimentally that the gas inlet with a straight tube in shape and a height of 2 mm from the substrate surface provides the deposited films with the highest deposition rate and reproducibility. Examples of the effect of another gas inlet configuration on the deposited films are shown in **Figure 4.5**, **Figure 4.6**, and **Figure 4.7**. Unlike that of films in **Figure 4.5** and **Figure 4.7**, the microstructure of film in **Figure 4.6** is rather different. This is due the film too thin. In addition, a 3-inlet configuration was also designed. This configuration induced the highly turbulent flow pattern; almost no film was formed on the substrate.

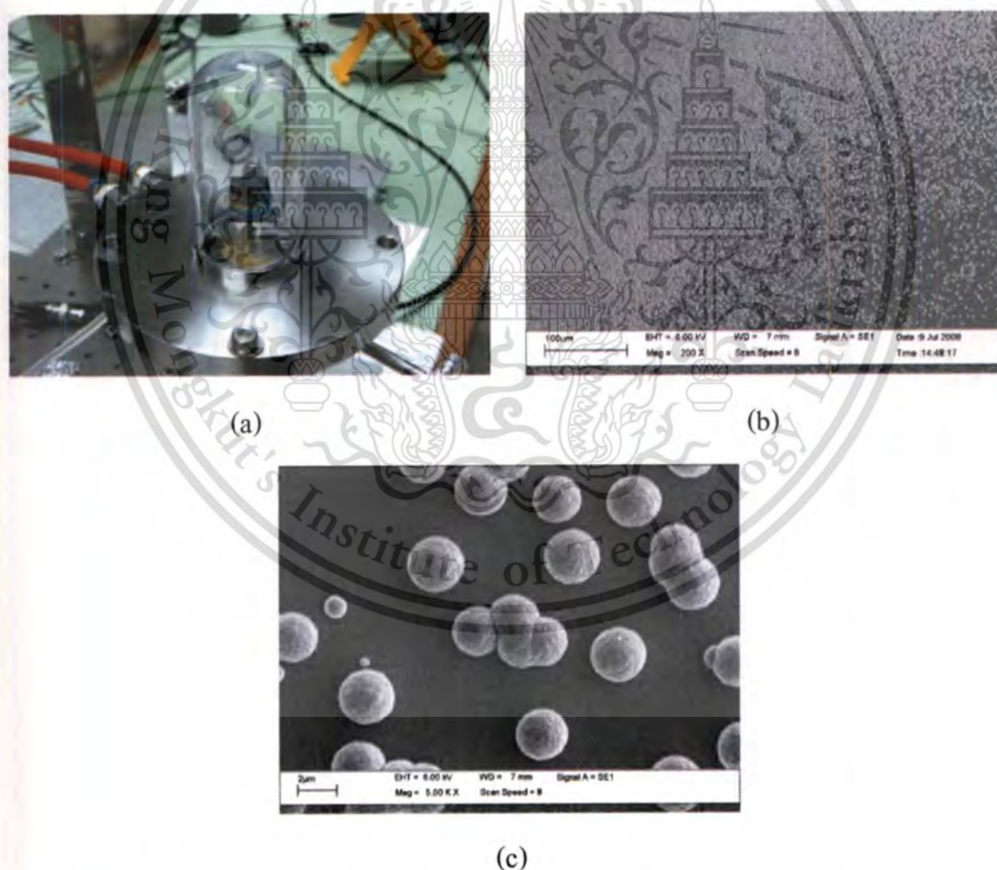

(a) (b)

(c)

Figure 4.5 (a) An U-shaped gas inlet, (b) SEM image showing the effect of configuration of gas inlet on the microstructure development of diamond films, and (c) isolated diamond particles of the ball-like-shaped clusters.

This material is reserved for educational use only, not allowed for commercial use.
Forbidden to modify the content, and cite the document when use.

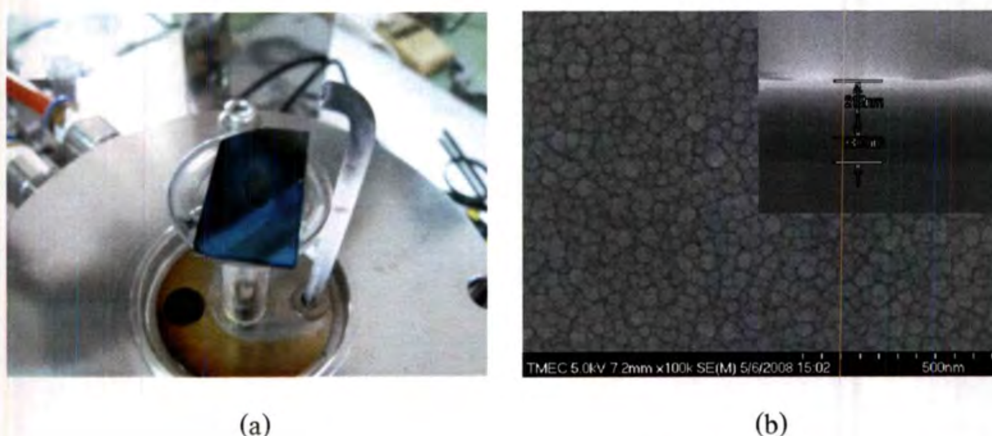

(a) (b)

Figure 4.6 (a) A L-shaped gas-inlet tube and (b) FE-SEM image shows the effect of configuration of gas inlet on the microstructure development of diamond films and an inset cross-section image.

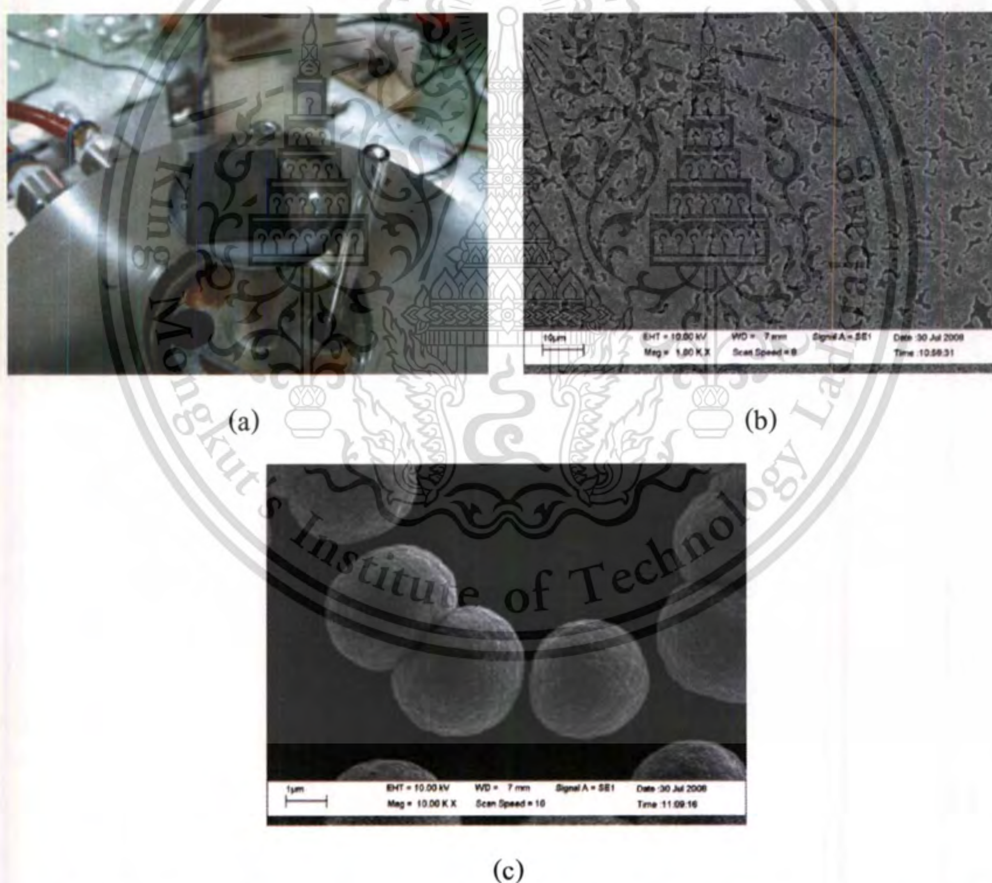

(a) (b)

(c)

Figure 4.7 (a) A straight gas-inlet tube with 15 mm high from the substrate surface, (b) SEM image showing the effect of configuration of gas inlet on the microstructure development of diamond films, and (c) isolated diamond particles of the ball-like-shaped clusters.

This material is reserved for educational use only, not allowed for commercial use.
Forbidden to modify the content, and cite the document when use.

4.3 Characterization of MPECVD Apparatus

The growth in CVD diamond research has led to many different areas of expertise being developed around the world. Characterization of the deposited films by electron microscopy and Raman spectroscopy form the most widely used CVD diamond diagnostic techniques as described in Section 2.9 of Chapter 2. Many successful recipes for CVD diamond growth have been found by trial and error techniques of growing films until the film properties match those required for a given application.

The CVD process for diamond growth is the main concern about the gas-phase species environment of the plasma. Therefore, mechanisms of chemical process occurring in the plasma and their reaction rates are an important first step in the know to have the optimize operating conditions in controlling film properties. In the case of diamond grown by the MPECVD technique, the mechanisms of chemical processes generally depend on density of charge particles and their attendant energy, especially electrons. These electrons associated with impedance of plasma have influenced chemical-process mechanisms occurring in a gas-phase environment to produce precursors for the growth of films. The monitor and manipulation of the electron density and gas-phase species can give an insight in further understanding and controlling the growth process. Both electron density and gas-phase species depend on essential process-parameters operating, including the microwave power, reactor pressure, and methane concentration. Therefore, the developed MPECVD apparatus has been had to characterize to investigate electron density and gas-phase species of experiments with different microwave powers, reactor pressures, and concentrations of methane.

4.3.1 Microwave Power-dependent MPECVD Apparatus

The plasma studied in this section was generated at a reactor pressure of 5 kPa with a total mass flow rate of 200 sccm. The absorbed microwave power was in various values. Both H_2 plasma and 0.9%CH_4 in H_2 plasma were investigated. The *in situ* impedance of plasma was monitored by the STHT 2.45 GHz AIAMS. The plasma impedance relates to electron density and temperature of the plasma. The *in situ* gas-phase species of the plasma was measured by optical emission spectroscopy.

This material is reserved for educational use only, not allowed for commercial use.
Forbidden to modify the content, and cite the document when use.

4.3.1.1 Power Dependence of Plasma Impedance

The plasma parameters consisting of electron density and temperature were extracted from impedance of plasma. The normalized impedance of H_2 plasma and 0.9% CH_4 in H_2plasma at various absorbed microwave power on a Smith charts is shown in **Figure 4.8**. The impedance of plasma was normalized by their values with that of the waveguide. The inductive component of plasma impedance decreased with increasing absorbed microwave power. The lowering of the inductive value indicates the electron density increases. The addition of CH_4 into H_2 plasma induced a more reactive value of plasma impedance suggesting decreasing electron density.

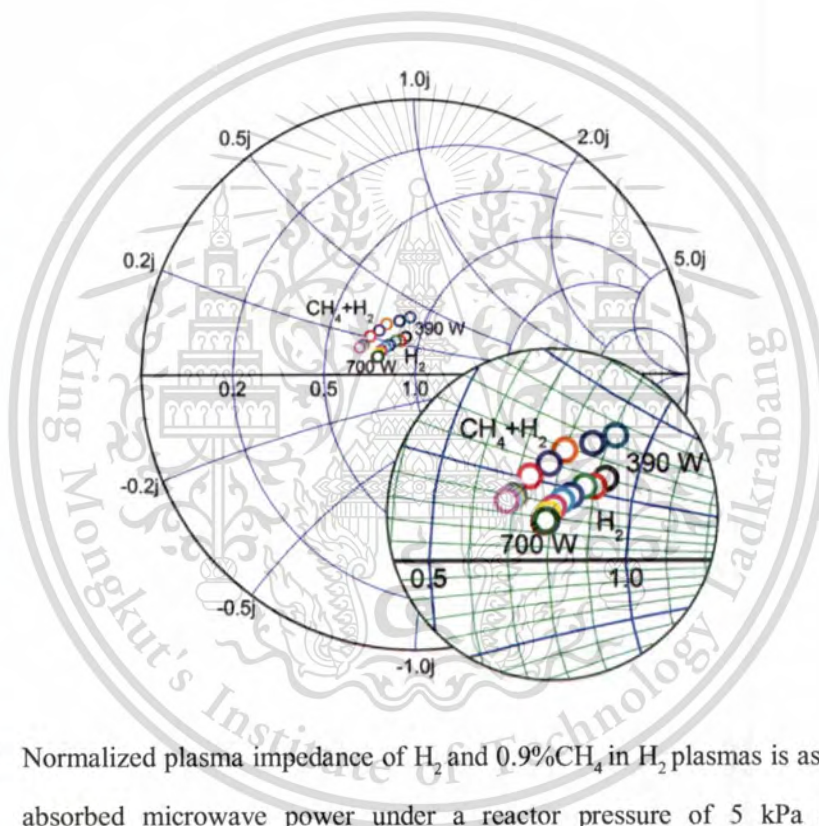

Figure 4.8 Normalized plasma impedance of H_2 and 0.9%CH_4 in H_2 plasmas is as a function of absorbed microwave power under a reactor pressure of 5 kPa and an inset magnified Smith chart.

The electron density was determined by Equation (2.18) and the electron temperature by Equation (2.25). Both electron density and temperature were normalized by correlating with those of H_2 plasma operated under an absorbed microwave power of 702 W and a reactor pressure of 5 kPa with a total mass flow rate of 200 sccm. The normalized electron density as a function of microwave power is shown in **Figure 4.9** and that for electron temperature shown in **Figure 4.10**. In order to achieve exact quantities of the both parameters, the calibration curve being the *STHT* 2.45 GHz AIAMS response must be prepared for converting the microwave plasma impedance to

This material is reserved for educational use only, not allowed for commercial use.
Forbidden to modify the content, and cite the document when use.

the plasma properties. Although the exact values are not determined, the trends of the both are not varied. Hence, the relative changes of electron density and temperature are used instead for this thesis.

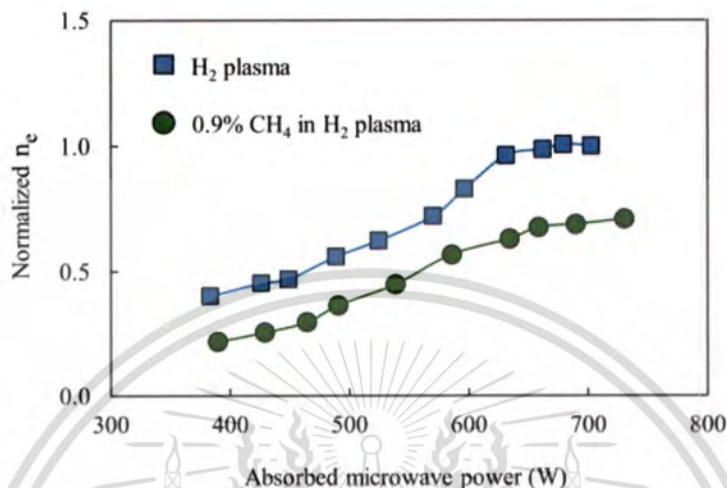

Figure 4.9 Normalized electron density as a function of absorbed microwave power under a reactor pressure of 5 kPa.

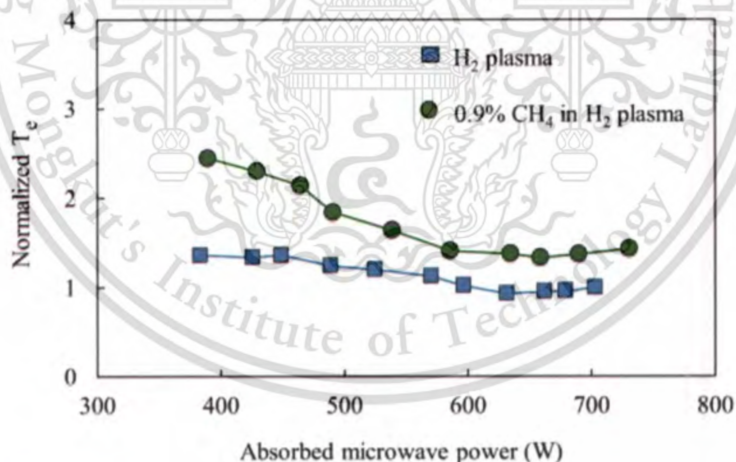

Figure 4.10 Normalized electron temperature as a function of absorbed microwave power at a reactor pressure of 5 kPa.

The electron density increased with microwave power and saturated after 660 W. Furthermore, as the methane was added into H_2 plasma, electron density was decreased. In contrast to the electron density, the normalized electron temperature decreased with increasing microwave power and then saturated at the high power; while the addition of methane into caused electron temperature to increase. From **Figure 4.10**, the electrons reserve their high energy at low

This material is reserved for educational use only, not allowed for commercial use.
Forbidden to modify the content, and cite the document when use.

microwave power due to insufficient energy for inelastic collision [6, 7]. As the microwave power increased, the electrons gained enough energy for inelastic collisions, and in the process, transferred almost all of the energy to the target particles during the collisions. This explains the rapid reduction in the electron temperature acting as electron energy as the microwave power was increased to around 600 W. After that, at the high microwave power, the energy gained and lost by electrons following the increase in microwave power limit itself. This results in the stable value of electron density and electron temperature.

To corroborate the relative changes of electron density and temperature, which are determined by measuring impedance, the optical emission intensities of Balmer series of hydrogen atom were monitored simultaneously. **Figure 4.11** shows only emission intensity of Hβ and intensity ratio of Hδ to Hβ under various absorbed microwave power in H_2 and CH_4-H_2 plasmas. The ratio of Hδ to Hβ acts as a measure of electron temperature. Compare to the normalized electron density and temperature, which are extracted by measuring impedance of plasma, the Hβ intensity and Hδ / Hβ ratio show the same manner.

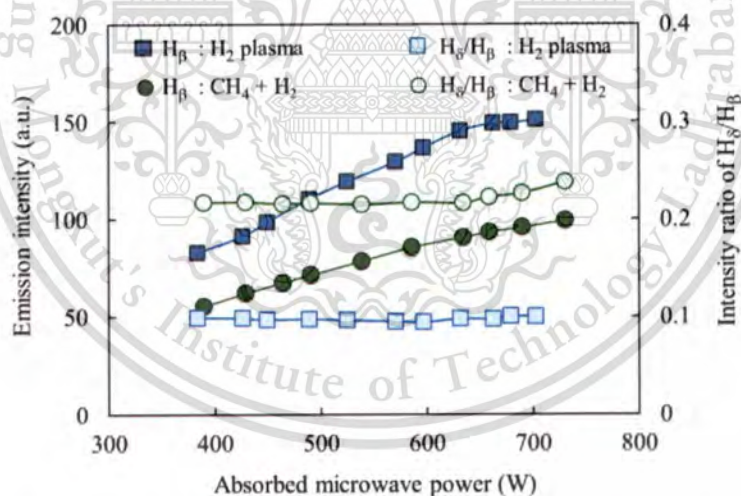

Figure 4.11 The optical emission intensity of Hβ and intensity ratio of Hδ to Hβ is as a function of absorbed microwave power at a pressure of 5 kPa in H_2 plasma and 0.9% CH_4 in H_2 plasma.

For the both plasmas, the intensity of Hβ initially increased with absorbed microwave power; more hydrogen atoms were excited. The microwave power promotes the generation of atomic-H as well as electron density. As long as the net production of atomic H radicals stem from dissociation of hydrogen molecules appearing to go through the repulsive $b^3\Sigma_u^+$ state by

This material is reserved for educational use only, not allowed for commercial use.
Forbidden to modify the content, and cite the document when use.

electron impact [8]. Thus, the increased electron density enhances atomic-H concentration. The CH_4 addition decreased the intensities of Hβ due to consumption of H radicals by the dehydrogenation-dissociation reaction with methane. The emission intensities of Hβ are in a parabolic manner to the normalized electron densities, as shown in **Figure 4.12**. In addition, my measured emission intensity of Hβ have the relative changes under various microwave-power conditions similar to those for H.C. Barshilia and V.D. Vankar [9] who gave a report on the effect of microwave power on atomic-H concentrations measured by actinometry. Consequently, the normalized electron densities extracted by measurements of plasma impedance can be a scale of the atomic-H concentration in the plasma.

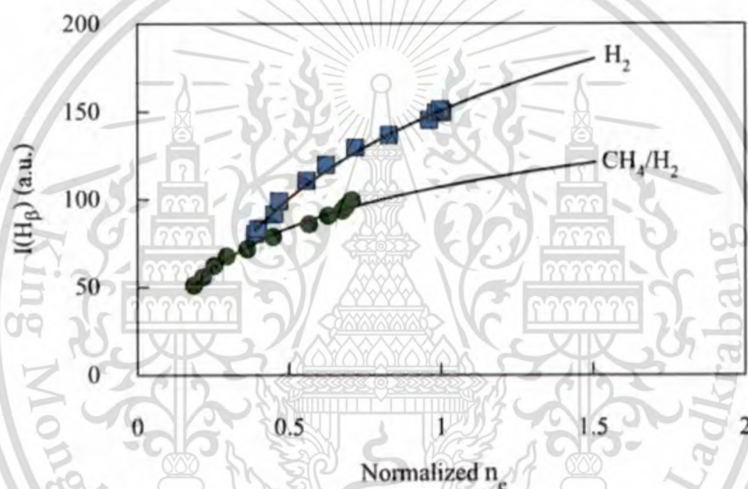

Figure 4.12 The normalized electron density versus the optical emission intensity of Hβ.

In other words, it can be seen from **Figure 4.11**, the emission intensity of Hβ directly increased with increasing microwave power from 380 to 630 W and then remained almost constant after 630 W. From Equation (2.26) in Chapter 2, an increase in the emission intensity of the excited state is caused by an increase in electron density n_e, amount of atomic hydrogen ground state N_x and rate constant k_x which reflects an electron mean energy in the plasma, i.e. the electron temperature T_e. The slightly change in the electron temperature with increasing absorbed microwave power means that the electron temperature does not affect the emission intensity. Consequently, the increase in emission intensity should be due to n_e and/or N_x. As long as the net production of H radicals stems only from dissociation of hydrogen molecules appearing to go through the repulsive $b^3\Sigma_u^+$ state [8]

This material is reserved for educational use only, not allowed for commercial use.
Forbidden to modify the content, and cite the document when use.

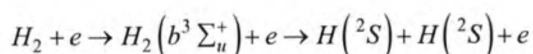

$$H_2 + e \rightarrow H_2\left(b^3\Sigma_u^+\right) + e \rightarrow H\left(^2S\right) + H\left(^2S\right) + e$$

Based on the spectroscopic result, it clarifies that the variation of emission intensity is due to exclusively electron density. The normalized electron density as well as intensity of atomic hydrogen emission first increase linearly with increasing absorbed microwave power and then become saturated after 630 W. Moreover, the electron temperature extracted by plasma impedance measurements (PIM) show the changing trend similar to that in the electron temperature extracted by OES. These indicate that, for measuring plasma impedance, the extracted electron density and temperature have the corrective trends.

4.3.1.2 Power Dependence of Gas-phase Species of 0.9%CH_4-H_2 plasma

The gas-phase species, excluding electron density, were measured by OES. **Figure 4.13** shows the typical optical emission spectra form the 0.9%CH_4-H_2 plasma under various microwave power. The gas-phase species of CH ($B^2\Delta \rightarrow X^2\Pi$) at the centered peak 387.0 nm, CH ($A^2\Delta \rightarrow X^2\Pi$) at 431.5 nm, CH^+ ($A'\Pi \rightarrow X'\Sigma$) at 417.1 nm, C_2 ($d^3\Pi_g \rightarrow a^3\Pi_u$)at 516.5 nm, and atomic hydrogen H_β at 486.1 nm appeared in the emission spectra. These gas-phase species under various microwave power is plotted in **Figure 4.14**.

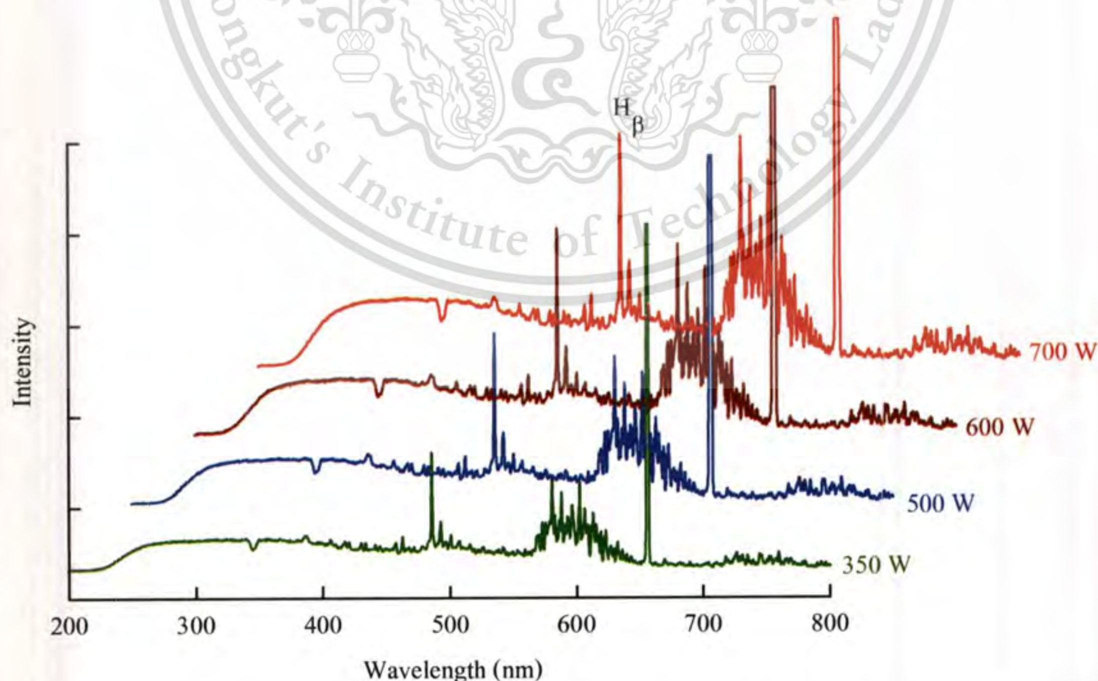

Figure 4.13 The *in situ* optical emission spectra from CH_4-H_2 mixed gas under various absorbed microwave power.

This material is reserved for educational use only, not allowed for commercial use.
Forbidden to modify the content, and cite the document when use.

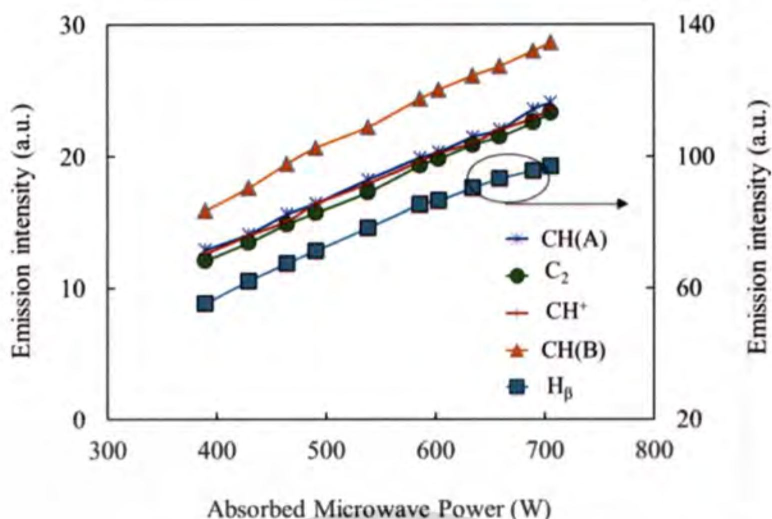

Figure 4.14 Emission intensities of CH(B), CH(A), C_2(d-a), CH^+, and H_β as a function of absorbed microwave power.

All gas species in the plasma increased linearly with microwave power. As the microwave electric field and microwave power are increased, the electron temperature will be increased to the level where some electron-neutral collisions are inelastic. Through this inelastic collision process the microwave excited electron gas produces new radical and excited species. However, microwave power did not affect intensity ratios of CH(B), CH(A), C_2(d-a) and CH^+ to H_β . Except for after 650 W, the power increased the intensity ratios of gas-phase species.

4.3.2 Reactor Pressure-dependent MPECVD apparatus

The H_2 plasma and 0.9%CH_4 in H_2 plasma studied in this section were generated at a total mass flow rate of 200 sccm. The reactor pressures were various values ranging from 2 to 30 kPa. The *in situ* impedance of plasma was monitored by the STHT 2.45 GHz AIAMS. The plasma impedance relates to electron density and temperature of the plasma. The *in situ* gas-phase species of the plasma was measured by optical emission spectroscopy.

4.3.2.1 Pressure Dependence of Plasma Impedance

Figure 4.15 illustrates the effect of reactor pressure on impedance of H_2 and 0.9%CH_4-H_2 plasmas. The inductive component increased with increasing reactor pressure. Electron densities and temperatures were extracted from these values of impedances. Both electron densities and temperatures were normalized by comparing their values with that of the H_2 plasma operated under an absorbed microwave power of 700 W and a reactor pressure of 5 kPa with a mass flow

This material is reserved for educational use only, not allowed for commercial use.
Forbidden to modify the content, and cite the document when use.

rate of 200 sccm. The influence of the reactor pressure on the normalized electron density and temperature is shown in **Figure 4.16**.

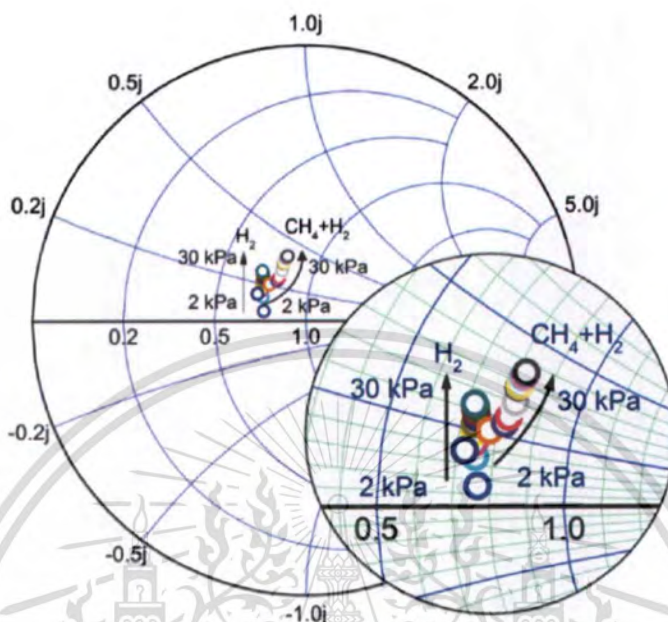

Figure 4.15 Normalized plasma impedance of H_2 and 0.9%CH_4- H_2 plasmas as a function of reactor pressure ranging from 2 to 30 kPa at a fixed applied microwave power and an inset magnified Smith chart.

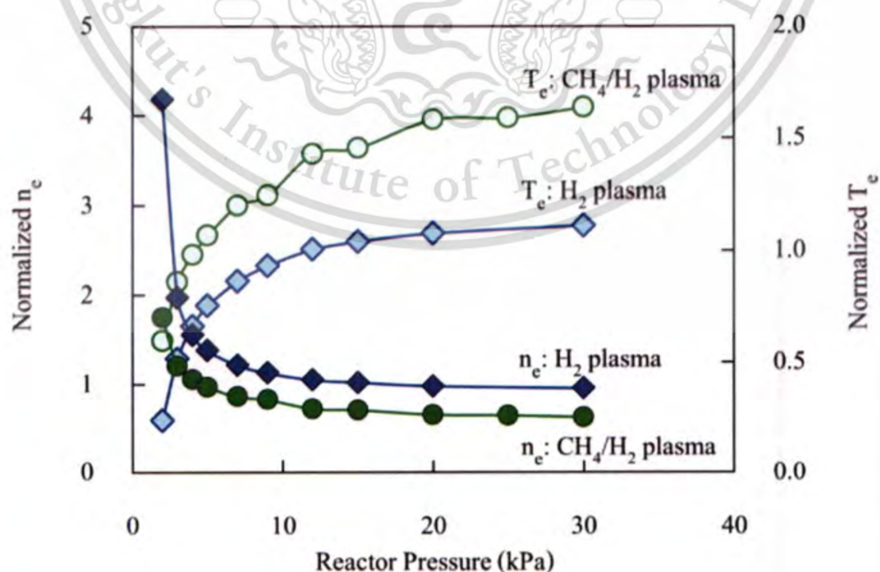

Figure 4.16 The normalized electron density and temperature as a function of reactor pressure. All electron densities are normalized to a measured value of H_2 plasma operated at a pressure of 5 kPa and absorbed microwave power of 702 W.

This material is ... for educational ... only, not for commercial use.
Forbidden to modify the content, and cite the document when use.

The electron density rapidly decreased with pressure and tended to be steady at pressure more than 10 kPa. The increasing pressure from 2 to 10 kPa also caused not only electron temperature but also absorbed microwave power to increase. The absorbed microwave power shows a changing trend significantly under various pressures identical to those for electron temperature; it was not shown here. At exceeding 100 mbar, both the electron temperature and the absorbed power tended to be steady. It means that when reactor pressure is increased, electrons can transfer less energy to the number of gas molecules while more energy is stored in them, leading to a sudden rise in the electron temperature. In other words, by lowering reactor pressure, the mean free path of electrons is prolonged, which increases the acceleration time between two collisions. Therefore, the electrons can gain more energy from field and then get enough energy. Consequently, they can make more an inelastic collision with gas molecules, which causes a reduction in energy stored in them. Thus, for the lowering of particularly the reactor pressure down to 2 kPa, the decreased reactor pressure causes electron density to increase fast but electron temperature to decrease suddenly.

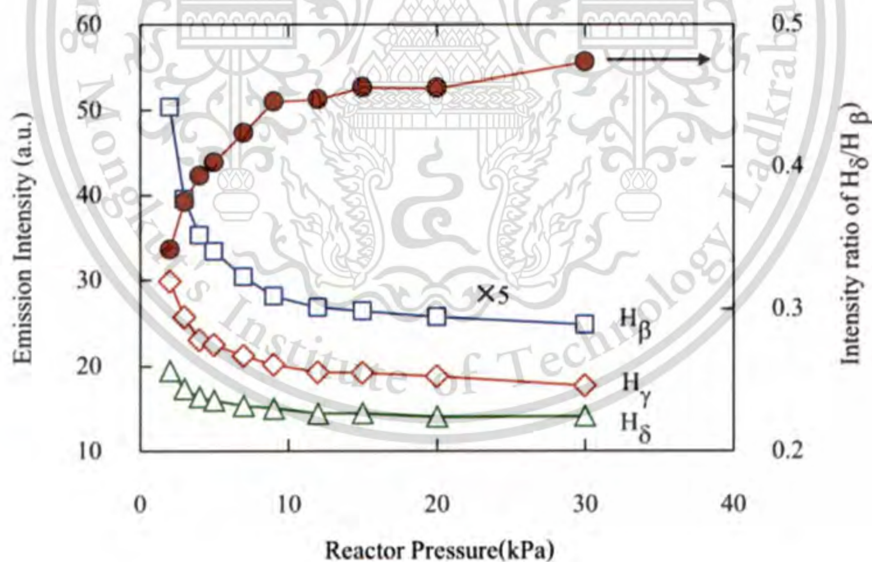

Figure 4.17 OES peak intensities from the H_2 plasma as a function of reactor pressure for $H\beta$, $H\gamma$, $H\delta$ and $I(H\delta)/I(H\beta)$ ratio acting as electron temperature T_e.

Figure 4.17 shows that the emission intensities of hydrogen atom dependent on reactor pressure. It was investigated for further corroborating the trends of electron density and electron temperature determined by measuring impedance of plasma. The optical emission intensity of

This material is reserved for educational use only, not allowed for commercial use.
Forbidden to modify the content, and cite the document when use.

Balmer series drastically decreased with reactor pressure ranging from 2 to 10 kPa whereas electron temperature increased. At higher than 10 kPa, both the intensity and electron temperature tended to become saturated. The H_β emission intensity decreased with the reactor pressure similar to that in the normalized electron density extracted by measuring plasma impedance. In addition, the $I(H_\delta)/I(H_\beta)$ ratio acting as electron temperature also increased with the reactor pressure similar to that in the normalized electron temperature. These results further substantiates that the relative changes of both electron density and temperature estimated by measuring impedance of plasma are corrective to describe properties in the plasma.

4.3.2.2 Pressure Dependence of Gas-phase Species of 0.9%CH_4-H_2 Plasma

Figure 4.18 shows the typical optical emission spectra form the 0.9%CH_4-H_2 plasma under various microwave power. The gas-phase species of CH(B), CH(A), C_2(d-a), CH^+, and H_β, as a function of power is plotted in **Figure 4.19.** All emissions decreased exponentially with reactor pressure. In contrast to the gas-phase species dependent on power, the ratios of gas-phase species to H_β increased with reactor pressure, as shown in **Figure 4.20**.

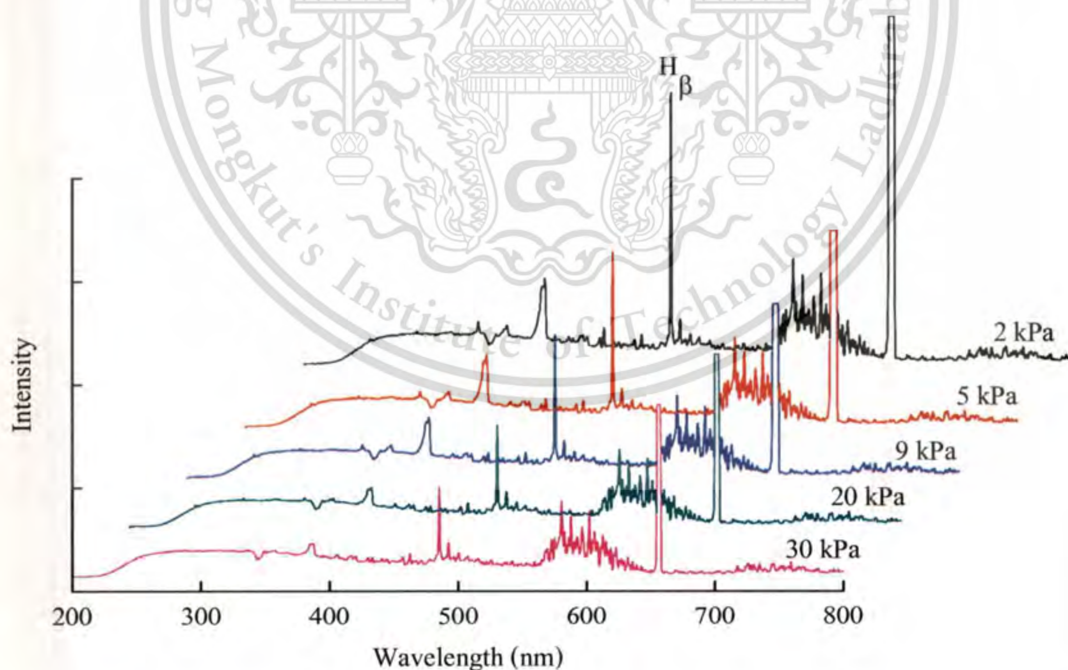

Figure 4.18 The *in situ* optical emission spectra from CH_4-H_2 mixed gas under various reactor pressures.

This material is reserved for educational use only, not allowed for commercial use.
Forbidden to modify the content, and cite the document when use.

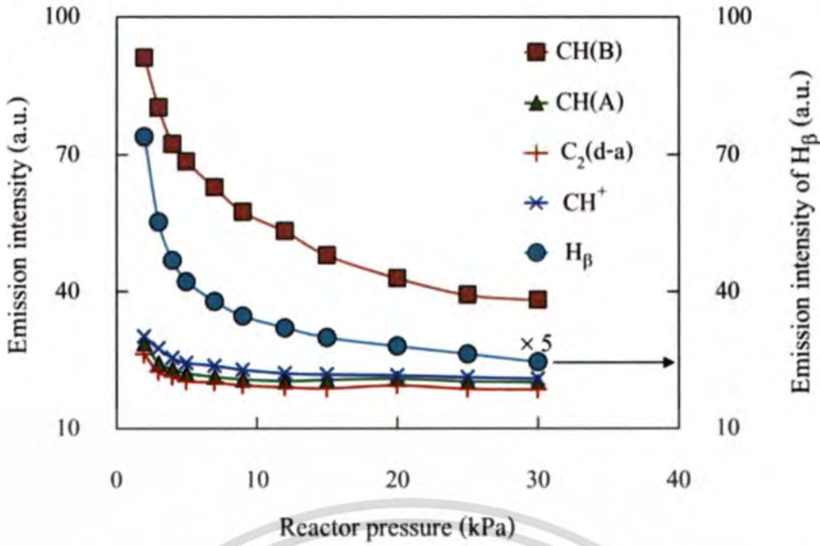

Figure 4.19 Emission intensities from CH(B), CH(A), C_2(d-a), CH^+, and H_β are plotted as a function of the reactor pressure.

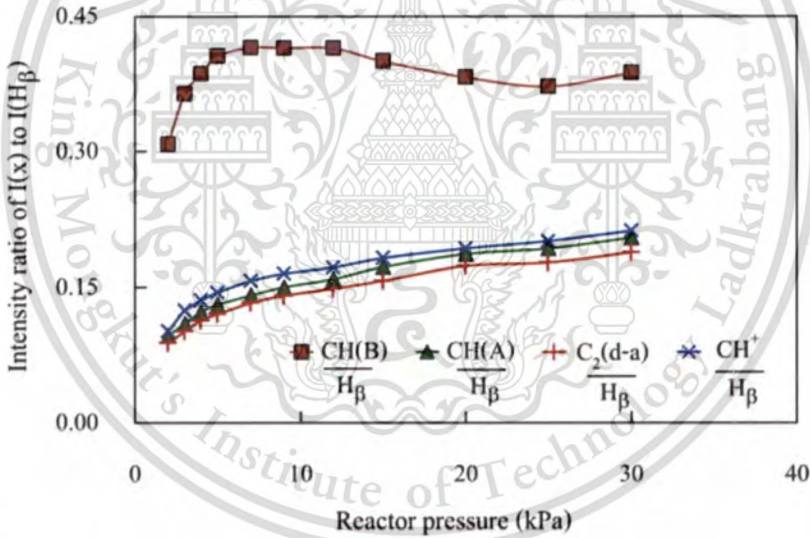

Figure 4.20 Emission intensity ratio of CH(B), CH(A), C_2(d-a), and CH^+ to H_β as a function of the reactor pressure.

4.3.3 Effect of Methane Concentration

Methane concentration is one of the most important parameters for the diamond film deposition in which methane and hydrogen are used as reactants. With increasing the ratio of methane in the standard CH_4/H_2 gas mixture from 1% to ~5%, the grain size of the films decreased and eventually become of the order of hundreds down to tens of nanometers (nanocrystalline diamond) [10-13].

This material is reserved for educational use only, not allowed for commercial use.
Forbidden to modify the content, and cite the document when use.

The purpose of this experiment is to investigate the effect of CH_4 flow rate on the plasma properties. The CH_4-H_2 was carried out under various CH_4 flow rates by adjusting the flow rate of hydrogen to maintain a constant total flow rate of 200 sccm. The reactor pressure was 5 kPa. The gas flow rate and reactor pressure can be controlled independently.

4.3.3.1. Methane Concentration on Plasma Impedance

The plasma impedance on a Smith chart as a function of CH_4 flow rate is shown in **Figure 4.21**. Inductive component of the plasma impedance tended to increase with methane concentration. Normalized electron density and temperature are shown in **Figure 4. 22**. The electron density drastically decreased with an addition of small amounts of methane with only 0.25 sccm whereas the electron temperature and the absorbed power increased. The slight addition in methane flow results in small changes in the gas composition but can perturb strongly the plasma. For the further addition of methane, the electron density gradually decreased and then tended to be steady whereas electron temperature had the opposite changing in trend.

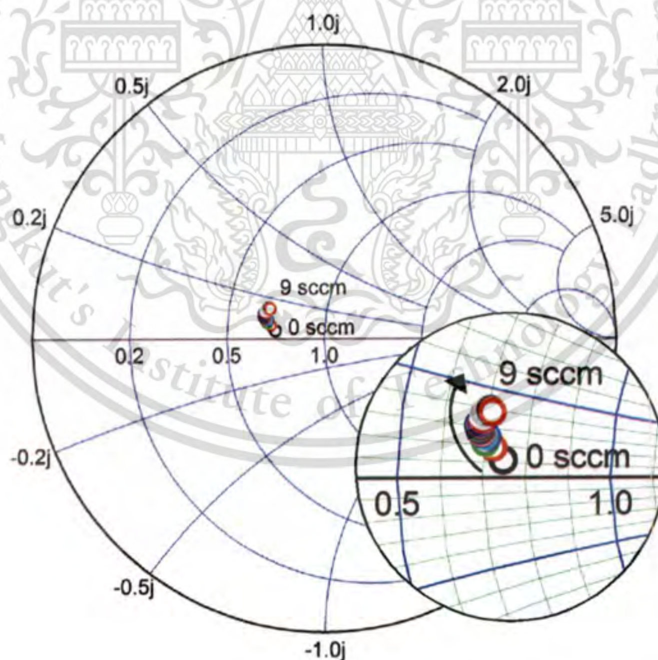

Figure 4.21 Plasma impedance under various methane concentrations.

This material is reserved for educational use only, not allowed for commercial use.
Forbidden to modify the content, and cite the document when use.

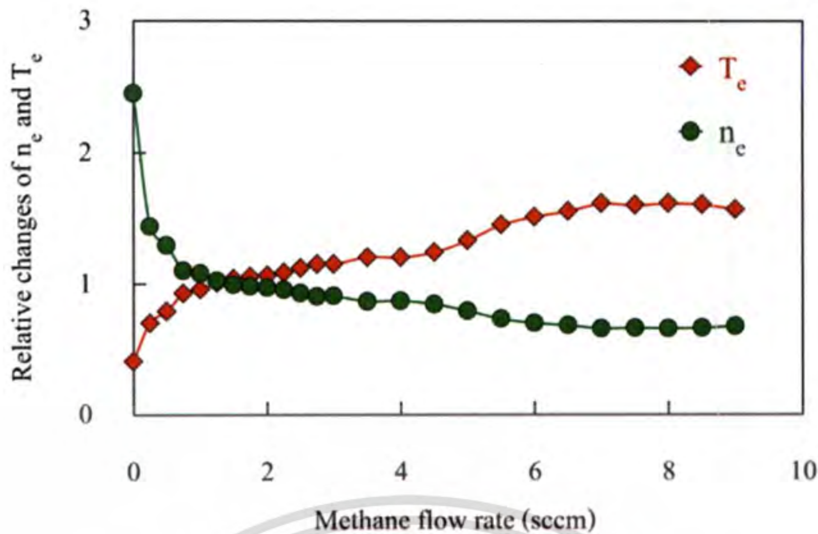

Figure 4. 22 The normalized electron density and temperature of CH_4-H_2 plasma at a reactor pressure of 5 kPa and under various CH_4 flow rates.

In case of $\upsilon_m > \omega$ at a constant power density [14], the decreased electron density leads to a reduction in collision frequency approaching the driven frequency whereas the higher energy is stored in the electron. Therefore, the addition of methane into the H_2 plasma induces electron density to decrease but electron temperature to increase.

As previously mentioned, the relative changes of electron temperature also relate to the optical emission ratio of Hδ to Hβ. However, the electron temperature extracted by OES shows a trend under various CH_4 flow rates different from those for the electron temperature extracted by measuring impedance, as shown in **Figure 4.23**. The main factor influencing the inconsistency is the problem with not following a Boltzmann distribution of OES, especially at methane flow rate higher than 4.0 sccm.

This material is reserved for educational use only, not allowed for commercial use.
Forbidden to modify the content, and cite the document when use.

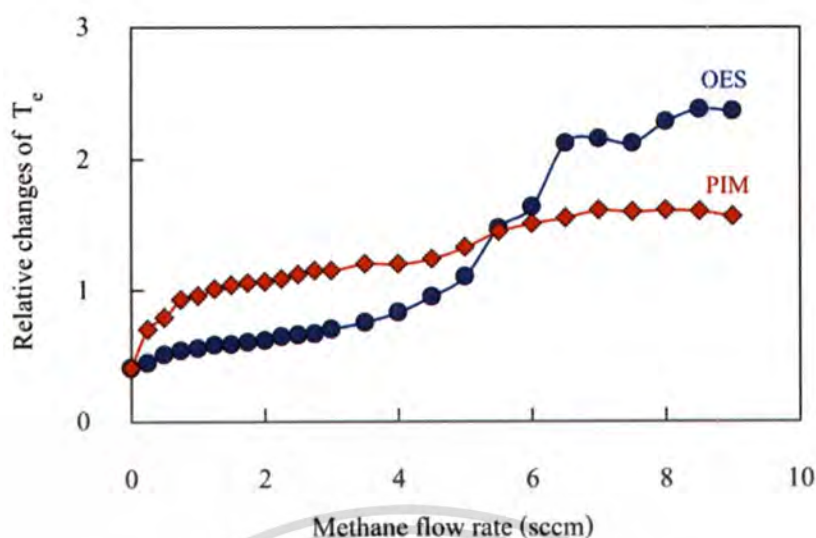

Figure 4.23 The relative changes of electron temperature determined by two methods: plasma impedance measurements (PIM) and optical emission spectroscopy (OES).

Due to the fact that the emission intensity is a function of many factors including Franck-Condon factor [15], the density of states, various quenching effects, etc., a quantitative description of the observation is very complicated and is beyond the scope of this thesis. In particular the collisional quenching effects, the collisional quenching involves collisions with heavy particles that result in the loss of excitation energy as heat instead of as emitted light. The excitation and collisional quenching rates are expected to change impressively [16, 17]. Nevertheless, the result of the trend of electron temperature determined by OES is in good agreement to the work of Jingbiao Cui and Rongchuan Fang [18]. They did not clarify the reason for the variation of electron temperature with the methane flow rate. It is due to the limitation of OES to specify the absorption of the microwave power and electron density in the plasma.

4.3.3.2. Methane Concentration on Gas-phase Species

Figure 4.24 shows some typical optical emission spectra of the H_2-CH_4 plasma used for the film deposition. The H_2 spectrum consists mainly of emission from atomic H Balmer lines (H_α line at 656.3 nm and H_β line at 486.1 nm). When methane was introduced in the system, CH B-X($^2\Sigma^-$-$^2\Pi$) at the centered peak 387.0 nm, CH A-X($^2\Delta$-$^2\Pi$) at 431.5 nm, CH^+ B-X($^2\Sigma^-$-$^2\Pi$) at 417.1 nm, C_2 d-a ($^3\Pi_g$-$^3\Pi_u$) at 516.5 nm, and atomic hydrogen H_β at 486.1 nm appeared in the emission spectra. Theses emission lines as a function of CH_4 concentration is also shown in **Figure 4.25**.

This material is reserved for educational use only, not allowed for commercial use.
Forbidden to modify the content, and cite the document when use.

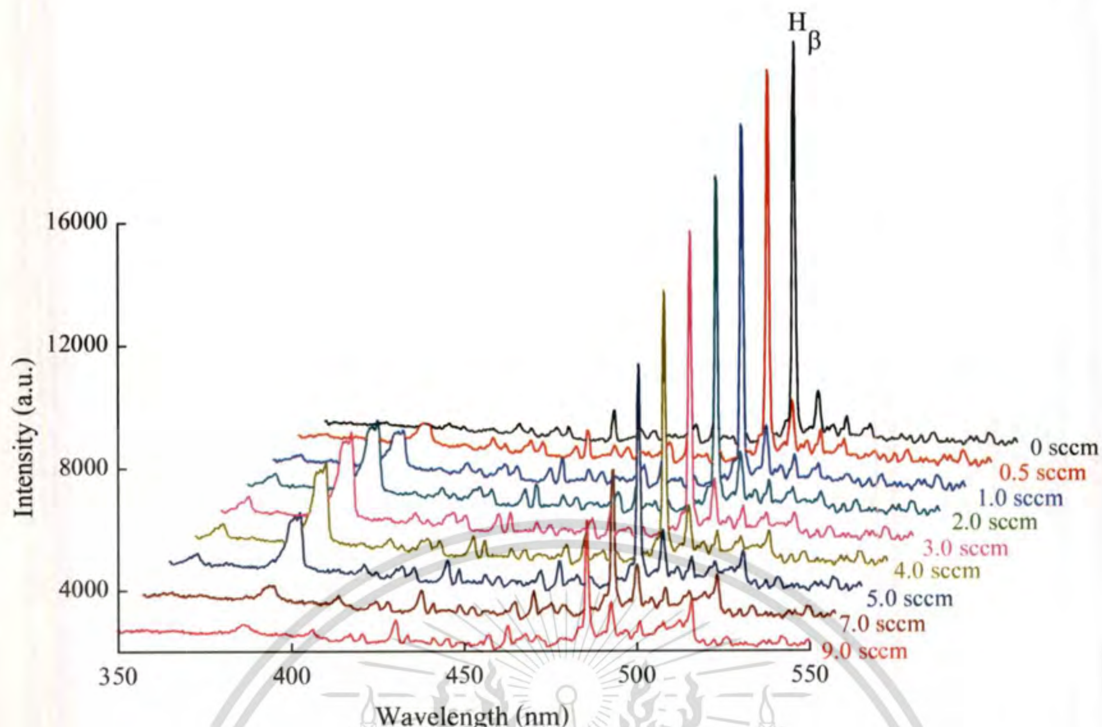

(a)

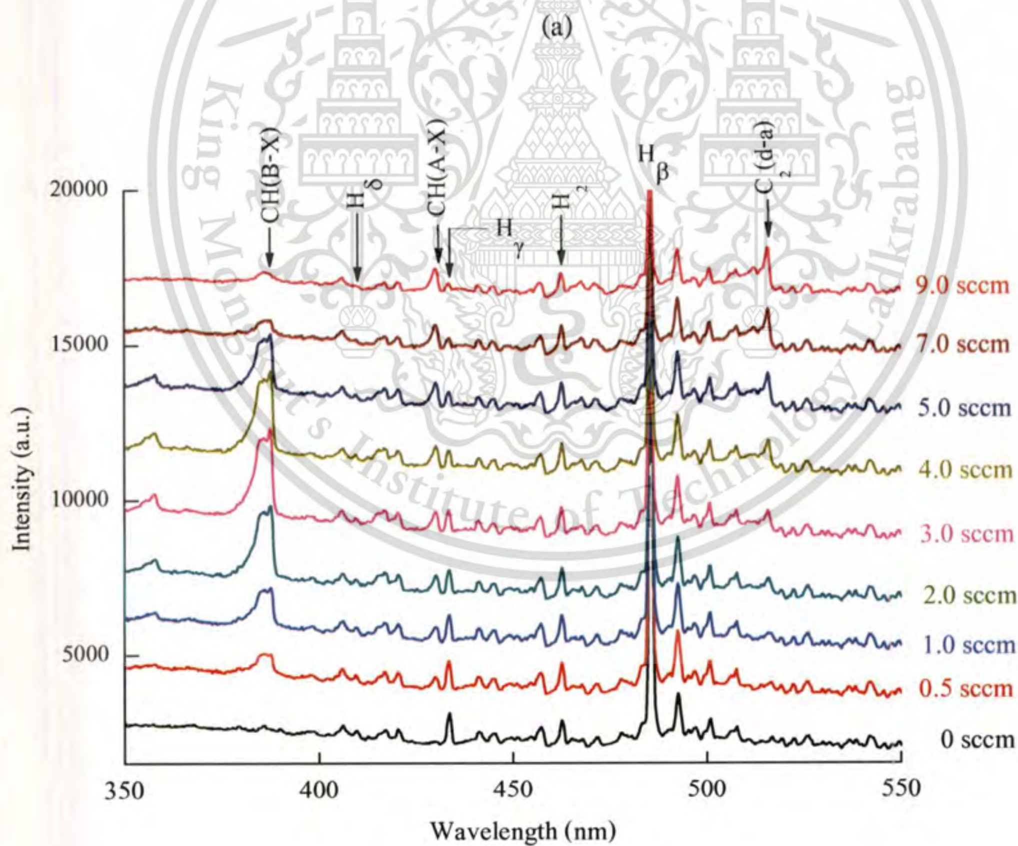

(b)

Figure 4.24 Optical emission spectra of the H_2-CH_4 plasma under various methane concentrations: Waterfall graph (a) and Stack lines graph (b).

This material is reserved for educational use only, not allowed for commercial use.
Forbidden to modify the content, and cite the document when use.

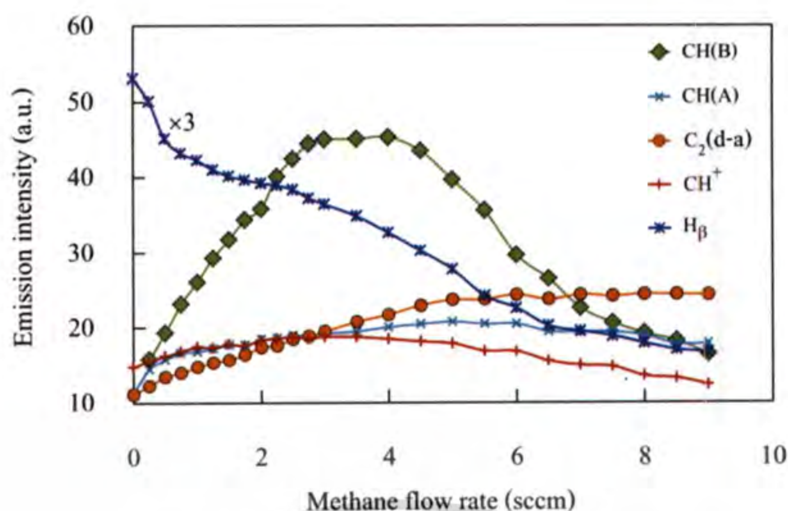

Figure 4.25 Optical emission lines of CH(B) CH(A), CH^+, C_2(d-a), and Hβ species as a function of CH_4 flow rate at the reactor pressure of 5 kPa

The emission intensity of CH and C_2 radicals was nonzero at a zero CH_4 flow rate in that the influx of carbon into the gas phase from the reactor wall. **Figure 4.25** also shows an increase in methane flow rate produced a weaker emission of H_β but a stronger emission of CH(A) and CH(B) radicals as the methane flow rate up to 4.5 sccm and 3.0 sccm, respectively. There are two satisfactory explanations of these behaviors. Firstly, the addition of methane into H_2 plasma causes electron density to reduce. Secondly, the hydrogen radicals are consumed by the dehydrogenation-dissociation reaction:

$$R-H + H \rightarrow R\bullet + H_2$$

where R is a carbon containing radical (mainly CH_3), leading to the presence of much more hydrocarbon species, particularly, CH radical which relates to CH_3 radical [19]. Although not detecting directly using OES, CH_3 radical can be inferred from CH radical. Moreover, experimental work and computational modeling on hydrogen-hydrocarbon mixture concur that, in microwave plasma under conditions common for diamond deposition, hydrogen abstraction from methane by atomic hydrogen dominates over dissociation by electron impact [20]. After 5.0 sccm, the figure also shows that all of optical emission intensities of hydrocarbon radicals reduced. The beginning of the drop in H_2 intensity implies that the dissociation of H_2 molecules is decreasing. This behavior results in the deficiency of hydrogen radicals. Thus, the gas phase reactions with atomic H in which generate hydrocarbon radical is also decreased. As observed in **Figure 4.25**,

This material is reserved for educational use only, not allowed for commercial use.
Forbidden to modify the content, and cite the document when use.

the behavior of all the CH electronic states present in the plasma is quite different due to the difference in rotational temperatures together with excitation and collisional quenching rates [21-24]. Using the H_β line as a reference, the relative intensities of emission from the four species as a function of the methane fraction in the source gas are shown in **Figure 4.26**.

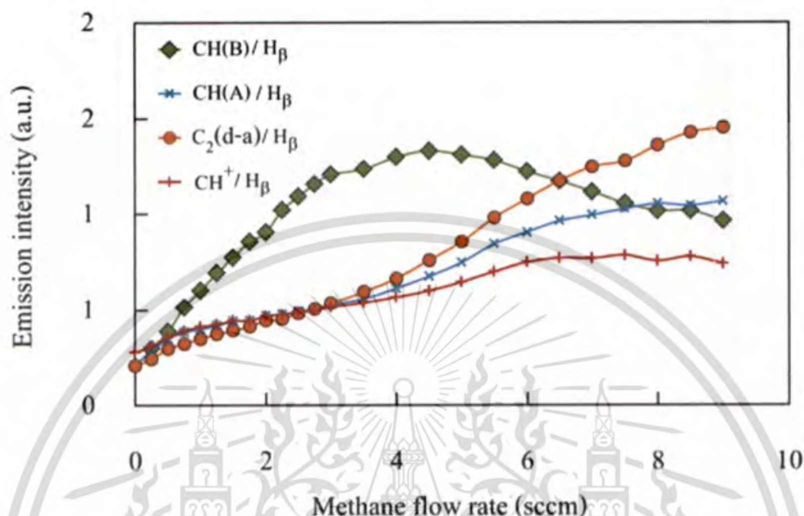

Figure 4.26 Emission intensities of CH(B), CH(A), C_2(d-a), and CH^+ to H_β as a function of the methane concentrations.

By observing the results with the combination usage of the *STHT* 2.45 GHz AIAMS and optical spectrometer, I infer that the rise and fall of the emission of all species with increasing methane flow rate are associated with the depletion of the electron number density and the augmentation of the average electron temperature. The number of atomic hydrogen in the plasma is proportional to the electron density. The electron density and temperature in the plasma have a significant effect on the lifetime of CH_3 radicals and gas-phase reaction rate constant [25, 26]. The both play a crucial role in the plasma chemistry.

This material is reserved for educational use only, not allowed for commercial use.
Forbidden to modify the content, and cite the document when use.

References

[1] Om P. Gandhi. **Microwave Engineering and Application.** New York: Pergamon Press 1989.

[2] Das S., Mukhopadhyay A. K., Datta S. and Basu D. "Prospects of Microwave Processing: An Overview" **Bull. Mater. Sci.** vol.32, 2009. Pp. 1–13.

[3] Andries B., Ravel G. and Peccoud L. "Electrical Characterization of Radio-frequency Parallel-plate Capacitively Coupled Discharge" **J. Vac. Sci. Technol. A.** vol.7, 1989. Pp. 2774-2783.

[4] Hiraki A. "Electron-emitter Fabricated at Low Temperature by Diamond-Nano-Seeding Technique" **Mater. Chemi. Phys.** vol.72, 2001. Pp.196-200.

[5] Allendort M.D. and Bernard C., Editors. **Chemical Vapor Deposition – Proceedings of the Fourteenth International Conference and EUROCVD-11.** Massachusetts: The Electrochemical Society, Inc. 1997.

[6] Yuri P. Raizer. **Gas Discharge Physics.** Berlin: Springer-Verlag GmbH. 1991.

[7] Sanborn C. Brown. **Basic Data of Plasma Physcis.** New York: American Institute of Physics (AIP) Press. 1994.

[8] Krogh O., Wicker T. and Chapman B. "Summary Abstract: Collisional Energy Transfer in Noble Gas/Hydrogen Plasmas" **J. Vac. Sci. Technol. A.** vol.4, 1986. Pp. 1796-1797.

[9] Barshilia H. C. and Vankar V. D. "Concentration of Atomic Hydrogen in the Ground State in a CH_4-H_2 Microwave Plasma" **J. Appl. Phys.** vol.80, 1996. Pp. 3694-3698.

[10] May P. W., Ashfold M. N. R. and Mankelevich Yu. A. "Microcrystalline, Nanocrystalline, and Ultrananocrystalline Diamond Chemical Vapor Deposition: Experiment and Modeling of the Factors Controlling Growth Rate, Nucleation, and Crystal Size" **J. Appl. Phys.** vol.101, 2007. 053115.

[11] Huang S. M. and Chau-Nan Hong F. "Low Temperature Growths of Nanocrystalline Diamond Films by Plasma-assisted Hot Filament Chemical Vapor Deposition" **Surf. Coat. Technol.** vol.200, 2006. Pp. 3160-3165.

This material is reserved for educational use only, not allowed for commercial use.
Forbidden to modify the content, and cite the document when use.

[12] Abu Suilik S. B., Shimamoto D., Kitagawa H., Hasezaki K. and Noda Y., "Experimental Study of Nucleation and Quality of CVD diamond Adopting Two-step Deposition Approach using MPECVD" **Diamond Relat. Mater.** vol.15, 2006. Pp. 1765-1772.

[13] You M. S., Hong F. C. N., Jeng Y. R. and Huang S. M., "Low Temperature Growth of Highly Transparent Nanocrystalline Diamond Films on Quartz Glass by Hot Filament Chemical Vapor Deposition" **Diamond Relat. Mater.** vol.18, 2009. Pp. 155-159.

[14] Alfred Grill. **Cold Plasma in Materials Fabrication: From fundamentals to Applications.** New York: The Institute of Electrical and Electronics Engineers, Inc., (1994)

[15] Chen L. C., Kichambare P. D., Chen K. H., Wu J. J., Yang J. R. and Lin S. T.. "Growth of Highly Transparent Nanocrystalline Diamond Films and a Spectroscopic Study of The Growth" **J. Appl. Phys.** vol.89, 2001. Pp. 753-759.

[16] Lang T., Stiegler J., Von Kaenel Y. and Blank E., "Optical Emission Diagnostics and Film Growth During Microwave-Plasma-Assisted Diamond CVD" **Diamond Relat. Mater.** vol.5, 1996. Pp. 1171-1184.

[17] Gorbachev A. M., Muchnikov A. B., Vikharev A. L., Radishchev D. B. and V. A. Koldanov, "Hydrocarbon Plasma Chemistry in a Continuous Microwave Discharge" **Plasma Phys. Rep.** vol.33, 2007. Pp. 871-879.

[18] Cui J. and Fang R., "Characterization of the Diamond Growth Process using Optical Emission Spectroscopy" **J. Appl. Phys.** vol.81, 1997. Pp. 2856-2862.

[19] Yoon S. F., Tan K. H., Ahn R. J. and Huang Q.F. "Effect of Microwave Power on Diamond-like Carbon Films Deposited using Electron Cyclotron Resonance Chemical Vapor Deposition" **Diamond Relat. Mater.** vol.9, 2000. Pp. 2024-2030.

[20] Heintze M., Magureanu M. and Kettlitz M., "Mechanism of C_2 Hydrocarbon Formation from Methane in a Pulsed Microwave Plasma" **J. Appl. Phys.** vol.92, 2002. Pp. 7022-7021.

[21] Furuya K., Ueda T., Tokeshi M. and Ogawa T. "Rotational Distributions and Threshold Energies of the CH(B-X) Emission by Controlled Electron Impact on Methane, Ethylene, and Ethane" **Chem. Phys.** vol.221, 1997. Pp. 303-309.

This material is reserved for educational use only, not allowed for commercial use.
Forbidden to modify the content, and cite the document when use.

[22] Luque J., Juchmann W., and Jeffries J. B., "Absolute Concentration Measurements of CH Radicals in a Diamond-depositing dc-arcjet Reactor" **Applied Optics.** vol.36, 1997. Pp. 3261-3270.

[23] Luque J., Juchmann W., Brinkman E. A., and Jeffries J. B., "Excited State Density Distributions of H, C, C_2, and CH by Spatially Resolved Optical Emission in a Diamond Depositing dc-arcjet Reactor" **J. Vac. Sci. Technol. A.** vol.16, 1998. Pp. 397-398.

[24] Iza F. and Hopwood J. A. "Rotational, Vibrational, and Excitation Temperatures of a Microwave-Frequency Microplasma" **IEEE Trans. Plasma Sci.** vol.32, 2004. Pp. 498-504.

[25] Ikeda MIto., H., Hiramatsu M., Hori M., and Goto T., "Effects of H, OH, and CH_3 Radicals on Diamond Film Formation in Parallel-plate Radio Frequency Plasma Reactor" **J. Appl. Phys.** vol.82, 1997. Pp. 4055-4061.

[26] Mao M. and Bogaerts A. "Investigating the Plasma Chemistry for the Synthesis of Carbon Nanotubes/Nanofibres in An Inductively Coupled Plasma Enhanced CVD System: the Effect of Different Gas Mixtures" **J. Phys. D: Appl. Phys.** vol.43, 2010. 205201.

King Mongkut's Institute of Technology Ladkrabang

This material is reserved for educational use only, not allowed for commercial use.

Forbidden to modify the content, and cite the document when use.

CHAPTER 5

SYNTHESIS AND CHARACTERIZATIONS OF NANOCRYSTALLINE DIAMOND FILMS

In the deposition of diamond and nanocrystalline diamond (NCD) films, nucleation and growth are a vital step. The desired morphology combined with controlled composition of NCD films greatly depends on the conditions for nucleation and growth steps [1]. The nucleation and growth dynamics of CVD diamond films involve gas-surface reaction and plasma chemistry. Therefore, topography of substrate surfaces as well as gas-phase species environment of the plasma powerfully influences the CVD diamond films to form on the substrate. Its effect on the nucleation density and film formation will be also examined. The influence of the operating conditions for generating plasma of the MPECVD apparatus such as reactor pressure, gas composition, and microwave power on properties of diamond films will be investigated. FE-SEM, Raman spectroscopy, and white-light reflectometry are main techniques used to characterize the deposited films.

This thesis also focuses on graphitization to specify morphological and structural changes related to gas-phase species present in deposition environment. Such gas-phase species, including electrons, were in situ and real-time monitored via an optical emission spectrometer and *STHT* 2.45 GHz automatic impedance analyzer and matching system (*STHT* 2.45 GHz AIAMS) Relative concentrations of such gas-phase species that explain an average crystal size, morphologies of subsequent films, and probability of a renucleation event occurrence for diamond growth will be also discussed.

5.1 Nucleation and Growth Dynamics of Diamond Films

The first difficulty that arises from the attempt to grow diamond on foreign substrates is that a continuous diamond film cannot be deposited unless a proper nucleation step precedes the growth. After a non-diamond substrate has been exposed to proper growth conditions without a nucleation procedure only a few isolated diamond crystallites (~10^5-10^6 cm^{-2}) will be found [2].

This material is reserved for educational use only, not allowed for commercial use.
Forbidden to modify the content, and cite the document when use.

This is due to a combinations of factors such as the high surface energy of diamond relative to silicon (6 J/cm^2 to 1.5 J/cm^2, respectively) [3], the relatively low sticking coefficient of gaseous precursors, and the competition of nondiamond phases. The initial nucleation density can greatly affect the subsequent microstructural development of CVD diamond films. The nucleation density depends on the number of activated nucleation sites available on the substrate surface. A higher initial nucleation density leads to shorter coalescence time and lower surface roughness.

To clarify the beginning of the deposition process, this thesis also focuses on surface studies of the kinetics of diamond nucleation and growth process on Si(100) substrate combined with FE-SEM observations. Three kinds of mirror-polished Si wafer substrates were used as follows: non-polishing, ultrasonic polishing with 0-3 micro-size diamond powder suspended in isopropyl, and manual polishing with 0-1/2 micro-size diamond powder mixed in minute isopropyl. The effect of polishing method on time-dependent nuclei density and formation of the films will be investigated. The surface pretreatment method affecting the surface energy will be also displayed via measuring contact angle.

5.1.1 Design of Experiment

The purpose of this experiment is to investigate time dependence of the nuclei density and diamond film formation on mirror-polished Si substrates scratched by two methods: manual and ultrasonic polishing. The deposition was performed under various process times: 15, 30, 45, 60, 120, and 360 min. The surfaces of substratess were pretreated with different methods: non-polishing, ultrasonic polishing with a 0–3 micro-size diamond powder suspension in isopropanol in ultrasonic bath, and manual polishing with 0–1/2 micro-size diamond powder mixed in minute isopropanol. A gas mixture was used with 0.75%CH_4 in H_2 at a total mass flow rate of 200 sccm and a reactor pressure around 20 kPa. The absorbed microwave power measured by the *STHT* 2.45 GHz AIAMS was around 600 W. Under these operating conditions, the substrate temperature was achieved by microwave induction around 780 °C. The substrates were cleaned by piranha clean procedure. Then a pretreatment of the substrate surface was performed by either

This material is reserved for educational use only, not allowed for commercial use.
Forbidden to modify the content, and cite the document when use.

mechanical polishing for 30 min or ultrasonic polishing for 90 min. After such pretreatment, the substrate was done by the following procedure as described in Section 3.2.1 of CHAPTER 3.

5.1.2 Effect of Surface Pretreatment Methods on Surface Morphology

Optical microscope images of the flaws on surfaces pretreated by manual polishing and ultrasonic polishing are shown in **Figure 5.1**. This figure also shows the surface with non-pretreated in **Figure 5.1**(a). The surface flaws on the pretreated Si surface are classified into dents and scratches. The pretreatment with mechanical polishing caused the sharp, narrow, deep, and long scratches sporadically to appear on the surfaces and dull-edged dents were also sporadically presented. While the pretreatment with ultrasonic polishing resulted in sharp-edged dents sporadically present on the surfaces.

(a) (b) (c)

Figure 5.1 Optical microscope images of Si wafer surfaces at different polishing methods: (a) untreated mirror-polished, (b) ultrasonic-polished, and (c) manual-polished Si substrates.

5.1.3 Time-dependent Nuclei Density of Diamond

The sequence of deposition of diamond nuclei on Si(100) substrates is displayed in **Figure 5.2** and **Figure 5.3** with the comparison of diamond nuclei on the substrates after using different pretreatment process. These FE-SEM images display the diamond nuclei at 15, 30, 45, 60, 120, and 360 min. Nucleation and growth occurred on defects or sites. Nucleation on the substrate with manual polishing occurred readily as 15 min as did nucleation on the substrate with ultrasonic polishing. The growth of the diamond nuclei on the substrate with manual polishing subsequently

This material is reserved for educational use only, not allowed for commercial use.
Forbidden to modify the content, and cite the document when use.

occurred up the formation of the film covering the substrate above 360 min but the other one still occurred isolated diamond nuclei with around 1 micron in diameter.

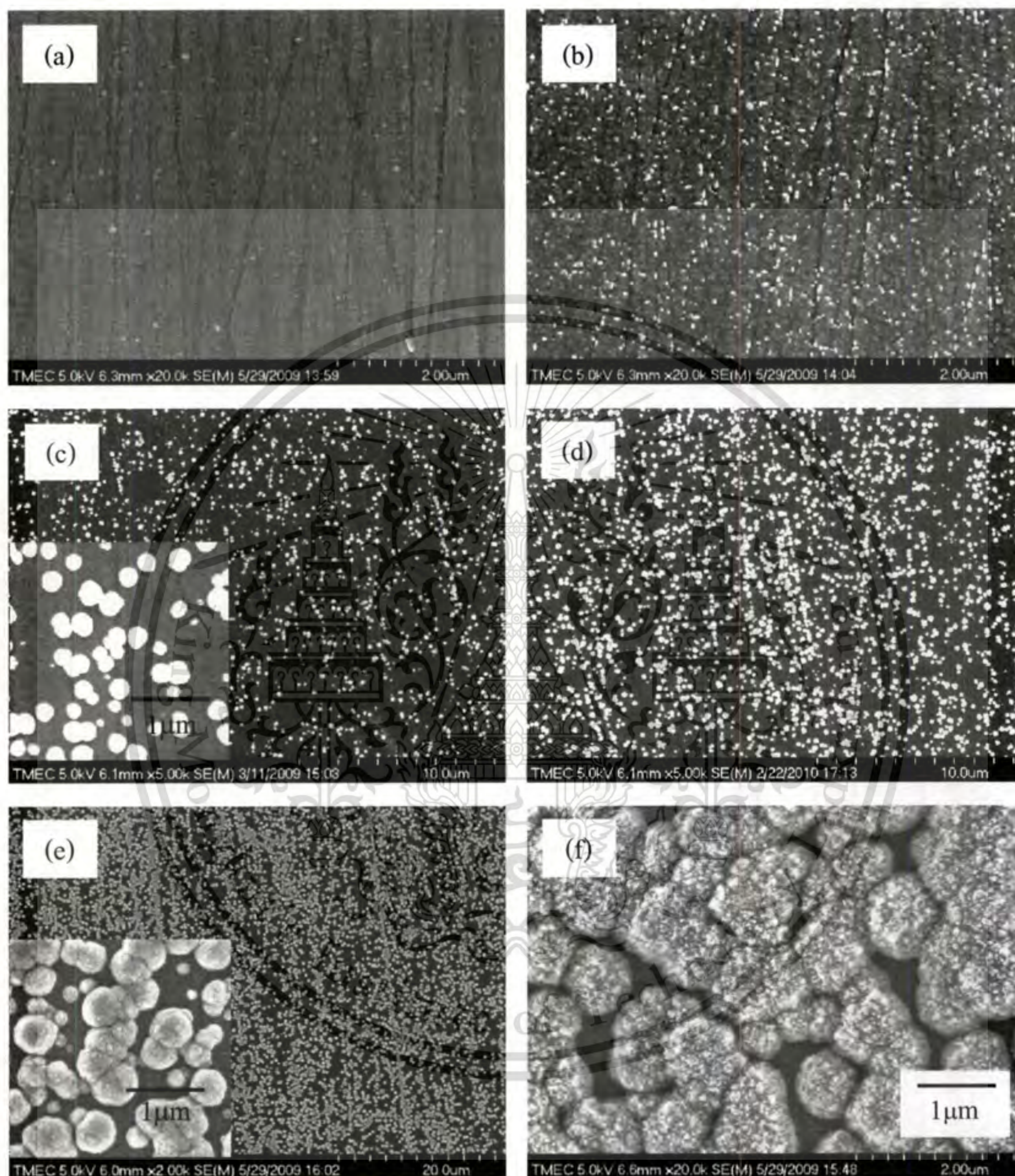

Figure 5.2 FE-SEM images of diamond nucleation on Si substrate surface polished by mechanically hand with 0-1/2 micro-size diamond powder for 30 min at different deposition times: (a) 15 min, (b) 30 min, (c) 45 min, (d) 60 min, (e) 120 min, and (f) 360 min.

This material is reserved for educational use only, not allowed for commercial use.
Forbidden to modify the content, and cite the document when use.

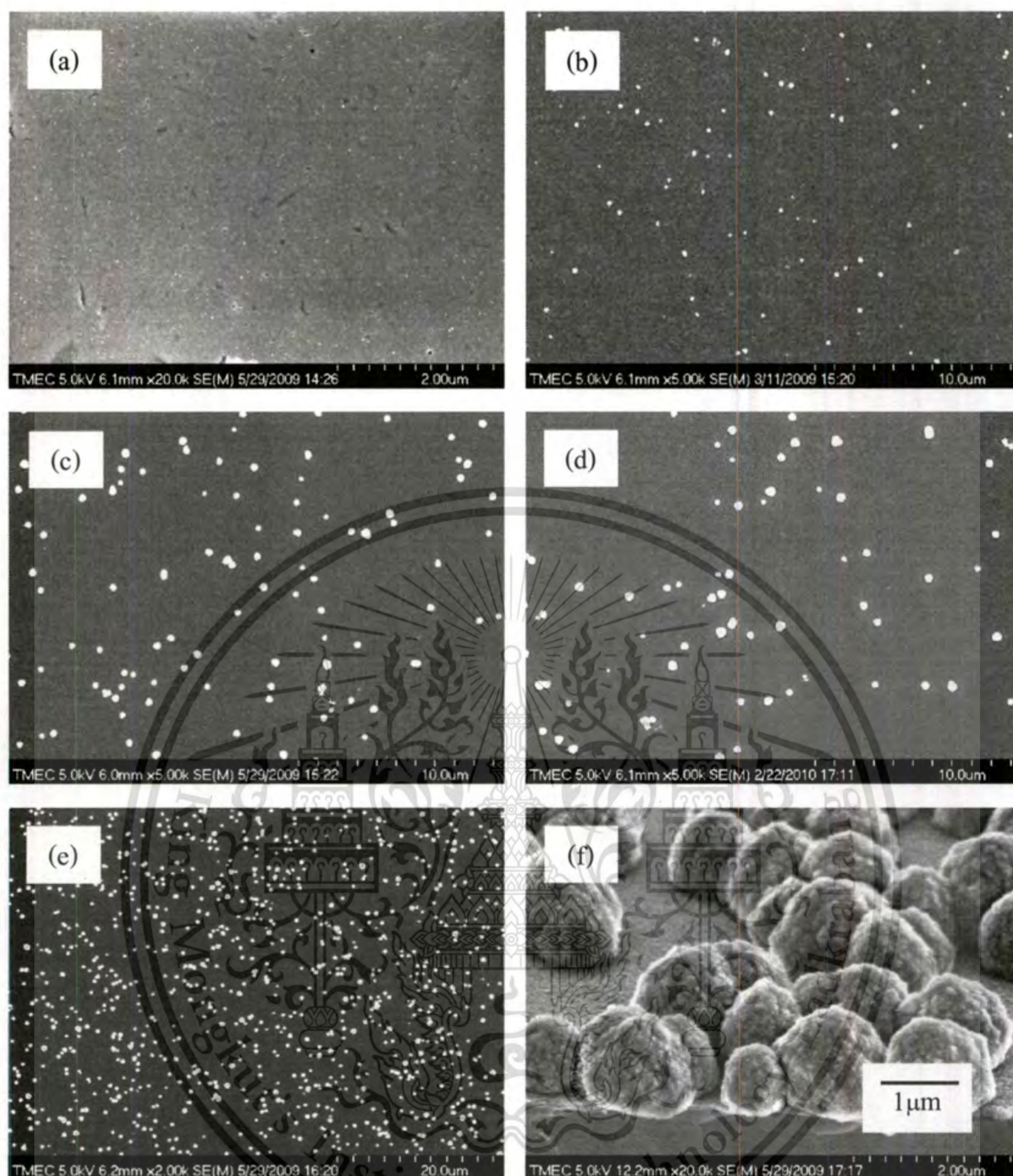

Figure 5.3 FE-SEM images of diamond nucleation on Si substrate surface polished by ultrasonically vibrating with 0-3 micro-size diamond powder for 90 min at different deposition times: (a) 15 min, (b) 30 min, (c) 45 min, (d) 60 min, (e) 120 min, and (f) 6 h.

This material is reserved for educational use only, not allowed for commercial use.
Forbidden to modify the content, and cite the document when use.

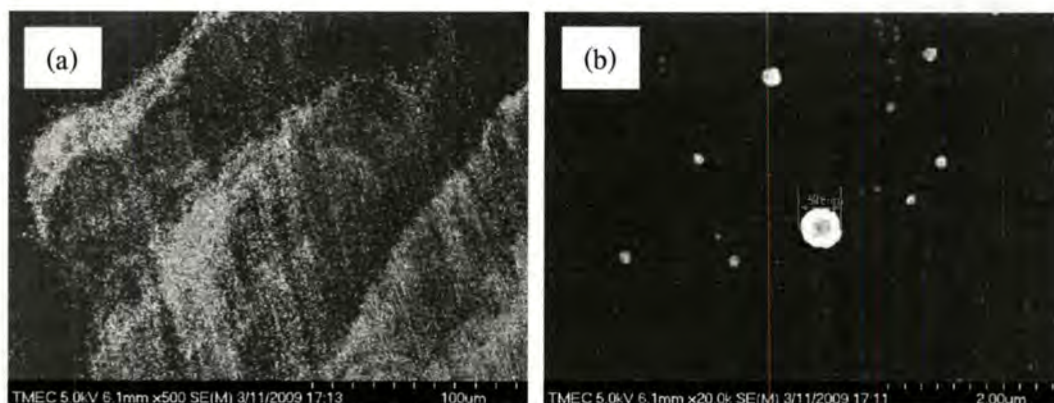

Figure 5.4 FE-SEM images of development of diamond growth on mirror-polished Si substrate-surface under deposition time of 6 h.

In the case of the substrate with manual polishing, the images express small crystallites with preferential nucleation along scratches on the silicon substrate. The distribution of those nuclei indicated that scratch paths is the preferential sites. The diamond particles increased linearly with the deposition time. In the other one, the nuclei randomly distributed on the surface and no indication gave that scratch point was preferred sites. In addition, **Figure 5.4** shows the formation of diamond nuclei on a mirror-polished surface after deposition time of 6 h. The biggest size of diamond nuclei was only 516 nm. The FE-SEM top-view images of all diamond nuclei appear extremely bright due to the strong charging effect in SEM, suggesting that these nuclei present the electrical resistivity property of diamond.

Nucleation densities on polished substrate surfaces were also estimated by counting the number of diamond nuclei from FE-SEM images at x100,000 and x20,000 magnification. The kinetics of nucleation density that was extracted from more than 400 particles is reported in **Figure 5.5**, and the kinetics of mean cluster size in **Figure 5.6**. After deposition time of 15 min, the nuclei density was about 1.5 x 10^{10} cm^{-2} for the both manual-polished and ultrasonic-polished surfaces. After 30 min, the nucleation density on the ultrasonic-polished surface decreased rapidly to 2 x10^{7} cm^{-2} and saturated; whereas, the other one, the nucleation density decreases from 5 x 10^{9} cm^{-2} after 30 min to 6 x 10^{8} cm^{-2} after 60 min. The nucleation density failed to increase with deposition time but the cluster size increased. The increased clusters in size coincided with the

This material is reserved for educational use only, not allowed for commercial use.
Forbidden to modify the content, and cite the document when use.

decreased nucleation density reveals that the agglomeration and merging of the diamond nuclei simultaneously took place and then those clusters fused to form a thick uniform film.

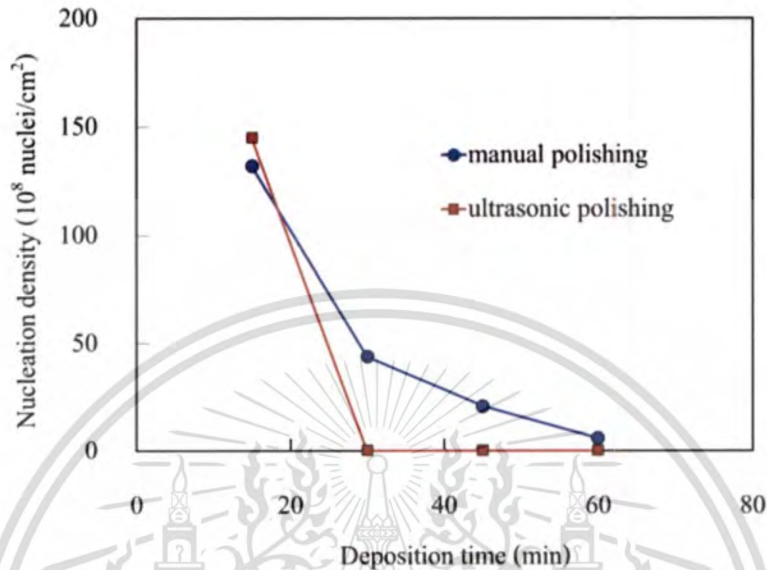

Figure 5.5 Kinetics of the nucleation density on Si substrate surfaces pretreated by two methods: manual and ultrasonic polishing.

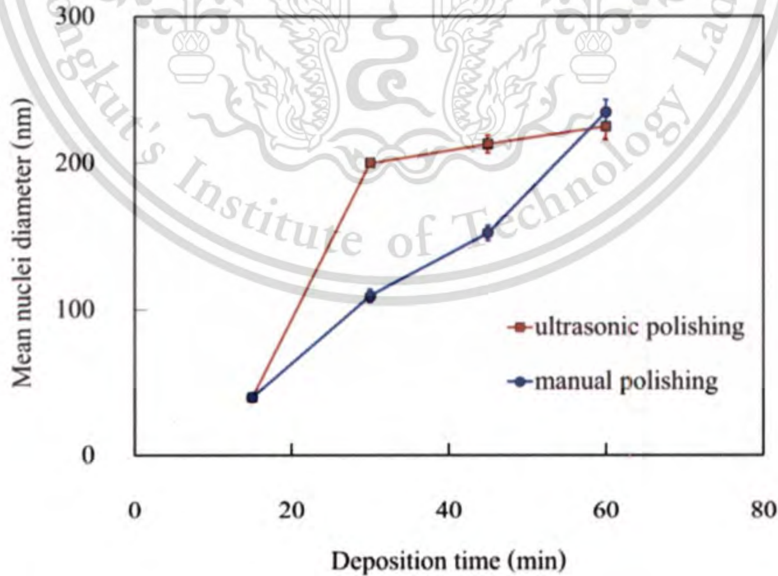

Figure 5.6 Kinetics of the mean size of the diamond nuclei on Si substrate surfaces pretreated by two methods: manual and ultrasonic polishing.

This material is reserved for educational use only, not allowed for commercial use.
Forbidden to modify the content, and cite the document when use.

5.1.4 Surface Energy of Substrate

The contact angles of the substrate surfaces under various polishing methods are shown in **Figure 5.7**. They strongly depend on the polishing methods. The contact angle of a liquid drop on the surface relates to the surface energy. The measuring contact angle expresses that the surface energy for the manual-polished surface was higher than that for ultrasonic-polished and mirror-polished surfaces.

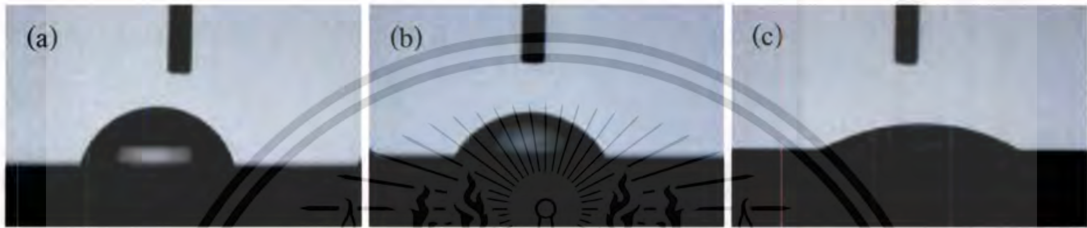

Figure 5.7 Images of deionized water contact angle on Si substrate surfaces under various pretreatment methods: (a) mirror polishing, (b) ultrasonic polishing for 90 min, and (c) manual polishing for 30 min.

5.1.5 Summary

In summary, film-deposition process needed to have vacancies on the surface, particularly, MPECVD process that was a growth process occurring diffusions [4]. Vacancy sites were important in the film nucleation and growth processes determined grain size. Nucleation and growth occurred on defects or sites that had the high bonding energy. The measurements of contact angle suggested the mechanical polishing method enhanced more nucleation density on the substrate surface than other methods due to the greater of surface energy. In addition, the defect and damage with sharper edges and deeper scratches on the manual-polished surface were greater than that on the ultrasonic- and mirror-polished surfaces. Therefore, the surface polished by manual had provided more high-energy nucleation sites of active sites and bettered sticking probability to the precursor of the diamond nucleation.

This material is reserved for educational use only, not allowed for commercial use.
Forbidden to modify the content, and cite the document when use.

5.2 Trace Composition of Diamond films

At the beginning of this thesis, the crystalline quality of diamond nuclei was interpreted by examining on FE-SEM image contrast that was due to a strong charging effect. This method cannot identify the compositions on the diamond films. The composition and structure on the surface and interlayer of the diamond films were investigated by energy dispersive spectroscopy (EDS) and Auger-electron spectroscopy (AES). Moreover, AES analysis can be also used to specify allotropic form of carbon. Each allotropic form of carbon yields a different AES spectrum.

5.2.1 Trace Element Composition of the Films by EDS Analysis

The EDS analysis was performed on five diamond films. These films were prepared under different reactor pressures and CH_4 concentrations and their thicknesses were ranged between 1 to 1.8 μm. The analysis shows the presence of carbon, oxygen, and silicon. All compositions of the deposited films are shown in **Figure 5.8**.

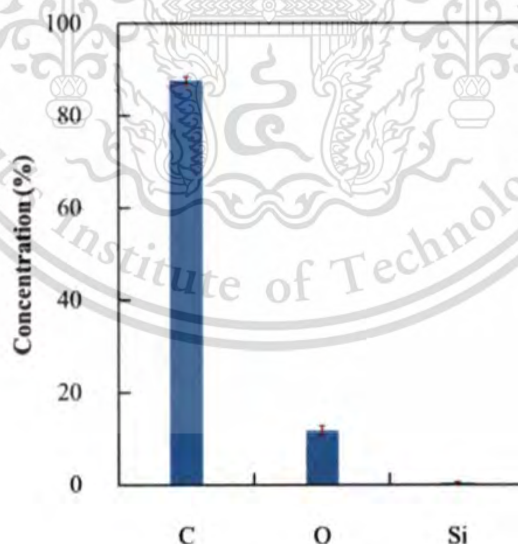

Figure 5.8 Diamond-film compositions measured by EDS analysis. The ratio of O to C was around 16 : 100.

The carbon concentration was calculated to be 87.72 ± 0.86 wt.%, oxygen concentration to be 11.92 ± 0.97 wt.%, and silicon concentration to be 0.36 ± 0.19 wt.%. The ratio of oxygen

This material is reserved for educational use only, not allowed for commercial use.
Forbidden to modify the content, and cite the document when use.

concentration to carbon concentration, O : C ratio, was only 16 : 100. This technique is not to be surface sensitive because its penetration depth is more than 3 μm [5, 6]. This leads to the presence of signal of silicon used as substrates.

Figure 5.9 (a) A cross-section image of the film measured composition of the interlayer near substrate and (b) the cross-section image showing positions on the interlayer measured by EDS.

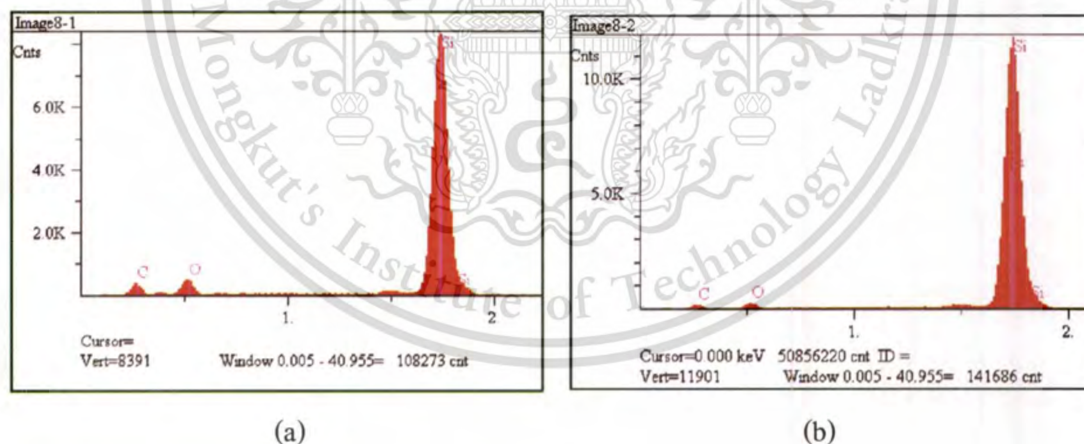

Figure 5.10 EDS analysis mapping images of the diamond film at two interlayer positions near substrate shown in **Figure 5.9**(b): (a) Position 1, and (b) Position 2. The ratio of O to C was around 15 : 1.

Due to EDS technique not to be surface sensitive, the compositions of the interlayer near substrate of the diamond film with thickness of only ~200 nm depicted in **Figure 5.9**(a) were also measured by EDS analysis. EDS spectra of the FE-SEM cross-section image in **Figure 5.9**(b) are

This material is reserved for educational use only, not allowed for commercial use.
Forbidden to modify the content, and cite the document when use.

shown in **Figure 5.10**. The composition of the film consist of carbon (0.28 keV), oxygen (0.53 keV), and silicon (1.74 eV). The O : C ratio for the interlayer was around 15:1; while the O : C ratio of the whole bulk was 100:16. The interlayer had a 93.75% greater increase in the O : C ratio than did the whole bulk. The greater O : C ratio for the interlayer or near substrate revealed that oxygen was composed of not the whole bulk but only near the substrate surface. The trace oxygen left in the deposited films will be discussed in the Section 5.2.3.

5.2.2 Trace Element Analysis of Diamond Films by AES Technique

AES spectrum of the film with thickness of 200 nm is shown in **Figure 5.11**. It displayed the SiO_x at 84 eV, C-KLL signal at 272 eV, and O-KLL signal at 508 eV. It also confirmed the composition of the deposited film that was composed of oxygen. Furthermore, AES analysis confirmed the allotrope of carbon of the film. The bonding structure of the deposited films was also investigated by AES; its derivative Auger C-KLL spectrum is shown in **Figure 5.12** together with the spectrum of graphite as references measured under the same conditions. The binding energy width D between the most positive maximum and the most negative minimum was also determined.

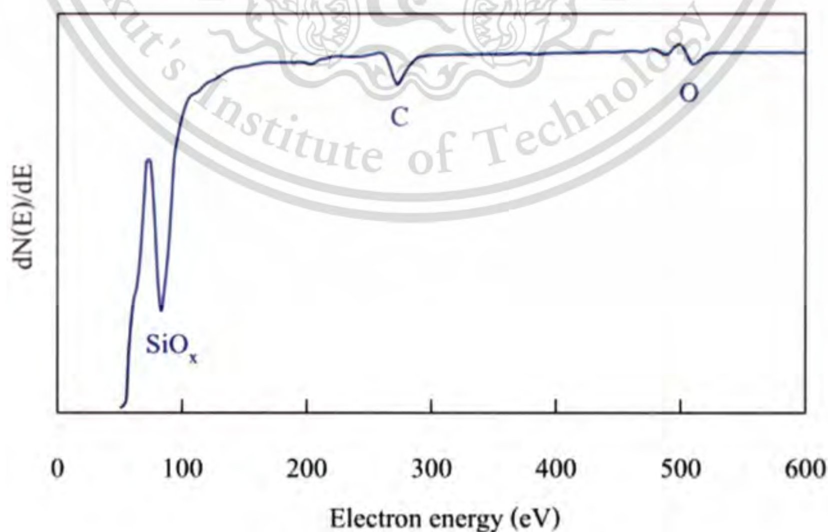

Figure 5.11 AES spectra of the deposited films

King Mongkut's Institute of Technology Ladkrabang
This material is reserved for educational use only, not allowed for commercial use.
Forbidden to modify the content, and cite the document when use.

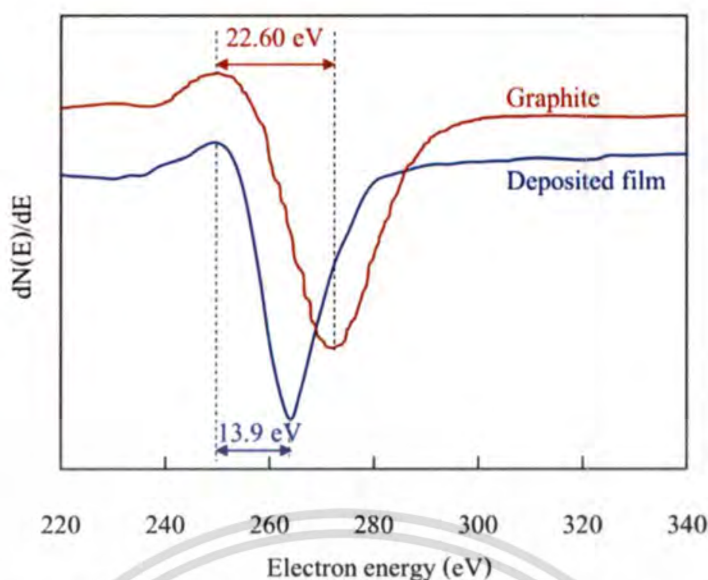

Figure 5.12 Auger spectra of (a) a deposited film and (b) graphite. The values of D width are given in the figure.

Taking into account the two extreme cases – diamond (100% sp^3-bonded carbon content) and graphite (100% sp^2-bonded carbon content) – a linear interpolation between the D values can be used to determine the ratio of sp^3/sp^2-hybridized atoms in any carbon film [7-9]. The D value was 13.0 eV for the PCD films [7], the same value was found for natural diamond. For my measurements, the D values were 22.60 eV for graphite and 13.91eV for the deposited film. In the case of graphite, the D value is within the range reported in literature (up to 22.8 eV for highly oriented pyrolytic graphite HOPG) [10]. For the deposited films, this D value corresponds to NCD films. My results are consistent with those of Mednikarov B. *et.al* [10]. The difference of D between diamond and graphite was 8.69 eV in my measurements. Therefore, the deposited NCD film with 13-eV-D value are composed of predominantly 90.52.0% sp^3- bonded carbon content and only 9.48% of sp^2- bonded carbon content.

5.2.3 Trace Oxygen Element in the Deposited Films

As stated in Section 5.2.1, the amount of oxygen relative to that of carbon for near substrate was detected higher 93.75 times than that for whole bulk of the film. This result attributed to the trace oxygen being only near the substrate. In other words, the substrate surfaces absorbed oxygen present on the surface before the deposition process was begun. In order to better understand and

This material is reserved for educational use only, not allowed for commercial use.

Forbidden to modify the content, and cite the document when use.

realize the initial oxygen coverage, it is important to systemically study and identify the main sources of oxygen. Before the beginning of the deposition process, the substrates were cleaned in an ultrasonic bath for degreasing as described in section 3.2.1 of chapter 3; after that, the substrates were loaded into the plasma reactor and then *in situ* cleaned by H_2 plasma for 20 min. Consequently, the coverage on the substrate surfaces after each cleaning process was analyzed by AES analysis.

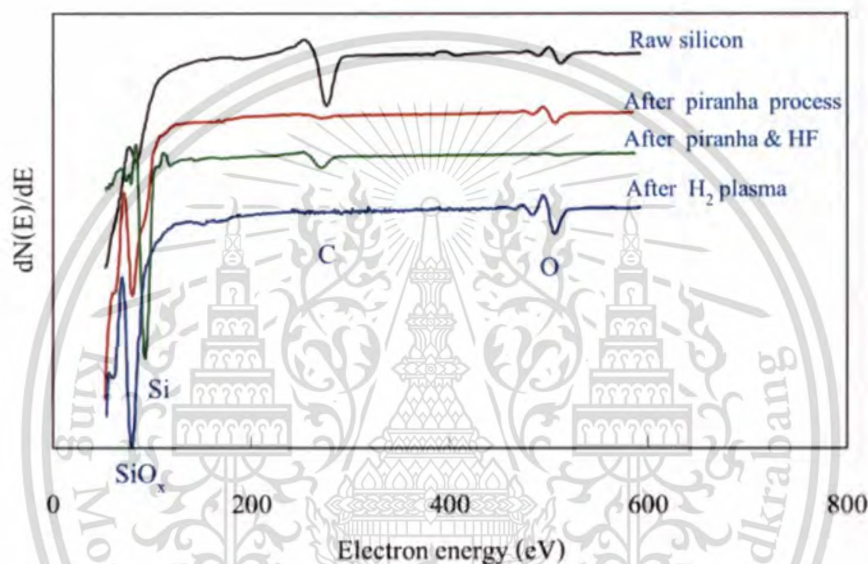

Figure 5.13 Auger spectra of the silicon surfaces (a) as-cleaned, (b) after a piranha process, (c) after (b) and then dipping in diluted HF solution, and (d) after (c) and then *in situ* cleaning in H_2 plasma.

Figure 5.13 shows AES spectra of the Si substrates after cleaning each process. These cleaning processes used for this thesis include piranha, dipping in diluted HF, and an *in situ* H_2-plasma process. The AES spectra present the SiO_x at 84 eV, C-KLL signal at 272 eV, and O-KLL signal at 508 eV. The strong line is due to Si-LVV at 92 eV present for only the substrate after dipping in diluted HF solution. After H_2 plasma cleaning process, the surface was again coverage of oxygen. Also, a longer cleaning time using H_2 plasma did not produce a cleaner surface and not cause oxygen to increase. In addition, the optical emission of plasma did not present the emission intensity of CN species, indicating the air leakage into the plasma reactor. It can be concluded that

This material is reserved for educational use only, not allowed for commercial use.
Forbidden to modify the content, and cite the document when use.

oxygen may come from the surface of the reactor wall during the early of plasma cleaning process and became adsorbed on the substrate surfaces.

5.2.4 Summary

Although AES technique can be determined the ratio of sp^3/sp^2-hybridized atoms of carbon films and easily distinguished from any other stable or unstable form of carbon; however, the analysis of diamond films with thickness greater than 500 nm by electron beam techniques such as AES has always proved difficult due to the sample charging effect. This causes secondary electron peaks to dominate the spectrum. While Raman spectroscopy is one technique that has proven to be very well suited many of the characterization needs with carbon nanomaterials. Raman spectroscopy is most sensitive to highly symmetric covalent bonds with little or no natural dipole moment. The carbon-carbon bonds that make up these materials fit this criterion perfectly and as a result Raman spectroscopy is highly sensitive to these materials and able to provide a wealth of information about their structure. Consequently, for this thesis, Raman spectroscopy is the main technique used to characterize NCD films synthesized by the purpose-built MPECVD apparatus.

5.3 Two-step Approach Deposition Process

The desired morphology combined with controlled composition of NCD films greatly depends on the conditions for nucleation and growth steps [1]. The deposition at specific deposition regimes enhances diamond nucleation although diamond quality is not necessarily favored. Therefore, a two-step deposition process is an interesting process. There are several means of operation of the two-step deposition process for each step: by means of using negative bias enhance nucleation, changing CH_4 concentration, and/or changing the deposition pressure in the growth step [11]. The two-step deposition process involves an initial rapid nucleation rate and subsequent high-quality growth. In condition of the high rate of secondary nucleation density that occurs during process is very high; the NCD films can be formed [12]. Such NCD films are grown with a significant renucleation rate and seem to form in an H-depleted deposition zone.

This material is reserved for educational use only, not allowed for commercial use.
Forbidden to modify the content, and cite the document when use.

Indeed, that reason for NCD film formation is major to vary of even the CVD reactor designs [13]. It is worthwhile for growth of NCD films from a traditional CH_4/H_2 gas mixture without the use of Argon gas or other special inert gas or high concentration of CH_4. Therefore, the two-step process that uses different CH_4 concentrations between the two steps is an interesting process.

In this dissertation, I investigated enhancement of the two-step deposition process by changing CH_4 concentration on morphology, structure, and optical properties of the deposited films. Three film samples were prepared by the purpose-built MPECVD reactor. Two of them were prepared by the single-step process with CH_4 concentrations of 0.9% and 2.0%. One of them was prepared by the two-step process. The effect of the two-step deposition process on morphology, structure, and optical properties of the deposited film will be discussed.

5.3.1 Design of Experiment

A gas mixture of CH_4 and H_2 was employed as reactant gases. Mirror-polished and B-doped Si(100) wafers were used as substrates. A pretreatment of the substrate surfaces was done by mechanical polishing with slurry of 0-1/2 μm diamond powder with *iso*-propanal for 1 h. Such the pretreatment method is useful to increase the surface energy and better the nucleation density. Before the beginning of the deposition, the substrate surface was *in situ* cleaned by H_2 plasma for 20 min with a H_2 flow rate of 200 sccm. Then methane gas was introduced to begin the deposition. Mass flow controllers controlled the gas flow rates.

The deposition was performed to grow three film samples. Two of three samples were carried out by the single-step deposition with CH_4 concentrations of 0.9% and 2.0%. One was carried out by the two-step deposition with changing CH_4 concentration. The CH_4 concentration was changed from 0.9% for the first step (nucleation step) to 2.0% for the second step (growth step). The process time was 12 min for the first step and 6 h for the second step. All deposited films were prepared under a total gas flow rate of 200 sccm, a reactor pressure of 5 kPa, and an absorbed microwave power of 750 W. The absorbed power was measured by the impedance analyzer. Under these operating conditions, the substrate temperature induced by microwave was between 830 and 850 $^{\circ}$C.

This material is reserved for educational use only, not allowed for commercial use.
Forbidden to modify the content, and cite the document when use.

5.3.2 Diamond Film Morphologies

The morphologies of all films deposited by the two-step process were imaged using FE-SEM as shown in **Figure 5.14**. All the deposited films consisted of grain clusters with individual grain sizes measuring less than 50 nm as determined by FE-SEM scale markers. The film grown by the single step with 0.9% CH_4 consisted of individual nodule-shape features and voids were clearly observed in the film. By increasing CH_4 concentration to 2.0%, the film surface became continuous and smooth as well as no void could be seen. Compared with the film grown by the single-step process with 0.9% CH_4, the film grown by the two-step process showed no voids at the interface and smaller diameter of individual nodules, indicating a higher nucleation density. The nodules coalesced to become more continuous.

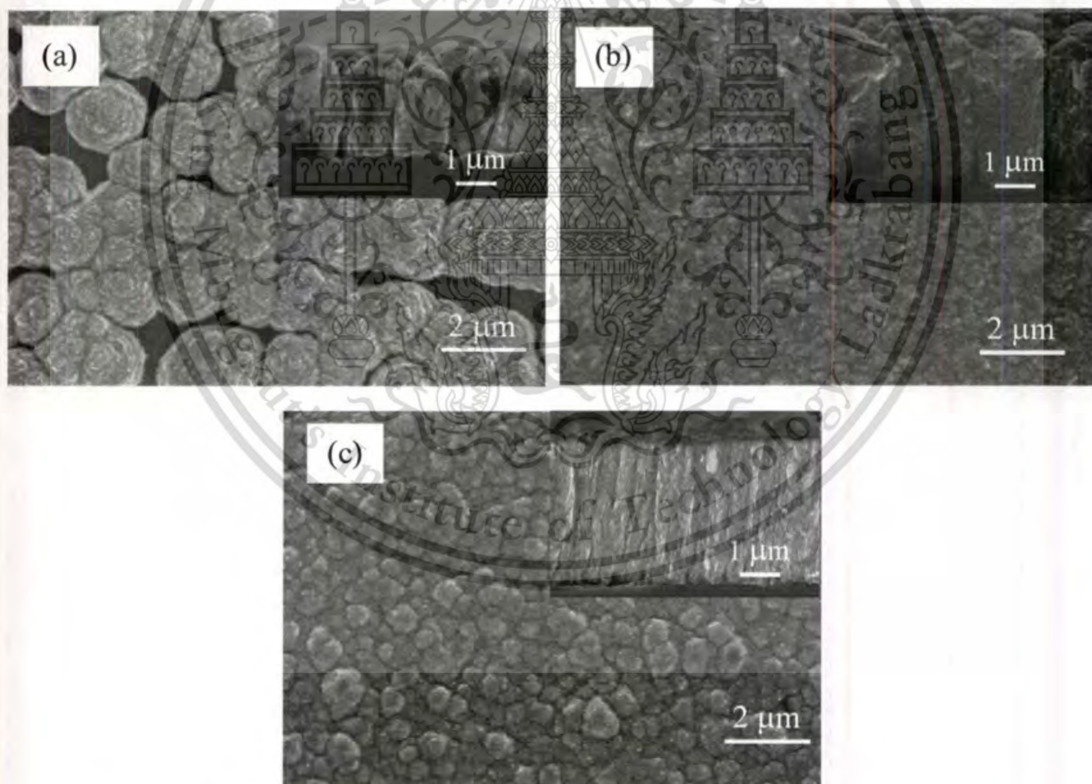

Figure 5.14 FE-SEM images and inset cross-section images of the films deposited by (a) single-step process with 0.9%CH_4, (b) single-step process with 2.0%CH_4, and (c) two-step process.

This material is reserved for educational use only, not allowed for commercial use.
Forbidden to modify the content, and cite the document when use.

The film thicknesses were evaluated from cross-section images and lateral structures of the films, shown in insets of **Figure 5.14**, present the grain structure of the films. The nodules of the film grown by the single-step process with 0.9% CH_4 were a height of 2.59 μm and their structures were grainy. For 2.0% CH_4, the film thickness was 4.72 μm and its structure was also grainy. Unlike those of the films grown by the single-step process, the grains of the film grown by the two-step process were now vertically aligned. The vertical grains are similar to the columnar growth seen for microcrystalline diamond, and which can sometimes be seen on a nanoscale in NCD film cross-section, as reported by P.W. May *et al.* [14]. Compared with the single-step process with 0.9% CH_4, the two-step process increased the film thickness. The thickness increased from 2.59 to 3.48 μm. The faster deposition kinetics of NCD films results in the formation of much thicker NCD films as well. The high CH_4 concentration promotes a fraction of reactive surface radical sites, both of monoradical sites and in particular biradical sites. The growth rate is determined by reactions between precursors and growth surfaces. Consequently, the high CH_4 concentration for both first and second steps induces the growth rate to more increase. However, the promoted biradical sites increases a renucleation process encouraging non-diamond content in the film structure that will be seen in the next.

5.3.3 Non-diamond Carbon Content by Raman Spectroscopy

Raman spectra of the films were deconvoluted after baseline subtraction using three fitting functions, i.e. Gaussian for the bands at 1140, 1250 and 1480 cm^{-1}, Lorentzian for the bands at 1332 and 1350 cm^{-1}, and Breit-Wigner-Fano (BWF) for the band at 1560 cm^{-1}, as shown in **Figure 5.15**. These bands are typically found in NCD film spectra [15] that exhibit a small diamond peak (1332 cm^{-1}) and several non-diamond phase contributions: graphite D and G bands (1350 and 1560 cm^{-1}) and trans-polyacetylene bands (1140 and 1480 cm^{-1}), trapped at nanograin boundaries. In addition, a broad component at around 1200-1250 cm^{-1} arises from a broadened vibration density of states (VDOS) contributions for small diamond grains.

This material is reserved for educational use only, not allowed for commercial use.
Forbidden to modify the content, and cite the document when use.

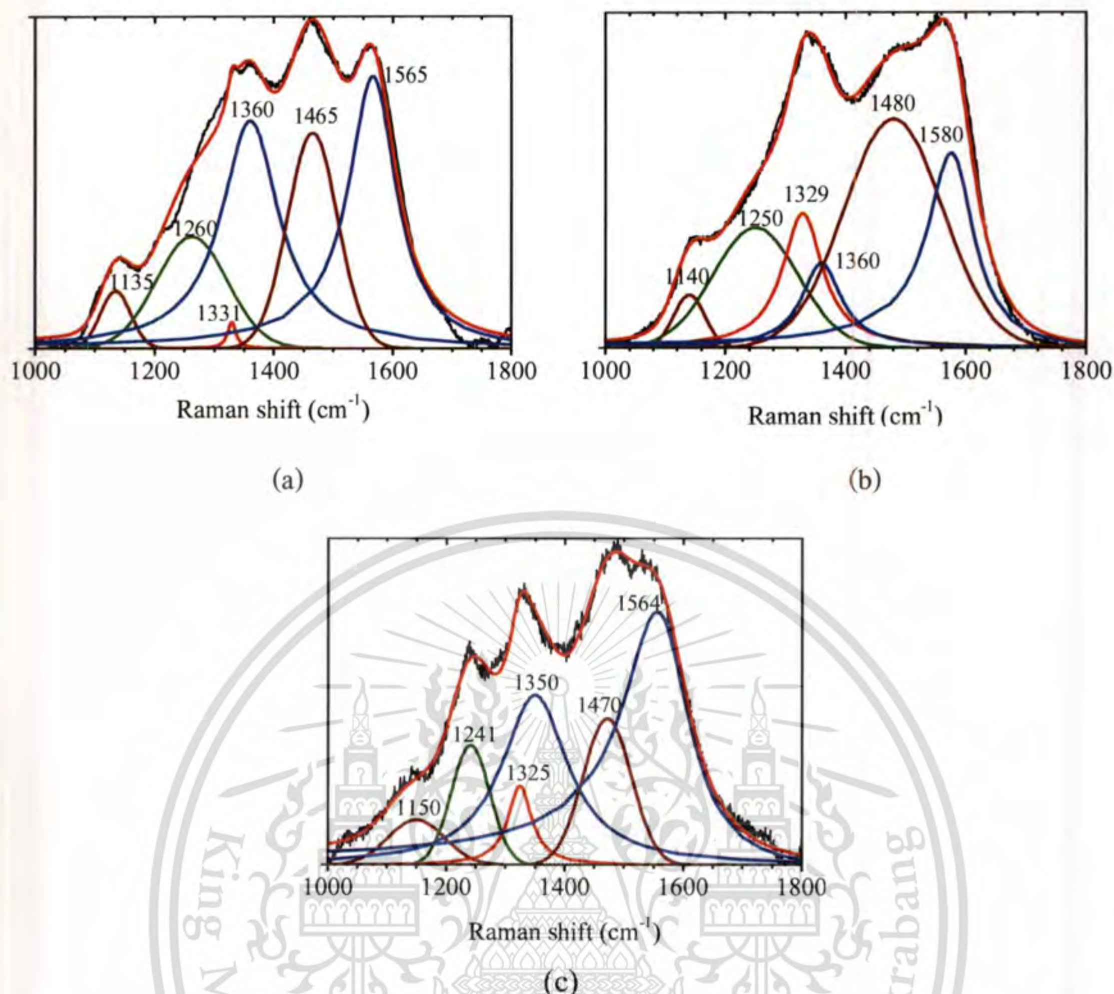

Figure 5.15 Raman spectra with raw data and various fit components of the deposited films after subtraction of the photoluminescence background: (a) single-step process with 0.9%CH_4, (b) single-step process with 2.0%CH_4, and (c) two-step process.

The shape of Raman spectra is strong affected by diamond grain size and by hydrogen atom concentration within the film. For single-step process, when CH_4 concentration increased from 0.9% to 2.0%, the diamond peak shifts from 1331 to 1329 cm^{-1} but its linewidth increased from 17 to 81 cm^{-1}. This behavior shows the crystallite size of diamond became smaller but the film became more graphitic. However, *trans*-polyacetylene band for the film grown at 0.9%CH_4 is more significant than that for the film grown at 2.0%CH_4. The greater of significance for *trans*-polyacetylene is a result of the higher amount of hydrogen incorporated in the films. For the film grown by the two-step process, the diamond peak shifted to 1325 cm^{-1}with only a 40 cm^{-1}

This material is reserved for educational use only, not allowed for commercial use.
Forbidden to modify the content, and cite the document when use.

linewidth. This shifting peak is due to the reductions in crystallite size [16]. The 1250 cm^{-1} band confirmed vibration density of state (VDOS) contributions to nanodiamond grains.

Another important of Raman spectra of diamond films is the significant shift in the G peak. The G-peak position shifted to higher frequencies as a result of the higher non-diamond carbon in the film structures [17]. For the single-step process, the G-peak position shifted from 1565 to 1580 $cm^{-1}$when CH_4 concentration increases from 0.9% to 2.0%. The film grown by the two-step process showed the G-peak position identical to that of the film grown by the single-step process with 0.9% CH_4. This suggested that the two-step process was changed feature co-deposition of non-diamond carbon along with diamond carbon.

5.3.4 Optical Properties via White-light Reflectometer

The optical properties of the NCD films were also investigated by white light reflectometry. The refractive index n was calculated from the reflectance spectra using the interference fringes as shown in **Figure 5.16**. The reflectance spectra of the film grown by the single-step process with 2.0%CH_4 show no obvious interference fringes. This behavior is due to too high content of non-diamond carbon incorporated in the film. The lowering of the refractive index for the films as compared with the single crystalline diamond (2.41) is due to the presence of the non-diamond carbon matrix. However, optical reflection by the films is governed not only by the film composition (which determines the optical constant of the film) but also by the surface roughness [18]. The greater surface roughness of the film promotes a higher light scattering and in turns a lower light reflectance. This result corresponds to the FE-SEM images.

This material is reserved for educational use only, not allowed for commercial use.
Forbidden to modify the content, and cite the document when use.

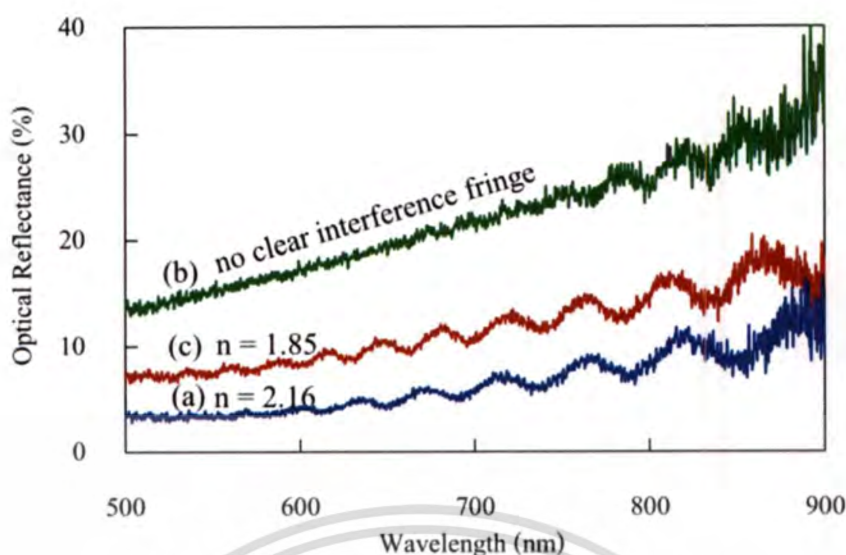

Figure 5.16 The reflectance spectra of the films deposited by (a) single step with 0.9% CH_4, (b) single step with 2.0% CH_4, and (c) two-step process with changing CH_4 concentration.

5.3.5 Plasma Impedance and Plasma Species

The plasma acts as an electrical load of the microwave circuit; therefore, changing of its physical and chemical properties becomes appearing as those of plasma impedance. In other words, the plasma impedance has associated with the chemical-process mechanism occurring in a gas-phase environment to produce the precursor of the growth.

The normalized electron density and temperature, which were extracted from plasma impedance, versus deposition time for each step process are shown in **Figure 5.17**. Although the normalized electron densities for each deposition process were got close together by controlling impedance of the plasma, the normalized electron temperatures were not. The plasma properties related to the emission ratios of C_2(d-a) to Hβ, shown in **Figure 5.18**, and CH(A) to Hβ, shown in **Figure 5.19**.

This material is reserved for educational use only, not allowed for commercial use.
Forbidden to modify the content, and cite the document when use.

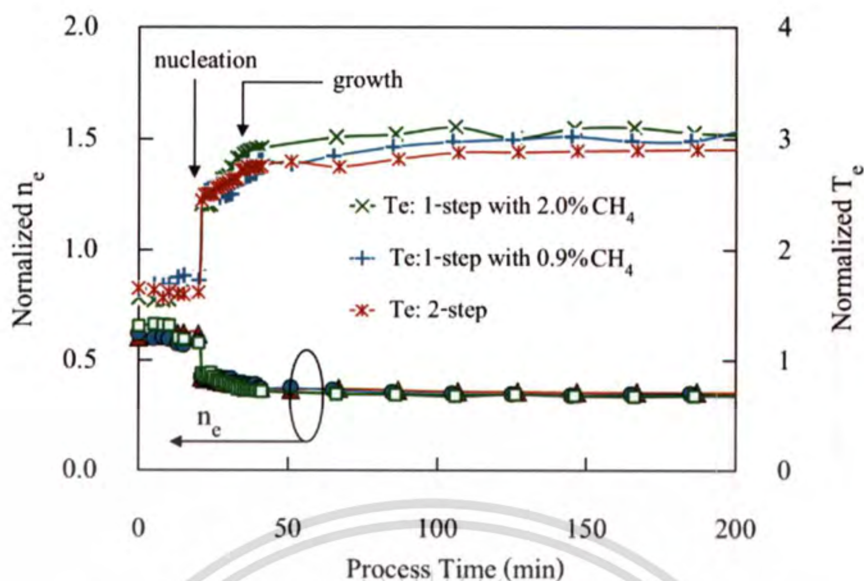

Figure 5.17 Normalized electron densities and electron temperatures versus process time for 2.0% CH_4 single-step, 0.9% CH_4 single-step and two-step deposition processes.

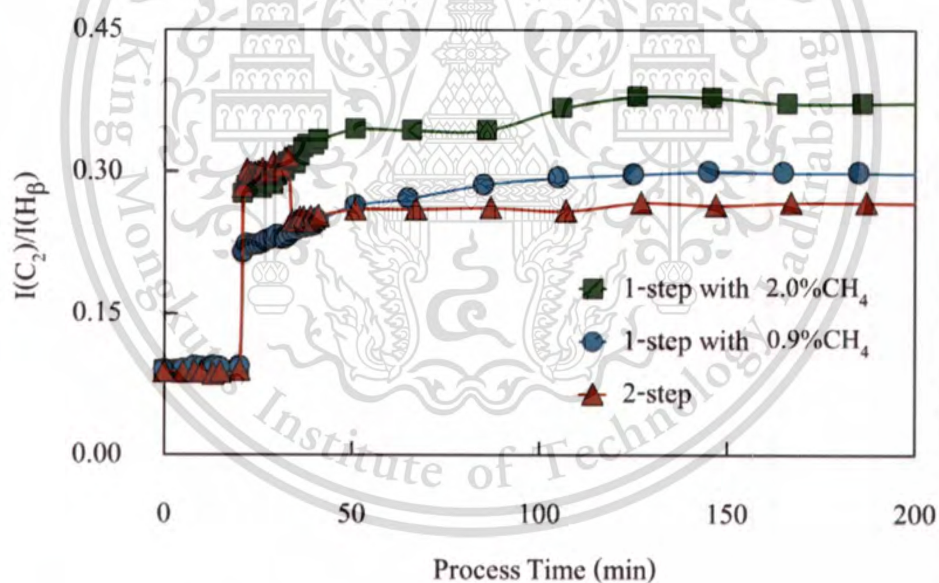

Figure 5.18 Emission intensities of C_2(d-a) to H_β versus process time for single-step and two-step approach deposition processes.

This material is reserved for educational use only, not allowed for commercial use.
Forbidden to modify the content, and cite the document when use.

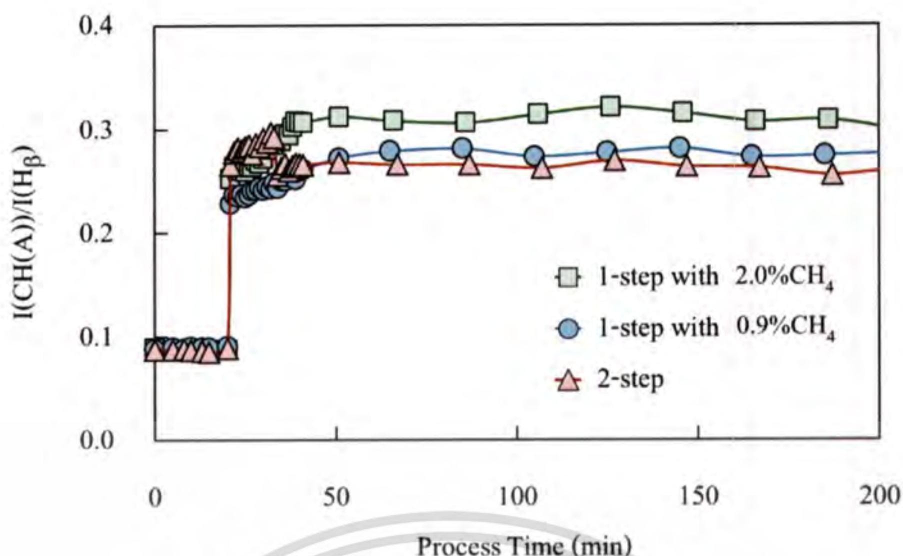

Figure 5.19 Emission intensities of CH(A) to H_β versus process time for single-step and two-step approach deposition processes.

The plasma diagnoses by OES and PIM (plasma impedance measurements) showed gas-phase species as well as electron density and temperature related to kinetics of NCD film formation. In addition to the electron density and amount of gas precursor, electron temperature also played a role in the chemical processes occurring in the plasma. The incorporation of gas-phase reactions, involving H abstraction to form surface sites and the subsequent reactions of these site with H and hydrocarbon radicals, sever to alter electron energy distribution function (EEDF) as well as the gas composition on the growth surface.

On the one hand, the greater of CH_4 concentration in nucleation step encouraged much more CH(A) and C_2(d-a) species related to H_β than its lowering. These species promoted a fraction of reactive surface radical sites, both of monoradical sites and in particular biradical sites. Although the growth rate of diamond films in the MPECVD reactor was determined by the values of concentrations of carbon-containing radicals and hydrogen atoms in the plasma. However, the greater of these surface sites induced the fast kinetics of the incorporation of gas-surface reactions. In the growth step, the lowering of the hydrocarbon species for the two-step process as compared with for the single-step with 0.9%CH_4 is due to this faster kinetics. In addition to the biradical sites, the greater of CH_4 concentration in the growth step also enhanced a rate of a renucleation process encouraging non-diamond content in the film structure.

This material is reserved for educational use only, not allowed for commercial use.
Forbidden to modify the content, and cite the document when use.

5.3.6 Summary

This experiment focused on the effect of the two-step deposition process on the morphology and compositions of the nanostructured diamond films. The two-step process was done by changing methane concentration. It consisted of a first step with 2.0% CH_4 and a second step with 0.9% CH_4. The higher CH_4 concentration for the first step encouraged nucleation density and the lower CH_4 concentration for the second step enhanced the quality of the films. For the single-step process with 0.9% CH_4, the film morphology showed individual nodules resulting in the low light reflectance. The enhanced diamond nucleation kinetics on the substrate surface with the two-step processes developed more uniform and much smoother diamond films as well as the higher light reflectance. Compared with the single-step process with 2.0%CH_4, the two-step process showed more enhancements of an increase in grain boundaries and a decrease in sp^2-bonded carbon content. These experimental results suggest that the two-step process leads to the fabrication of the NCD films with a large number of grain boundaries, a lowering of graphitic impurities, and obtaining strong adherent diamond coating. The nanocrystalline columnar-structured diamond film can be grown by the two-step process.

5.4 Surface Pretreatment on the Film Formation with Two-step Approach

It is well known that the surface energy of diamond is the highest among any known materials, which is about four times larger than that of Si [19]. So, the affinity between Si and diamond is rather weak, making the diamond film difficult to grow on the mirror-like Si surface. The deposition of a well adherent diamond coating is a great problem. Even under the two-step approach process with high CH_4 concentration in the nucleation step, the pretreatment of the substrates is indispensable.

5.4.1 Design of Experiment

The deposition was performed to grow three film samples on mirror-polished Si substrates. Each substrate was scratched by different methods: non-polishing, ultrasonic polishing, and manual polishing methods. All samples were carried out by the two-step approach process with

This material is reserved for educational use only, not allowed for commercial use.
Forbidden to modify the content, and cite the document when use.

2.0%CH_4 for the nucleation step and 0.9%CH_4 for growth step. The process time was 12 min for the nucleation step and 6 h for the growth step. The values of plasma impedance were also controlled. All deposited films were prepared under a total gas flow rate of 200 sccm and the absorbed microwave power of around 730 W. The reactor pressures were 5 and 2 kPa. The substrate temperature induced by microwave was 840 $^{\circ}$C under the pressure of 5 kPa and 870 $^{\circ}$C under the pressure of 2 kPa.

5.4.2 Diamond Films Formation at 5 kPa: FE-SEM and Raman Studies

A comparison of three NCD films grown on the surfaces that are pretreated by different surface-polishing methods at a reactor pressure of 5 kPa is shown in **Figure 5.20**. The topography of the NCD films was significantly modified by changing the pretreatment methods. After 6 h deposition, the continuous diamond thin films did not formed onto the mirror-polished and ultrasonic-polished surfaces, as shown in **Figure 5.20**(a) and (b). The isolated nodules with various sizes in diameter appeared on the both-type surfaces. The highest of isolated nodule on the mirror-polished surface was around only 1.82 μm and on the ultrasonic-polished surface around 3.31 μm. The film did not continuously cover the substrate but instead formed three-dimensional island. The film atoms more strongly bond to each other than to substrate; island growth (Volmer-Weber) occurs [20]. Volmer-Weber 3-D island growth is the mode of nucleation and growth of diamond films directly on non-diamond substrates owing to the highest surface energies of diamond among any known materials [19]. Unlike the NCD films on the mirror- and ultrasonic-polished surfaces, the NCD film on the manual-polished surface was almost continuous. In addition, **Figure 5.20**(c) shows top-view and cross-section FE-SEM images taken from the film deposited onto the substrate surface pretreated by mechanical polishing. The film thickness was 3.61 μm, resulting in an average growth rate of 0.60 μm/h. The increased surface energy due to surface pretreatment by manual polishing causes the film to continue forming and good adhesion of diamond films.

This material is reserved for educational use only, not allowed for commercial use.
Forbidden to modify the content, and cite the document when use.

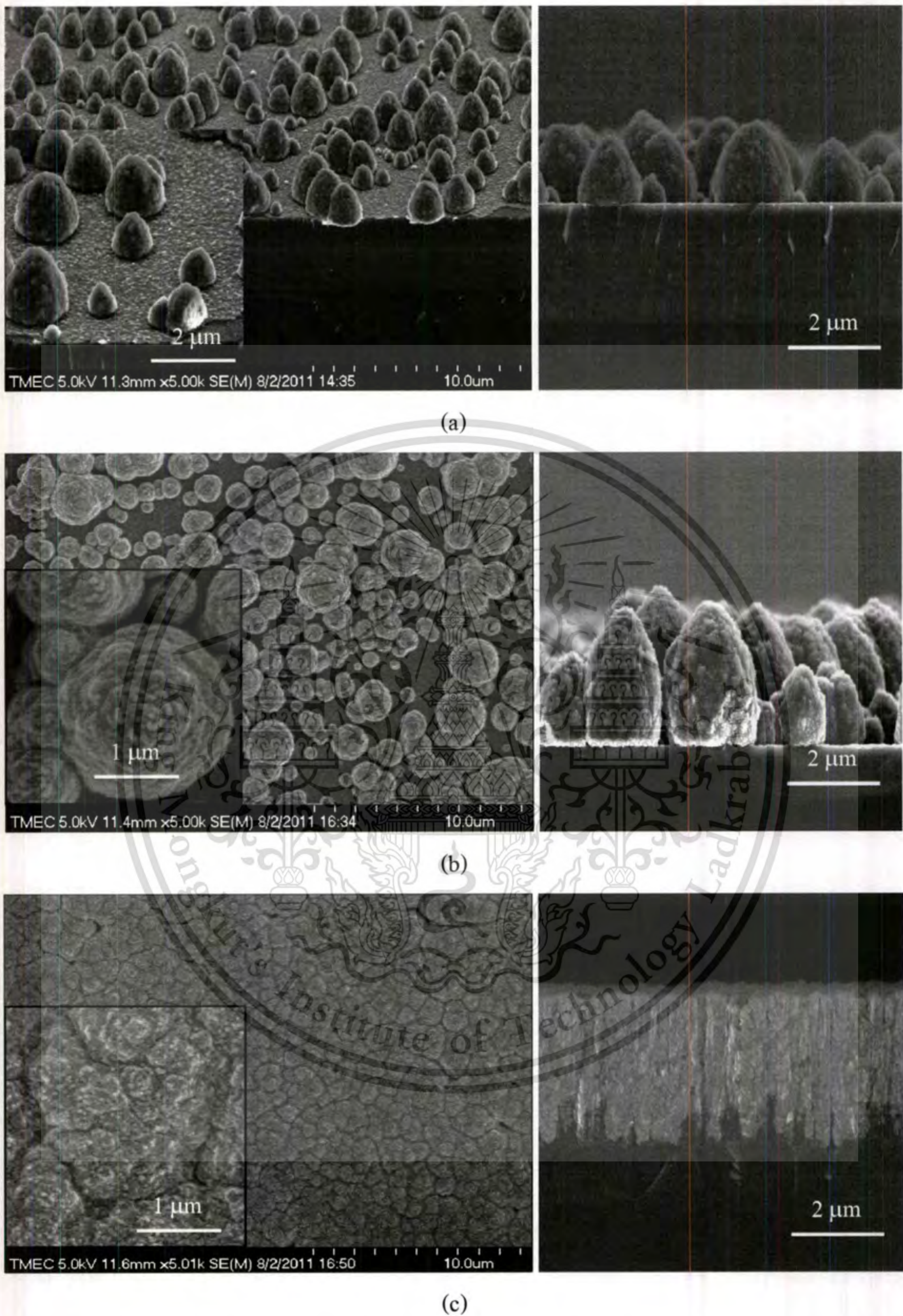

Figure 5.20 FE-SEM top-view and cross-section images of microstructure of the films deposited under a reactor pressure of 5 kPa and on the substrate surface pretreated by three polishing methods: (a) no pretreatement (mirror), (b) ultrasonic polishing, and (c) manual polishing.

This material is reserved for educational use only, not allowed for commercial use.
Forbidden to modify the content, and cite the document when use.

The cross-section images also present the grain structures of the films. The film grown on the manual-polished surface is vertically aligned, the vertical grains that are similar to the columnar growth seen for microcrystalline diamond, and which can sometimes be seen on a nanoscale in NCD film cross-sections, as reported by P.W. May *et al.* [14]. However, the films grown on mirror- and ultrasonic-polished surfaces showed their structures to be grainy.

Raman spectra of the films grown on the Si substrate surfaces pretreated with three polishing methods are shown in **Figure 5.21**. The Raman spectra were characterized by six signals labeled from 1 to 6 with increasing Raman shift. On the film deposited onto the mirror-polished Si substrate, only the second order signal from silicon substrate (1) appeared in the Raman spectrum owing to the limited surface coverage and relatively small quantities of the deposited diamond [21].

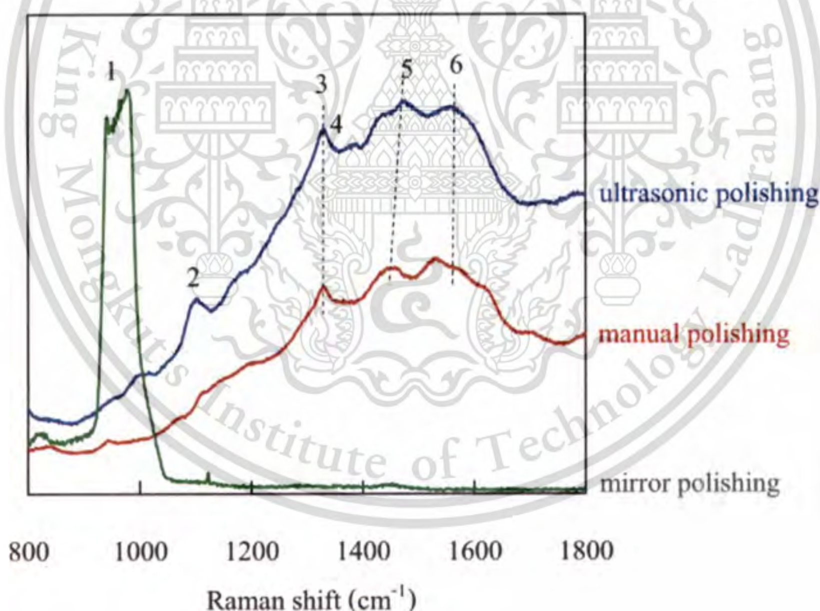

Figure 5.21 Raman spectra of NCD films deposited on surfaces pretreated with different pretreatment methods and under a reactor pressure of 5 kPa. The large feature around 900-1000 cm^{-1} is the second order from Si substrate.

The diamond peak (3) was centered at 1332 cm^{-1}. This peak in the spectra confirms that the films are diamond. The Raman signals corresponding to the so-called D-band (4) at 1350 cm^{-1} and G-band (6) at 1560 cm^{-1} of graphite were also observed. At around 1120 cm^{-1} (2) and 1480 cm^{-1}

This material is reserved for educational use only, not allowed for commercial use.
Forbidden to modify the content, and cite the document when use.

(5) signals relating to *trans*-polyactylene (t-PA) at the grain boundaries and surface can be observed. The t-PA band has always been accepted as the indicator of NCD films [22].

5.4.3 Diamond Film Formation at 2 kPa: FE-SEM and Raman Studies

The decreasing reactor pressure from 5 to 2 kPa resulted in morphology and atomic-bonding structure. FE-SEM top-view (left) and cross-section (right) images of the diamond films deposited on the substrate surfaces pretreated by three methods and under a reactor pressure of 2 kPa are shown in **Figure 5.22**. The reduced reactor pressure enhanced adhesion of the films on the surface. No void can be seen on the film deposited on the substrate pretreated by manual polishing, indicating a higher nucleation density. The nodules coalesce to become more continuous. In contrast to the film grown on the manual-polished substrate, the films grown on the mirror- and ultrasonic-polished substrates formed into island growth and voids appeared.

The cross-section images also present the grain structures of the films. Their structures were granular. The surface polishing method also influenced film thickness. Thicknesses were 2.10 μm for the film grown on the manual-polished substrate, 2.06 μm for that on the ultrasonic-polished substrate, and 1.60 μm for that on the mirror-polished substrate.

All films were also evaluated the atomic-bonding structure by Raman analysis, that Raman spectra are shown in **Figure 5.23**. The shape of Raman spectra is affected by diamond grain size and, therefore, composition in the films. The diamond peak was feebly seen in the spectrum of the film grown on the manual-polished substrate. Compared to the film grown on the manual-polished substrate, the films grown on the ultrasonic- and mirror-polished substrate did not show the diamond peak, that the peak was obscured by D-band. This behavior suggests that the diamond grain size become smaller and the composition of the films become more graphitic. In addition to the morphology of the films, different types of surface damage influence significantly the atomic-bonding structure.

This material is reserved for educational use only, not allowed for commercial use.
Forbidden to modify the content, and cite the document when use.

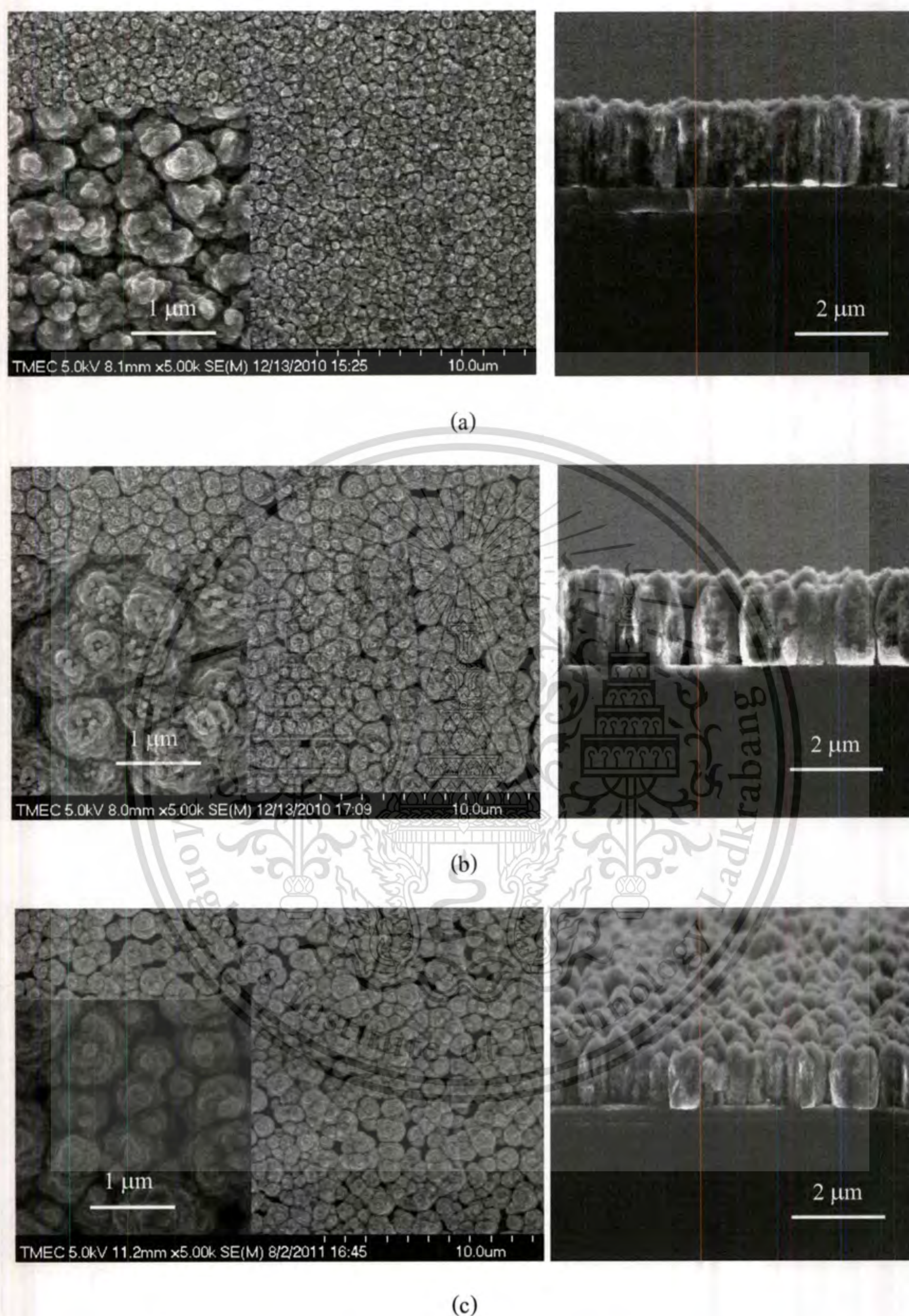

Figure 5.22 FE-SEM top-view and cross-section images of microstructure of the films deposited under a reactor pressure of 2 kPa and on the substrate surface pretreated with three polishing methods: (a) no pretreatement (mirror), (b) ultrasonic polishing, and (c) manual polishing.

This material is reserved for educational use only, not allowed for commercial use.
Forbidden to modify the content, and cite the document when use.

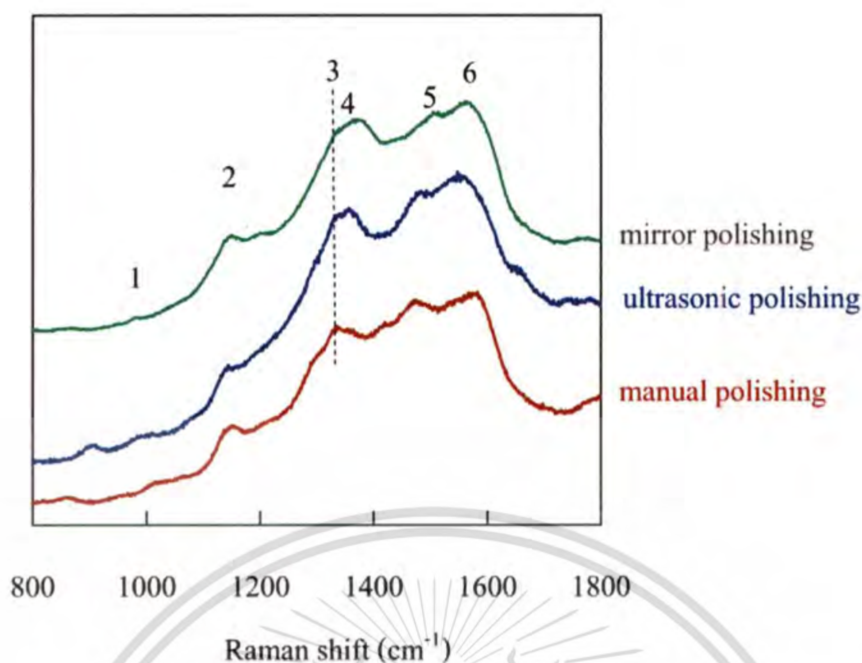

Figure 5.23 Raman spectra of NCD films deposited on surfaces pretreated with different pretreatment methods and under a reactor pressure of 2 kPa.

5.4.4 Summary

This experiment investigated the effect of surface polishing methods on the morphology, atomic-bonding structure, and adhesion of the diamond films. The Si substrates were polished by three methods: manual, ultrasonic, and mirror polishing. As previously mentioned in Section 5.1, such different polishing procedures induced rather different types of surface damage on which the operating nucleation modes differed from each other, leading to the different morphology and atomic-bonding structure. The manual polishing caused the sharp, narrow, deep, and long scratches to occur on the surface; whereas the ultrasonic polishing caused dent scratches. This experiment revealed that the sharp, deep, and long scratches favored more the diamond nucleation than non-diamond or carbon amorphous and that the dent scratches induce carbon amorphous to form initially. Furthermore, this experiment also presented that carbon species were supposed to be lowered when pressure increased, which explained the diminished diamond nucleation at higher deposition pressure.

This material is reserved for educational use only, not allowed for commercial use.
Forbidden to modify the content, and cite the document when use.

5.5 Pressure-dependent Nanocrystalline Diamond Films

A number of depositions [23] have been used to deposit NCD films. Each deposition technique provides particular forms of the NCD films, differing in terms of diamond particle size, grain boundary nature, amorphous or graphitic matrix, and morphological, structural and optical properties. The film properties also depend on the deposition parameters, resulting in different type of NCD films. Haitao Ye *et al.* [1] have been conducted orthogonal experiments to optimize the processing conditions. These orthogonal experiments predict that the total pressure is the most significant parameter. A few publication reports effect of pressure on NCD films grown by the MPECVD technique, although this technique is one of the most popular techniques for preparing NCD films.

In this work, I also focused on the influence of reactor pressure on NCD films prepared by a MPECVD technique in CH_4/H_2 gas mixture with a two-step deposition process. The two-step process is necessary for diamond film deposition because the energy for the diamond nucleation is not the same as for the diamond growth. This two-step deposition applied for better surface roughness of the films and nucleation density was performed with the higher concentration of CH_4 in a CH_4/H_2 gas mixture for the nucleation step than for the growth step. The NCD films obtained under different reactor pressures were characterized by FE-SEM, Raman spectroscopy, and white-light reflectometry. In addition, gas-phase species in the plasma were monitored by an optical emission spectrometer. Plasma impedance was monitored and measured by an impedance analyzer. The measured plasma-impedance has provided electron density in the plasma. Correlation between NCD films grown and gas-phase species, including electron density, present in the plasma will be discussed.

5.5.1 Design of Experiment

The p-type mirror-polished Si(100) wafer was used as a substrate. A pretreatment of the substrate surface was performed by mechanical polishing with a 0-0.5 μm diamond powder suspended in isopropanol for 1 h. Before the deposition was begun, H_2 plasma was introduced to clean the substrate surface for 20 min with a flow rate of 200 sccm. Then CH_4 gas was introduced

This material is reserved for educational use only, not allowed for commercial use.

Forbidden to modify the content, and cite the document when use.

to begin the deposition process. The deposition with the two-step approach was carried out under various reactor pressures. The pressures were 25, 9, 5, 2, and 1 kPa The two-step deposition process consisted of a nucleation step and a growth step. It was performed by decreasing CH_4 concentration from 2.0% for the nucleation step to 0.9% for the growth step. The process time was 15 min for the nucleation step and 6 h for the growth step. The total gas flow rate was 200 sccm. The reactor pressure and flow rate can be controlled independently. The absorbed microwave power measured by the impedance analyzer was around 720 W. Under these operating conditions, the substrate temperature was achieved by microwave induction around 850 $^{\circ}$C. The substrate was placed on a quartz holder and immersed in the plasma.

5.5.2 FE-SEM Analysis

FE-SEM images permit detailed observation of NCD film morphologies as a function of the reactor pressure ranging from 1 to 25 kPa, as shown in **Figure 5.24**. The SEM cross-section images show in insets of **Figure 5.24**. The crystallite size was estimated by inspecting SEM images. All films have crystallite size < 50 nm. The surface morphologies of the films grown at 1 and 2 kPa were rougher than that of the films grown at other pressures. These resulted from the higher kinetic energy of species arriving at the growth surface. The morphologies of the films grown at 1 and 2 kPa are similar to those of UNCD films as reported by May and Mankelevich [24]. They also show that the surface morphologies for UNCD films prepared by the MPCVD technique are much rougher than that for UNCD films prepared by the hot filament-CVD technique.

The growth rates plotted as a function of the pressure are shown in **Figure 5.25**. The growth rate was calculated by the film thickness divided by the growth time. The curve of the growth rates can be divided into three parts. The growth rates rapidly decreased from 370 to 320 nm/h when the reactor pressure increased from 1 to 2 kPa. After the further increase in the pressure, the growth rate rapidly increased to 460 nm/h for 9 kPa, and then it gradually decreased to 450 nm/h for 25 kPa.

This material is reserved for educational use only, not allowed for commercial use.
Forbidden to modify the content, and cite the document when use.

Figure 5.24 FE-SEM images of NCD films grown on Si substrates under various pressures: (a) 25 kPa, (b) 9 kPa, (c) 5 kPa, (d) 2 kPa, and (e) 1 kPa and cross-section images.

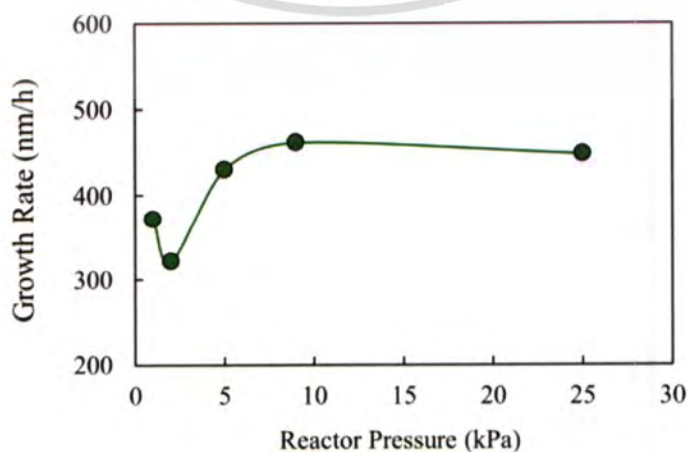

Figure 5.25 Growth rate of NCD films as a function of the reactor pressure.

This material is reserved for educational use only, not allowed for commercial use.
Forbidden to modify the content, and cite the document when use.

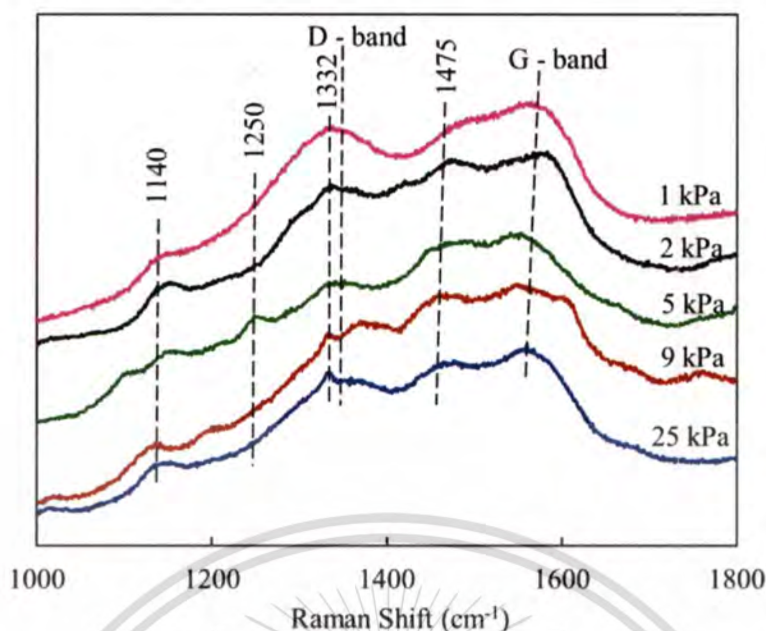

Figure 5.26 Raman spectra with the photoluminescence background of NCD films under various pressures: 1, 2, 5, 9, and 25 kPa.

5.5.3 Raman Spectroscopy

The atomic-bonding structures of the films were evaluated by Raman analysis. Raman spectra with the photoluminescence background are shown in **Figure 5.26.** They are composed of five features [25]. These features exhibit a diamond peak at 1332 cm^{-1} and several non-diamond phase contributions: disordered-graphite D-band at 1350 cm^{-1}, graphite G-band around 1560 cm^{-1} and *trans*-polyacetylene (t-PA) band around 1140 and 1475 cm^{-1}. The appearance of the t-PA band has always been accepted as the indicator of NCD films [22]. In addition, the broad peak at 1250 cm^{-1}, which is observed in only the film grown at 5 kPa, arises from a broadened vibration density of states of small diamond grains [15].

Raman spectra show drastic changes with decreasing pressure. The 1332 cm^{-1} peak became weaker while the D peak became stronger and overlapped the 1332 cm^{-1} peak. The D peak is related to the small-sized graphitic domains. The G-peak position shifted from 1560 to 1580 cm^{-1}. The weaker intensity of diamond peak and the shift of G peak to higher frequencies suggested the diamond grain size decreases, and grain boundary increases; thus resulting in sp^2 in detriment of sp^3 phase increment with decreasing pressure [26]. In addition, the broad peak at 1250 cm^{-1} was observed in only the film grown at 5 kPa. The appearance of this peak implied that the film

This material is reserved for educational use only, not allowed for commercial use.
Forbidden to modify the content, and cite the document when use.

formation begins transition from NCD to UNCD phase at this pressure. Moreover, Raman spectrum with no background (not shown here) of the film grown at 1 kPa showed more intense D band than G band, and the *trans*-polyacetylene band showed up only as a small shoulder. This spectrum can be considered as fingerprints for the fine diamond grained structure, related as UNCD [26].

5.5.4 Optical Properties via Reflectometry

The reflectance spectra of the films grown at pressures of 25, 9, and 5 kPa are shown in **Figure 5.27**. However, the reflectance spectra of the films grown at 2 and 1 kPa were obstructed due to highly light absorption. The highly light absorption has been explained by the nanocomposite nature of the films, and it is also the characteristic of UNCD films. As reported by Buijnsters *et al* [27], UNCD is a highly light absorbing material because it is synthesized with a high renucleation rate and composed of a relatively high fraction of sp^2-bonded carbon connecting the grains.

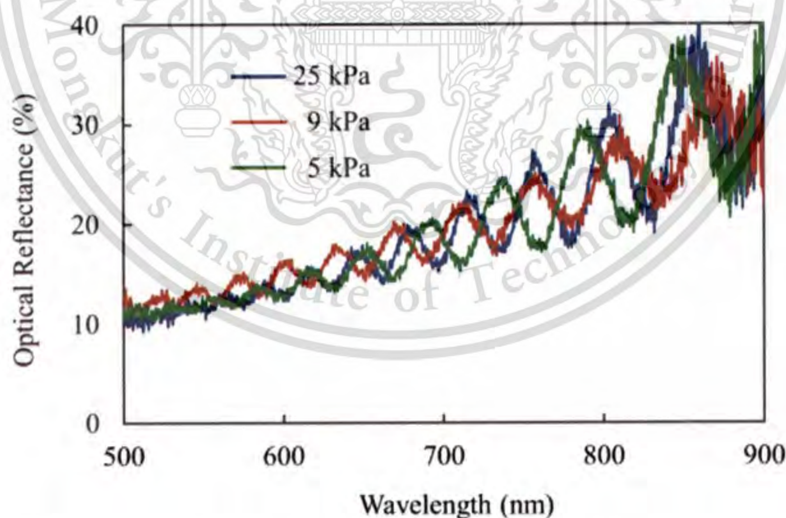

Figure 5.27 Reflectance spectra of the NCD films grown under various reactor pressures: (a) 25 kPa, (b) 9 kPa, and (c) 5 kPa.

The refractive indices of the NCD films were calculated from the reflectance spectra with the interference fringes as shown in **Figure 5.27**. They were 2.38 for 25 kPa, 2.21 for 9 kPa, and 2.16 for 5 kPa, increasing with reactor pressure. The refractive index n of those three films gets

This material is reserved for educational use only, not allowed for commercial use.
Forbidden to modify the content, and cite the document when use.

close to that of diamond (2.41) and quite different from that of graphite (n=1.37) [15]. The presence of the sp^2-bonded carbon matrix lowers the refractive index of the NCD films.

5.5.5 Measurements of Plasma Impedance

The plasma acts as an electrical load of the microwave circuit. The changing of its physical and chemical properties becomes appearing as those of plasma impedance. The plasma impedance normalized by an impedance value of the waveguide was measured by the impedance analyzer. The normalized plasma impedance Z_p and electron density n_e in the plasma are related as [28] shown in Equation (2.18). The electron density was determined from this equation and then normalized by n_e of H_2 plasma at a pressure of 1 kPa to become the relative change of n_e. Therefore, the relative changes of n_e were used instead for this work. Those relative changes of n_e as a function of the reactor pressure in each step-deposition process are showed in **Figure 5.28**.

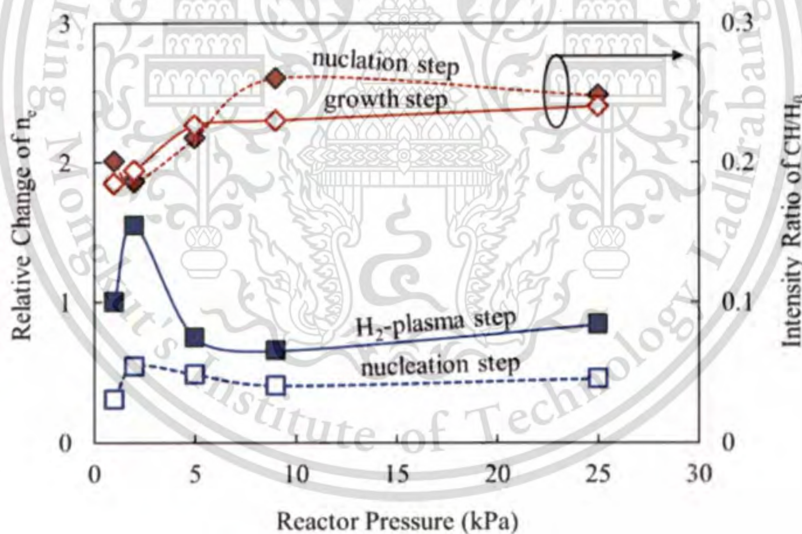

Figure 5.28 Relative change of n_e and ratios of optical emission intensity of CH(A-X) to $H\beta$, $I(CH)/I(H\beta)$, as a function of the reactor pressure.

The relative changes of n_e were identical for the nucleation and growth steps. The electron density can be a scale of atomic-H concentration in the plasma due to the breaking-down process of H_2 molecules through an inelastic collision with the energetic electrons. Our measured results also confirm that the emission intensity of H atom changes in a parabolic manner to n_e. The

This material is reserved for educational use only, not allowed for commercial use.
Forbidden to modify the content, and cite the document when use.

emission intensity of gas-phase species measured by optical emission spectroscopy (OES) directly relates to the density of the species.

Regarding the relative changes of n_e as a function of the reactor pressure shown in **Figure 5.28**, it can be speculated that trend of atomic-H concentration increased as the pressure increased from 1 to 2 kPa. After 2 kPa, the trend rapidly decreased and then gradually increased at the reactor pressure higher than 9 kPa. In contrast to that at 25 kPa, atomic-H concentration at 1 kPa decreased due to too low gas-molecule density. For the CVD growth of diamond films, H atoms (H radicals) in the plasma are consumed by two main reactions [24] . The first one is the dehydrogenation-dissociation reaction to produce the precursor of diamond growth. This reaction caused H radicals to reduce when CH_4 gas was added into H_2 plasma, shown in **Figure 5.28**. The second one is gas-surface reactions, involving H abstraction to form surface sites and subsequent reactions of these sites with H radicals. According to Langmuir isotherm [29], the coverage fraction of H radicals at high pressure is higher than at low pressure. However, it also is affected by concentration of the radicals. Indeed, n_e is not only proportional to the residue of H radical from these reactions but also in inverse relation to the coverage fraction of H radicals.

Figure 5.28 also shows ratios of *in situ* optical emission intensities of CH (431.0 nm) to Hβ (486.1 nm), I(CH)/I(Hβ), as a function of the pressure. CH_3 radical that plays a role in the growth mechanism can be inferred from CH radical. Although OES cannot provide quantitative information, the emission intensities are still carried out to confirm the relative changes of gas-phase species in the plasma [30]. As shown in the figure, I(CH)/I(Hβ) in nucleation step was in inverse relation to the relative changes of n_e in H_2-plasma step; as the H-radical residue, mentioned in the previous section, was not. These results indicated that the lower initial-residue of H radicals in the plasma increases CH_3 density in nucleation step.

5.5.6 NCD Films and Gas-phase Species

Considering the results as depicted in **Figure 5.25** and **Figure 5.28**, the growth rate as function of the reactor pressure changed in an inverse manner to the relative change of n_e for H_2-plasma step. On the other hand, it changed on the same manner to the coverage fraction of H

This material is reserved for educational use only, not allowed for commercial use.

Forbidden to modify the content, and cite the document when use.

radical on the growth surface. This implied that the initial coverage-fraction promotes the diamond growth kinetics and demotes the renucleation rate. In addition, the growth rate also changed in the same manner to the I(CH)/I(Hβ) ratio for the nucleation step. Trend of this ratio can be indicative of trend of amount of the surface-radical sites for carbon containing radical to absorb. These amounts proportionally depend on the initial coverage fraction of atomic H on the surface.

Raman spectra, as shown in **Figure 5.26**, also related to the intensity ratio, as shown in **Figure 5.28**. The sp^3-bonded carbon content and diamond grain size of the NCD films directly related with I(CH)/I(Hβ) ratio in the growth step. This result confirmed that C_1 hydrocarbon radicals (CH_x radicals) are precursors of sp^3 diamond phase for the growth. The changing of these gas-phase species in each step-deposition process can explain pressure dependence of the growth rate, sp^2 and sp^3 carbon content of the subsequent film, and the probability of a renucleation event occurrence.

5.5.7 Summary

This experiment focused on the influence of reactor pressure on the morphology, growth rate, grain size, atomic-bonding structure, and optical properties of NCD films as well as the gas-phase species, including electron density, in plasma. The NCD films were prepared by a MPECVD technique with CH_4/H_2 precursor mixture and two-step approach. Before the beginning of deposition, the Si(100) substrate surface was also cleaned by *in situ* H_2-plasma. The deposition for the films was performed under reactor pressures of 1, 2, 5, 9, and 25 kPa. As the reactor pressure increased, the surface smoothness and diamond grain size of the films increased while amorphous carbon content decreased. The pressure influenced the refractive index of the NCD films: 2.38 for 25 kPa, 2.21 for 9 kPa and 2.16 for 5 kPa. However, the NCD films grown under 1 and 2 kPa provided highly light absorption. The growth rates rapidly decreased from 370 to 320 nm/h when the reactor pressure increased from 1 to 2 kPa. As the pressure increased to 9 kPa, the growth rate rapidly increased to 460 nm/h and then decreased with a much slow rate after 9 kPa.

This material is reserved for educational use only, not allowed for commercial use.
Forbidden to modify the content, and cite the document when use.

Correlation between materials grown and gas-phase species present in the plasma is important to identify the species driving the process mechanism. The growth rates were in inverse proportion to the n_e relative changes extracted from measurements of plasma impedance in the H_2-plasma step. However, they directly related to the I(CH)/I(Hβ) ratio in the nucleation step. These behaviors revealed that the surface-coverage fraction of H radicals occurring during the H_2-plasma cleaning step and the density ratio of CH_x radical to H radical for the nucleation step were important to determine the growth rate of the film deposition. Furthermore, the diamond grain size and sp^3 carbon content in the films strongly depended on the I(CH)/I(Hβ) ratio for the growth step. This result confirmed that C_1 hydrocarbon radicals were precursors of sp^3 diamond phase for the growth of diamond.

The reactor pressure influenced not only concentration of the decomposed radicals but also the coverage fraction of the radicals on the growth surface. The concentration of the radicals and the surface-coverage fraction of radicals manipulated diamond growth kinetics. Generally, the concentration of the decomposed radicals, including H and CH_x radicals, are proportional to the reactor pressure. Those radicals increased not only growth rate but also sp^3 carbon content in the films. However, only increasing CH_x radicals in the gas led to more grain boundaries, sp^2 carbon content, and phase transition unless the atomic-H density increased as well.

5.6 Plasma Impedance Tuning Effect on Nanostructured Diamond Films

In MPECVD apparatus, one of the important process parameters leading to encounter a problem of accurate control of the plasma process is an impedance tuning. Typical MPECVD apparatus consists of only matching system (microwave stub tuner). The MPECVD apparatus, which consists of both an impedance analyzer and matching system, can monitor and manipulate plasma impedance simultaneously. The plasma acts as an electrical load of the microwave circuit. The changing of its physical and chemical properties becomes appearing as those of plasma impedance. The plasma impedance has influenced chemical-process mechanisms occurring in a gas-phase environment to produce precursors for the film growth. Therefore, the monitor and manipulation of the plasma impedance can give an insight in further understanding and

This material is reserved for educational use only, not allowed for commercial use.

Forbidden to modify the content, and cite the document when use.

controlling the growth process. As reported by Muller *et al.* [31], plasma-working conditions affect plasma impedance associating with electron density in the plasma. In addition, Hosomi *et al.* [32, 33] reported the effect of the xenon addition into CH_4-H_2 plasma on plasma impedance and diamond film growth. They suggested the xenon addition increases electron density promoting atomic-H and CH_3 radical in the gas phase.

This work focuses on influence of impedance of the plasma on the morphology and atomic-bond structure of NCD films prepared by a MPECVD technique. We found experimentally that when all process parameters, including absorbed microwave power, were keeping constant, the films grown with two values of plasma impedance differed in formation and optical properties. These two values of plasma impedance can be realized by the matching system that is a three-stub tuner immersed in the waveguide and were found to confer on the same stability to the plasma. The films were examined by FE-SEM, Raman spectroscopy, and white light reflectometry. Gas-phase species in the plasma was monitored by OES and electron density was examined from plasma impedance measured by an impedance analyzer. The effect of plasma impedance on plasma chemistry as well as morphology and atomic-bonding structure of the films is discussed. To our knowledge the study, which covers the morphology and structure of the films as well as plasma chemistry dependence of diamond film growth on plasma impedance changed by matching system, is not present in the literature. The results of this present are expected to contribute the science and technology of diamond growth with MPECVD technique.

5.6.1 Design of Experiment

The H_2 plasma was carried out for offering the first insight into correlation between Z_p and n_e. It was operated with a H_2 mass flow rate of 200 sccm and a reactor pressure of 5 kPa. Its plasma impedance and optical emission intensities were measured under various microwave power. The impedance of the mixture of 0.9%CH_4 in H_2 plasma as a function of microwave power was also investigated.

Two NCD films were grown under two values of plasma impedance while all other conditions were kept constant. The two values of plasma impedance induced two plasma modes:

This material is reserved for educational use only, not allowed for commercial use.

Forbidden to modify the content, and cite the document when use.

a low electron density and a high electron density. The plasma impedance was controlled via insertion depths of a three-stub tuner. The films were deposited on mirror-polished and B-doped Si(100) substrates from CH_4-H_2 gas mixture. The pre-treatment of the substrates was prepared by mechanically polishing the surface using 0-1/2 μm diamond powder/*iso*-propanal solution for 1 h. The substrates were further *in situ* cleaned by H_2 plasma for 20 min before the nucleation step was begun. The nanodiamond films were grown by the two-step approach with decreasing methane concentration from 2.0% for the nucleation step to 0.9% for the growth step. The process time for the nucleation step was 12 min and that for the growth step 6 h. The absorbed microwave power was 740 - 760 W, a reactor pressure was 5 kPa, and a total gas flow rate was 200 sccm. Under these conditions, the substrate temperature due to microwave induction heating and plasma-gas collision was achieved at 830 - 850 °C. It was measured by a chromel-alumel thermocouple contacted at the back of the substrate.

The surface morphology and thickness of the deposited films were examined by FE-SEM (Hitachi S-4700). Micro-Raman spectroscopy (Renishaw inVia Raman microscope) at room temperature using an Ar-ion laser $\lambda = 514.5 nm$ was employed for bonding-structure characterization of the deposited films. The optical properties were also characterized using white light reflection spectroscopy (reflectometry).

5.6.2 Plasma Chemistry

Figure 5.29 shows normalized plasma impedance at all process steps for the two plasma modes: low and high electron density modes. The mode of plasma was altered by adjusting insertion depths of the three-stub tuner in the matching system. Compared to the case of the increasing microwave power, as described in section 4.3.1.1, the case of the adjusting depths of the tuner showed a change in the impedance value of plasma. This adjustment decreased the inductive component of Z_p. The lowering of the inductive value suggested an increasing electron density shown in **Figure 5.30**. This figure also shows the relative changes of electron density for the both plasma modes in all process steps. For H_2-plasma cleaning step, the H-atomic concentration at the high n_e plasma mode was higher than that of the other one by about two

This material is reserved for educational use only, not allowed for commercial use.

Forbidden to modify the content, and cite the document when use.

times. Furthermore, the addition of CH_4 to nucleation and growth steps increased the inductive component of Z_p, thus making n_e drop.

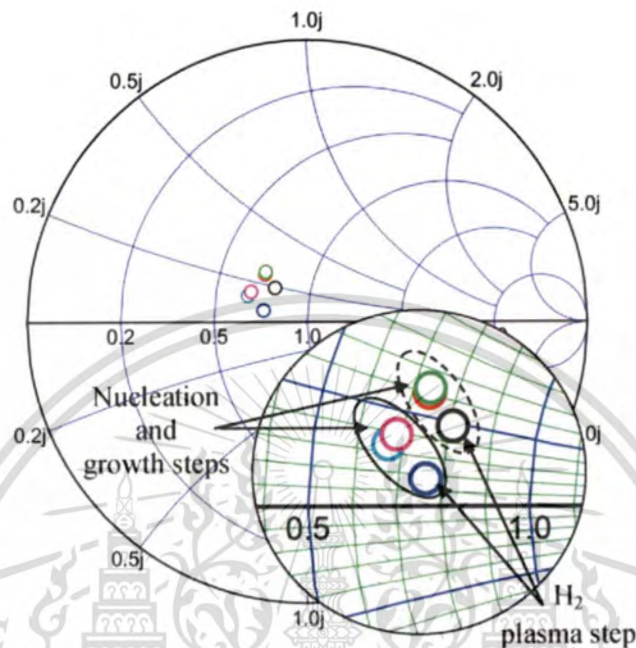

Figure 5.29 Normalized plasma impedance of H_2 and CH_4-H_2 plasma under different plasma impedances: (solid oval line) impedance inducing a high n_e, and (dashed oval line) impedance inducing a low n_e.

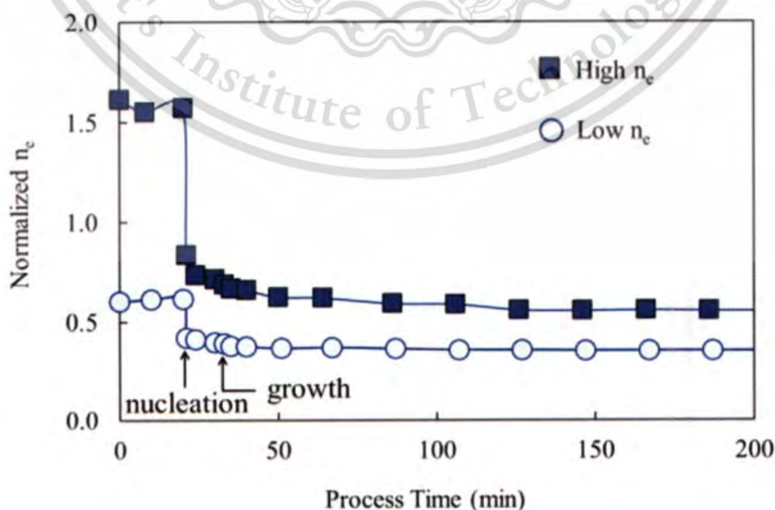

Figure 5.30 Electron density versus process time under different impedances of the plasma.

This material is reserved for educational use only, not allowed for commercial use.
Forbidden to modify the content, and cite the document when use.

The gas species in the plasma as well as the species on the substrate were *in situ* monitored by OES, as shown in **Figure 5.31**. The square of the ratios of the CH(B-X) (387 nm), and CH(A-X) (431 nm) to Hβ (486.1 nm) intensities were plotted with process time under two plasma modes. Indeed, gas phase analysis by OES technique (or any single technique) is far from complete because this technique is not quantitative and other possible growth species, such as CH_3 and C_2H_2, are not directly detectable by emission. However, it confirmed the relation between the change of radical density, including hydrocarbon species, and it is quite clear that as the value of plasma impedance changed, the gas phase experienced substantial change. In the growth step, the hydrocarbon species for the low electron density plasma were higher than that for the high electron density plasma.

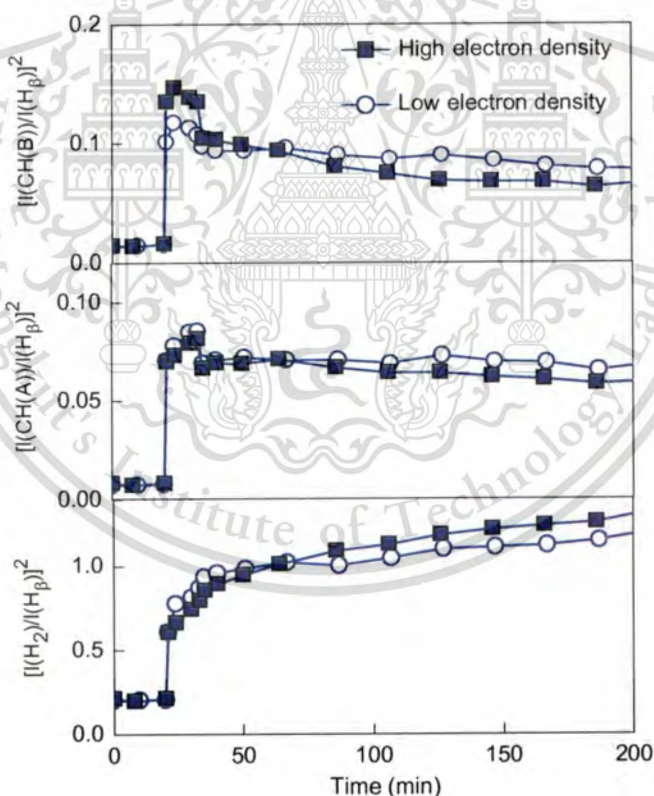

Figure 5.31 The square of ratios of CH(B), CH(A), and H_2 to Hβ versus process time under two plasma modes: low and high electron density plasmas.

This material is reserved for educational use only, not allowed for commercial use.
Forbidden to modify the content, and cite the document when use.

5.6.3 Morphology and Structure of the Films

The FE-SEM images of the films deposited under two plasma modes are shown in **Figure 5.32**(a) and **Figure 5.32**(b). It is difficult to define particular forms of nanodiamond films. Those particular forms are caused by some experimental parameters, such as microwave power, reactor pressure, methane concentration, etc., and even designed reactors. These parameters also caused transition in phase of the diamond films. These FE-SEM images show the deposited films consisted of grain clusters with individual grain sizes. The size of individual nodules was greater for the film grown under the high n_e plasma mode than for the film grown under the other one. In addition, no voids can be seen at each the individual nodule of the film grown under low n_e mode, indicating a higher renucleation rate. Due to the greater of electron density in the plasma during the H_2-plasma step, the higher H atoms for high n_e plasma mode relative to the other one increased the coverage fraction of H radical on the surface. The increased coverage fraction of H radicals induces the renucleation rate to slow.

The growth rate calculated from the film thickness divided by the growth time did not vary significantly with changing plasma impedance, with a rate of ~0.6 $\mu m.h^{-1}$. The grains were vertically aligned as shown in **Figure 5.33**(a) and **Figure 5.33** (b) The vertical grains are similar to the columnar growth seen for MCD, and which can sometimes be seen on a nanoscale in NCD film cross-sections, as reported by Buijnsters *et al.* [27] and P.W. May *et al.* [14].

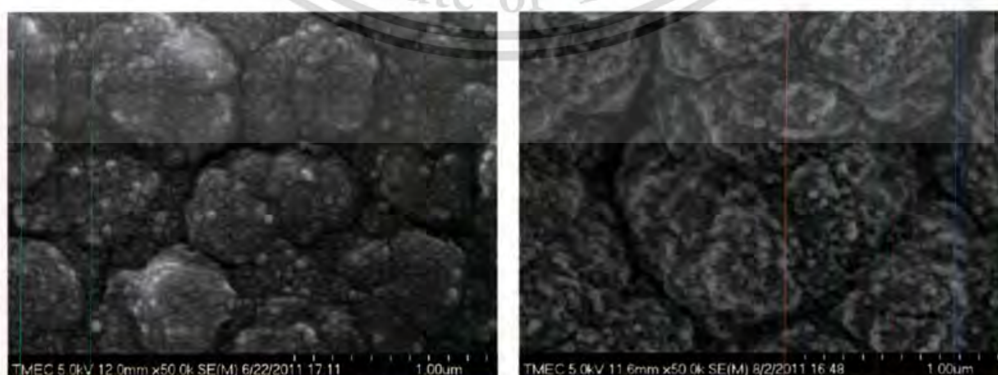

(a) (b)

Figure 5.32 Surface morphologies of nanodiamond films under two electron-density plasmas: (a) low electron density and (b) high electron density.

This material is reserved for educational use only, not allowed for commercial use.
Forbidden to modify the content, and cite the document when use.

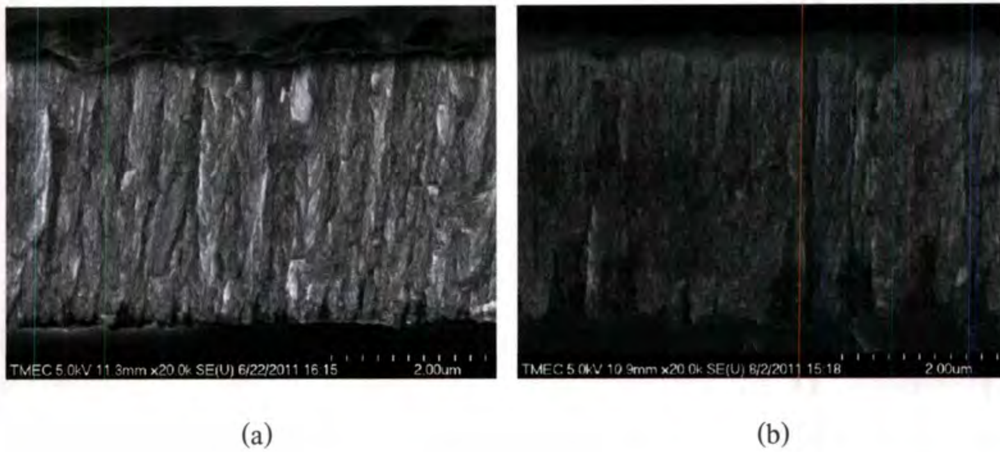

(a) (b)

Figure 5.33 FE-SEM cross-section images of nanodiamond films under two electron-density plasmas: (a) low electron density and (b) high electron density.

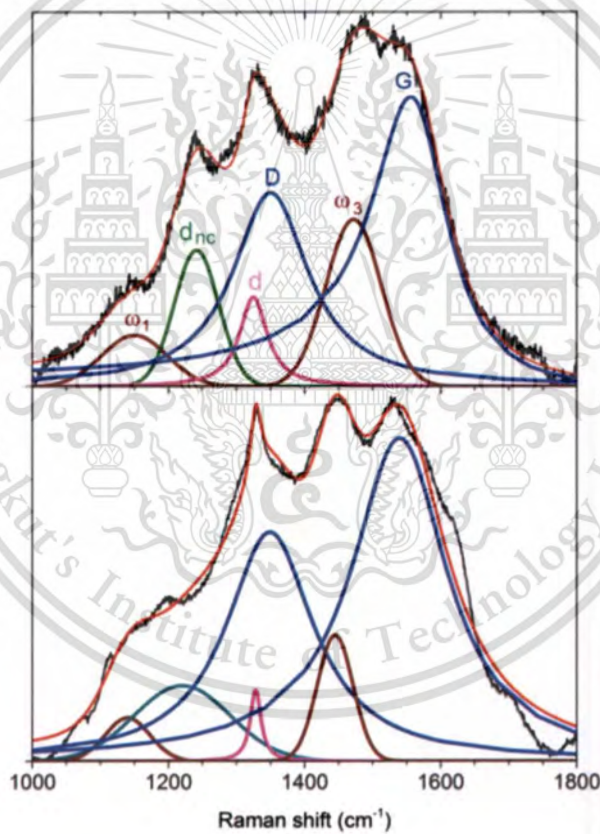

Figure 5.34 Raman spectra of both films after subtraction of the photoluminescence background (top) low and (bottom) high electron density in plasma.

Figure 5.34 shows Raman spectra of the both films grown at the two modes of plasma. Raman spectra were deconvoluted using Gaussian curve for the bands at 1140, 1250, and 1475 cm^{-1}, Lorentzian curve for the 1350 and 1332 cm^{-1}, and Breit-Wigner-Fano curve for the band at

This material is reserved for educational use only, not allowed for commercial use.
Forbidden to modify the content, and cite the document when use.

1550 cm^{-1} (G-band). These features exhibit diamond peak at 1332 cm^{-1} and several non-diamond phase contributions: graphite D-band at 1350 cm^{-1} and G-band at 1570 cm^{-1} as well as *trans*-polyacetylene (t-PA) – like fragments trapped at nanograin [15, 21, 25, 34]. A sixth feature at around 1200-1250 cm^{-1} (d_{nc}) arising from a broadened vibration density of states contributions from small diamond grains [17, 25, 35].

Raman spectra show drastic changed with the plasma impedance. Raman spectra show that the d peak shifted from 1325 cm^{-1} with a 40 cm^{-1} linewidth to 1328.5 cm^{-1} with a 19 cm^{-1} linewidth when the plasma mode was changes to the high electron-density plasma. The redshifts and linewidth broadening of this peak for the deposited films are consistent with that for nanodiamond as reported by K.W. Sun *et al.* [36]. The observed energy redshift to higher frequency approaching 1332 cm^{-1} and the narrower broadening suggested that the nanodiamond grain size increased. The observed shifts and linewidth broadening are attributed to the phonon-confinement effect [16]. Another important feature of Raman spectra was the shift of G-peak position from 1564 to 1541 cm^{-1} due to the reduction in film stress and lowering of sp^2 carbon content in the film structures [17]. Raman peaks also show the shift in the two-broad peaks, ω_1 and ω_3, from 1150 to 1140 cm^{-1} and from 1470 to 1445 cm^{-1}. The shift of this pair of peaks proposed that the longer t-PA chain lengths terminated on the diamond surface.

The influence of the plasma impedance on optical properties of NCD films was also investigated by white light reflectometry. The refractive index n was calculated from the reflectance spectra using the interference fringes as shown in **Figure 5.35**. The refractive index increased from 1.84 to 2.16 after the plasma mode was changed to high electron density plasma. The lowering of the refractive index for the NCD films as compared with the single crystalline diamond (2.41) is due to the presence of an amorphous carbon matrix. However, optical reflection by the films is governed not only by the film composition (which determines the optical constant of the film) but also by the surface roughness [18, 37]. The greater surface roughness of the film grown under the high electron-density condition relative to the film grown under the low electron-density condition promotes a higher light scattering and in turns a lower light reflectance.

This material is reserved for educational use only, not allowed for commercial use.
Forbidden to modify the content, and cite the document when use.

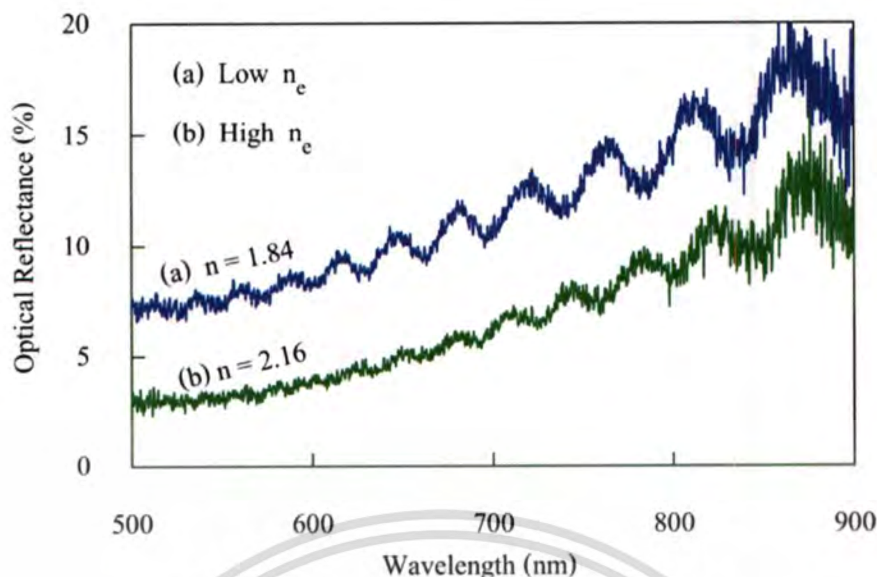

Figure 5.35 The reflectance spectra of films grown under two plasma modes: low and high electron densities.

Correlation between films grown and gas species present in the gas-phase environment is an important step in identify the primary growth species. The relative concentration of those species, including electron and hydrocarbon species, close to the growing surface explains an average crystal size, morphology of the subsequent film, and the probability of a renucleation event occurrence. From the characterization of the films by FE-SEM, Raman spectroscopy, and reflectometry, we found the crucial results as follows: (i) the growth rates of the both films were nearly identical; (ii) the present of an amorphous carbon matrix was lower for film grown at high n_e plasma than for film grown at the other one.

As stated by D.G. Goodwin [38], the growth rate G and relative defect density X_{def} determining film quality can be estimated by the following formulae:

$$G=1.8\times10^{11}\frac{[CH_3]_{sur}[H]_{sur}}{5\times10^{-9}+[H]_{sur}}$$

and

This material is reserved for educational use only, not allowed for commercial use.
Forbidden to modify the content, and cite the document when use.

$$X_{def} \propto \frac{G}{[H]_{sur}^2}.$$

Here $[CH_3]$ and $[H]$ are the methyl and atomic hydrogen concentrations at the surface. In addition, this model suggests that a renucleation site outcome from the reaction on surface of two hydrocarbon species absorbed on adjacent surface sites. Clearly, our experimental data showed that the change of plasma impedance to higher electron density increased atomic H (H radical) in the plasma and decreased hydrocarbon species absorbed on the surface. This results in characteristics of the films.

On the other hand, the relation between the relative defect density and growth rate demonstrates that electron density enhanced film quality owing to the H radical concentration as a function of electron density. The increasing H radical encourages hydrogen-etching increment. Although the increasing atomic-H also increases the formation of cluster necessary for diamond growth, especially CH_3 radicals with the gas-phase reaction of $CH_4 + H \rightarrow CH_3 + H_2$. However, the growth rate fails to increase with atomic-H. This may be attributable to a decrease in concentration of CH_3 radicals as compared to H radical, corresponding with optical emission intensity measured by OES shown in **Figure 5.31**. When H radical increased, the concentration of CH_3 radicals became low. Consequently, the rate reaction constant for the loss reaction $CH_3 + H \rightarrow CH_4$ was much higher than that for the generation reaction $CH_4 + H \rightarrow CH_3 + H_2$. The lifetime of CH_3 radicals decreases with increasing atomic H [30, 39]. The shorter lifetime of CH_3 radicals also makes CH_x radicals in gas phase reduce. By the usage of film characterizations and plasma diagnoses, it can be interpreted that electron density promotes H radicals but lowers ratio of the hydrocarbon species absorbed on the surface to H radicals in the gas phase. Increasing electron density serves to enhance the H radical concentration, facilitating a rise in etching of sp^2 carbon and a drop of renucleation rate. Thus, at the higher electron density in the plasma, the NCD films with large grain size and high film quality can be formed due to the greater of H radical concentration but the growth rate is discourage due to the lowering of CH_3 radical concentration.

This material is reserved for educational use only, not allowed for commercial use.
Forbidden to modify the content, and cite the document when use.

5.6.4 Summary

Nanodiamond film growth was carried out at two modes of plasma: low- and high- n_e. The mode of plasma was altered by varying plasma impedance with a matching system. FE-SEM images showed cluster sizes of the film grown at high- n_e mode were greater than that at low-n_e mode. The increasing n_e increased the atomic-H concentration that encouraged an increase in hydrogen-etching process and a reduction in rate of renucleation process. Raman spectra showed the shifting of d-peak from 1325 cm^{-1} with a linewidth of 40 cm^{-1} to 1328.5 cm^{-1} with a linewidth of 19 cm^{-1} that corresponded to grain-size increment and the sp^2 carbon matrix decrement. From white light reflectance spectra, the refractive index increased from 1.84 to 2.16 after the plasma was changed to operate in high-electron density mode. Based on film characterizations and plasma diagnosis, the results clarified the dependence of film properties and plasma chemistry on the plasma impedance. The plasma impedance acted as an agent of plasma chemistry and an electrical load of microwave circuit in the microwave plasma apparatus. Therefore, the varying plasma impedance changed electron density and radicals in the gas-phase environment.

5.7 Methane concentration on Phase Transformation of NCD Films

In conventional diamond growth for MCD, typical deposition conditions involve the use of a dilute concentration of CH_4 in highly relative concentrations of H_2 (up to 99%). The NCD films prepared by the MPECVD reactor can be performed by modifying the typical deposition conditions in various ways: 1) by increasing the percentage of CH_4 from 10% and up to 50% [40-42] 2) by applying negative bias on the substrate on which the film is deposited during the growth [43, 44], or 3) by replacing H_2 with either Ar gas or N_2 gas [45-47]. These works reported the use of high power more than 1000 W and up to 3 kW for the deposition. Indeed, it is difficult to define even morphological and structural forms of the films due to the variation between laboratories and even reactor configurations.

The purpose of this work is to study phase transition of the NCD films by adding CH_4 concentration ranged between 1.5% and 4.0% into the gas mixture. The transition in phase from NCD to ultrananocrystalline diamond (UNCD) can be observed in this CH_4 concentration range.

This material is reserved for educational use only, not allowed for commercial use.

Forbidden to modify the content, and cite the document when use.

A high diamond nucleation density is initially obtained by ultrasonically vibrating the substrate surface. Although there have been many reports on the growth of diamond films by the MPECVD system from the CH_4/H_2 gas mixture. To our knowledge, it is the first report on the growth of NCD and UNCD films at microwave power as low as 650 W using CH_4 concentration ranging from 1.5% to 4.0% on Si substrates without the bias-enhanced nucleation step and the use of argon gas or other special gas by MPECVD reactor.

In addition, the growth mechanism of the NCD and UNCD films is still unclear and lack of understanding remains. Numerous published papers reported an increase in growth rate with CH_4 concentration [17, 42, 48]; however, the data representation of gas-phase species of the deposition environment disappeared. Originally, it was suggested that C_2 radical plays a major role in the growth mechanism for the NCD and UNCD [49]. A lot of experiments [12, 50, 51] recently showed that hydrocarbon radicals, including C, CH, CH_2 and CH_3, are more significant growth species than C_2 radicals. Nevertheless, this work also focuses on graphitization with specifying morphological and structural changes compared to gas-phase species of the deposition environment. Such gas-phase species, including electron density, were monitored via an optical emission spectrometer and impedance analyzer. Relative concentrations of the gas-phase species explain an average crystal size, morphology of the subsequent film, and the probability of a renucleation event occurrence for the NCD and UNCD growth.

5.7.1 Design of Experiment

The p-type mirror-polished Si(100) wafer was still used as a substrate. The piranha cleaning process was used to clean the substrates, and then cleaned them by the following clean procedure as described in the section 3.2.1. The pretreatment of the substrate surface was performed using an ultrasonic bath with a 0-3 μm diamond powder suspension in isopropanol for 3 h. Such the pretreatment method is useful for enhancement of the initial diamond nucleation density.

The deposition was carried out under various CH_4 concentrations of 1.5%, 3.0%, 3.5%, and 4.0% by adjusting the flow rate of hydrogen to maintain a constant total flow rate of 200 sccm.

This material is reserved for educational use only, not allowed for commercial use.

Forbidden to modify the content, and cite the document when use.

The reactor pressure was 4 kPa. The gas flow rate and pressure can be controlled independently. The absorbed microwave power measured by the impedance analyzer was around 650 W. Under these operating conditions, the substrate temperature was achieved by microwave induction between 730 and 750 °C. The substrate was placed on a quartz holder and immersed in the plasma. The thicknesses of deposited films were between 1.75 and 2.0 μm.

In this experiment, an optical spectrometer and an impedance analyzer were used for *in situ* and real-time measurements. The spectrometer (HR4000 OceanOptics) was used to measure optical emission from the plasma. Simultaneously, the impedance analyzer was used to monitor and measure impedance of the plasma. It provided further information on the relative changes of electron density. In addition, the deposited films were characterized using field emission scanning electron microscopy (FE-SEM: S-4700 Hitachi) and Raman spectroscopy (NT-MDT NTEGRA spectra). The Raman measurements were performed at room temperature with argon-ion laser excitation wavelength of 488 nm.

5.7.2 Surface Morphology and Structure of the Films

Figure 5.36 shows FE-SEM images of the films prepared under various CH_4 concentrations: 1.5%, 3.0%, 3.5%, and 4.0%. The morphology of the film dramatically changes when the CH_4 concentration increases from 1.5% to 3.0%. At the CH_4 concentrations of 3.5% and 4.0%, the film surfaces become smoother and form clusters. The clusters were composed of very fine grains and the cluster boundaries can be identified.

This material is reserved for educational use only, not allowed for commercial use.
Forbidden to modify the content, and cite the document when use.

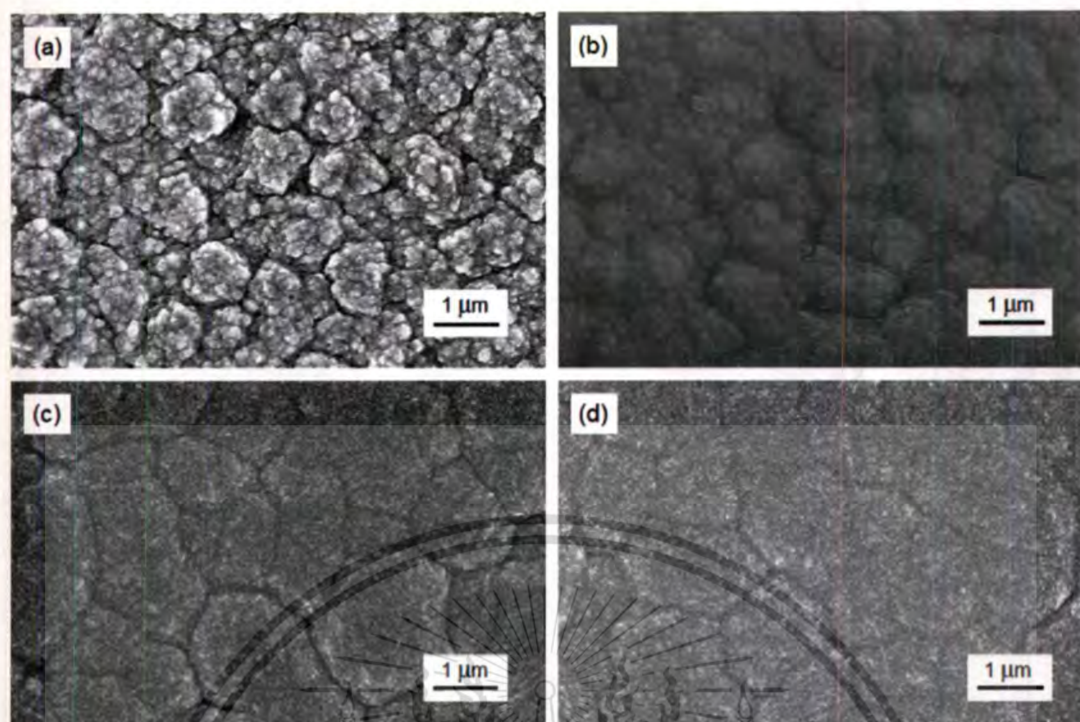

Figure 5.36 FE-SEM images of diamond films grown on Si substrates under various CH_4 concentrations: (a) 1.5%, (b) 3.0%, (c) 3.5%, and (d) 4.0%. Film changes from NCD to UNCD phase.

The magnified FE-SEM images and cross-section view of the films prepared at CH_4 concentrations of 1.5% and 4.0% are shown in **Figure 5.37**. The growth rates decreased with increasing CH_4 concentration, from 300 nm/h for 1.5%CH_4 to 210 nm/h for 4.0%CH_4. For 1.5%CH_4, the morphology of the film surface was very rough and the grains were vertically aligned and embedded in a columnar-type structure. The vertical grains can sometimes be seen on a nanoscale in NCD film cross-section [14, 27]. Unlike the film grown at 1.5% CH_4, the film grown at 4.0%CH_4 was composed of fine grains with a needle-like nanostructure aggregated from very small crystallites, as shown in **Figure 5.37**(b) and **Figure 5.37**(c). The film with an aggregate of crystallites of less than tens of nanometers in size as well as a granular structure is typical of UNCD [52, 53]. Similar aggregation was observed by X. Xiao *et al.* [46] who grew UNCD by the MPECVD process by the use of 0.9%CH_4/Ar.

This material is reserved for educational use only, not allowed for commercial use.
Forbidden to modify the content, and cite the document when use.

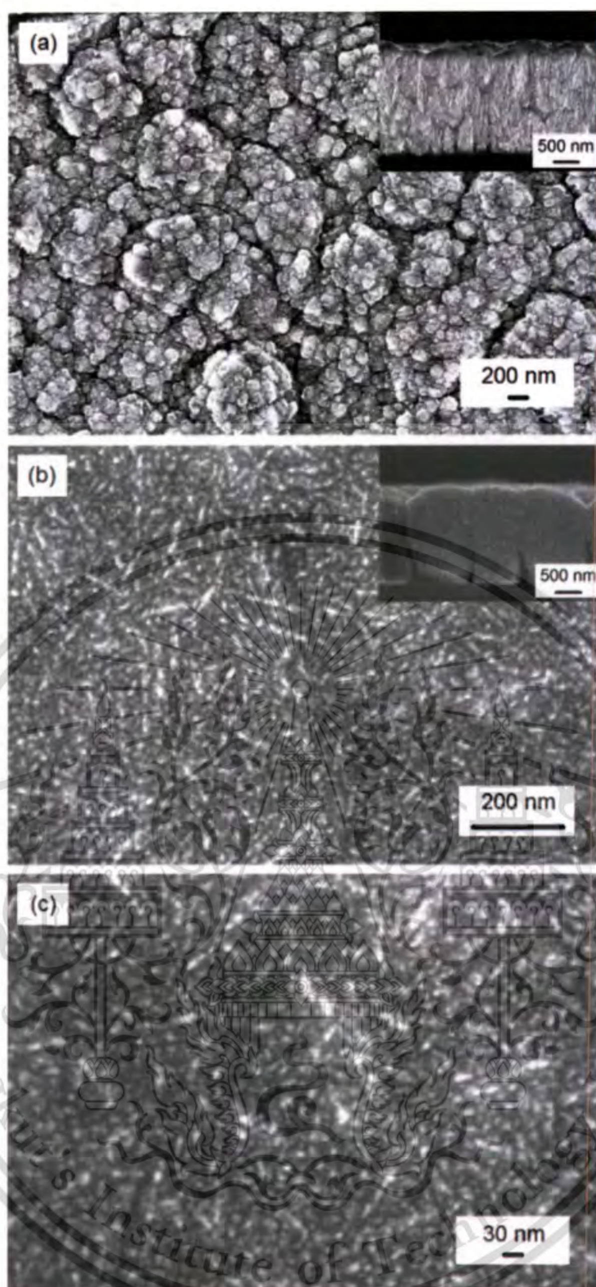

Figure 5.37 Magnified and inset cross-section images of the films synthesized at two CH_4 concentrations: (a) 1.5%, (b) and (c) 4.0%.

Raman measurements showed good agreement with morphological changes presented by FE-SEM analyses. The Raman spectra of the deposited films presented variations in the material bonding with the CH_4 concentration are shown in **Figure 5.38**. They were composed of five features at around 1140, 1333 (diamond peak), 1350 (D-band), 1475 and 1550 (G-band) cm^{-1}. These features are characteristic of NCD film spectra that exhibit a small diamond peak at 1333

This material is reserved for educational use only, not allowed for commercial use.
Forbidden to modify the content, and cite the document when use.

cm^{-1} and several non-diamond phase contributions [17, 54, 55]: graphite D-band at 1350 cm^{-1} and G-band at 1560 cm^{-1} as well as *trans*-polyacetylene band at 1140 and 1475 cm^{-1}.

The shape of Raman spectra is affected by diamond grain size and, therefore, composition in the films. The diamond peak was feebly seen in the spectrum of the film grown at 1.5%CH_4. As the CH_4 concentration was increased, this peak was obscured by D-band. This behavior suggested that the diamond grain size became smaller and the composition of the films became more graphitic. However, the higher intensities for graphite band than for the diamond peak in Raman spectra does not necessarily represent a higher fraction of sp^2-bonded carbon in the film, due to the 50 times higher visible Raman sensitivity for sp^2-bonded carbon (non-diamond phase) than that for sp^2-bonded carbon (diamond phase) [15].

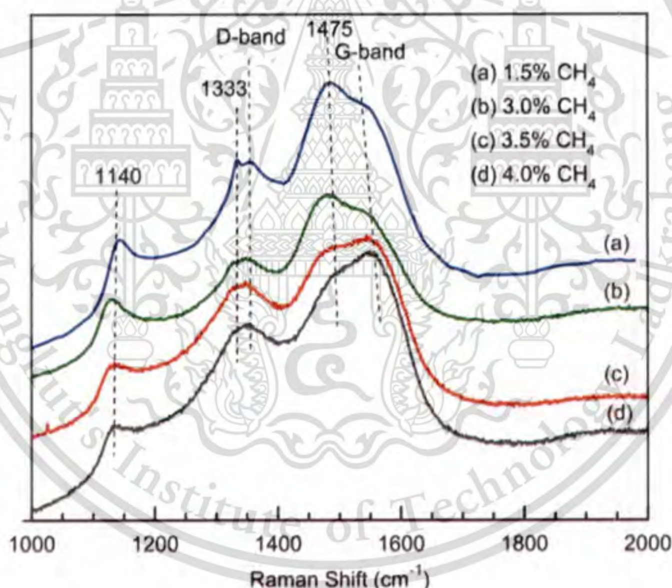

Figure 5.38 Raman spectra of the films grown at different CH_4 concentrations: 1.5%, 3.0%, 3.5%, and 4.0%.

The Raman spectra show clear evidence that the G-peak position shifted to higher frequencies and became dominant with increasing CH_4 concentration. It is well established in the shift in the G peak due to applied stress. Hoffman [4] was the first who suggested that the induced stress is developed due to coalescence of isolated crystallites when forming grain boundaries. Therefore, this shift in the G-peak position can be attributed to the increase in grain boundary

This material is reserved for educational use only, not allowed for commercial use.
Forbidden to modify the content, and cite the document when use.

enhancing the higher sp^2 content. In addition, the line broadening of the peaks at 1140 and 1475 cm^{-1} were also observed simultaneously. The greater broadening of linewidth of these both peaks for the film grown at 4.0% CH_4 as compared with the film grown at 1.5% CH_4 is due to the difference in the crystal size between NCD and UNCD films [53].

5.7.3 Plasma Impedance and Plasma Species

Figure 5.39 shows the normalized impedance of CH_4/H_2 plasma and **Figure 5.40** shows emission spectra under various CH_4 concentrations. The plasma impedance was normalized by the waveguide impedance. The addition of methane changes the value of plasma impedance. The measured plasma impedance Z_p relates to electron density n_e in the plasma [28, 56], as shown in Equation (2.18). This equation shows that the inductive component of plasma impedance increases with decreasing electron density. Therefore, an increase in the measured inductive component can be used as an indicator of the electron density decrement as shown in **Figure 5.41**.

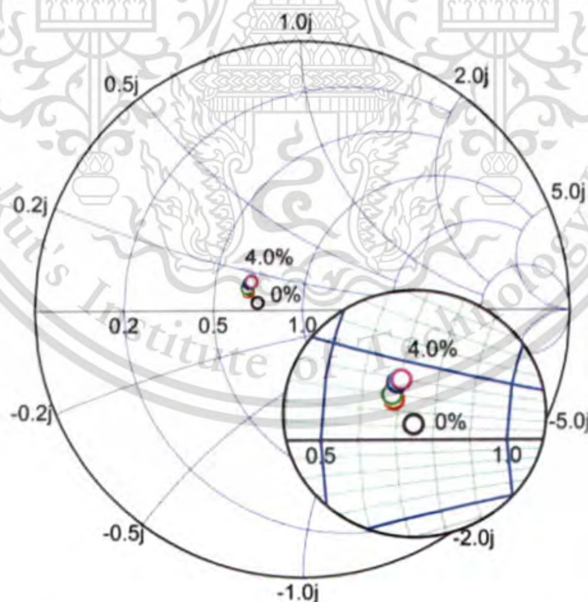

Figure 5.39 Normalized impedance of CH_4/H_2 plasma under various CH_4 concentrations: 0%, 0.75%, 1.5%, 3.0%, 3.5% and 4.0%, and an inset magnified Smith chart.

This material is reserved for educational use only, not allowed for commercial use.
Forbidden to modify the content, and cite the document when use.

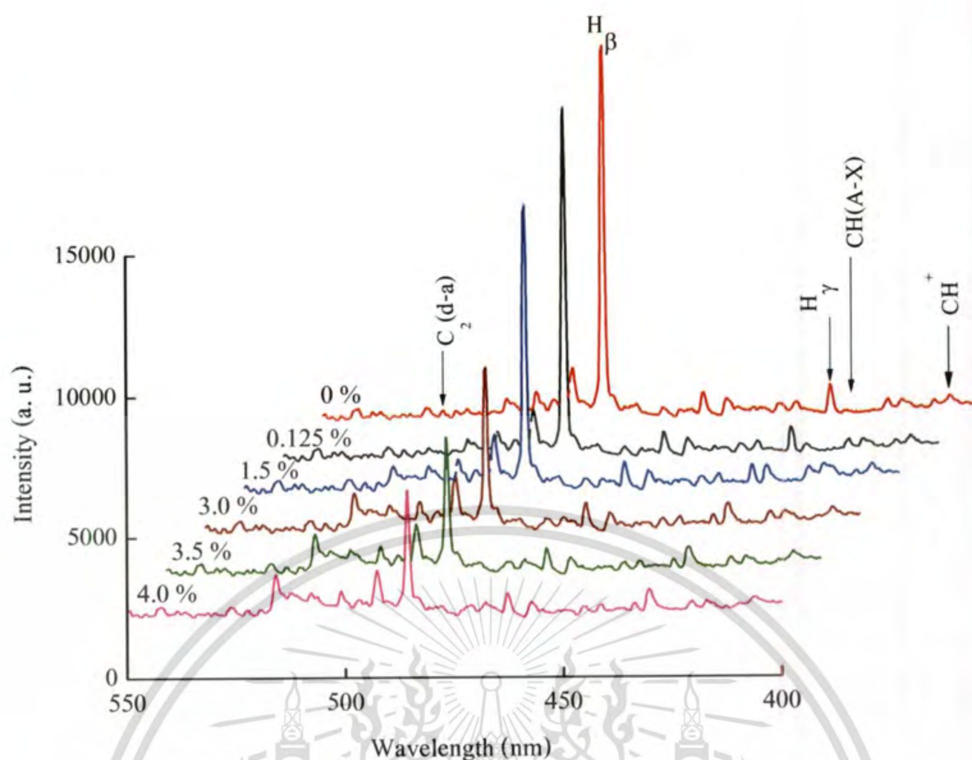

Figure 5.40 Emission spectra of CH_4-H_2 plasma under various methane concentrations.

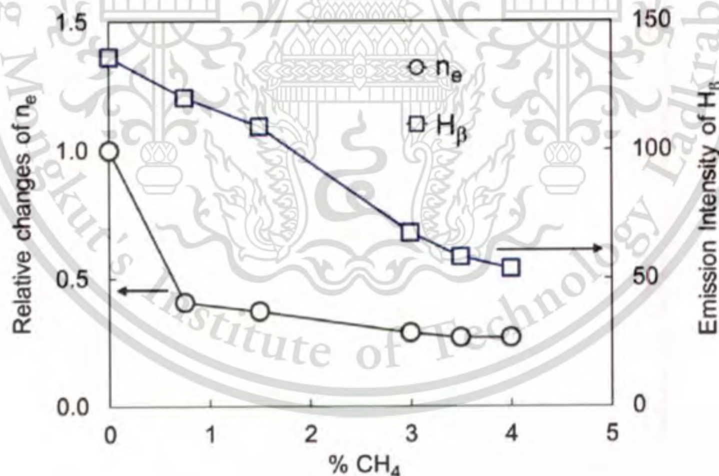

Figure 5.41 The relative changes of electron density and emission intensity of Hβ as a function of CH_4/H_2 concentration.

The relative changes of electron density and the optical emission intensity of H_β as a function of CH_4concentration are shown in **Figure 5.41**. The electron density was determined from Equation (2.18) and then normalized by electron density at CH_4 concentration of 0%. The electron density initially decreases with increasing CH_4 concentration and then saturates after CH_4

This material is reserved for educational use only, not allowed for commercial use.
Forbidden to modify the content, and cite the document when use.

concentration higher than 3.0%. The increasing CH_4 concentration also lowers the emission intensity of Hβ. Our measured intensity of Hβshows the trend identical to that for atomic-H concentration reported by Barshilia and Vankar [57] who gave a report on the effect of CH_4 on atomic-H concentration by actinometry. Thus, for this work, the relative changes of Hβ intensity are used to speculate on the change of atomic-H concentration.

Based on measurements of plasma impedance, the decrease in the amount of hydrogen atom can be explained as a result of a decrease in electron density with increasing CH_4 concentration. Namely, the net production of atomic-H stems only from dissociation of hydrogen molecules appearing to go through the repulsive $b^3\sum_u^+$ state [58] as follows:

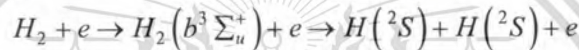

$$H_2 + e \rightarrow H_2\left(b^3\Sigma_u^+\right) + e \rightarrow H\left(^2S\right) + H\left(^2S\right) + e$$

The CH_4 addition also reduces the collision frequency between electron and H_2 molecules due to the higher cross sections of the CH_4 molecules. The collision frequency is also one of the factors influencing the produced atomic-H.

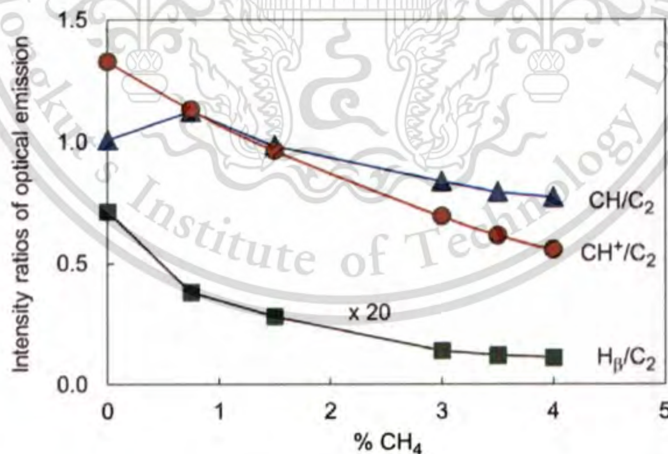

Figure 5.42 The emission intensity ratios of CH, CH^+, and Hβ to C_2 as a function of CH_4 concentration.

Figure 5.42 shows the intensity ratios of CH^+ (417.1 nm), CH(A) (431 nm), and H_β (486.1 nm) to C_2 (515 nm) under various CH_4 concentrations. The emission intensities of hydrocarbon radicals are nonzero at a zero CH_4 flow rate due to the influx of carbon into the gas phase from

This material is reserved for educational use only, not allowed for commercial use.

Forbidden to modify the content, and cite the document when use.

the reactor wall. The lowering of the emission intensities for CH and CH^+ radicals as compared with C_2 radical was obviously observed after CH_4 concentration greater than 3.0%. As reported by Rabeau *et al.* [50] and Fox *et al.* [12], the relative changes for the optical emission intensities measured by optical emission spectroscopy (OES) correspond with those for the gas-phase species density measured by cavity ring-down spectroscopy. Although OES could not provide quantitative information, the emission spectra are still carried out to confirm the relationship between the changes in density of gas-phase species.

From **Figure 5.41** and **Figure 5.42**, the relative changes for electron density are a function of the CH_4 concentration similar to that for the emission intensity ratios of hydrocarbon and atomic H to C_2. This behavior implies that the trend of electron density examined from the measurements of plasma impedance can be used to predict the relative changes of not only H-radical but also the relative changes of the ratios of hydrocarbon species and atomic H to C_2.

Regarding to the NCD and UNCD growth mechanisms described by May *et al.*, [14, 59], hence we suppose that C_1 hydrocarbon radicals (CH_3, CH_2 , CH and C atoms) are precursors of sp^3 diamond phase but the other reactive hydrocarbon species of C_2H_x (C_2,C_2H , etc.) are unlikely to be responsible for the diamond growth. The species of C_2H_x influence the renucleation rate of the NCD and UNCD deposition process.

The correlation between the films grown (**Figure 5.37** and **Figure 5.38**) and gas-phase species in the plasma environments (**Figure 5.41** and **Figure 5.42**) corresponds to the above-mentioned growth mechanisms. For increasing CH_4 concentration, the growth rate fails to increase while the ratios of C_2/CH and C_2/CH^+ increase. These reverse tendencies indicate that the greater density of C_2 radical relative to CH and CH^+ radicals does not enhance the growth of UNCD phase. Therefore, C_2 radical cannot play a role in the growth mechanism of the UNCD films while it influences the NCD phase in transition to UNCD phase. That greater density of C_2 enhances the opportunity to create a strongly-bonded defect on the surface. In addition, the decrease in atomic H with CH_4 addition, resulting in a reduction of the growth rates, enhances the defect being non-etchable from the surface. Such surface defect promotes a renucleation rate

This material is reserved for educational use only, not allowed for commercial use.
Forbidden to modify the content, and cite the document when use.

leading to a decrease in the crystallite size, increase in the grain boundary and film is grown without columnar structure. Consequently, the films with smaller grain size, smoother and uniform top surface morphology, and higher degree of sp^2 carbon content can be prepared from the high CH_4 concentrations.

5.7.4 Summary

This experiment focused on the influence of CH_4 concentration ranging from 1.5% to 4.0% on the nanostructure of diamond films and gas-phase species in the plasma. The films were prepared using a CH_4/H_2 gas mixture at microwave power as low as 650 W. The FE-SEM images and Raman spectra showed that the increasing CH_4 concentration from 1.5% to 4.0% can change the morphology and structure of the films from NCD to UNCD phase and the growth rate failed to increase, from a value of ~300 nm/h for 1.5% CH_4 to ~210 nm/h for 4.0% CH_4. OES and the plasma-impedance measurement showed that, by increasing CH_4 concentration, the density for C_2 species was higher than that for CH species while electron density decreased. The decreasing electron density reduced atomic-H and CH radical in the plasma environment.

My experimental results clarified that correlation between materials grown and gas-phase species, including electron density, present in the gas-phase environment is more important to identify the species driving the mechanism of deposition process. The mechanism for NCD and UNCD deposition was seen as the competition among diamond deposition, etching, and renucleation. The CH radical could play a role in the growth mechanism. The atomic-H led to the etching of non-diamond phase and protected a renucleation occurrence. The reverse tendencies between the C_2/CH and C_2/CH^+ ratios and the growth rate revealed that the C_2 radical did not play a role in the growth mechanism but it promoted the renucleation rate. The promoted renucleation rate caused a decrease in the diamond crystal size, increase in the grain boundary, and film grown with no columnar structure. The elevated CH_4 concentration can induce the phase transition from NCD to UNCD.

This material is reserved for educational use only, not allowed for commercial use.
Forbidden to modify the content, and cite the document when use.

References

[1] Ye H., Sun C. Q., Hing P., Xie H., Zhang S. and Wei J. "Nucleation and Growth Dynamics of Diamond Films by Microwave Plasma-Enhanced Chemical Vapor Deposition (MPECVD)" **Surf. Coat. Technol.** vol.123, 2000. Pp. 129-133.

[2] Gracio J. J., Q H Fan Q. H. and Madaleno J. C. "Diamond Growth by Chemical Vapour Deposition" **J. Phys. D: Appl. Phys.** vol.43, 2010. 374017.

[3] Jiang X., Schiffmann K., and Klages C.-P. "Nucleation and initial growth phase of diamond thin films on (100) silicon" **Phys. Rev. B**. vol.50, 1994. Pp. 8402-8410.

[4] Milton Ohring. **Materials Science of Thin Films: Deposition and Structure.** 2nd ED. San Diego: Academic Press. 2002.

[5] Loretto M. H. **Electron Beam Analysis of Materials.** 2nd ED. London: Chapman & Hall Press. 1994.

[6] Micro and Trace Analysis Centre. **"Chapter 2. X-Ray Photoelectron and Auger Electron Spectroscopy"** [online]. Available: http://webhost.ua.ac.be/mitac4/micro_xpsaes.pdf. 2013.

[7] Montero I., Galan L., Laurent A., Perriere J. and Sposta J. "X-ray Photoelectron Spectroscopy and X-Ray-Excited Auger Electron Spectroscopy Studies of the Initial Deposition of Hydrogenated Amorphous Carbon" **Thin Solid Films.** vol.228, 1993. Pp. 72-75.

[8] Jackson S. T. and Nuzzo R.G. "Determining Hybridization Differences for Amorphous Carbon from the XPS C 1s Envelope" **Appl. Surf. Sci.** vol.90, 1995. Pp. 195-203.

[9] Lascovich J. C. and Scaglione S. "Comparison among XAES, PELS and XPS Techniques for Evaluation of sp^2 Percentage in a-C:H" **Appl. Surf. Sci.** vol.78, 1994. Pp. 17-23.

[10] Mednikarov B., Spasov G., Babeva Tz., Pirov J., Sahatchieva M., Popova C. and Kulisch W. "Optical Properties of Diamond-like Carbon and Nanocrystalline Diamond Films" **Journal of Optoelectronics and Advanced Materials.** vol.7, 2005. Pp.1407-1413.

This material is reserved for educational use only, not allowed for commercial use.
Forbidden to modify the content, and cite the document when use.

[11] S.B. Abu Suilik, D. Shimamoto, H. Kitagawa, K. Hasezaki and Y. Noda: "Experimental Study of Nucleation and Quality of CVD Diamond Adopting Two-step Deposition Approach using MPECVD" **Diamond Relat. Mater.** vol.15, 2006. Pp. 1765-1772.

[12] Fox O.J.L., Ma J., May P.W., Ashfold M.N.R. and Mankelevich Yu.A. "The Role of Inert Gas in MW-enhanced Plasmas for the Deposition of Nanocrystalline Diamond Thin Films" **Diamond Relat. Mater.** vol. 18, 2009. Pp. 750-758.

[13] Williams O. A. "Nanocrystalline Diamond" **Diamond Relat. Mater.** vol. 20, 2011. Pp. 621-640.

[14] P.W. May, N.L. Allan, M.N.R. Ashfold, J.C. Richley and Yu.A. Mankelevich: "Simulations of polycrystalline CVD Diamond Film Growth using a Simplified Monte Carlo Model" **Diamond Relat. Mater.** vol.19, 2010. Pp. 389-396.

[15] Klauser F., Steinmüller-Nethl D., Kaindl R., Bertel E. and Memmel N. "Raman Studies of Nano- and Ultra-nanocrystalline Diamond Films Grown by Hot-Filament CVD" **Chem. Vap. Deposition.** vol.16, 2010. Pp. 127-135.

[16] Arora A.K., Rajalakshmi M. and Ravindran T.R. "Phonon Confinement in Nanostructured Materials" **Encyclopedia of Nanoscince and Nanotechnology.** vol.8, 2004. Pp. 499-512.

[17] Ramos S. C., Azevedo A. F., Baldan M. R. and Ferreira N. G. "Effect of Methane Addition on Ultrananocrystalline Diamond Formation: Morphology Changes and Induced Stress" **J. Vac. Sci. Technol. A.** vol.28, 2010. Pp. 27-32.

[18] Yin Z., Tan H. S. and Smith F. W. "Determination of the Optical Constants of Diamond Films with a Rough Growth Surface" **Diamond Relat. Mater.** vol.5, 1996. p. 1490-1496.

[19] Liu H. and Dandy D. S. "Studies on Nucleation Process in Diamond CVD: An Overview of Recent Developments" **Diamond Relat. Mater.** vol.4, 1995. Pp. 1173-1188.

[20] Donald L. Smith. **Thin-Film Deposition: Principles and Practice.** New York: McGraw-Hill Companies, Inc. 2001.

This material is reserved for educational use only, not allowed for commercial use.
Forbidden to modify the content, and cite the document when use.

[21] Ferrari A. C. and Robertson J. "Origin of the 1150 cm^{-1} Raman mode in Nanocrystalline Diamond" **Phys. Rev. B.** vol.63, 2001. 121405.

[22] Sharda T., Soga T. and Jimbo T. "Optical Properties of Nanocrystalline Diamond Films by Prism Coupling Technique" **J. Appl. Phys.** vol. 93, 2003. Pp. 101-105.

[23] Yury Gogotsi, Editor. **Nanomaterials Handbook.** In: Nanocrystalline Diamond, New York: CRC Press. 2006.

[24] May P. W. and Mankelevich Y. A. "From Ultrananocrystalline Diamond to Single Crystal Diamond Growth in Hot Filament and Microwave Plasma-Enhanced CVD Reactors: a Unified Model for Growth Rates and Grain Sizes" **J. Phys. Chem. C. vol.**112, 2008. Pp. 12432-12441.

[25] Ferrari A.C. and Robertson J. "Raman Spectroscopy of Amorphous, Nanostructured, Diamond–like Carbon, and Nanodiamond" **Phil. Trans. R. Soc. Lond A.** vol. 362, 2004. Pp. 2477-2512.

[26] Heiman A., Lakin E., Zolotoyabko E. and Hoffman A. "Microstructure and Stress in Nano-crystalline Diamond Films Deposited by DC Glow Discharge CVD" **Diamond Relat. Mater.** vol. 11, 2002. p. 601-607.

[27] Buijnsters J. G., Vázquez L., Van Dreumel G. W. G., Ter Meulen J. J., Van Enckevort W. J. P. and Celis J. P. "Enhancement of the Nucleation of Smooth and Dense Nanocrystalline Diamond Films by Using Molybdenum Seed Layers" **J. Appl. Phys.** vol. 108, 2010. 103514.

[28] Moisan M. and Pelletier J. **Microwave Excited Plasmas.** Amsterdam: Elsevier Inc., 1999

[29] Zhang Y. and Chen G. "Surface Free Energies for Diamond Growth from Hydrogen–Hydrocarbon Mixtures" **J. Vac. Sci. Technol. A.** vol.13, 1995. Pp. 183-187.

[30] Ikeda M., Ito H., Hiramatsu M., Hori M. and Goto T. "Effects of H, OH, and CH_3 radicals on Diamond Film Formation in Parallel-Plate Radio Frequency Plasma Reactor" **J. Appl. Phys.** vol.82, 1997. Pp. 4055-4061.

[31] Müller A., Emme M., Korzec D. and Engemann J. "Direct Power Coupling into a Waveguide Cavity Plasma Source" **Surf. Coat. Tech.** vol. 116-119, 1999. Pp. 674-678.

This material is reserved for educational use only, not allowed for commercial use.
Forbidden to modify the content, and cite the document when use.

[32] Hosomi T, Maki T., Kobayashi T. "Enhanced Diamond Film Growth by Xe-added Microwave Plasma CVD" **Thin Solid Films.** vol.368, 2000. Pp. 269-274.

[33] Hosomi T., Maki T., Kobayashi T., YoshizakoY., Taniguchi M. and Sugiyo M. "Role of Xenon Additive in Microwave Plasma-Assisted (H_2+CH_4) Chemical Vapor Deposition of Diamond Thin Film" **J. Appl. Phys.** vol.84, 1998. Pp. 6059-6063.

[34] Michaelson Sh., Ternyak O., Hoffman A. and Lifshitz Y., "Hydrogen Incorporation Processes in Nanodiamond Films Studied by Isotopic Induced Modifications of Raman Spectra" **Appl. Phys. Lett.** vol.89, 2006. 131918.

[35] Jiang N., Eguchi K., Noguchi S., Inaoka T., Shintani Y. "Structural Characteristics and Field Electron Emission Properties Of Nano-Diamond/Carbon Films" **J. Crys. Growth.** vol.236, 2002. Pp. 577-582.

[36] Sun K. W., Wang J. Y. and Ko T. Y. "Raman Spectroscopy of Single Nanodiamond: Phonon-Confinement Effects" **Appl. Phys. Lett.** vol.92, 2008. 153115.

[37] Wang S.G., Zhang Q., Yoon S.F., Ahn J., Wang Q., Yang D. J., Zhou Q. and Yue N. L. "Optical properties of nano-crystalline diamond films deposited by MPECVD" **Opt. Mater.** vol.24, 2003. Pp. 509-514.

[38] Goodwin D. G. "Scaling Laws for Diamond Chemical-Vapor Deposition. I. Diamond surface chemistry" **J. Appl. Phys.** vol.74, 1993. Pp. 6888-6894.

[39] Mao M. and Bogaerts A. "Investigating the Plasma Chemistry for the Synthesis Of Carbon Nanotubes/Nanofibres in an Inductively Coupled Plasma Enhanced CVD System: the Effect of Different Gas Mixtures" **J. Phys. D: Appl. Phys.** vol.43, 2010. 205201.

[40] Yoshikawaa H., Morela C. and Koga Y. "Synthesis of Nanocrystalline Diamond Films using Microwave Plasma CVD" **Diamond Relat. Mater**. vol.10, 2001. Pp. 1588-1591.

[41] Hiramatsu M., Kato K., Lau C.H., Foord J. S. and Hori M. "Measurement of C_2 Radical Density in Microwave Methane/Hydrogen Plasma used for Nanocrystalline Diamond Film Formation" **Diamond Relat. Mater.** vol.12, 2003. Pp. 365-368.

This material is reserved for educational use only, not allowed for commercial use.
Forbidden to modify the content, and cite the document when use.

[42] Yang Q., Yang S., Li Y. S., Lu X. and Hirose A., "NEXAFS Characterization of Nanocrystalline Diamond Thin Films Synthesized with High Methane Concentrations" **Diamond Relat. Mater**. vol.16, 2007. Pp. 730-734.

[43] Lee Y.C., Lin S. J., Chia C. T., Cheng H. F. and Lin I. N. "Synthesis and Electron Field Emission Properties of Nanodiamond Films" **Diamond Relat. Mater.** vol.13, 2004. Pp. 2100-2104.

[44] Zhong X. Y., Chen Y. C., Tai N. H., Lin I. N., Hiller J. M. and Auciello O. "Effect of Pretreatment Bias on the Nucleation and Growth Mechanisms of Ultrananocrystalline Diamond Films via Bias-Enhanced Nucleation and Growth: An Approach to Interfacial Chemistry Analysis via Chemical Bonding Mapping" **J. Appl. Phys.** vol.105, 2009. 034311.

[45] Wu K., Wang E. G., Cao Z. X., Wang Z. L. and Jiang X. "Microstructure and Its Effect on Field Electron Emission of Grain-size-controlled Nanocrystalline Diamond Films" **J. Appl. Phys.** vol.88, 2000. Pp. 2967-2974.

[46] Xiao X., Birrell J., Gerbi J. E., Auciello O. and Carlisle J. A. "Low Temperature Growth of Ultrananocrystalline Diamond" **J. Appl. Phys.** vol. 96, 2004. Pp. 2232-2239.

[47] G. Cicalaa, D. Monégerb, D. Cornacchiab, P. Pesceb, V. Magalettic, G. Pernad, V. Capozzid, M. Tamborrae, "Toward Smooth MWPECVD Diamond Films: Exploring the Limits of the Hydrogen Percentage in $Ar/H_2/CH_4$ Gas Mixture" **Surf. Coat. Technol.** vol.211, 2012. Pp. 152-157.

[48] Li X., Perkins J., Collazo R., Nemanich R. J., Sitar Z., Investigation of the Effect of the Total Pressure and Methane Concentration on the Growth Rate and Quality of Diamond Thin Films Grown by MPCVD, **Diamond Relat. Mater.** vol.15, 2006. Pp. 1784-1788.

[49] Gruen D. M., Nanocrystalline Diamond Films, **Annu. Rev. Mater. Sci.** vol.29, 1999. Pp. 211-259.

[50] Rabeau J. R., John P., Wilson J. I. B. and Fan Y. "The Role of C_2 in Nanocrystalline Diamond Growth" **J. Appl. Phys.** vol.96, 2004. Pp. 6724-6732.

[51] May P. W., Ashfold M. N. R. and Mankelevich Y. A. "Microcrystalline, Nanocrystalline, and Ultrananocrystalline Diamond Chemical Vapor Deposition: Experiment and

This material is reserved for educational use only, not allowed for commercial use.
Forbidden to modify the content, and cite the document when use.

Modeling of the Factors Controlling Growth Rate, Nucleation, and Crystal Size" **J. Appl. Phys.** vol.101, 2007. 053115.

[52] Liang X., Wang L., Zhu H. and Yang D. "Effect of Pressure on Nanocrystalline Diamond Films Deposition by Hot Filament CVD Technique from CH_4/H_2 Gas Mixture" **Surf. Coat. Tech.** vol.202, 2007. Pp. 261-267.

[53] Liao W. H., Wei D. H., Lin C. R., "Synthesis of Highly Transparent Ultrananocrystalline Diamond Films from a Low-pressure, Low-temperature Focused Microwave Plasma Jet, **Nanoscale Research Letters**. 7:82 2012.

[54] Fayette L., Marcus B., Mermoux M., Tourillon G., Laffon K., Parent P., and Le Normand F., "Local Order in CVD Diamond Films: Comparative Raman, X-Ray-Diffraction, and X-ray-Absorption Near-Edge Studies" **Phy. Rev. B.** vol.57, 1998. Pp. 14123-14132.

[55] Lin T., Yu G. Y., Wee A. T. S., Shen Z. X. and Loh K. P. "Compositional Mapping of the Argon–Methane–Hydrogen System for Polycrystalline to Nanocrystalline Diamond Film Growth in a Hot-Filament Chemical Vapor Deposition System" **Appl. Phys. Lett.** vol.77, 2000. Pp. 2692-2694.

[56] Michael A. Lieberman, and ALlan J. Lichtenberg **Principles of Plasma Discharges and Materials Processing.** New York: John Wiley& Sons Inc., 1994.

[57] Barshilia H. C. and Vankar V. D. "Concentration of Atomic Hydrogen in the Ground State in a CH_4-H_2 Microwave Plasma" **J. Appl. Phys.** vol.80, 1996. Pp. 3694-3698.

[58] Krogh O., Wicker T. and Chapman B., "Summary Abstract: Collisional Energy Transfer in Noble Gas/Hydrogen Plasmas" **J. Vac. Sci. Technol. A**. vol.4, 1986. Pp. 1796-1797.

[59] P. W. May, J. N. Harvey, N. L. Allan, J. C. Richley, Yu. A. Mankelevich, "Simulations of Chemical Vapor Deposition Diamond Film Growth using a Kinetic Monte Carlo Model" **J. Appl. Phys.** vol. 108, 2010. 014905.

This material is reserved for educational use only, not allowed for commercial use.
Forbidden to modify the content, and cite the document when use.

CHAPTER 6

CONCLUSION

In conclusion, the microwave plasma-enhanced chemical vapor deposition reactor has been constructed at Surface Physics and Laser Laboratory, Department of Physics, King Mongkut's Institute of Technology Ladkrabang. The purpose-designed and built MPECVD reactor is composed of three parts: a plasma reactor for precursor vapor production and deposition, a part for the microwave power generation and transfer of the power to the reactor, and a gas injection and pressure control system. It is successfully used to grow of NCD films. All NCD films are deposited using a CH_4/H_2 gas mixture and on Si(100) substrate. The factors influencing the morphology and atomic-bonding of the films are studied. These factors are surface-pretreatment method, two-step approach deposition, reactor pressure, value of plasma impedance, and methane concentration.

6.1 Nucleation and Growth Dynamics of Diamond Films

This thesis firstly focused surface studies of the kinetics of diamond nucleation and growth process on Si(100) substrate. Three kinds of mirror-polished Si wafer substrates were used as follows: non-polishing, ultrasonic polishing with 0-3 micro-size diamond powder suspended in isopropyl, and manual polishing with 0-1/2 micro-size diamond powder mixed in minute isopropyl. The time dependence also studies; the nucleation decreased but particle size increased due to the surface diffusion and the merging of the nucleated particle. FE-SEM images indicated that the diamond film with the formation continuous and high quality has been obtained by pretreatement of surface with manual polishing. This provided a guideline to do research on the diamond film growth by the propose-built MPECVD apparatus.

6.2 Two-step Approach Deposition Process

This deposition process has influenced the morphology and compositions of the nanostructured diamond films. The two-step process was done by changing methane concentration. It consisted of a first step with 2%CH_4 and a second step with 1%CH_4. The higher CH_4 concentration for the first step encouraged nucleation density and the lower CH_4 concentration for the second step enhanced the quality of the films. For the single-step process with 1%CH_4, the film morphology showed individual nodules resulting in the low light

This material is reserved for educational use only, not allowed for commercial use.

Forbidden to modify the content, and cite the document when use.

reflectance. The enhanced diamond nucleation kinetics on the substrate surface with the two-step processes developed more uniform and much smoother diamond films as well as the higher light reflectance. Compared with the single-step process with 2%CH_4, the two-step process showed more enhancements of an increase in grain boundaries and a decrease in sp^2-bonded carbon content. My experimental results suggest that the two-step process leaded to the fabrication of the NCD films with a large number of grain boundaries as well as a lowering of graphitic impurities. In addition, the nanocrystalline columnar-structured diamond film can be grown by the two-step process.

6.3 Reactor Pressure on NCD Films

This thesis also focused the influence of reactor pressure on the morphology, growth rate, grain size, atomic-bonding structure, and optical properties of NCD films as well as the gas-phase species, including electron density, in plasma. The NCD films were prepared by a MPECVD technique with CH_4/H_2 precursor mixture and two-step approach. Before the beginning of deposition, the Si(100) substrate surface was also cleaned by ***in situ*** H_2-plasma. The deposition for the films was performed under reactor pressures of 1, 2, 5, 9, and 25 kPa.

As the reactor pressure increased, the surface smoothness and diamond grain size of the films increased while amorphous carbon content decreased. The pressure influenced the refractive index of the NCD films: 2.38 for 25 kPa, 2.21 for 9 kPa and 2.16 for 5 kPa. However, the NCD films grown under 1 and 2 kPa were highly light absorbing materials. The growth rates rapidly decreased from 370 to 320 nm/h when the reactor pressure increased from 1 to 2 kPa. As the pressure increased to 9 kPa, the growth rate rapidly increased to 460 nm/h and then decreased with a much slow rate after 9 kPa.

Correlation between materials grown and gas-phase species present in the plasma is important to identify the species driving the process mechanism. The growth rates were in inverse proportion to the n_e relative changes extracted from measurements of plasma impedance in the H_2-plasma step. However, they directly related to the $I(CH)/I(H\beta)$ ratio in the nucleation step. These behaviors revealed that the surface-coverage fraction of H radicals occurring during the H_2-plasma cleaning step and the density ratio of CH_x radical to H radical for the nucleation step were important to determine the growth rate of the film deposition. Furthermore, the diamond grain size and sp^3 carbon content in the films strongly depended on the $I(CH)/I(H\beta)$ ratio for the growth

This material is reserved for educational use only, not allowed for commercial use.
Forbidden to modify the content, and cite the document when use.

step. This result confirms that C_1 hydrocarbon radicals were precursors of sp^3 diamond phase for the growth of diamond.

The reactor pressure influenced not only concentration of the decomposed radicals but also the coverage fraction of the radicals on the growth surface. The concentration of the radicals and the surface-coverage fraction of radicals manipulated diamond growth kinetics. Generally, the concentration of the decomposed radicals, including H and CH_x radicals, are proportional to the reactor pressure. Those radicals increased not only growth rate but also sp^3 carbon content in the films. However, only increasing CH_x radicals in the gas led to more grain boundaries, sp^2 carbon content, and phase transition unless the atomic-H density increased as well.

6.4 Plasma Impedance Tuning Effect on Nanostructured Diamond Films

Nanodiamond film growth was carried out under different plasma impedance that caused the plasma become low and high electron density for plasmas. The impedance was altered by adjusting insertion depths of the three-stub tuner. FE-SEM images showed cluster sizes of the film grown under the high n_e condition were greater than that under low n_e condition. The increasing n_e increased the atomic-H concentration that encouraged an increase in hydrogen-etching process and a reduction in rate of renucleation process. Raman spectra showed the shifting of d-peak from 1325 cm^{-1} with a linewidth of 40 cm^{-1} to 1328.5 cm^{-1} with a linewidth of 19 cm^{-1} that corresponded to grain-size increment and the sp^2 carbon matrix decrement. From white light reflectance spectra, the refractive index increased from 1.84 to 2.16 after the plasma was changed to operate in high-electron density mode.

Based on film characterizations and plasma diagnosis, the correlation between films grown and gas species present in the gas-phase environment was an important step in identify the primary growth species. The relative concentration of those species, including electron and hydrocarbon species, close to the growing surface explained an average crystal size, morphology of the subsequent film, and the probability of a renucleation event occurrence. Consequently, changing in plasma impedance acting as an agent of plasma chemistry influenced the morphology and structure of the nanodiamond films.

6.5 Methane Concentration on Phase Transformation of NCD Films

This thesis also focused on the influence of CH_4 concentration ranging between 1.5% and 4.0% on the nanostructure of diamond films and gas-phase species in the plasma. The films were

This material is reserved for educational use only, not allowed for commercial use.

Forbidden to modify the content, and cite the document when use.

prepared from using a CH_4/H_2 gas mixture at microwave power as low as 650 W. FE-SEM images and Raman spectra showed that the increasing CH_4 concentration from 1.5% to 4.0% can change the morphology and structure of the films from NCD to UNCD phase and the growth rate failed to increase, from a value of ~300 nm/h for 1.5% CH_4 to ~210 nm/h for 4.0% CH_4. OES and the plasma-impedance measurement showed that, by increasing CH_4 concentration, the density for C_2 species was higher than that for CH species while electron density decreased. The decreasing electron density reduced atomic-H and CH radical in the plasma environment.

My experimental results clarified that correlation between materials grown and gas-phase species, including electron density, present in the gas-phase environment is more important to identify the species driving the mechanism of deposition process. The mechanism for NCD and UNCD deposition was seen as the competition among diamond deposition, etching, and renucleation. The CH radical could play a role in the growth mechanism. The atomic-H led to the etching of non-diamond phase and protected a renucleation occurrence. The reverse tendencies between the C_2/CH and C_2/CH^+ ratios and the growth rate revealed that the C_2 radical did not play a role in the growth mechanism but it promoted the renucleation rate. The promoted renucleation rate caused a decrease in the diamond crystal size, increase in the grain boundary, and film grown with no columnar structure. The elevated CH_4 concentration induced the phase transition from NCD to UNCD.

This material is reserved for educational use only, not allowed for commercial use.
Forbidden to modify the content, and cite the document when use.

APPENDIX A

PAPER I

This material is reserved for educational use only, not allowed for commercial use.
Forbidden to modify the content, and cite the document when use.

Advanced Materials Research Vol. 651 (2013) pp 148-153
Online available since 2013/Jan/25 at www.scientific.net
© (2013) Trans Tech Publications, Switzerland
doi:10.4028/www.scientific.net/AMR.651.148

Effect of Two-step Deposition Process on Morphology and Optical Properties of Nanostructured Diamond Films

S.Tipawan Khlayboonme*[1,a], Wicharn Techitdheera[2,b] and Warawoot Thowladda[1,c]

[1]Surface Physics and Laser Research Laboratory, Department of Physics, Faculty of Science, King Mongut's Institute of Technology Ladkrabang, Bangkok Thailand, 10520

[2]Computational Physics Research Laboratory, Department of Physics, Faculty of Science, King Mongut's Institute of Technology Ladkrabang, Bangkok Thailand, 10520

[a]kktipawa@kmitl.ac.th, [b]ktwichar@kmitl.ac.th, [c]ktwarawo@kmitl.ac.th

Keywords: Two-step process; nanostructured diamond films; Raman spectroscopy; reflectometry.

Abstract. The morphology and optical properties of nanostructured diamond films affected by the two-step deposition process with changing CH_4 concentration were investigated. The CH_4 concentration was 1% for the first step and 2% for the second step. The films were prepared by chemical vapor deposition in a microwave plasma reactor with a CH_4/H_2 gas mixture. Nanocrystalline columnar-structured diamond film with lowering of sp^2-bonded carbon content was achieved by the two-step deposition process. Unlike that of the single-step process with 1%CH_4, the two-step process promoted the morphology to more uniform and smoother film. The two-step process increased the higher grain boundary as well as decreased the sp^2-bonded carbon content in the film, as compared with the single-step process with 2%CH_4.

Introduction

Diamond films have become an increasing attention material because of their extreme and in many case superlative properties [1]. The particular nanocrystalline diamond (NCD) films have been identified as a potentially useful material due to their excellent mechanical and optical properties as well as their high surface areas [2]. They are also non-toxic, which makes them well suited to biomedical applications [3]. Depending on the morphology and amount of sp^2, the NCD films show an important for specific applications.

The desired morphology combined with controlled composition of NCD films greatly depends on the conditions for nucleation and growth steps [4]. The deposition at specific deposition regimes enhances diamond nucleation although diamond quality is not necessarily favored. Therefore, a two-step deposition process is an interesting process. There are several means of operation of the two-step deposition process for each step: by means of using negative bias enhance nucleation, changing CH_4 concentration, and/or changing the deposition pressure in the growth step [5]. The two-step deposition process involves an initial rapid nucleation rate and subsequent high-quality growth. In condition of the high rate of secondary nucleation density that occurs during process is very high; the NCD films can be formed [6]. Such NCD films are grown with a significant renucleation rate and seem to form in an H-depleted deposition zone. Indeed, that reason for NCD film formation is major to vary of the design even CVD reactors [1]. It is worthwhile for growth of NCD films from a traditional CH_4/H_2 gas mixture without the use of Argon gas or other special inert gas or high concentration of CH_4. Therefore, the two-step process that uses different CH_4 concentrations between the two steps is an interesting process.

In the present, we investigate enhancement of the two-step deposition process by changing CH_4 concentration on morphology, structure, and optical properties of the deposited films. For the investigation, three film samples were prepared by microwave plasma-assisted CVD (MPACVD) system. Two of them were prepared by the single-step process with CH_4 concentrations of 1% and 2%. One of them was prepared by the two-step process. The effect of the two-step deposition process on morphology, structure, and optical properties of the deposited film will be discussed.

This material is reserved for educational use only, not allowed for commercial use.

Experiment

Deposition of diamond films was performed using a MPACVD bell jar reactor as shown in Fig.1. A 900 W air-cooled magnetron with frequencies of 2.45 GHz was coupled to a WR340 rectangular waveguide. A mode converter being a section of a cylindrical waveguide couples microwave energy into the reactor by an antenna. A quartz bell jar with a diameter of 45 mm and a height of 90 mm was used as the plasma reactor. The reactor was placed on a stainless steel based plate attached to the cylindrical waveguide. The plasma impedance in that reactor was detected by an impedance analyzer (HOMER-Series STHT V 1.5, S-TEAM Lab) included in the section of the rectangular waveguide. The impedance analyzer can serve as a means of plasma-impedance control. It was controlled via S-TEAM Homer Windows Visualization and Control software, named *Homsoft*.

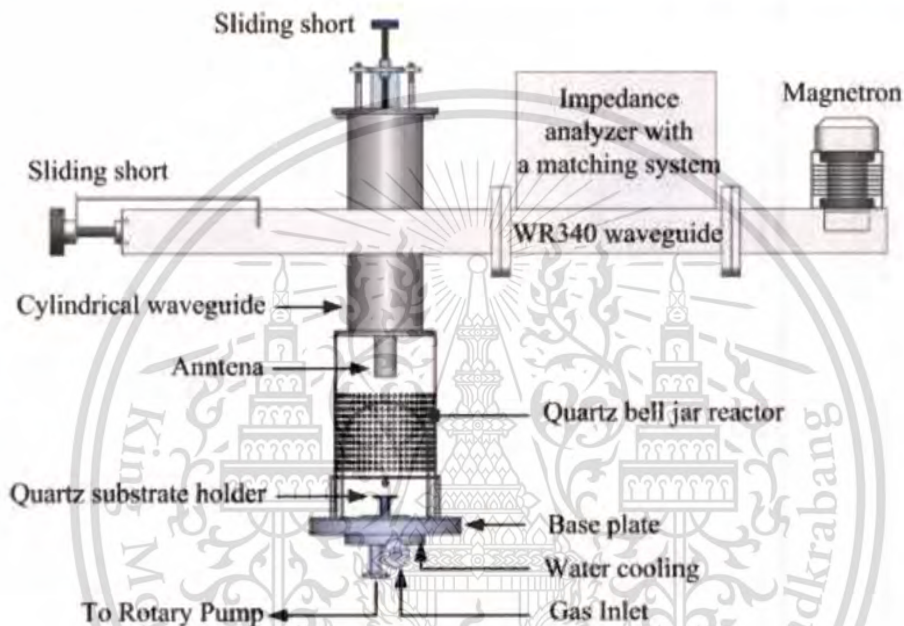

Fig. 1. MPACVD apparatus

A mixture of CH_4 and H_2 was employed as reactant gases. Mirror-polished and B-doped Si(100) wafers were used as substrates. A pretreatment of the substrate surfaces was done by mechanical polishing with slurry of 0-1/2 μm diamond powder with *iso*-propanal for 1 h. Such the pretreatment method is useful to increase the surface energy and better the nucleation density. Before deposition, the substrate surface was *in-situ* cleaned by H_2 plasma for 20 min with a H_2 flow rate of 200 sccm. The gas flow rates were controlled by mass flow controllers. Then methane gas was introduced to begin the deposition.

The deposition was performed to grow three film samples. Two of three samples were carried out by the single-step deposition with CH_4 concentrations of 1% and 2%. One was carried out by the two-step deposition by changing CH_4 concentration. The CH_4 concentration was changed from 1% for the first step to 2% for the second step. The process time was 12 min for the first step and 6 h for the second step. All deposited films were prepared under a total gas flow rate of 200 sccm, a reactor pressure of 5 kPa, and absorbed microwave power of 750 W. The absorbed power was measured by the impedance analyzer. Under these operating conditions, the substrate temperature induced by microwave was between 830 and 850 °C.

The morphology, thickness, and lateral structure of the films were investigated by a field emission scanning electron microscope (FE-SEM; Hitachi S-4700). The bonding structures were characterized by micro-Raman (Renishaw inVia Raman microscope) using an Ar-ion laser with wavelength of 514.5 nm and by reflectance measurements with a laboratory set-up for a visible light reflectometer. In addition, the lowering of surface energy for a mechanic-scratched surface as compared with a mirror-polished surface was measured by contact angle measurements.

Forbidden to modify the content, and cite the document when use.

Results and Discussion

Surface Energy of Substrate. The contact angles of the substrate surfaces under various scratch methods are shown in Fig.2. They strongly depend on the scratch methods. The contact angle of a liquid drop on the surface relates to the surface energy. Based on the measurements, the surface energy for the mechanical scratched surface is higher than that for ultrasonic scratched and mirror-polished surfaces. This suggests that the mechanical scratched method enhances more nucleation density on the substrate surface than other methods.

Fig. 2. Images of deionized water contact angle on Si substrate surfaces under various pretreatment methods: (a) mirror polish, (b) ultrasonic scratch, and (c) mechanical scratch.

Fig. 3. FE-SEM images and inset cross-sectional images of the films deposited by (a) single-step process with 1% CH_4, (b) single-step process with 2% CH_4, and (c) two-step process.

Diamond Film Morphology. The morphologies of all deposited films were imaged using FE-SEM, as shown in Fig. 3. All the deposited films consist of grain clusters with individual grain sizes measuring less than 50 nm as determined by SEM scale markers. The film grown by the single step with 1%CH_4 consists of individual nodule-shape features and voids are clearly observed in the film. By increasing CH_4 concentration to 2%, the film surface becomes continuous and smooth as well as no void can be seen. Compared with the film grown by the single-step process with 1%CH_4, the film grown by the two-step process shows no voids at the interface and smaller diameter of individual nodules, indicating a higher nucleation density. The nodules coalesce to become more continuous.

This material is reserved for educational use only, not allowed for commercial use.
Forbidden to modify the content, and cite the document when use.

The film thicknesses were evaluated from cross-sectional images and lateral structures of the films, shown in insets of Fig. 3, present the grain structure of the films. The nodules of the film grown by the single-step process with 1%CH_4 are a height of 2.59 μm and their structures are grainy. For 2%CH_4, the film thickness is 4.72 μm and its structure is also grainy. Unlike those of the films grown by the single-step process, the grains of the film grown by the two-step process are now vertically aligned. The vertical grains are similar to the columnar growth seen for microcrystalline diamond, and which can sometimes be seen on a nanoscale in NCD film cross-sections, as reported by P.W. May et al. [7]. Compared with the single-step process with 1%CH_4, the two-step process increases the film thickness. The thickness increases from 2.59 to 3.48 μm. The faster deposition kinetics of NCD films results in the formation of much thicker NCD films as well. The high CH_4 concentration promotes a fraction of reactive surface radical sites, both of monoradical sites and in particular biradical sites. The growth rate is determined by reactions between precursors and growth surfaces. Consequently, the high CH_4 concentration for both first and second steps induces the growth rate to more increase. However, the promoted biradical sites increases a renucleation process encouraging non-diamond content in the film structure.

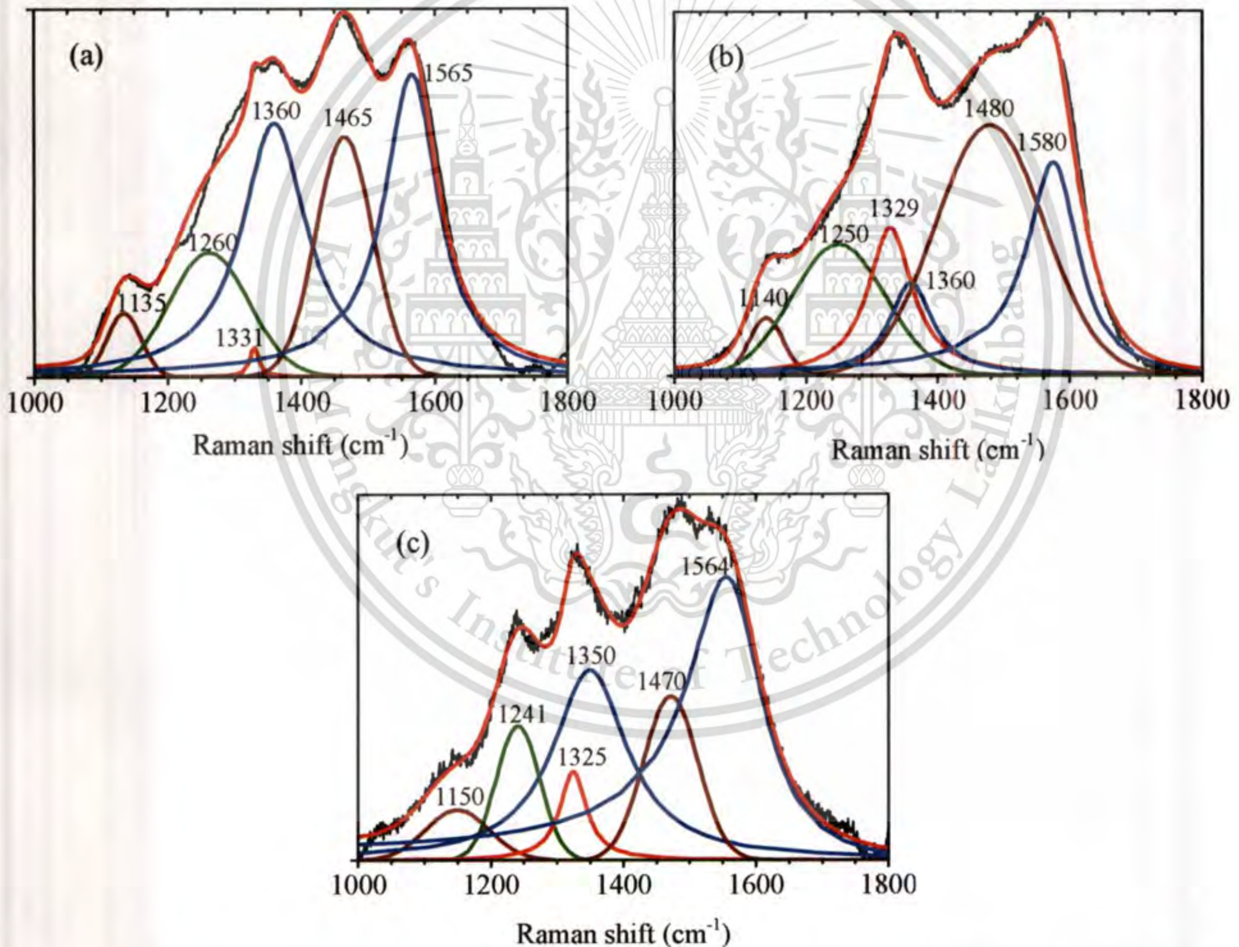

Fig. 4. Raman spectra with raw data and various fit components of the deposited films after subtraction of the photoluminescence background: (a) single step with 1% CH_4, (b) single step with 2% CH_4, and (c) two-step process.

Non-diamond Carbon Content. Raman spectra of the films were deconvoluted after baseline subtraction using three fitting functions, i.e. Gaussian for the bands at 1140, 1250 and 1480 cm^{-1}, Lorentzian for the bands at 1332 and 1350 cm^{-1}, and Breit-Wigner-Fano (BWF) for the band at 1550 cm^{-1}, as shown in Fig. 4. These bands are typically found in NCD film spectra [8] that exhibit a small diamond peak (1332 cm^{-1}) and several non-diamond phase contributions: graphite D and G

This material is reserved for educational use only, not allowed for commercial use.
Forbidden to modify the content, and cite the document when use.

bands (1350 and 1550 cm^{-1}) and *trans*-polyacetylene bands (1140 and 1480 cm^{-1}), trapped at nanograin boundaries. In addition, a broad component at around 1200-1250 cm^{-1} arises from a broadened vibration density of states (VDOS) contributions for small diamond grains.

The shape of Raman spectra is strong affected by diamond grain size and by hydrogen atom concentration within the film. For single-step process, when CH_4 concentration increases from 1% to 2%, the diamond peak shifts from 1331 to 1329 cm^{-1} but its linewidth increases from 17 to 81 cm^{-1}. This behavior shows the crystallite size of diamond becomes smaller but the film becomes more graphitic. However, *trans*-polyacetylene band for the film grown at 1%CH_4 is more significant than that for the film grown at 2%CH_4. The greater significance of *trans*-polyacetylene is due to the higher amount of hydrogen incorporated in the films. For the film grown by the two-step process, the diamond peak shifts to 1325 cm^{-1} with linewidth of only 40 cm^{-1}. This shifting peak is due to the reductions in crystallite size [9]. The band at 1250 cm^{-1} confirms VDOS contributions to nanodiamond grains.

Another important of Raman spectra of diamond films is the significant shift in the G peak. The G-peak position shifts to higher frequencies as a result of the higher non-diamond carbon in the film structures [10]. For the single-step process, the G-peak position shifts from 1565 to 1580 cm^{-1} when CH_4 concentration increases from 1% to 2%. It for the two-step process is similar to that for the single-step process with 1%CH_4. This suggests that the two-step process is changed feature co-deposition of non-diamond carbon along with diamond carbon.

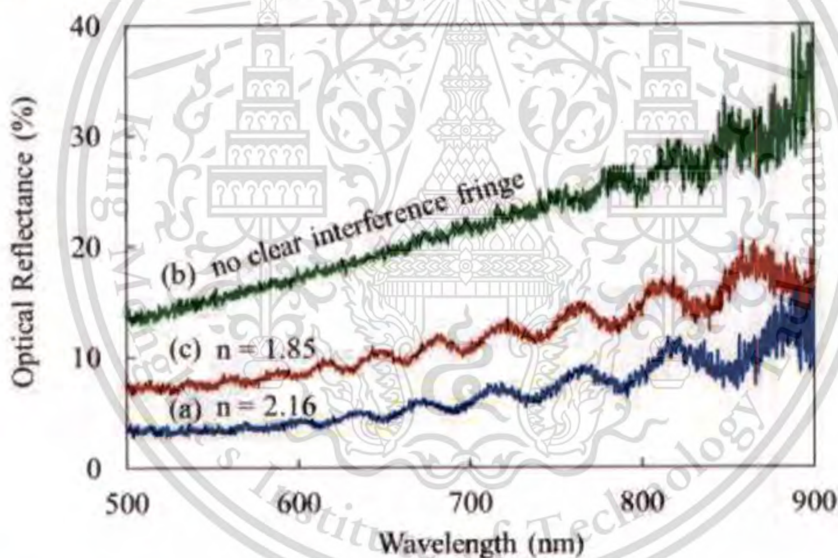

Fig. 5. The reflectance spectra of the films deposited by (a) single step with 1% CH_4, (b) single step with 2% CH_4, and (c) two-step process with changing CH_4 concentration.

Furthermore, the optical properties of the NCD films were also investigated by white light reflectometry. The index of refraction n was calculated from the reflectance spectra using the interference fringes as shown in Fig. 5. The reflectance spectra of the film grown by the single-step process with 2%CH_4 show no obvious interference fringes. This behavior is due to too high content of non-diamond carbon incorporated in the film. The lowering of the refractive index for the films as compared with the single crystalline diamond (2.41) is due to the presence of the non-diamond carbon matrix. However, optical reflection by the films is governed not only by the film composition (which determines the optical constant of the film) but also by the surface roughness [11]. The greater surface roughness of the film promotes a higher light scattering and in turns a lower light reflectance. This result corresponds to the FE-SEM images.

This material is reserved for educational use only, not allowed for commercial use.
Forbidden to modify the content, and cite the document when use.

Summary

This work focused on the effect of the two-step deposition process on the morphology and compositions of the nanostructured diamond films. The two-step process was done by changing methane concentration. It consisted of a first step with 2%CH_4 and a second step with 1%CH_4. The higher CH_4 concentration for the first step encouraged nucleation density and the lower CH_4 concentration for the second step enhanced the quality of the films. For the single-step process with 1%CH_4, the film morphology showed individual nodules resulting in the low light reflectance. The enhanced diamond nucleation kinetics on the substrate surface with the two-step processes developed more uniform and much smoother diamond films as well as the higher light reflectance. Compared with the single-step process with 2%CH_4, the two-step process showed more enhancements of an increase in grain boundaries and a decrease in sp^2-bonded carbon content. Our experimental results suggest that the two-step process leads to the fabrication of the NCD films with a large number of grain boundaries as well as a lowering of graphitic impurities. In addition, the nanocrytalline columnar-structured diamond film can be grown by the two-step process.

Acknowledgements

This work was financially supported by Faculty of Science at King Mongkut's Institute of Technology Ladkrabang, Thailand.

Corresponding Author

S.Tipawan Khlayboonme, kktipawa@kmitl.ac.th , 66-081-296-2134.

References

[1] O.A. Williams: Diamond Relat. Mater. Vol. 20 (2011), p. 621

[2] V. N. Mochalin, O. Shenderova, D. Ho and Y. Gogotsi: Nature Nanotechnology Vol. 7 (2012), p.11

[3] J. E. Butler and A. V. Sumant: Chem. Vap. Deposition, Vol. 14 (2008), p. 145

[4] H. Ye, C. Q. Sun, P. Hing, H. Xie, S. Zhang and J. Wei: Surf. Coat. Technol. Vol. 123 (2003), p. 129

[5] S.B. Abu Suilik, D. Shimamoto, H. Kitagawa, K. Hasezaki and Y. Noda: Diamond Relat. Mater. Vol. 15 (2006), p. 1765

[6] O.J.L. Fox, J. Ma, P.W. May, M.N.R. Ashfold and Yu.A. Mankelevich: Diamond Relat. Mater. Vol. 18 (2009), p. 750

[7] P.W. May, N.L. Allan, M.N.R. Ashfold, J.C. Richley and Yu.A. Mankelevich: Diamond Relat. Mater. Vol. 19 (2010), p. 389

[8] F. Klauser, D. Steinmüller-Nethl, R. Kaindl, E. Bertel and N. Memmel: Chem. Vap. Deposition Vol. 16 (2010), p. 127

[9] A.K. Arora, M. Rajalakshmi and T.R. Ravindran: Encyclopedia of Nanosicence and Nanotechnology Vol. 8 (2004), p.499

[10] S. C. Ramos, A. F. Azevedo, M. R. Baldan and N. G. Ferreira: J. Vac. Sci. Technol. A Vol. 28 (2010), p. 27

[11] Z.Yin, H. S. Tan and F. W. Smith: Diamond Relat. Mater. Vol. 5 (1996), p. 1490

This material is reserved for educational use only, not allowed for commercial use.
Forbidden to modify the content, and cite the document when use.

Engineering Materials and Application

10.4028/www.scientific.net/AMR.651

Effect of Two-Step Deposition Process on Morphology and Optical Properties of Nanostructured Diamond Films

10.4028/www.scientific.net/AMR.651.148

This material is reserved for educational use only, not allowed for commercial use.
Forbidden to modify the content, and cite the document when use.

APPENDIX B

PAPER II

This material is reserved for educational use only, not allowed for commercial use.
Forbidden to modify the content, and cite the document when use.

Applied Mechanics and Materials Vol. 339 (2013) pp 657-664
© (2013) Trans Tech Publications, Switzerland
doi:10.4028/www.scientific.net/AMM.339.657

Nanocrystalline Diamond Films Deposited by Two-step Approach from CH_4/H_2 Microwave Plasma: The Influence of Reactor Pressure

S.T. Khlayboonme*[1,a] and W. Thowladda[1,b]

[1] Surface Physics and Laser Research Laboratory, Department of Physics, Faculty of Science, King Mongkut's Institute of Technology Ladkrabang, Bangkok 10520 Thailand

[a]kktipawa@kmitl.ac.th, [b]ktwarawo@kmitl.ac.th

Keywords: Nanostructure; Chemical vapor deposition; Nanocrystalline diamond film; Plasma impedance.

Abstract. The morphology, growth rate and atomic-bonding structure of nanocrystalline diamond films deposited on Si substrates were investigated under various pressures of the reactor. The films were deposited by CH_4/H_2 microwave plasma with two-step deposition and H_2-plasma cleaning processes. The pressures of 1, 2, 5, 9, and 25 kPa were used for deposition. *In situ* gas-phase species, including electron density, were monitored by an optical spectrometer and impedance analyzer. The films were characterized by SEM, Raman microscope, and white light reflectrometer. When the pressure increased, the surface smoothness and diamond grain size increased, amorphous carbon content decreased, and the intensity ratio of CH/H_β for the growth step increased. The growth rate was in proportional to the ratio of CH/H_β for the nucleation step but in inverse proportion to the electron density. The growth rates decreased from 370 nm/h for 1 kPa to 320 nm/h for 2 kPa. After that, the growth rate rapidly increased to 460 nm/h for 9 kPa, but it gradually decreased to 450 nm/h for 25 kPa. The film refractive indices were 2.16 for 5 kPa, 2.21 for 9 kPa, and 2.38 for 25 kPa. The films grown under 1 and 2 kPa showed highly light absorption.

Introduction

Nanocrystalline diamond (NCD) films have appeared as an innovative material in many applications for their many advantages: advanced combination of intrinsic properties like smooth surface, excellent optical, mechanical and thermal properties, bio-compatibility and chemical inertness [1,2]. The NCD films, which consist of a quantum-sized network of diamond nanocrystals and amorphous carbon matrix, are the novel form of microcrystalline diamond films.

A number of deposition techniques [3] have been used to deposit NCD films. Each deposition technique provides particular forms of the NCD films, differing in terms of diamond particle size, grain boundary nature, amorphous or graphitic matrix, and morphological, structural and optical properties. The film properties also depend on the deposition parameters, resulting in different type of NCD films. Haitao Ye *et al.* [4] have been conducted orthogonal experiments to optimize the processing conditions. These orthogonal experiments predict that the total pressure is the most significant parameter. A few publication reports effect of pressure on NCD films grown by microwave plasma-enhanced chemical vapor deposition (MPECVD) technique, although MPEVCD is one of the most popular techniques for preparing NCD films.

In this work, we focus the influence of reactor pressure on NCD films prepared by a MPECVD technique in CH_4/H_2 gas mixture with a two-step deposition process. The two-step process is necessary for diamond film deposition because the energy for the diamond nucleation is not the same as for the diamond growth. This two-step deposition applied for better surface roughness of the films and nucleation density was performed with the higher concentration of CH_4 in a CH_4/H_2 gas mixture for the nucleation step than for the growth step. The NCD films obtained under different reactor pressures were characterized by field emission scanning electron microscopy (FE-SEM), Raman spectroscopy, and white light reflectrometry. In addition, gas-phase species in the plasma were monitored by an optical emission spectrometer. Plasma impedance was monitored and measured by an impedance analyzer. The measured plasma-impedance has provided electron density in the plasma. Correlation between NCD films grown and gas-phase species, including electron density, present in the plasma will be discussed.

This material is reserved for educational use only, not allowed for commercial use.
Forbidden to modify the content, and cite the document when use.

Experimental

CVD Reactor. The diamond films were performed in a MPECVD bell jar reactor. A 900 W air-cooled magnetron with frequencies of 2.45 GHz was coupled to a WR340 rectangular waveguide. A mode converter being a section of a purpose-designed cylindrical waveguide couples microwave energy from the rectangular waveguide into the reactor by an antenna. A quartz bell jar with 45 mm in diameter and a height of 90 mm was used as a plasma reactor. It was placed on a stainless steel based plate and then attached to the cylindrical waveguide. This MPECVD system also consisted of an impedance analyzer (HOMER-Series STHT V 1.5, S-TEAM Lab), including a matching system. The impedance analyzer was included in the section of the rectangular waveguide and controlled via S-TEAM Homer Windows Visualization and Control software, named Homsoft.

Deposition. The p-type mirror-polished Si(100) wafer was used as a substrate. A pretreatment of the substrate surface was performed by mechanical polishing with a 0-0.5 μm diamond powder suspended in isopropanol for 1 h. Before deposition, H_2 plasma was introduced to clean the substrate surface for 20 min with a flow rate of 200 sccm. Then CH_4 gas was introduced to begin the deposition process. The deposition with two-step approach was carried out under various reactor pressures of 25, 9, 5, 2, and 1 kPa. The two-step deposition process consisted of a nucleation step and a growth step. It was performed by decreasing CH_4 concentration from 2% for the nucleation step to 0.9% for the growth step. The process time was 15 min for the nucleation step and 6 h for the growth step. The total gas flow rate was 200 sccm. The reactor pressure and flow rate can be controlled independently. The absorbed microwave power measured by the impedance analyzer was around 720 W. Under these operating conditions, the substrate temperature was achieved by microwave induction around 850°C. The substrate was placed on a quartz holder and immersed in the plasma.

Plasma Monitor and Material Characterization. To clarify the correlation between gas-phase species in the plasma and the morphology and atomic-bonding structure of the deposited films, we used a spectrometer (HR4000 OceanOptics) and an impedance analyzer. The spectrometer was used to measure *in situ* optical emission intensities of gas-phase species from the plasma. Simultaneously, the impedance analyzer was used to monitor and measure *in situ* impedance of the plasma. It provided further information on the relative changes of electron density. The morphology, thickness, and lateral structure of the films were investigated by FE-SEM (Hitachi S-4700). The bonding structures were characterized by micro-Raman (Renishaw inVia Raman microscope) using an Ar-ion laser with wavelength of 514.5 nm. Optical properties were examined by reflectance measurements with a laboratory set-up for a visible light reflectometer.

Results and Discussion

SEM Analysis. FE-SEM images permit detailed observation of NCD film morphologies as a function of the reactor pressure ranging from 1 to 25 kPa, as shown in Figs. 1(a) - 1(e). The SEM cross-section images show in insets of Fig. 1. The crystallite size was estimated by inspecting SEM images. All films have crystallite size < 50 nm. The surface morphologies of the films grown at 1 and 2 kPa were rougher than that of the films grown at other pressures. These resulted from the higher kinetic energy of species arriving at the growth surface. The morphologies of the films grown at 1 and 2 kPa are similar to those of UNCD films as reported by May and Mankelevich [5]. They also show that the surface morphologies for UNCD films prepared by the MPCVD technique are much rougher than that for UNCD films prepared by the hot filament-CVD technique.

The growth rates plotted as a function of the pressure are shown in Fig. 2. The growth rate was calculated by the film thickness divided by the growth time. The curve of the growth rates can be divided into three parts. The growth rates rapidly decreased from 370 to 320 nm/h when the reactor pressure increased from 1 to 2 kPa. After the further increase in the pressure, the growth rate rapidly increased to 460 nm/h for 9 kPa, and then it gradually decreased to 450 nm/h for 25 kPa.

This material is reserved for educational use only, not allowed for commercial use.
Forbidden to modify the content, and cite the document when use.

Fig. 1. FE-SEM images of NCD films grown on Si substrates under various pressures: (a) 25 kPa, (b) 9 kPa, (c) 5 kPa, (d) 2 kPa, and (e) 1 kPa and cross-section images.

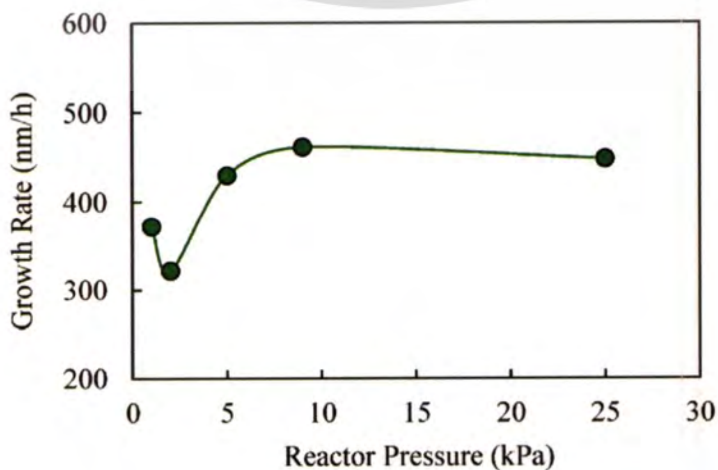

This material is reserved for educational use only, not allowed for commercial use.

Fig. 2. Growth rate of NCD films as a function of the reactor pressure.

Forbidden to modify the content, and cite the document when use.

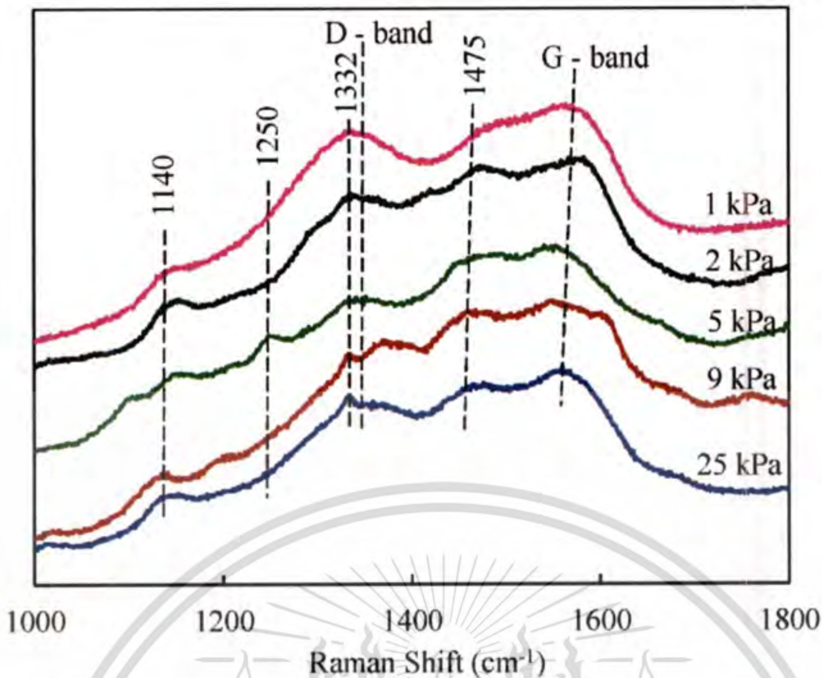

Fig. 3. (Color online) Raman spectra with the photoluminescence background of NCD films under various pressures: 1, 2, 5, 9, and 25 kPa.

Raman Spectroscopy. The atomic-bonding structures of the films were evaluated by Raman analysis. Raman spectra with the photoluminescence background are shown in Fig. 3. They are composed of five features [6]. These features exhibit a diamond peak at 1332 cm^{-1} and several non-diamond phase contributions: disordered-graphite D-band at 1350 cm^{-1}, graphite G-band around 1560 cm^{-1} and *trans*-polyacetylene (t-PA) band around 1140 and 1475 cm^{-1}. The appearance of the t-PA band has always been accepted as the indicator of NCD films [7]. In addition, the broad peak at 1250 cm^{-1}, which is observed in only the film grown at 5 kPa, arises from a broadened vibration density of states of small diamond grains [8]

Raman spectra show drastic changes with decreasing pressure. The 1332 cm^{-1} peak became weaker while the D peak became stronger and overlapped the 1332 cm^{-1} peak. The D peak is related to the small-sized graphitic domains. The G-peak position shifted from 1560 to 1580 cm^{-1}. The weaker intensity of diamond peak and the shift of G peak to higher frequencies suggested the diamond grain size decreases, and grain boundary increases; thus resulting in sp^2 in detriment of sp^3 phase increment with decreasing pressure [9]. In addition, the broad peak at 1250 cm^{-1} was observed in only the film grown at 5 kPa. The appearance of this peak implied that the film formation begins transition from NCD to UNCD phase at this pressure. Moreover, Raman spectrum with no background (not shown here) of the film grown at 1 kPa showed more intense D band than G band, and the *trans*-polyacetylene band showed up only as a small shoulder. This spectrum can be considered as fingerprints for the fine diamond grained structure, related as UNCD [9].

Reflectometry. The reflectance spectra of the films grown at pressures of 25, 9, and 5 kPa are shown in Fig. 4. However, the reflectance spectra of the films grown at 2 and 1 kPa were obstructed due to highly light absorption. The highly light absorption has been explained by the nanocomposite nature of the films, and it is also the characteristic of UNCD films. As reported by Buijnsters *et al.*,[10], UNCD is a highly light absorbing material because it is synthesized with a high renucleation rate and composed of a relatively high fraction of sp^2-bonded carbon connecting the grains.

The refractive indices of the NCD films were calculated from the reflectance spectra with the interference fringes as shown in Fig. 4. They were 2.38 for 25 kPa, 2.21 for 9 kPa, and 2.16 for 5 kPa, increasing with reactor pressure. The refractive index n of those three films gets close to that of diamond (2.41) and quite different from that of graphite (n=1.37) [8]. The presence of the sp^2-bonded carbon matrix lowers the refractive index of the NCD films.

Forbidden to modify the content, and cite the document when use.

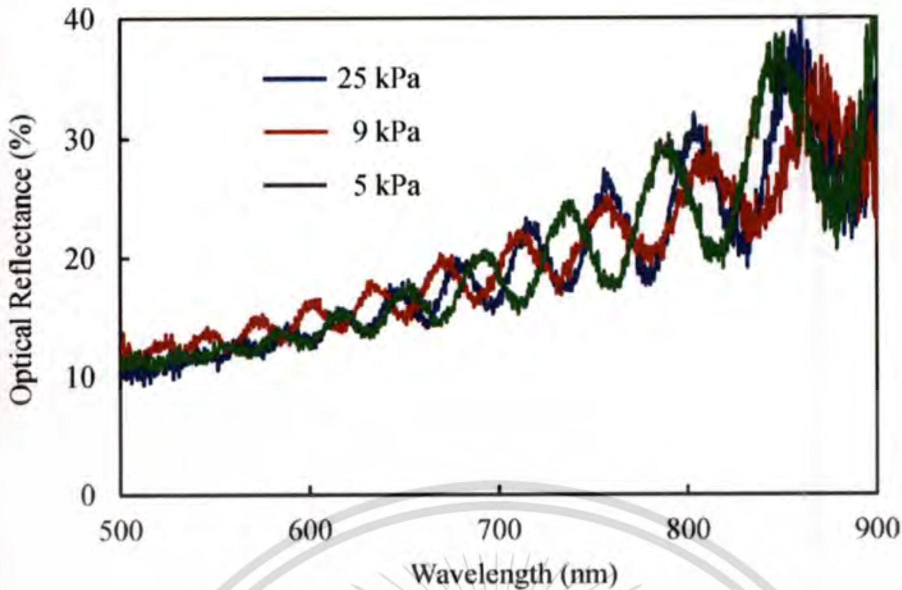

Fig. 4. (Color online) Reflectance spectra of the NCD films grown under various reactor pressures: (a) 25 kPa, (b) 9 kPa, and (c) 5 kPa.

Measurements of Plasma Impedance. The plasma acts as an electrical load of the microwave circuit. The changing of its physical and chemical properties becomes appearing as those of plasma impedance. The plasma impedance normalized by an impedance value of the waveguide was measured by the impedance analyzer. The normalized plasma impedance Z_p and electron density n_e in the plasma are related as [11]

$$n_e = \frac{m_e}{Z_p e^2}(\upsilon_m + j\omega). \quad (1)$$

Here, m_e is the electron mass, ω is the driving frequency, and υ_m is the average elastic collision frequency. The electron density was determined from Eq. 1 and then normalized by n_e of H_2 plasma at a pressure of 1 kPa to become the relative change of n_e. Therefore, the relative changes of n_e were used instead for this work.

The relative changes of n_e as a function of the reactor pressure in each step-deposition process are showed in Fig. 5. They were identical for the nucleation and growth steps. The electron density can be a scale of atomic-H concentration in the plasma due to the breaking-down process of H_2 molecules through an inelastic collision with the energetic electrons. Our measured results also confirm that the emission intensity of H atom changes in a parabolic manner to n_e. The emission intensity of gas-phase species measured by optical emission spectroscopy (OES) directly relates to the density of the species.

Regarding the relative changes of n_e as a function of the reactor pressure shown in Fig. 5, it can be speculated that trend of atomic-H concentration increased as the pressure increased from 1 to 2 kPa. After 2 kPa, the trend rapidly decreased and then gradually increased at the reactor pressure higher than 9 kPa. In contrast to that at 25 kPa, atomic-H concentration at 1 kPa decreased due to too low gas-molecule density. For the CVD growth of diamond films, H atoms (H radicals) in the plasma are consumed by two main reactions [5]. The first one is the dehydrogenation-dissociation reaction to produce the precursor of diamond growth. This reaction caused H radicals to reduce when CH_4 gas was added into H_2 plasma, shown in Fig. 5. The second one is gas-surface reactions, involving H abstraction to form surface sites and subsequent reactions of these sites with H radicals. According to Langmuir isotherm [12], the coverage fraction of H radicals at high pressure is higher than at low pressure. However, it also is affected by concentration of the radicals. Indeed, n_e is not only proportional to the residue of H radical from these reactions but also in inverse relation to the coverage fraction of H radicals.

Forbidden to modify the content, and cite the document when use.

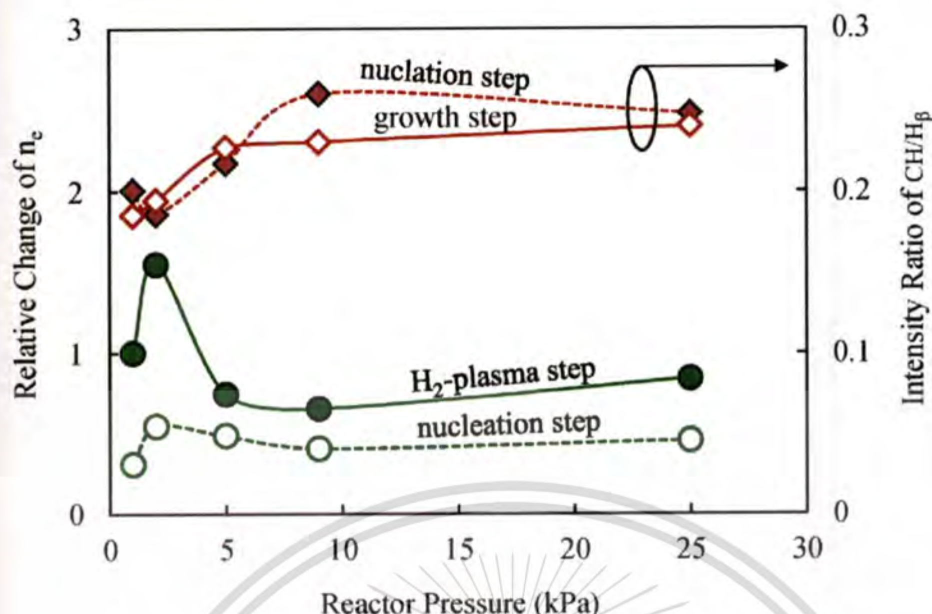

Fig. 5. (Color online) Relative change of n_e and ratios of optical emission intensity of CH(A-X) to H_β, $I(CH)/I(H_\beta)$, as a function of the reactor pressure.

Optical Emission Spectroscopy. Fig. 5 also shows ratios of in situ optical emission intensities of CH (431.0 nm) to H_β (486.1 nm), $I(CH)/I(H_\beta)$, as a function of the pressure. CH_3 radical that plays a role in the growth mechanism can be inferred from CH radical. Although OES cannot provide quantitative information, the emission intensities are still carried out to confirm the relative changes of gas-phase species in the plasma [13]. As shown in the figure, $I(CH)/I(H_\beta)$ in nucleation step was in inverse relation to the relative changes of n_e in H_2-plasma step; as the H-radical residue, mentioned in the previous section, was not. These results indicated that the lower initial-residue of H radicals in the plasma increases CH_3 density in nucleation step.

NCD Films and Gas-phase Species. Considering the results as depicted in Figs. 2 and 5, the growth rate as function of the reactor pressure changed in an inverse manner to the relative change of n_e for H_2-plasma step. On the other hand, it changed on the same manner to the coverage fraction of H radical on the growth surface. This implied that the initial coverage-fraction promotes the diamond growth kinetics and demotes the renucleation rate. In addition, the growth rate also changed in the same manner to the $I(CH)/I(H_\beta)$ ratio for the nucleation step. Trend of this ratio can be indicative of trend of amount of the surface-radical sites for carbon containing radical to absorb. These amounts proportionally depend on the initial coverage fraction of atomic H on the surface.

Raman spectra shown in Fig.3 also related to the intensity ratio shown in Fig. 5. The sp^3-bonded carbon content and diamond grain size of the NCD films directly related with $I(CH)/I(H_\beta)$ ratio in the growth step. This result confirmed that C_1 hydrocarbon radicals (CH_x radicals) are precursors of sp^3 diamond phase for the growth. The changing of these gas-phase species in each step-deposition process can explain pressure dependence of the growth rate, sp^2 and sp^3 carbon content of the subsequent film, and the probability of a renucleation event occurrence.

Summary

This work focused the influence of reactor pressure on the morphology, growth rate, grain size, atomic-bonding structure, and optical properties of NCD films as well as the gas-phase species, including electron density, in plasma. The NCD films were prepared by a MPECVD technique with CH_4/H_2 precursor mixture and two-step approach. Before the beginning of deposition, the Si(100) substrate surface was also cleaned by *in situ* H_2-plasma. The deposition for the films was performed under reactor pressures of 1, 2, 5, 9, and 25 kPa. As the reactor pressure increased, the surface

This material is reserved for educational use only, not allowed for commercial use.
Forbidden to modify the content, and cite the document when use.

smoothness and diamond grain size of the films increased while amorphous carbon content decreased. The pressure influenced the refractive index of the NCD films: 2.38 for 25 kPa, 2.21 for 9 kPa and 2.16 for 5 kPa. However, the NCD films grown under 1 and 2 kPa provided highly light absorption. The growth rates rapidly decreased from 370 to 320 nm/h when the reactor pressure increased from 1 to 2 kPa. As the pressure increased to 9 kPa, the growth rate rapidly increased to 460 nm/h and then decreased with a much slow rate after 9 kPa.

Correlation between materials grown and gas-phase species present in the plasma is important to identify the species driving the process mechanism. The growth rates were in inverse proportion to the n_e relative changes extracted from measurements of plasma impedance in the H_2-plasma step. However, they directly related to the $I(CH)/I(H_\beta)$ ratio in the nucleation step. These behaviors revealed that the surface-coverage fraction of H radicals occurring during the H_2-plasma cleaning step and the density ratio of CH_x radical to H radical for the nucleation step were important to determine the growth rate of the film deposition. Furthermore, the diamond grain size and sp^3 carbon content in the films strongly depended on the $I(CH)/I(H_\beta)$ ratio for the growth step. This result confirmed that C_1 hydrocarbon radicals were precursors of sp^3 diamond phase for the growth of diamond.

The reactor pressure influenced not only concentration of the decomposed radicals but also the coverage fraction of the radicals on the growth surface. The concentration of the radicals and the surface-coverage fraction of radicals manipulated diamond growth kinetics. Generally, the concentration of the decomposed radicals, including H and CH_x radicals, are proportional to the reactor pressure. Those radicals increased not only growth rate but also sp^3 carbon content in the films. However, only increasing CH_x radicals in the gas led to more grain boundaries, sp^2 carbon content, and phase transition unless the atomic-H density increased as well.

Acknowledgment

This work was financially supported by Faculty of Science at King Mongkut's Institute of Technology Ladkrabang, Thailand.

Corresponding Author

S.Tipawan Khlayboonme, kktipawa@kmitl.ac.th , 66-081-296-2134.

References

[1] O.A. Williams: Diamond Related. Mater. Vol. 20 (2011), p. 621

[2] S. Mitura, K. Mitura, P. Niedzielski, P. Louda and V. Danilenko: Journal of Achievements in Materials and Manufacturing Engineering Vol. 16 (2006), p. 9

[3] O. Shenderova and G. McGuire, in: Nanocrystalline Diamond, edited by Y. Gogotsi CRC Press, New York (2006)

[4] H. Ye, C. Q. Sun, P. Hing, H. Xie, S. Zhang and J. Wei: Surf. Coat. Technol. Vol. 123 (2000), p. 129

[5] P. W. May and Y. A. Mankelevich: J. Phys. Chem. C Vol. 112 (2008), p. 12432

[6] A.C. Ferrari and J. Robertson: Phil. Trans. R. Soc. A Vol. 10 (2004), p. 1098

[7] T. Sharda, T. Soga and T. Jimbo: J. Appl. Phys. Vol. 93 (2003), p. 101

[8] F. Klauser, D. Steinmuller-Nethl, R. Kaindl, E. Bertel and N. Memme: Chem. Vap. Deposition Vol. 16 (2010), p. 127

[9] A. Heiman, E. Lakin, E. Zolotoyabko and A. Hoffman: Diamond Related. Mater. Vol. 11 (2002), p. 601

This material is reserved for educational use only, not allowed for commercial use.
Forbidden to modify the content, and cite the document when use.

[10] J. G. Buijnsters, L. Vázquez, G. W. G. van Dreumel, J. J. ter Meulen,W. J. P. van Enckevort and J. P. Celis: J. appl. Phys. Vol. 108 (2010), 103514

[11] M. Moisan and J. Pelletier: Microwave Excited Plasmas, Elsevier Inc, Amsterdam, (1999)

[12] Y. Zhang and G. Chen: J. Vac. Sci. Technol. A Vol. 13 (1995), p. 183

[13] F. J. Kampas: J. Appl. Phys. Vol. 54 (1983), p. 2276

[14] M. Ikeda, H. Ito, M. Hiramatsu, M. Hori and T. Goto: J. Appl. Phys. Vol. 82 (1997), p. 4055

This material is reserved for educational use only, not allowed for commercial use.
Forbidden to modify the content, and cite the document when use.

APPENDIX C

ABOUT AUTHOR

This material is reserved for educational use only, not allowed for commercial use.
Forbidden to modify the content, and cite the document when use.

ABOUT THE AUTHOR

S.Tipawan Khlayboonme was born on January 26, 1975 in Bangkok, Thailand. She has received Bachelor and Mater degrees of applied physics in 1997 and 2001, respectively, from King Mongkut's Institute of Technology Ladkrabang, Bangkok, Thailand, where she has continued working toward the doctoral degree from the year 2007. Now, she is a lecturer at the Department of Physics, Faculty of Science, King Mongkut's Institute of Technology Ladkrabang, Bangkok, Thailand.

This material is reserved for educational use only, not allowed for commercial use.
Forbidden to modify the content, and cite the document when use.